University of Louisville
ThinkIR: The University of Louisville's Institutional Repository

Electronic Theses and Dissertations

5-2017

Development and evaluation of a biocompatible electroactive sensor for continuous blood pressure measurement.

Scott D. Cambron
University of Louisville

Follow this and additional works at: https://ir.library.louisville.edu/etd

 Part of the Biomechanical Engineering Commons, Biomedical Devices and Instrumentation Commons, and the Molecular, Cellular, and Tissue Engineering Commons

Recommended Citation
Cambron, Scott D., "Development and evaluation of a biocompatible electroactive sensor for continuous blood pressure measurement." (2017). *Electronic Theses and Dissertations.* Paper 2622.
https://doi.org/10.18297/etd/2622

This Doctoral Dissertation is brought to you for free and open access by ThinkIR: The University of Louisville's Institutional Repository. It has been accepted for inclusion in Electronic Theses and Dissertations by an authorized administrator of ThinkIR: The University of Louisville's Institutional Repository. This title appears here courtesy of the author, who has retained all other copyrights. For more information, please contact thinkir@louisville.edu.

DEVELOPMENT AND EVALUATION OF A BIOCOMPATIBLE ELECTROACTIVE SENSOR FOR CONTINUOUS BLOOD PRESSURE MEASUREMENT

By

Scott D. Cambron
B.S., University of Louisville, 2003
M.Eng., University of Louisville, 2007
USA

A Dissertation
Submitted to the Faculty of the
J.B. Speed School of Engineering of the University of Louisville
in Partial Fulfillment of the Requirements
for the Degree of

Doctor of Philosophy in Mechanical Engineering

Department of Mechanical Engineering
University of Louisville
Louisville, Kentucky

May 2017

Copyright 2017 by Scott Douglas Cambron

All rights reserved

DEVELOPMENT AND EVALUATION OF A BIOCOMPATIBLE ELECTROACTIVE SENSOR FOR CONTINUOUS BLOOD PRESSURE MEASUREMENT

By

Scott D. Cambron
B.S., University of Louisville, 2003
M.Eng., University of Louisville, 2007

A Dissertation Approved on

March 29, 2017

by the following Dissertation Committee:

_____
Dissertation Co-Director
Robert Keynton, Ph.D

_____
Dissertation Co-Director
Stuart J. Williams, Ph.D

_____
Thomas A. Berfield, Ph.D

_____
Martin O'Toole, Ph.D

_____
Gamini U. Sumanasekera, Ph.D

DEDICATION

This dissertation is dedicated to my father Doug Cambron.

Dad, I promised you I would finish.

And I did.

Dad, I would like to thank you for being my father and my friend, my only male companion in the Cambron household full of women, my mentor - teaching me how to also be a Jack-of-all-trades, my hunting buddy, my coach - showing me that sports are and will always be a game and that they should always be simply enjoyed being played.

"Life isn't about waiting for the storm to pass. It's about learning to dance in the rain."

I Love You Dad and Miss You Everyday

ACKNOWLEDGEMENTS

I would like to first thank my wife and best friend, Jessica Cambron: Thank you for rewarding me with our beautiful and intelligent daughter Sophia and for keeping everything together through all the late nights and long weekends while I worked towards this goal. My parents, Doug and Janie Cambron, and my sisters, Terri Lynn, Renee, Ramona, Regina and Kimberly for being there through thick and thin, and understanding the sacrifices that needed to be made for me to succeed with my education, career and life. Their support has meant the world to me.

Special thanks to Dr. Tommy Roussel, Doug Jackson, Alex Isham, Hanwen Yuan, and Dr. Mark Crain for assisting me with many aspects of my project and for putting up with all my disruptive questions and venting over the years. Many thanks to Dr. O'Toole, Dr. Berfield, Dr. Sumanasekera, and Dr. Williams for the contributions and insight throughout this project and participating on my defense committee.

Most of all I am greatly appreciative to Dr. Robert Keynton for not only being my advisor throughout this arduous and ongoing dissertation project but also giving that 19-year-old "kid" a chance. By giving me the opportunity as an undergraduate research assistant so long ago, to make all this happen. He has undoubtedly assisted in molding me into not only the researcher/engineer that I am today, but also the man as well. Thanks again for your guidance, patience and friendship Dr. K.

ABSTRACT

DEVELOPMENT AND EVALUATION OF A BIOCOMPATIBLE ELECTROACTIVE SENSOR FOR CONTINUOUS BLOOD PRESSURE MEASUREMENT

Scott Douglas Cambron

March 29, 2017

Piezo-active composites have been implemented for sensing and transduction for decades. The 0-3 ceramic/polymer composite is one of the most common composite types used for sensing applications, owing to their tailorable properties of the two-phase composition, consisting of a three-dimensionally connected polymer/rubber matrix (inactive phase) with a dispersion of isolated piezo-ceramic particles (active phase).

This thesis describes a method to develop novel biocompatible perivascular band comprised of a two-phase piezo-active composite to be fabricated using simple manufacturing processes. Biomaterials such as tissue scaffolds comprised of silk fibroin (SF) and chitosan (CS), and biocompatible soft rubbers will be implemented as the three dimensional inactive matrix, while a biocompatible piezo-ceramic nanoparticle such as Zinc Oxide (ZnO) will be pursued as the piezo-active ceramic particles. Two compositions were pursued, 1.) a biocompatible/biodegradable approach consisting of tissue scaffold

(SFCS) and ZnO particle formulation and 2.) a biocompatible soft rubber and ZnO particle formulation. Test samples were fabricated using aforementioned formulations and tested on a custom built dynamic biaxial testing apparatus to correlate mechanical strain to piezoelectric output correlation.

TABLE OF CONTENTS

LIST OF FIGURES

Other techniques for characterizing the viscoelastic time dependent behavior of the SFCS-ZnO blended materials are creep and creep recovery tests, where a constant force

LIST OF TABLES

CHAPTER 1: INTRODUCTION

Cardiovascular disease is the leading cause of death for both men and women in America. Approximately 600,000 Americans die from heart disease each year (1 in every 4 deaths) [1] [2] [3]. Blood pressure is the internal pressure of the circulating blood pushing against the arterial walls, which is pumped from the heart to the rest of the body within the systemic cardiovascular loop. This systemic arterial pressure (SAP) normally rises and falls throughout the day depending on levels of exertion. Normal resting blood pressure in adults is approximately 120/80 mmHg. Systemic hypertension or high blood pressure (HBP) (typically 140+/90+ mmHg) increases a person's risk of cardiovascular disease. Nearly 70 million Americans currently have HPB (1 in every 3 adults) which contributed to more than 360,000 American deaths in 2013 [4].

The pulmonary loop of the cardiovascular system carries deoxygenated blood from the right side of the heart, to the lungs and returns oxygenated blood back to the left side of the heart, only to then return to the systemic loop through the aortic valve. The pulmonary loop is significantly shorter than the systemic, therefore the resting pulmonary arterial pressure (PAP) is normally much lower than SAP. Normal resting PAP in adults is approximately 20/8 mmHg [6]. Pulmonary hypertension (PH) occurs when the pressure in the blood vessels leading from the heart to the lungs within the pulmonary loop is abnormally high (typically 30+/12+ mmHg), resulting in a narrowing of the arteries in the lungs, reducing blood flow, subsequently reducing oxygenation of blood. Pulmonary

hypertension is a rare, devastating disease in which HPB in the pulmonary arteries can lead to right heart failure [7]. The number of PH related deaths and hospitalizations have significantly increased from 15,500 and 260,000 respectively in 2001 to 21,250 and 405,000 respectively in 2010, a 36.5% and 96.7% increase respectively [8]. Ideal medical management requires regular PAP monitoring.

Measurement of systemic blood pressure has been utilized by the medical field since the mid-18th century. In 1733, Reverend Stephen Hales first measured blood pressure by inserting tubes directly into the arteries of animals [9]. Riva Rocci, an Italian physician, developed the first conventional cuff based sphygmomanometer in 1896, when later in 1905, Nicolai Korotkoff described various sounds while auscultating over the brachial artery during deflation of a Rocci style cuff. Later coined Korotkoff Sounds, are used to determine the systolic and diastolic blood pressures. The combination of these 2 noninvasive techniques is still employed today and is considered the gold standard in the medical field for accurate intermittent noninvasive systemic blood pressure measurement [10]. Other noninvasive BP measurement approaches have been implemented in recent years. The oscillometric method employs a sphygmomanometer cuff, similar to the auscultatory method, but with an electronic pressure sensor to monitor cuff pressure oscillations [10]. This method employs proprietary algorithms for calculating systemic systolic and diastolic blood pressure values. Similar to the auscultatory method, the oscillometric method can only record intermittent blood pressure measurements. As of late, systems similar to the CNAP Monitor 500 HD (CN Systems, Austria), a continuous noninvasive hemodynamic monitoring system, have been implemented primarily for surgical procedures such as cesarean section, orthopedic, laparoscopic and vascular surgery

[11]. All of the blood pressure measurement devices/systems mentioned above can and will only measure the SAP of the cardiovascular system.

The most accurate method and the gold standard of measuring SAP is intra-arterial pressure measurement. An invasive surgical procedure where a catheter based hydraulically coupled pressure sensor is typically inserted via radial (wrist), brachial (elbow), femoral (groin), or dorsalis pedis artery (foot). This measurement system allows for continuous SAP monitoring.

Pulmonary arterial pressure cannot be accurately measured via any noninvasive technique. Echocardiography has been pursued as an avenue of noninvasive PAP measurement but has yet to yield repeatable and reliable results [12]. Intra-arterial PAP measurement, otherwise known as right heart catheterization is considered the gold standard, and currently the only reliable method of PAP measurement. The CardioMEMS^{TM} HF wireless measurement system, recently FDA approved (June 2014), is capable of monitoring PAP via a capacitive pressure sensor. Intra-arterial pressure measurement being highly accurate can have negative attributes to overcome such as risk of post-op infection. In the case of the CardioMEMS^{TM} device, migration of device further into the pulmonary system potentially causing an embolism is possible as well as the possibility of post-op infection.

A device that can measure arterial pressure of a vessel without penetrating the vessel wall would be beneficial, devoid of any cardiovascular issues of foreign objects being in the blood stream for an extended amount of time, such as thrombosis or pulmonary embolism.

1.1 Purpose of Study

The overall goal of this project is to *design, develop, characterize and experimentally test an electroactive banding device consisting of organic and/or inorganic materials such as silk fibroin, chitosan, and zinc oxide particles*. The studies presented in this work will focus on: 1.) developing a recipe for manufacturing a material comprised of the ingredients previously listed that can withstand the strain generated by the distension of the pulmonary artery during normal and elevated cardiovascular function, 2.) determining the mechanical properties of said material via ASTM and or ISO standard testing procedures, 3.) determining an association between local mechanical strain and piezoelectric response of the biodegradeable electroactive material, and 4.) designing a band like geometry to be placed around a porcine pulmonary artery ex vivo, properly secured and evaluated on a custom built vascular distension simulation rig.

1.2 Specific Aims

The specific aims for this project are:

Specific Aim 1: *Develop compositions to create moldable biocompatible electroactive piezo-composite (0-3) materials.* Organic and inorganic materials such as silk fibroin (Bombyx mori silkworm), high molecular weight chitosan, and zinc oxide particles will be implemented to produce a band like structure that will be designed to withstand the stresses and strains experienced during distension.

Specific Aim 2: *Determine mechanical properties of the electroactive composite(s).* Following ASTM and or ISO standard procedures, mechanical properties such as elastic modulus, tensile strength, elongation (ASTM D412-06a, ASTM D638-14, ASTM D882-12), and viscoelasticity (ASTM-E328-02, ASTM-D2990-09) will be determined using the eXpert 4000 MicroTest System (Admet,).

Specific Aim 3: *Determine the correlation between mechanical strain and electrical response of the biocompatible electroactive composite material.* The piezoelectric performance of the device will be determined using two different experimental methods: 1.) dynamic testing to apply mechanical strain to the sample; and, 2.) dynamic expansion of an engineered tubular structure by means of a custom vessel distension simulation system, where the fabricated device would be attached or adhered.

Specific Aim 4: *Benchtop ex vivo testing of porcine arterial tissue.* Apply dynamic expansion of porcine pulmonary arterial tissue by means of a custom vessel distension simulation system, where the fabricated device would be attached or adhered around the perimeter of the vessel.

1.3 Significance of Study

In this project, an electroactive 0-3 connectivity piezo-composite sensing device will be developed and fabricated. This device will be comprised of silk fibroin, chitosan, and zinc oxide particles.

This project aims to generate a supplementary viable solution for measuring continuous or real time in vivo pulmonary arterial pressure by developing a compliant electroactive band that will circumscribe the vessel and monitor internal arterial pressure by correlating the circumferential and lateral strains to the electroactive devices response. To date, this type of 0-3 connectivity piezo-composite device for continuous in vivo pulmonary arterial pressure has not been reported.

CHAPTER 2: BACKGROUND

2.1 Cardiovascular Anatomy, Physiology and Disease Review

2.1.1 The Cardiovascular System

The cardiovascular system consists of three primary components, 1.) blood – the biofluid that circulates throughout the body carrying oxygen and nutrients to vital organs and cells, 2.) vasculature – the conduit through which the blood flows and 3.) heart – the pump that drives the flow of the blood through the vasculature [13]. Often referred to as the circulatory system, blood follows a circular path through the body. The general pattern of the circulatory blood flow is shown in Figure 2.1 and comprises of two loops: the pulmonary loop consisting of all vasculature within the lungs and those connecting the heart to the lung, and the systemic loop which includes the vasculature of the rest of the body. The pulmonary loop of the cardiovascular system carries deoxygenated blood (blue in Figure 2.1) from the right side of the heart, to the lungs and returns oxygenated blood (red in Figure 2.1) back to the left side of the heart, only to then return to the systemic loop through the aortic valve to then be pumped to the rest of the body [13] [14].

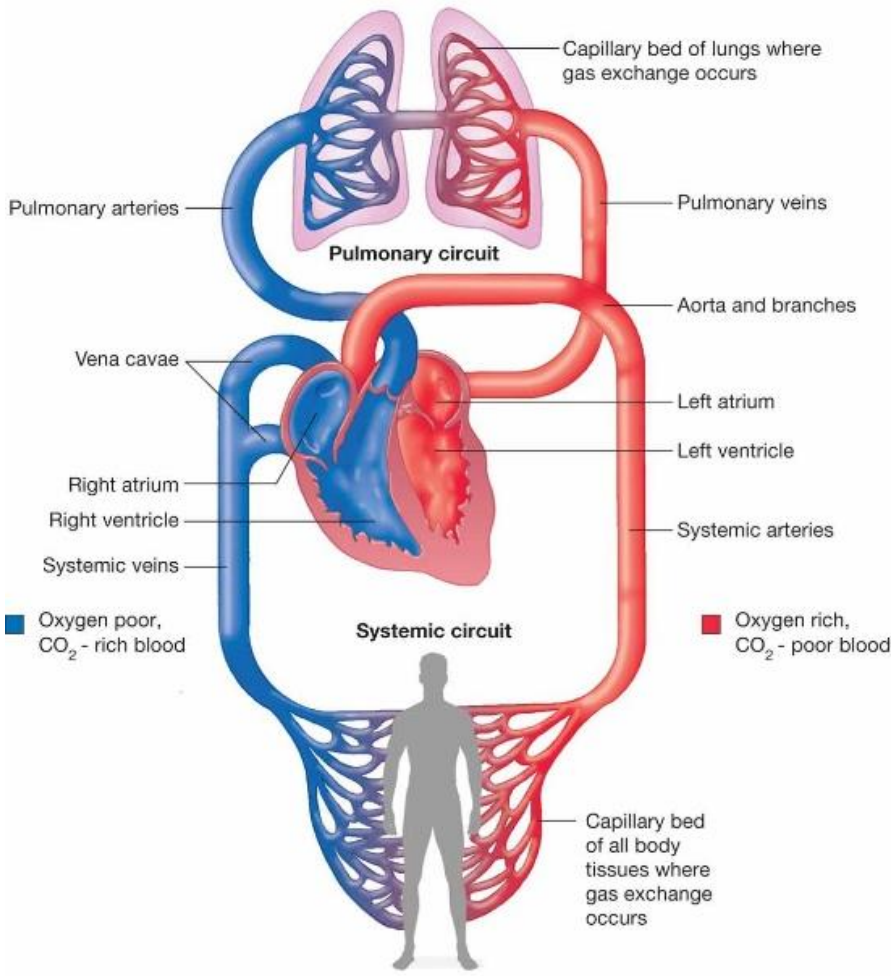

Figure 2.1. Illustration of the cardiovascular system, displaying the pulmonary and systemic flow circuits. [9]

2.1.2 Cardiovascular Disease and Heart Failure

Cardiovascular disease is the leading cause of death in both men and women in America**.** Approximately 600,000 Americans die from heart disease each year (1 in every 4 deaths) [3] [4]. Heart failure is typically the final path of most chronic cardiovascular diseases. In 2005, Approximately 6 million Americans are currently living with heart

failure, of those, approximately 25% had advanced or end stage heart failure (ESHF) [15]. Advanced forms of heart failure typically involve transplantation of the heart for patients who are eligible. Ineligible patients whether due to age or other health problems are typically given a ventricular assist device (VAD) that can potentially extend the life of the patient [16].

2.1.3 Ventricular Assist Devices

The introduction of the ventricular assist device in the 1980's alongside the advances in cardiac transplantation, VADs were used for the salvage of patients with advanced heart failure accompanied by shock and multiple organ dysfunction, with the goal of future heart transplantation [15]. Traditionally a Left Ventricular Assist Device (LVAD) is employed to assist the left side of the heart (as an unloading mechanism) in pumping oxygenated blood through the systemic circuit, connecting the inflow cannula of the pump to the apex of the left ventricle and the pump outlet to the outflow cannula in the ascending aorta (Figure 2.2a). Right Ventricular Assist Devices (RVAD) are typically employed to assist the right side of the heart in pumping deoxygenated blood through the pulmonary circuit [17], the inflow cannula channels blood from the right ventricle to the pump, and the outflow cannula channels blood from the pump to the pulmonary artery (Figure 2.2b).

It is common for VAD patients to develop HBP; physicians overseeing patients with implanted VADs will attempt to maintain normal blood pressure, by adjusting pump performance in combination with prescribing HBP medication [18]. The VAD performance adjustments are typically made while in the heart/device specialist office while closely monitoring BP.

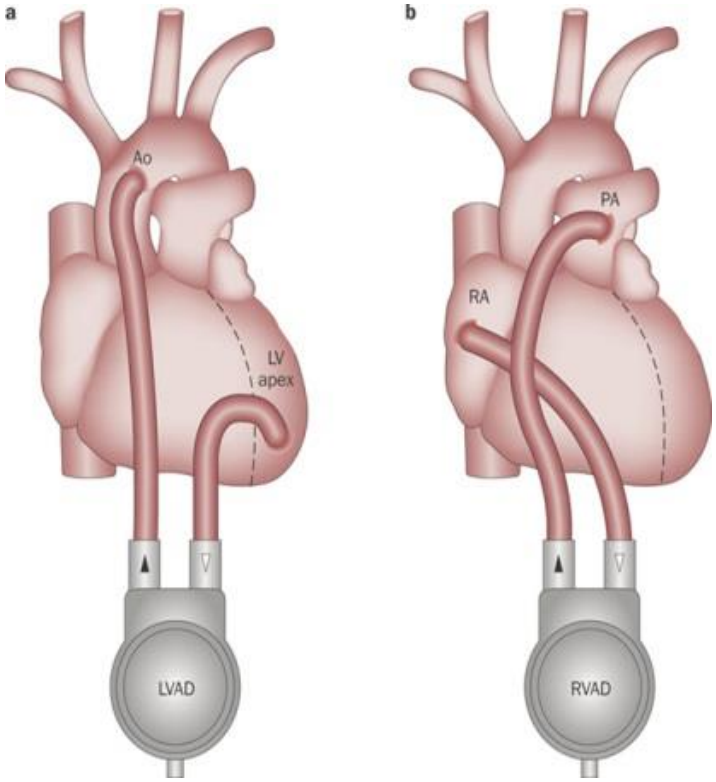

Figure 2.2. Examples of ventricular assist devices a.) Left Ventricular Assist Device LVAD, b.) Right Ventricular Assist Device RVAD [13]

2.1.4 The Baroreflex

In a healthy cardiovascular system, BP is stabilized and kept near homeostasis with the assistance of the baroreflex [19]. This reflex is initiated by a series of internal pressure sensors termed baroreceptors, which are primarily located within the large arteries of thoracic and neck regions (i.e. carotid, aorta, and pulmonary artery) that sense the rapid change in blood pressure via distension of the blood vessel and sending that signal to the nervous system to make the desired adjustment to rapidly raise or lower SAP and/or PAP. This baroreflex is ineffective in patients with VADs, there is currently no feedback

mechanism that actively monitors BP and communicates said rapid changes to the VAD for immediate adjustment.

2.1.5 Blood Pressure and Hypertension

Blood pressure (BP) is the internal pressure of the circulating blood pushing against the vessel walls, which is pumped from the heart to the rest of the body within the systemic loop [19]. This systemic arterial pressure (SAP) normally rises and falls throughout the day depending on levels of exertion. Normal resting BP in adults is approximately 120/80 mmHg (Table 2.1). Systemic hypertension or high blood pressure (HBP) (typically 140+/90+ mmHg) increases a person's risk of cardiovascular disease. Patients with SAP or left heart related heart failure will typically have a Left Ventricular Assist Device (LVAD) implanted to assist in pumping blood through the systemic loop [17]. Maintaining a stable systemic BP is critical for proper cardiovascular and other vital organ function throughout a healthy body.

Table 2.1. Normal and Hypertensive Systemic and Pulmonary Loop Blood Pressure Values [14]

UNITS mmHg	**Systemic Loop**		**Pulmonary Loop**	
	Normal	**Hypertensive**	**Normal**	**Hypertensive**
Systolic	90-140	140+	20-30	30+
Diastolic	60-90	90+	8-12	12+
Mean	70-100	100+	25	25+

The pulmonary loop is significantly shorter than the systemic loop; therefore the resting pulmonary arterial pressure (PAP) is normally much lower than SAP. Normal resting PAP in adults is approximately 20/8 mmHg [8]. Pulmonary hypertension (PH) occurs when the pressure in the blood vessels leading from the heart to the lungs within the pulmonary loop is abnormally high (typically 30+/12+ mmHg) shown in Table 2.1, resulting in a narrowing of the arteries in the lungs, reducing blood flow, subsequently decreasing oxygenation of blood. Pulmonary hypertension is a rare and devastating disease in which HBP in the pulmonary arteries can lead to right heart failure [7]. The number of PH related deaths and hospitalizations have significantly increased from 15,500 and 260,000 respectively in 2001 to 21,250 and 405,000 respectively in 2010, a 36.5% and 96.7% increase respectively [8]. Patients with PAP or right heart related heart failure will typically have a RVAD implanted to assist in pumping blood through the pulmonary loop.

Pulse pressure (PP) is

$$PP = SP - DP \tag{1}$$

where the systolic pressure (SP) is the point of maximum pressure in the Systole Period of ventricular contraction, forcing of blood into aorta and pulmonary artery, and the diastolic pressure (DP) is the point of minimum pressure in the Diastole Period of ventricular relaxation [13]. Figure 2.3 shows representative pulse pressure waveforms for normal SAP and PAP.

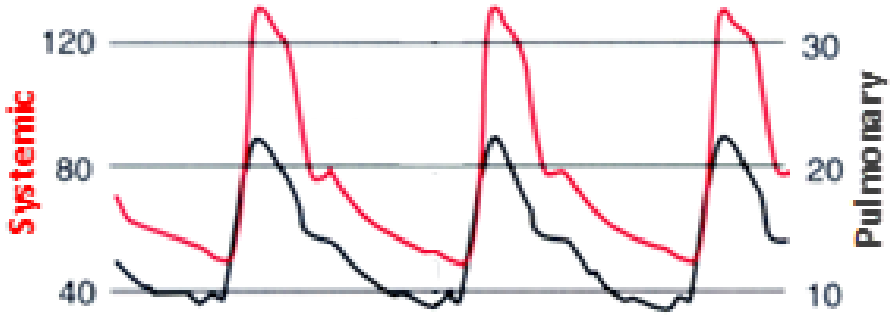

Figure 2.3. Representation of the pulse pressure waveform for the systemic loop (red) and the pulmonary loop (black). *(Redrawn from [16]*)

2.1.6 Arterial Wall Mechanics

Arterial stiffness plays an essential role in cardiovascular disease and end stage heart failure. During HBP progression, SAP and or PAP increases, the arterial vessels undergo remodeling, the vessel walls become thicker and the modulus of elasticity increases [20] [21] [22]. Both changes considerably affect arterial stiffness. Figure 2.4 shows a general representation of changes in diameter within a vessel during changes in pulse pressure. The amount of expansion depends on the mechanical condition of the artery.

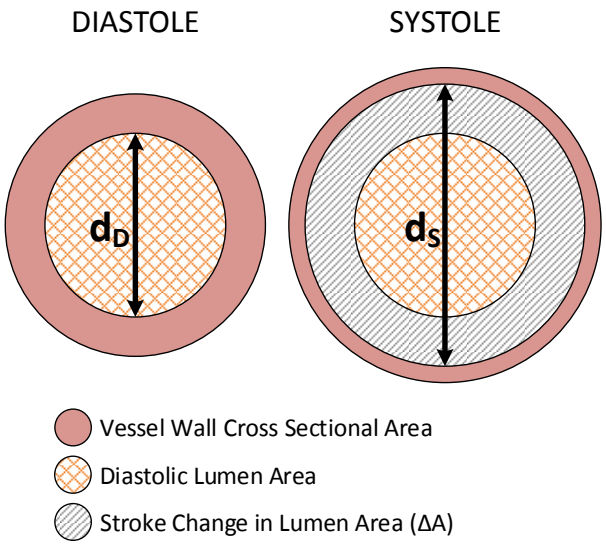

Figure 2.4. Schematic representation of change in diameter of arterial vessel during change in pulse pressure

As an arterial vessel remodels with increased stiffness, there are measurable metrics for evaluation, all of which are typically based upon the non-invasive measurement of vessel diameters and lumen areas during the cardiac cycle via techniques such as ultrasound, magnetic resonance imaging (MRI), and echo tracking [17]. Echo tracking devices can accurately measure diameter (d) and the stroke change in diameter (Δd) of various large arteries [23] [24]. Distension is the measurement of the change in vessel diameter

$$D = d_S - d_D \tag{2}$$

where d_S is the systolic diameter and d_D is the diastolic diameter. The cross-sectional distensibility coefficient (DC) is considered a determinant of stress of the vessel wall is the relative change in lumen area for a given change in pressure

$$DC = \frac{A_S - A_D}{A_D \times PP} \tag{3}$$

where the A_S is the systolic cross-sectional lumen area, A_D is the systolic cross-sectional lumen area and PP is the pulse pressure. Cross-sectional compliance coefficient is the absolute change in lumen area for a given pulse pressure by

$$CC = \frac{A_S - A_D}{PP} \tag{4}$$

The cross-sectional measurements can be implemented assuming the arterial vessels predominantly change in diameter and not length during the cardiac cycle [25]. Peterson's Modulus is the inverse of distensibility and represents the ratio of stress to strain in terms of the pulse pressure and measurable lumen area parameters [26]

$$E_P = \frac{1}{DC} = \frac{A_D \times PP}{A_S - A_D} \tag{5}$$

The elastic modulus of the arterial wall is denoted as

$$E_{inc} = \frac{3\left(1 + \frac{A_D}{WCSA}\right)}{DC} \tag{6}$$

where

$$WCSA = \frac{\pi(d_O^2 - d_I^2)}{4} \tag{7}$$

where d_O is the outer diameter and d_I is the inner diameter of the arterial vessel. Circumferential strain is the measure of change in circumference of a vessel through diastole and systole, which is equivalent to

$$\varepsilon_C = \frac{\pi(d+\Delta d)}{\pi d} = \frac{d_S - d_D}{d_D} \tag{8}$$

where the changes circumference can be reduced to changes in diameter. Table 2.2 shows measured systolic and diastolic lumen areas of healthy patients and patients with pulmonary hypertension [21]. Distension and circumferential strain were calculated from the measured lumen areas.

Table 2.2. Pulmonary arterial distension and circumferential strain in healthy patients and patients with PH [18]

	Systolic Area (mm^2)	**Diastolic Area (mm^2)**	**ΔA**	**Δd**	**ε_c (%)**
Healthy Patient	710	450	260	6.13	25.6
PH during exertion	620	480	140	3.37	13.7
PH at rest	1070	850	220	4.01	12.2

The above-mentioned indices are a means of non-invasively quantifying the regional arterial stiffness of a patient to determine the level of severity of arterial stiffness related to hypertension and or other cardiovascular related diseases.

2.2 Blood Pressure Measurement and Sensing Technologies

Measurement of systemic BP has been utilized by the medical field since the mid-18th century. In 1733, Reverend Stephen Hales first measured BP by inserting tubes directly into the arteries of animals [9]. Riva Rocci, an Italian physician, developed the first conventional cuff based sphygmomanometer in 1896, when later in 1905, Nicolai Korotkoff described various sounds while auscultating over the brachial artery during deflation of a Rocci style cuff. Later coined Korotkoff Sounds, are still used to determine the systolic and diastolic blood pressures.

2.2.1 Noninvasive Measurement Techniques

The combination of the two abovementioned noninvasive techniques is still employed today and is considered the gold standard in the medical field for accurate intermittent noninvasive systemic BP measurement [10]. Other noninvasive BP measurement approaches have been implemented in recent years. The oscillometric method employs a sphygmomanometer cuff, similar to the auscultatory method, but with an electronic pressure sensor to monitor cuff pressure oscillations [10]. This method employs proprietary algorithms for calculating systemic systolic and diastolic blood pressure values. Similar to the auscultatory method, the oscillometric method can only record intermittent blood pressure measurements. Recently, systems similar to the CNAP Monitor 500 HD (CN Systems, Austria), a continuous noninvasive hemodynamic monitoring system, have been implemented primarily for surgical procedures such as cesarean section, orthopedic, laparoscopic and vascular surgery [11]. All of the blood

pressure measurement devices/systems mentioned above can and will only measure the SAP of the cardiovascular system.

2.2.2 Invasive Measurement Techniques

The most accurate method of measuring SAP is intra-arterial pressure measurement. An invasive surgical procedure where a catheter based hydraulically coupled pressure sensor is typically inserted via radial (wrist), brachial (elbow), femoral (groin), or dorsalis pedis artery (foot). This measurement system allows for continuous SAP monitoring [27].

Cong et al developed an in vivo blood pressure monitoring system for small laboratory animals such as rats for real time measurement to be employed in biomedical and genetic research to identify genetic variation susceptibility to diseases such as hypertension [28] [29]. This type of perivascular device is placed around the carotid artery of a rat, a capacitive pressure sensor is immersed in silicone oil and continuously monitors the systemic blood pressure (Figure 2.5). Figure 2.5 displays actual laboratory rat blood pressure waveform recorded wirelessly with high fidelity and accuracy.

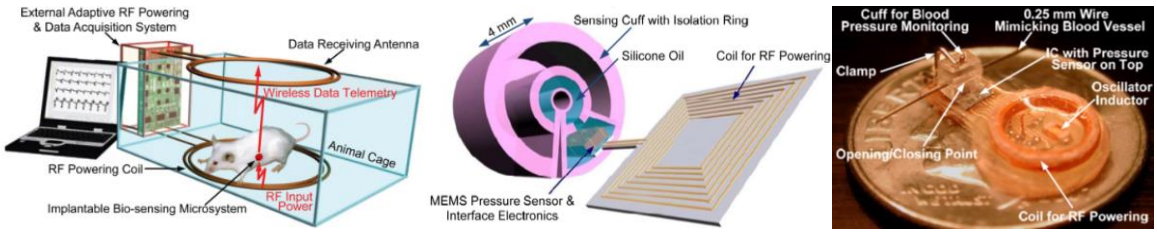

Figure 2.5. In vivo blood pressure cuff. [28]

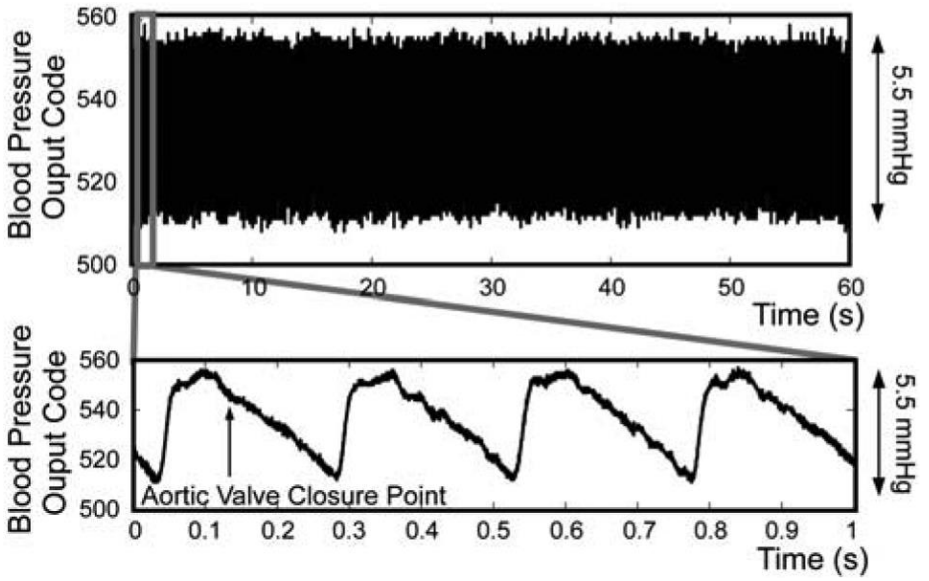

Figure 2.6. In vivo data from In vivo blood pressure cuff. [28]

Pulmonary arterial pressure cannot be accurately measured via any noninvasive technique. Echocardiography and MRI have been pursued as avenues of noninvasive PAP measurement but has yet to yield repeatable and reliable results [30]. Intra-arterial PAP measurement, otherwise known as right heart catheterization is considered the benchmark, and currently the only reliable method of PAP measurement [12]. The CardioMEMS^{TM} HF wireless measurement system, recently FDA approved (June 2014), is capable of wireless monitoring PAP via a capacitive pressure sensor [7].

None of the aforementioned devices directly have the ability to act as a feedback control sensor to mimic the functionality of the baroreceptors of a healthy human cardiovascular and nervous systems.

2.3 Introduction Piezo-Composites

2.3.1 Piezo Composites

Piezo-active composites have been implemented for sensing and transduction for decades [31]. A traditional 2-phase composite is identified with a two number notation "*m*-*n*," where *m* represents the connectivity of the active phase and *n* for the inactive phase. Figure 2.7 shows an array of possible connectivity configurations of piezocomposites between active and inactive phases (i.e. piezo ceramic rods within polymer matrix respectively, a 1-3 piezocomposite) [31] [32] [33].

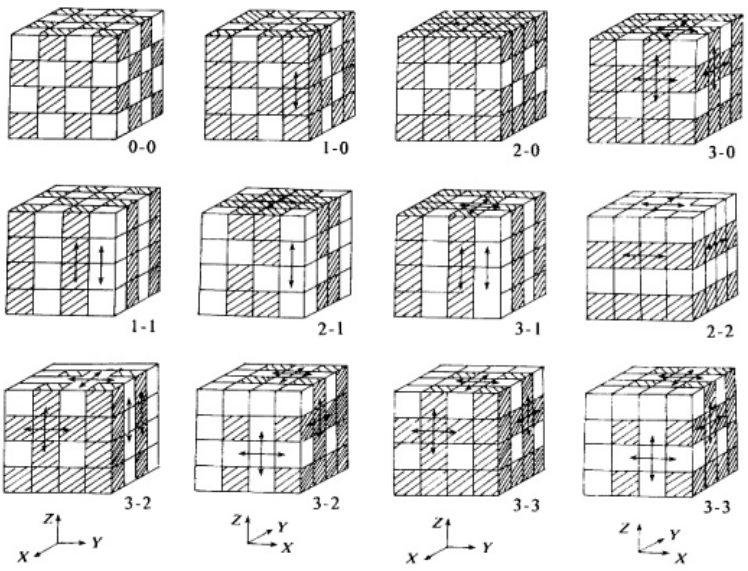

Figure 2.7. Illustration displaying connectivity of piezocomposites. Active phase (hatched cubes), inactive phase (white cubes) [31]

The 0-3 ceramic/polymer composite is one of the most common composite types used for sensing applications, owing to their tailorable properties of the two-phase composition

[31], consisting of a three-dimensionally connected polymer/rubber matrix (inactive phase) with a dispersion of isolated piezo-ceramic particles (active phase), shown in Figure 2.8 [34]. The 0-3 composite can have a high range of mechanical flexibility depending on whether a polymer or rubber is employed.

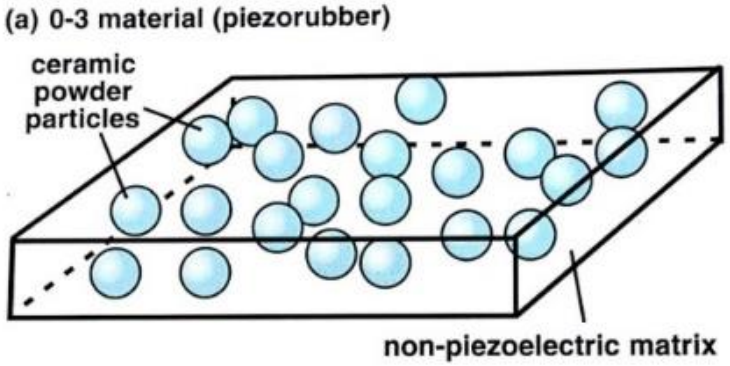

Figure 2.8. Illustration of a 0-3 composite [34]

2.3.2 Tissue Scaffolds

Tissue engineering arose in the early 1990s to address boundaries of tissue grafting and repair [35]. There are a number of essential considerations when determining a suitable scaffold material: 1.) *biocompatibility* allowing cells to adhere, function normally and migrate onto and through the scaffold in order to proliferate, 2.) *biodegradability* permitting the cells to produce their own extracellular matrix (ECM) over time to replace the implanted scaffold without any toxic byproducts to effect other organs or functions, 3.) *mechanical properties* analogous to the implanted scaffold anatomical site and also strong enough to withstand physician handling during implantation, 4.) *architecture* primarily having a highly porous interconnected structure to ensure cellular growth penetration and

biofactor diffusion, and 5.) *manufacturability* being clinically and commercially viable fabrication procedure [36]. The concept of a scaffold is to transplant biofactors such as cells, genes and/or proteins, within the porous degradable scaffold to stimulate tissue repair. The scaffold material and porous architecture play a significant role in tissue regeneration by preserving tissue volume, providing temporary mechanical function, and delivering biofactors. A successful scaffold should balance mechanical function with biofactor delivery, providing a successive transition in which the regenerated tissue assumes function as the scaffold degrades.

Silk fibroin (SF) is a natural fibrous protein employed in tissue scaffold applications due to having high permeability to water and oxygen, cell adhesion and growth characteristics, low inflammatory response and high tensile strength with flexibility [37] [38] [39]. The *Bombyx mori* silkworm cocoon shown in Figure 2.9 is one source for silk fibroin extraction.

Figure 2.9. Image of Bombyx mori silkworm, moth and cocoons.

Chitosan (CS) is a partially deacetylated product of chitin, a crystalline polysaccharide found in crustaceans such as shellfish. This material has great potential as a component within tissue scaffolds due to being nontoxic, biodegradable, and having excellent wound healing characteristics [40] [41].

The combination of the aforementioned biomaterials provides exceptional chemical, architectural, and mechanical properties which can be implemented into a highly porous tissue scaffold for tissue engineering applications. This porous scaffold could act as the inactive *n* phase of a 0-3 piezocomposite.

2.3.3 Zinc Oxide Nanoparticles

Zinc Oxide (ZnO) nanoparticles are a class of engineered ceramic particles that exhibit unique semiconducting and piezoelectric properties. The crystal structure of ZnO can either be cubic zinc blende (Figure 2.10a) or hexagonal wurtzite (Figure 2.10b) where each anion is surrounded by four cations at the corners of a tetrahedron. The natural and most stable crystalline structure is the wurtzite configuration, having low symmetry resulting in spontaneous polarization [42].

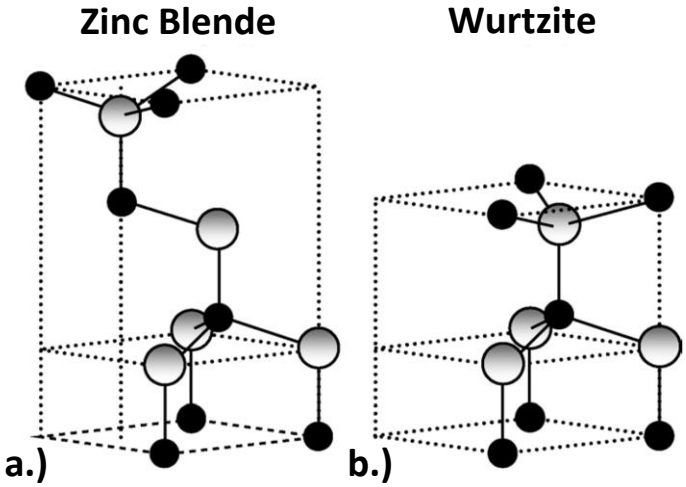

Figure 2.10. Illustration of a.) cubic zinc blende and b.) hexagonal wurtzite. Shaded gray and black spheres represent Zn and O atoms, respectively [42].

ZnO has high piezoelectric constants with electromechanical coupling, making it an important material for piezo-transduction. ZnO also possesses excellent antibacterial, antimicrobial, and biocompatible properties with no adverse effect on cellular function [41] [43]. This engineered ceramic nanoparticle is a viable option as the active *m* phase of a 0-3 piezocomposite.

CHAPTER 3: MATERIALS AND METHODS

3.1 Instrumentation and Equipment

3.1.1 Laser Cutting System

The LS1630 laser cutting system (Boss Lasers, LLC, Sanford, FL, www.bosslaser.com) consists of a 60W CO_2 laser tube traversing over a 30 inch (X) by 16 inch (Y) honeycomb and knife blade material supporting platform (Figure 3.1). The X-Y-Z axis stage has an operational volume of 30.5 by 15.5 by 10 inches respectively with a positioning resolution of 0.001 inches along all three axes. The Z axis has a contact based linear potentiometer auto focus attachment that rapidly adjusts the distance between the laser cutting head and material to be cut for optimal focal distance. While the system is in operation and cutting materials such as sheet form of polymer, wood, or rubber, volatile fumes and particulates are typically released from the material. They have to be safely evacuated and/or filtered from the laser cutting enclosure. A 250 cubic foot per minute (CFM) exhaust fan system is employed to vent the volatile fumes/particulates out of the laser cutting system enclosure and safely into the building HVAC fume extraction system.

Figure 3.1. Image of Boss LS1630 60 Watt CO_2 laser cutting system.

3.1.1.1 Operation - File Generation

Design the desired structure of interest using SolidWorks or other computer-aided design (CAD) package of choice. Import the 3D part file into a 2D drawing environment. Save the 2D file as an Adobe Illustrator file (.AI), then open the .AI file in adobe illustrator and immediately save it as .ai again. This procedure repairs a conversion issue generated by the SolidWorks software within the *.AI file. Import .ai file into the RDWorks software.

3.1.1.2 Operation - Laser Cutter

Turn on chiller. Home the laser head. Turn on laser cutter via key on top of enclosure near integrated control panel. Open RD Works software. Manipulate imported .ai file in RDWorks, creating an array of said part to generate an efficient nested group for cutting if needed. Go to Handle > Cut Optimize to improve the order of cut operations between the part features to be cut. Set cutting speed and laser power settings within the Work tab. A power setting of 41% and cutting speed of 18 mm/s is utilized for cutting 3 mm thick acrylic. Load material onto honeycomb material holding platform, tape edges down if material does not maintain stable flatness. Position laser head to desired location over material to be cut. Focus the laser head employing the auto focus attachment. Save machine output file. Turn on exhaust blower and laser head compressor via surge protector switch. Run the machine output file.

3.1.2 Custom Material Mixing System

The Tri-R Stir-R Model X63C 1/15 HP variable speed laboratory mixer (Tri-R Instruments, Jamaica, NY) has a functioning range of 0 – 12,000 RPM (Figure 3.2a). This device was utilized to mechanically mix the SFCS and SFCS-ZnO blends using a custom made wire mixer head (Figure 3.2b) and modified laboratory spatula (Figure 3.2c). The mixer was rigidly attached to the z-axis of a mechanical translation stage. To allow for easy and precise placement of the mixer head within the sample vials.

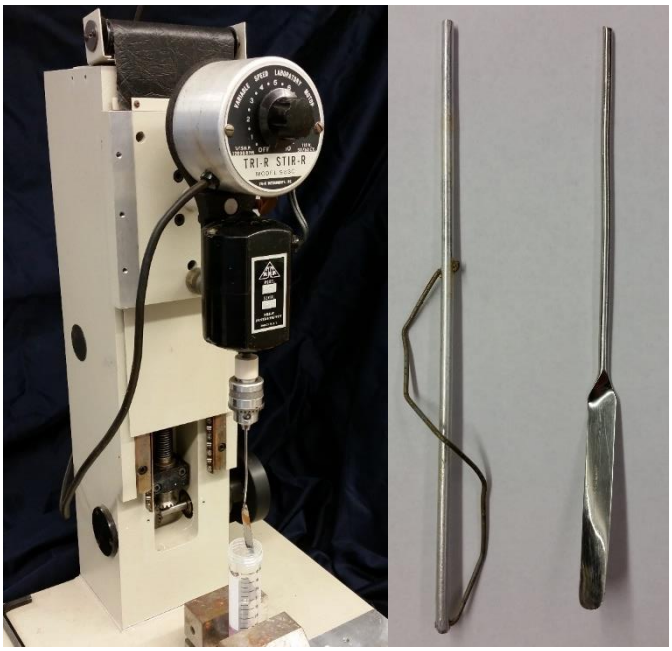

Figure 3.2. Image of Tri-R Stir-R Model X63C 1/15 HP variable speed laboratory mixer with modified laboratory spatula mounted in the ¼ inch Jacobs chuck.

3.1.3 Viscometer

The LVDV-II+ Viscometer (Brookfield Ametek, Middleboro, MA) instrumented with cone and plate configuration (CP-52) is employed to measure the viscosities of the SFCS-ZnO blends. This device operates by applying shear on a fluid between the rotating cone and the static plate, then measuring the rotational resistance exerted by the fluid. Using preprogrammed algorithms, the viscometer hardware converts the resistance torque to viscosity. A constant, controllable temperature of the cone and plate assembly is maintained via the water jacketed assembly that is plumbed to a heated/refrigerated bath and circulator (TC-500, Brookfield Ametek, Middleboro, MA; Figure 3.3).

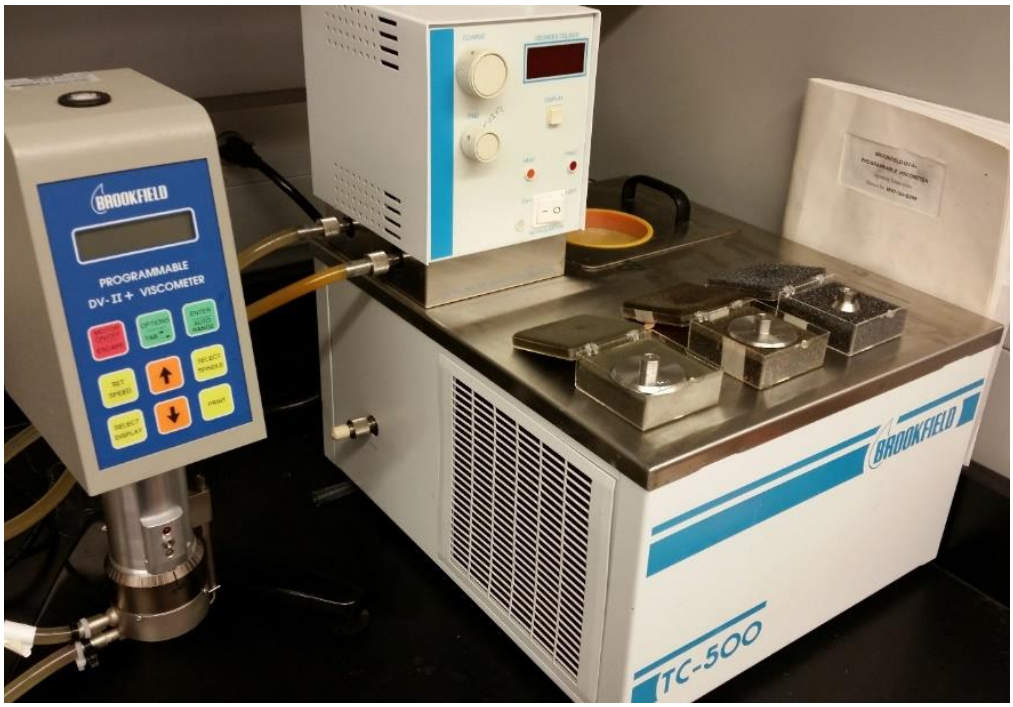

Figure 3.3. Cone and plate viscometer with water bath circulator.

3.1.3.1 Operation

Remove the cone from the viscometer spindle if one is mounted. Turn on the viscometer (switch in rear) for the system to run an auto-diagnostic procedure with the spindle unloaded. Mount the desired cone to the spindle when prompted by the viscometer Graphical User Interface (GUI). The CP-52 is utilized for this investigation due to its broad viscosity and shear rate range (Table 3.1).

Table 3.1. Cone and plate viscometer parameter ranges.

Cone Spindle	CP-52
Shear Rate (s^{-1})	0 - 400
Viscosity Range (cP)	4.6 – 92,130
Sample Volume (mL)	0.5
SMC	9.83
SRC	2

The full scale viscosity range is given by:

$$\eta_s = TK \times SMC \times \frac{10000}{RPM} \tag{9}$$

where TK is the torque constant, equal to 0.03973 for the LVDV-II+, SMC is the spindle multiplier constant, shown in Table 3.1, and RPM is the spindle rotational speed in revolutions per minute. While the Shear Rate is calculated by:

$$SR = SRC \times RPM \tag{10}$$

where SRC is the shear rate constant (Table 3.1). In order to determine the viscoelastic characteristics of the SFCS-ZnO blends, sample measurements are taken at varying shear

rates of 3, 6, 12, and 24 s^{-1}, to determine the shear thinning phenomenon and non-Newtonian nature of the blends.

3.1.4 PH Meter

The pH and Electrochemistry Meter (Phi 570, Beckman Coulter Inc., Fullerton, CA) measures the pH of a solution, indicating its acidity or alkalinity (Figure 3.4). The pH meter has a detection range from 0.00 to 14.00 pH with a resolution of 0.01 and an accuracy of ±0.01 pH. The pH meter measures the difference in electrical potential between a pH sensing electrode and a reference electrode. pH measurements sare recorded fromfor the pure SFCS blends, ZnO nanoparticle dispersions and SFCS-ZnO blends prior to fabrication of the final tissue scaffold structures.

Figure 3.4. pH Meter

pH measurements were recorded from the pure SFCS blends, ZnO nanoparticle dispersions and SFCS-ZnO blends prior to fabrication of final tissue scaffold structures.

3.1.5 Lyophilization System

Upon blending of the SFCS-ZnO tissue engineered scaffold solution, in order to achieve high porosity, the lyophilization or freeze drying process was implemented. During freeze-drying, the sample is frozen using a -80°C freezer and then placed in glass vacuum jars that are plumbed to a refrigerated vacuum chamber of the FreeZone Plus 4.5 Liter Cascade Console Lyophilization System (7751040, Labconco, Kansas City, MO; Figure 3.5). A rotary vane vacuum pump (M8C Maxima™ C Plus, Fisher Scientific™) evacuates the air from the chamber and an upright refrigerated stainless steel moisture collector coil removes a maximum of 1.8 liters of water in 24 hours. The water in the frozen samples sublimates from ice directly into water vapor and collects onto the cold collector coil.

Figure 3.5. FreeZone Plus 4.5 Liter Cascade Console Freeze Dry System

3.1.5.1 Operation

Verify that the vacuum chamber lid, drain tube cap and all vacuum jar chamber ports are closed. Press the button labeled “auto” to initially enable the refrigeration system. Once the temperature reaches -40°C in the collector coil, the vacuum pump engages and pumps down until ~50 mTorr. Load frozen samples into vacuum jars and insert into the chamber ports. Gradually open chamber port valves until the vacuum chamber pressure stabilizes below 100 mTorr and maintain this pressure for at least 24 hours to allow for

complete removal of water from the samples. Initiate the shutdown procedure by pressing the "auto" button to disable the vacuum pump and refrigeration system. Purge the vacuum chamber with atmospheric air and remove the samples from vacuum jars. Remove vacuum chamber lid and drain tube cap. Place open drain tube into a 4 liter Erlenmeyer flask to collect the melted ice from the collector coil and turn off the switch on right side of cabinet.

3.1.6 Digital-Control Water Bath

The fabricated SFCS-ZnO are samples suspended in phosphate buffered saline (PBS) solution are placed water bath at 37°C to incubate the samples in 4 hour intervals, replenishing the PBS in order to leach out any residual chemicals implemented in the scaffold construction process. The IsoTemp 215 digital temperature-controlled water bath (IsoTemp 215, Fisher Scientific, Hampton, NH; Figure 3.6), with an operating temperature range from ambient to 100°C at a resolution of 0.1°C and thermal uniformity of ±0.24°C,

is thermally controlled via PID closed loop feedback system. At a set temperature of 37°C, the water bath has an increased accuracy and stability of ±0.5°C.

Figure 3.6. Image of IsoTemp 215 digital control water bath

3.1.7 Scanning Electron Microscope

The LEO Supra 35 variable pressure scanning electron microscope (VPSEM) (Carl Zeiss, Oberkochen, Germany) was used to image the SFCS-ZnO scaffolds in this investigation. The VPSEM has a nominal resolution of 1.7 nanometers at 15 kV, and a nominal resolution of 2.0 nanometers at 30 kV in variable pressure (VP) mode (Figure 3.7). It has a magnification range of 12x to 900,000x, and a VP vacuum range of 2 to 133 Pa in steps of 1 Pa. The focused beam of electrons from the VPSEM impacts an electrically-grounded sample with a focused beam of electrons, which dislodge additional electrons from the sample. While the beam scans the sample, the extricated electrons are collected

and converted to representative topographical imagery with a resolution of approximately 2 nm.

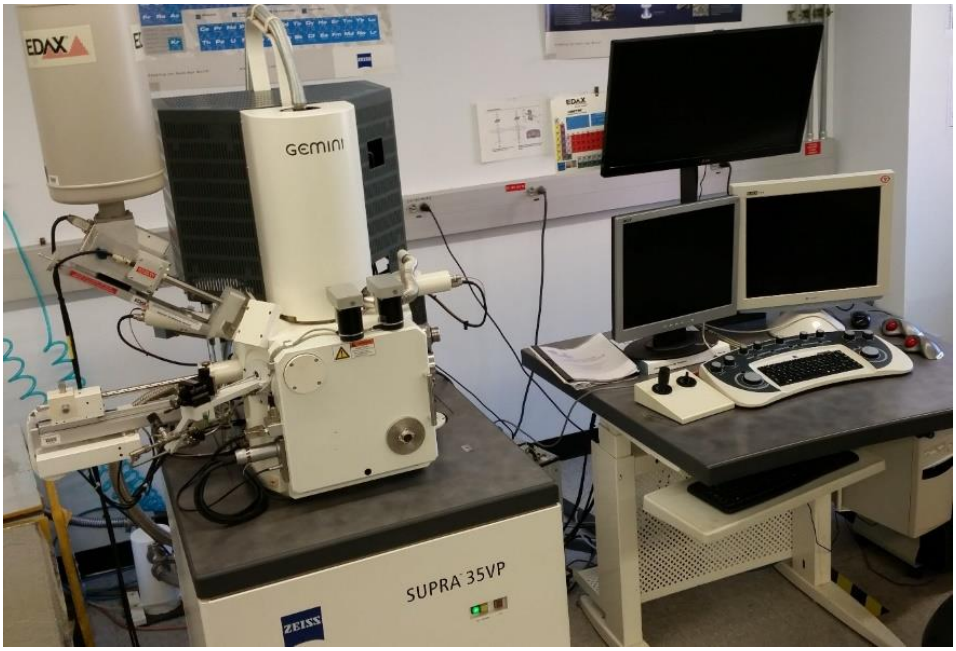

Figure 3.7. Carl Zeiss LEO Supra 35VP Scanning Electron Microscope

3.1.7.1 Operation

Typically, SEM samples must be electrically conductive, thereby providing a pathway for the bombarding of electrons to reach ground. The SFCS samples were mounted to a custom laser cut acrylic platform for imaging the sample cross section (Figure 3.8) and then attached to the SEM stage with conductive carbon tape. Samples requiring a high magnification are sputter coated with a thin layer of gold-palladium alloy to increase conductivity. The sample door is sealed and the chamber evacuated to $<7 \times 10^{-5}$ Torr for samples requiring high magnification. A potential of 2 - 10 kV was applied to drive the electrons toward the sample at a working distance of approximately 8 mm from the gun

aperture. The image was focused and raster scanned (nominal scan speed = 5) to produce a high-quality image.

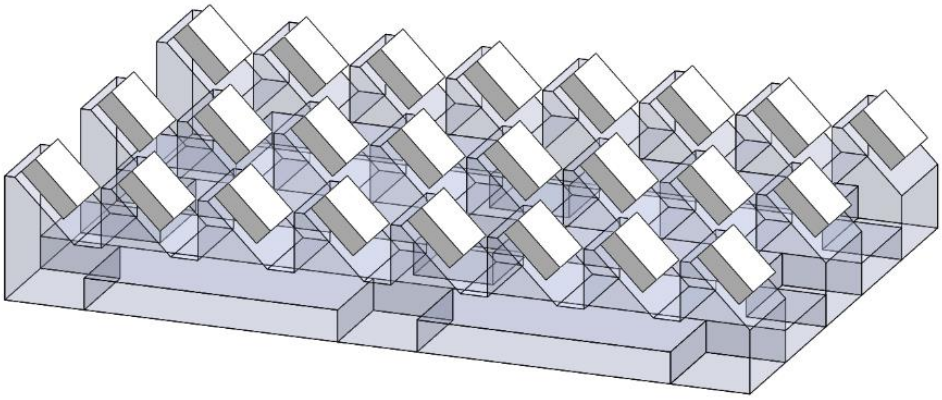

Figure 3.8. 3D rendering of custom lasercut SEM sample imaging array fixture

To reduce the overall time required to image a total of 27 SFCS-ZnO samples in the SEM; each individual SFCS-ZnO sample was mounted to the custom lasercut acrylic 45° sample holder to effectively and efficiently image the sliced cross sections, using the chart below which identifies each specimen location (Table 3.2).

Table 3.2. Layout map of SEM specimen fixture.

5050 30 nm 2%	5050 45 nm 2%	5050 200 nm 2%	3070 30 nm 2%	3070 45 nm 2%	3070 200 nm 2%	7030 30 nm 2%	7030 30 nm 5%
●							
5050 30 nm 5%	5050 45 nm 5%	5050 200 nm 5%	3070 30 nm 5%	3070 45 nm 5%	3070 200 nm 5%	7030 45 nm 2%	7030 45 nm 5%
5050 30 nm 10%	5050 45 nm 10%	5050 200 nm 10%	3070 30 nm 10%	3070 45 nm 10%	3070 200 nm 10%	7030 200 nm 2%	7030 200 nm 5%

To reduce charging effects of the SFCS-ZnO samples, the custom sample holder was strategically mounted with copper tape to generate a conductive path from the sputtered SFCS-ZnO specimens to the grounded SEM stage (Figure 3.9).

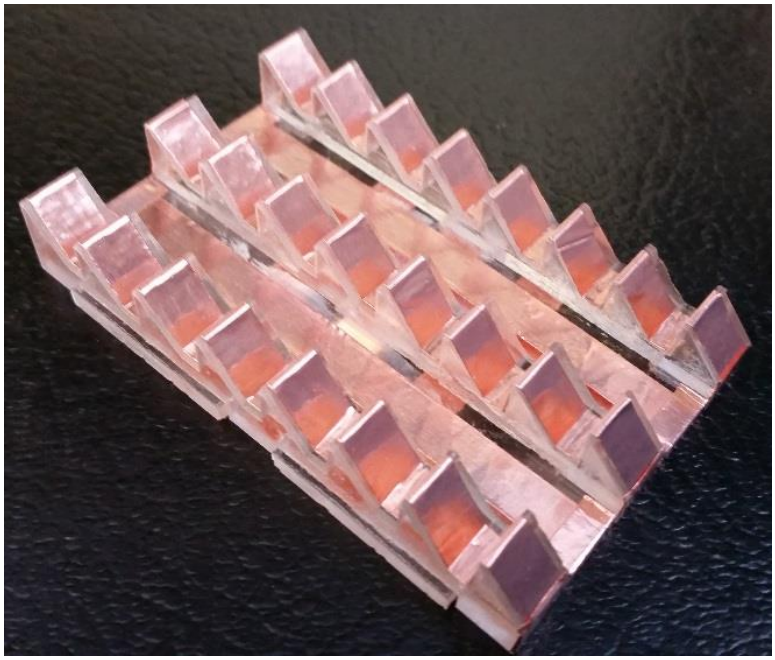

Figure 3.9. Image of SEM sample holder for capturing cross sections of lyopholized SFCS-ZnO blends.

The SEM specimens were then placed on their corresponding locations with respect to the sample layout map (Figure 3.10) and then sputtered to ensure minimal charging effects during imaging.

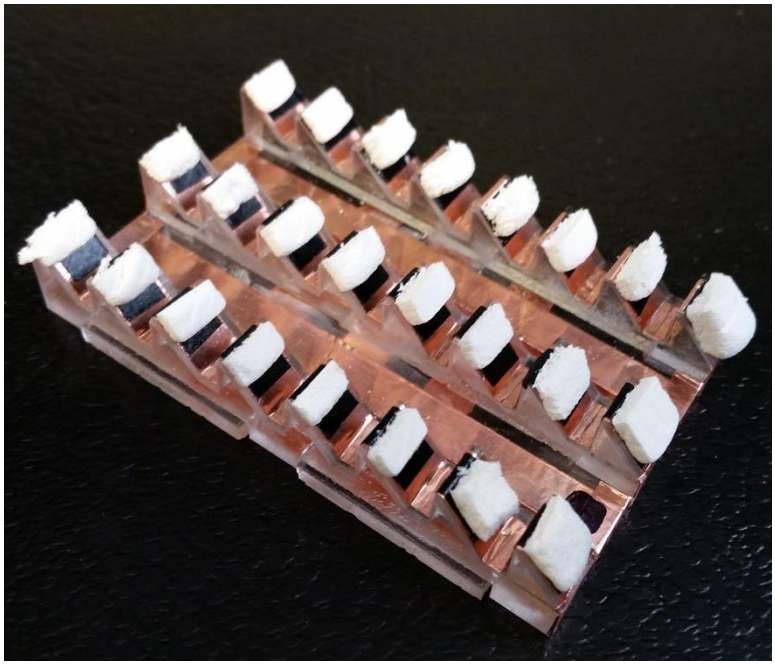

Figure 3.10. Image of SEM sample holder for capturing cross sections of lyopholized SFCS-ZnO blends.

3.1.8 Sputtering Machine

The benchtop sputtering machine (Quorum Technologies, Ltd., East Sussex, England) is employed to deposit a uniform thickness thin film of gold-palladium (Figure 3.11).

Figure 3.11. DC Sputtering System for applying gold onto SFCS substrates.

3.1.8.1 Operation

Open the valve on the argon tank. Turn on the power to the sputtering machine digital voltage meter. Place sample on platen and close lid. Turn the right most knob to "Pump". Once e thvacuum gauge reads 0.1 Torr or less, introduce Argon into the chamber by turning the left most knob, the "Argon Leak Valve", a full turn counter-clockwise. Once the pressure levels reach 0.5 Torr, immediately close the valve. Turn right most knob to

"Set HT" and slowly turn the center dial to increase the voltage to 1.4 kV. Turn the right most knob to "Mode" and press "Timer" to start the timer as well as the sputtering process. When the timer has stopped, the high voltage will disengage. Turn the right most knob to "Pump", close the "Argon Leak Valve", decrease the voltage knob to zero, and turn the unit off. Release vacuum on the chamber and open the lid to remove the sample.

3.1.9 Uniaxial Micro Tensile Tester System

A uniaxial micro tensile testing system (Admet Expert Microtester 4000, Admet, Inc., Norwood, MA) is used to apply a uniaxial tension/compression loads to the small of biomaterials. The unit is comprised of a heated fluid bath () with compatible temperature controller (Omega Engineering, Stamford, CT), a 150 gram tension/compression load cell (Honeywell Sensotech, Columbus, OH), an electromechanical linear actuator (Physik Instrumente (PI), Auburn, MA), and the MTESTQuattro controller unit (Admet, Inc., Norwood, MA). The heated fluid bath reservoir is comprised of stainless steel and has a 100 cc fluid capacity. The bath is actively heated via two ceramic rod heating elements embedded within the fluid bath reservoir housing body and controlled via a closed loop PID feedback controller unit. The effective controllable temperature range is 27.0°C up to 70.0°C with a resolution of 0.1°C. The 150 gram tension/compression load cell is constructed of stainless steel and has an accuracy, non-linearity and hysteresis of ±0.70%, 0.25%, and 0.5% of full scale, respectively. The load cell is submersible and mounted directly to the fluid bath reservoir housing body. The linear actuator is driven by means of a stepper motor and leadscrew assembly and has a 25 mm stroke with a positional

repeatability of 0.1 μm and a maximum velocity of 50 mm/min. The MTESTQuattro is a PC (Pavilion m7, Hewlett Packard, Palo Alto, CA) connected controller unit for the mechanical testing system. The MTESTQuattro GUI provides connectivity and control to all the electromechanical testing systems. The integrated analysis suite provides the flexibility to perform tests in accordance to ASTM, ISO or custom user test specifications.

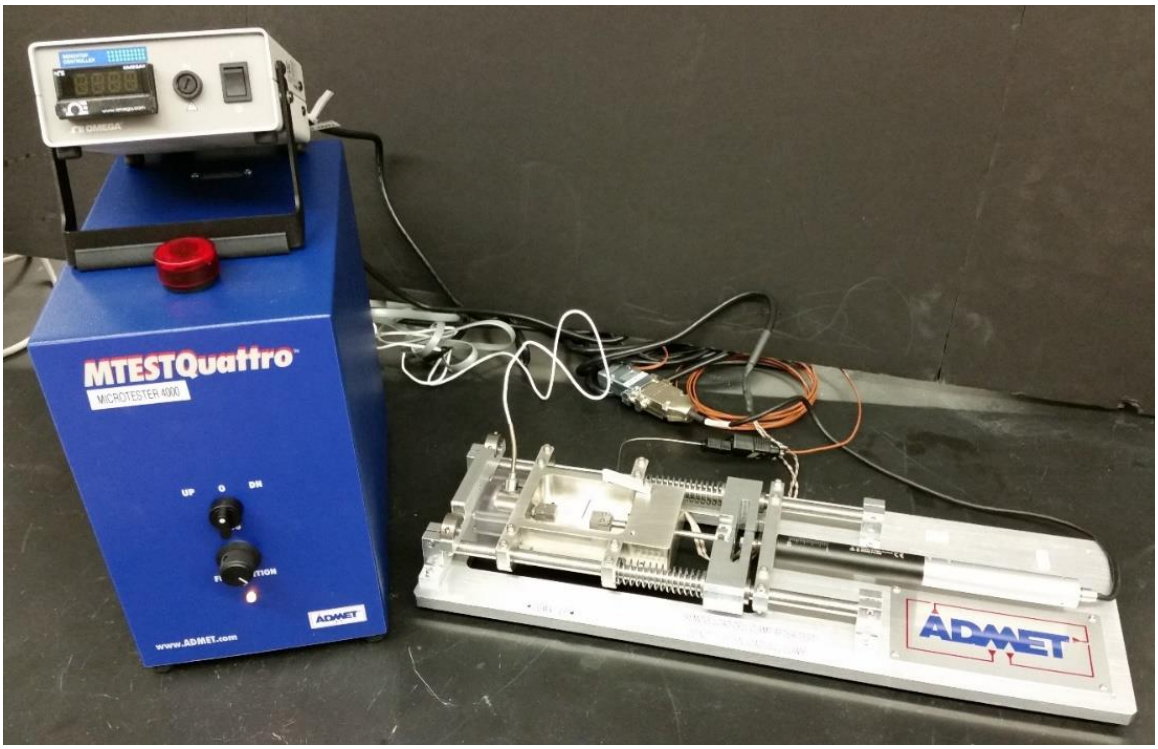

Figure 3.12. Admet eXpert 4000 Microtester alongside MTESTQuattro Controller, and Omega Temperature Controller.

3.1.9.1 Operation

Log into the PC connected to the tensile testing system. Open the Expert 4000 Microtester software (MTESTQuattro-4000.exe) and wait for initialization. Turn the red

button on top of the MTESTQuattro controller clockwise to enable the controller. Fill the fluid bath with water via the plumbed 120 mL syringe, ensuring the Type K shrouded thermocouple is submerged in the fluid bath. Open the temperature controller software (Device Interface.exe) and set to COM2 and reconfigure. Turn on the temperature controller unit that is programmed to a set point of 37°C. Run the test procedure titled "Temp Settle", for the programmed 1.5 hours to ensure that the temperature has stabilized along with the temperature compensated load cell. Place a test sample in the heated bath and allow to acclimate for at least 15 minutes. Mount the acclimatized ring sample in the custom fabricated loop tensile grips. Run the desired test procedure. Note: Individual test procedures will be discussed later in this chapter.

3.1.10 Electrodynamic Shaker, Amplifier, and Waveform Generator

The LW126.138-13 electrodynamic system (EDS) (Labworks, Inc, Costa Mesa, CA; www.labworks-inc.com) is comprised of an electrodynamic shaker (ET-126-1; Figure 3.13a) and linear power amplifier, (PA-138; Figure 3.13b) and a supplemental function generator (Model 33220A, Agilent Technologies, Santa Clara, CA). The permanent magnet shaker generates a peak shock and sine wave force of 53 and 13 pounds, respectively, producing a maximum displacement of 0.75 inches peak-to-peak at zero load. The functional operating frequency range is from DC up to 8,500 Hertz. The power amplifier electrically drives the shaker and can output up to 25 Volts rms and 20 Amps rms with a maximum continuous power dissipation of 450 Watts. A function waveform generator is employed to drive the electrodynamic shaker at a user defined waveform (i.e.

sine, ramp, square wave) at a particular amplitude and frequency. A calibration curve iss generated, correlating amplifier input voltage and measured shaker armature displacement.

Figure 3.13. Images of a.) electrodynamic shaker, b.) linear power amplifier, and waveform generator.

3.1.10.1 Operation

Plug function generator into the PC (Pavilion m7, Hewlett Packard, Palo Alto, CA) via a USB connection and turn the power on. Turn on the power amplifier and turn the amperage control knob to the 9 o'clock position. Wait for the NI Function VISA software to open. Plug in the USB cable from the NI-6353 USB DAQ card (National Instruments Corporation, Austin, TX) into the PC. Select the desired waveform on the function generator and push the output button to initiate shaker displacement.

3.1.10.2 Keithley Source Measure Unit

A Source Measure Unit (SMU; Keithley 2410, Keithley Instruments, Cleveland, OH) is a single-channel, DC parametric tester designed specifically for test applications demanding coupled sourcing and measurement. The 2410 (Figure 3.14) is both a DC power source (up to 1100V, 1A, or 20W) and a true instrument-grade multimeter (with 0.012% measurement accuracy). In operation, this instrument can act as a voltage source, a current source, a voltage meter, a current meter, and an ohmmeter. The SMU is employed to apply a DC electric field of up to 1 kV during the electrical poling process on the ZnO nanoparticle filled composites.

Figure 3.14. Keithley 2410 Source Measure Unit

3.1.11 Hipotronics High Voltage DC Power Supply

A high voltage power supply (Hipotronics R30B High Voltage DC Power supply, Hubbell Inc., Brewster, NY) is employed to pole the SFCS-ZnO blends. This high voltage power supply (Hubbell Inc., Brewster, NY) has a maximum DC voltage of 30 kV and a

maximum current of 50 μA. The Hipotronics supply is employed to apply a DC electric field of up to 6 kV in during the electrical poling process on the ZnO nanoparticle filled composites. The functional poling voltage applied to the SFCS-ZnO blends is between 3 and 6 kV.

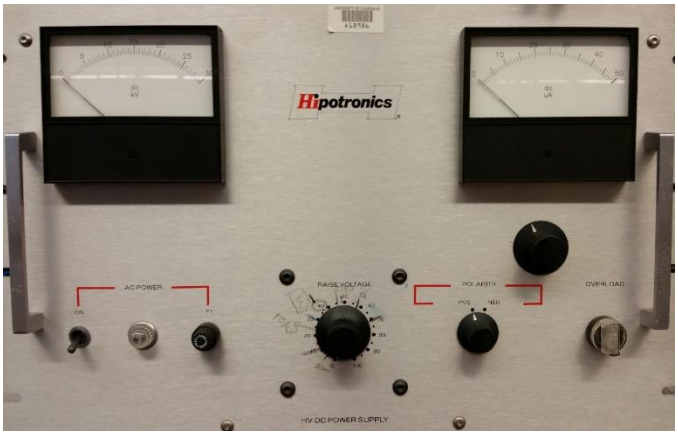

Figure 3.15. Image of front panel of the Hipotronics R30B HV DC power supply.

3.1.12 High Voltage Probe and Measurement Setup

A high voltage probe (Fluke 80K-15, Fluke Corporation, Everett, WA) was implemented for measuring the output of the high voltage power supply. This high voltage probe (Figure 3.16) is rated up to 15 kV DC with an accuracy of ±2% and is typically used in low energy applications. The probe is a precision 1000:1 voltage divider formed via two matched resistors and can be simply plugged into a multimeter for an accurate readout. For these experiments, the multimeter is set to measure the DC voltage (V), and for easy conversion, the appropriate voltage range is set (i.e. 1 V reading per 1000 V input), then

the HV measurements are performed with the attached probe and multiply the multimeter reading by 1000 to retrieve the actual HV output.

Figure 3.16. Fluke HV Probe plugged into a multimeter.

3.1.13 Analog to Digital Conversion

The Multi-Function X Series USB data acquisition unit (USB-6353, National Instruments Corp, Austin, TX) is implemented as the analog-to-digital (A/D) conversion unit for this investigation (detailed technical specifications are outlined in the Appendix). The unit shown in Figure 3.17 was inserted into the PC (Pavilion m7, Hewlett Packard, Palo Alto, CA) running Windows 7 (Microsoft Corporation, Redmond, WA). The USB-6353 A/D converts analog signals into an approximate digital representation at 16-bit (2^{16} levels) resolution and at a maximum acquisition rate of 1,250,000 samples/second within a maximum measurement range of ±10V. The 16-bit resolution determines the smallest theoretical measurement level by the following relationship

$$\frac{Voltage\ Range}{A/D\ \ Resolution} = \frac{V_{max} - V_{min}}{2^{16}} = \frac{20\ V}{65536\ steps} = 0.0003052\ {}^{V}/_{step}$$

where V_{max} and V_{min} are the maximum and minimum values of the measurement range, +10 and -10 volts, respectively.

Figure 3.17. NI USB-6353 A/D converter

3.2 Custom Designed and Fabricated Devices and Instrumentation

3.2.1 Custom Electrodynamic Planar Shear Displacement Apparatus

3.2.1.1 Design Implemented in Investigation

With the purpose of reducing specimen slippage and damage during shear tests, the custom electrodynamic planar shear displacement apparatus was designed and fabricated. Mr. Grip Stripped Screw Hole Repair Kit friction electrode plates were mounted to the laser-cut acrylic framework of the developed piece of equipment (Figure 3.18). A linear potentiometer was employed to accurately measure the displacement of the moving electrode of the electrodynamic shearing device. A 6-inch digital caliper was used to apply a known displacement to the potentiometer while recording the voltage from the digital

multimeter (Figure 3.19 Left). A calibration curve was plotted for displacement – response of the linear potentiometer. Figure 3.19 (Right) demonstrates the linear relationship, showing the slope and offset. This data was then input into the LabVIEW program to directly convert change in the potentiometer voltage to displacement.

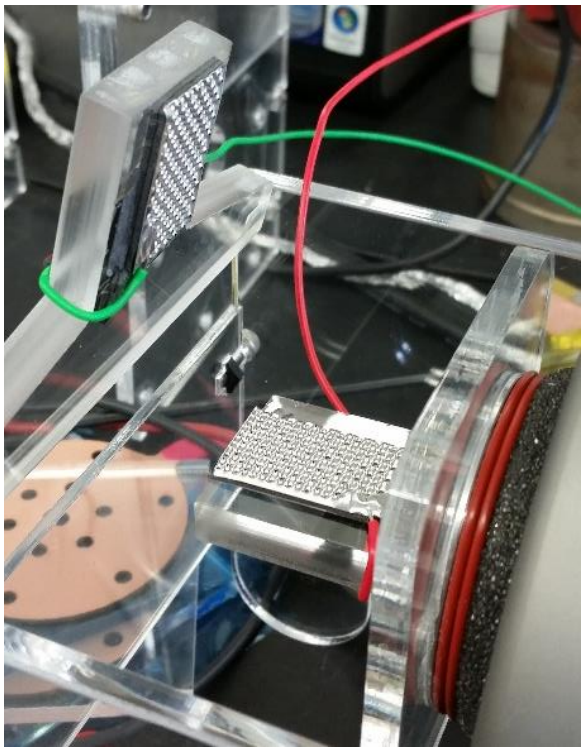

Figure 3.18. Image of the fabricated and assembled custom electrodynamic planar shear displacement apparatus.

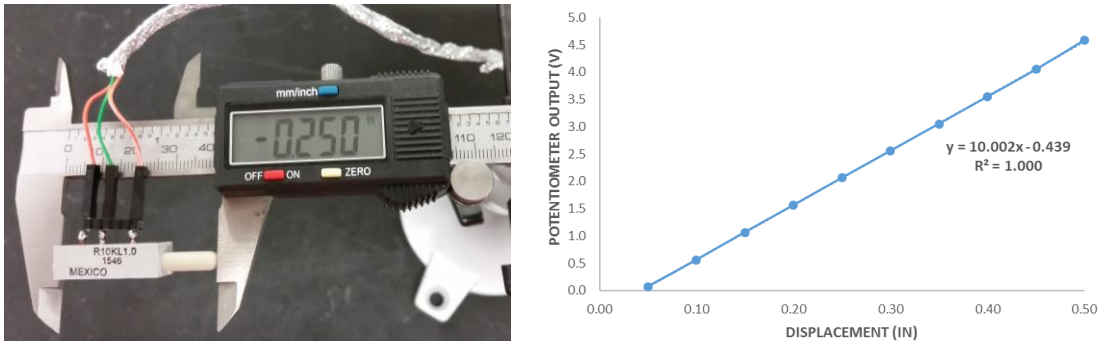

Figure 3.19. (Left) Image of displacement application to the linear potentiometer and (Right) Plot of Displacement – Potentiometer Output for position calibration.

Upon testing, the SFCS-ZnO disc specimens were loaded between the parallel electrodes as shown in Figure 3.20. The top electrode in Figure 3.20 was fixed and the bottom electrode was movable and attached to the electrodynamic shaker platen via an acrylic block. The electrodes were wired directly into the differential amplifier before entering data acquisition system for recording. A gauge block (not shown) was used to ensure a 2-mm gap was set between the electrodes for each sample. The electrodes were mounted to the frame via high bond double-sided adhesive (3M, Model #414/DC). Multiple layers were added to the fixed electrode to account for fabrication and assembly errors to ensure the proper electrode gap distance.

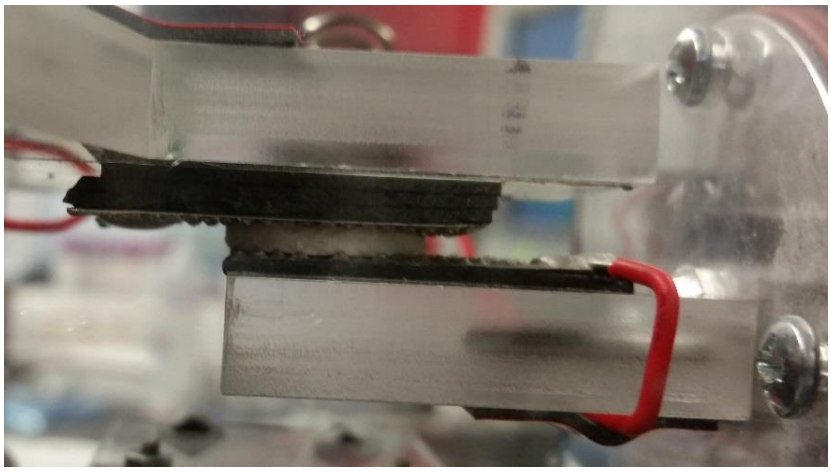

Figure 3.20. Image of shear electrode assembly with 2 mm gap set.

3.2.2 Custom Electrodynamic Vessel Distension Simulation Apparatus

To mimic anatomical blood vessel distension a custom electrodynamic vessel distension simulation simulation apparatus (EVDSA) is developed. A lasercut acrylic frame (6.34 mm thick) is designed to mount directly to the EDS support and isolation structure under the shaker unit. The EDS is oriented in a horizontal position and two legs

are incorporated into the frame to level and stabilize the vessel distension unit (Figure 3.21).

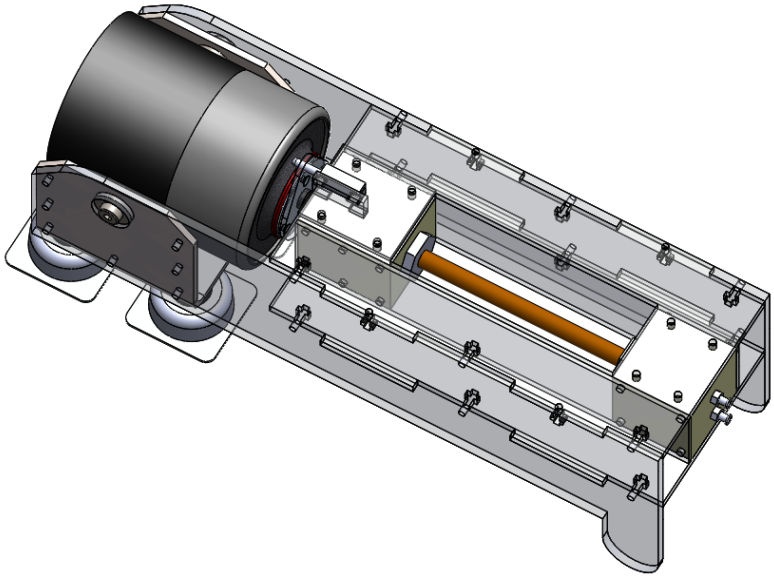

Figure 3.21. 3D CAD rendering of vessel distension simulation system.

The secondary vessel attachment subassembly (VAS) is designed to incorporate an internal closed volume where an engineered or anatomical blood vessel would be placed (Figure 3.22). The compliant vessel would attach to the barbed fittings on both ends of the subassembly via clamps or zip ties to seal off the closed internal volume. The subassembly is mounted into the test frame that is attached to the EDS.

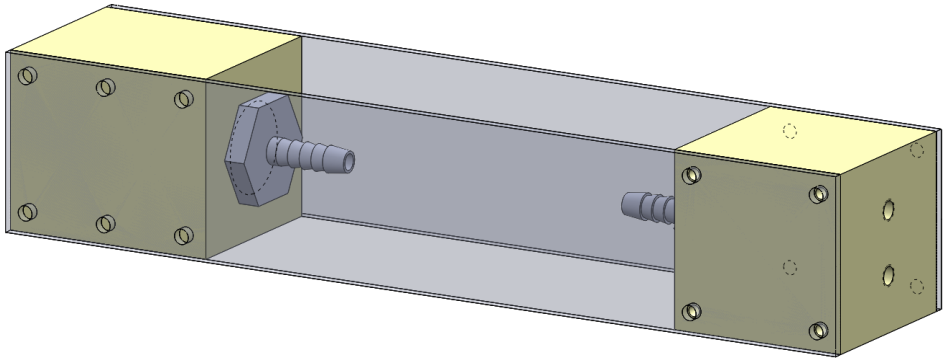

Figure 3.22 3D CAD rendering of the closed volume subassembly for mounting an engineered or actual blood vessel.

A 12.7 mm diameter piston is fabricated from aluminum and mounted to the movable EDS platen. The piston is enclosed and sealed via an o-ring within the cylinder block housing of the VAS. With the fully assembled system and vessel mounted to barbed fittings, the closed volume can be filled with saline solution via the fluid inlet and outlet luer fittings.

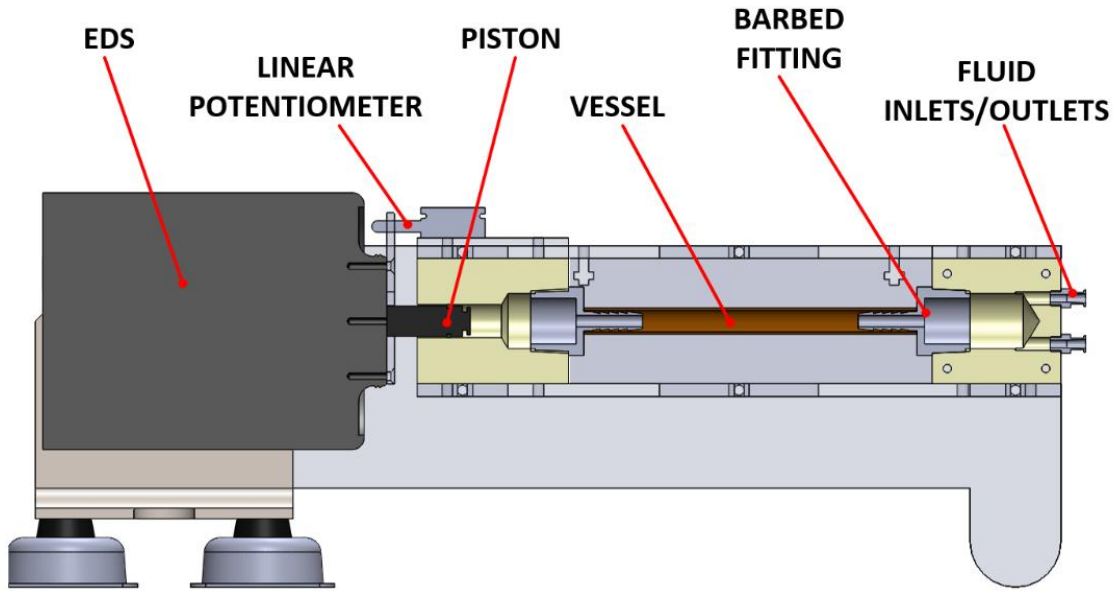

Figure 3.23. Cross Section View of a 3D CAD rendering of the vessel distension system.

3.2.2.1 EVDSA Filling and Draining

Prior to filling, an inline pressure sensor (PRESS-S-000, PendoTECH, Princeton, NJ) is mounted to the lower luer fitting. The pressure sensor is comprised of polycarbonate with inlet and outlet luer fittings (Figure 3.25). It has an operating range of -362 mmHg to 3879 mmHg, with an accuracy better than ±2% of reading within a range of 0 to 300 mmHg. Stopcock valves are then mounted on each luer fitting and used to close off the internal volume.

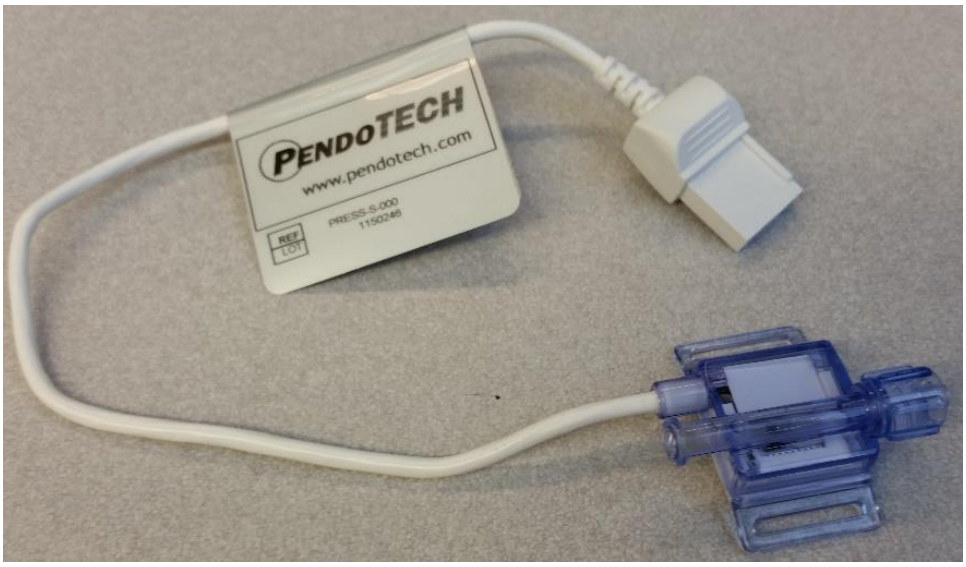

Figure 3.24. Image of PendoTECH luer style pressure sensor.

To effectively fill the internal volume of the test sample with incompressible saline, the distal end of the EVDSA must be raised approximately 65 mm to allow for the compressible air to be evacuated during the filling procedure. Both inlet and outlet stopcock valves are opened. Saline is injected into the lower luer port shown in Figure 3.25. This inclined orientation allows for air to escape from the upper open luer port during filling process. The internal volume is slowly filled using a 50 mL syringe, while gently

squeezing the attached and sealed compliant tube, whether engineered or anatomical, to assist in evacuation of air bubbles that may be trapped, until the saline begins to exit the upper luer fitting.

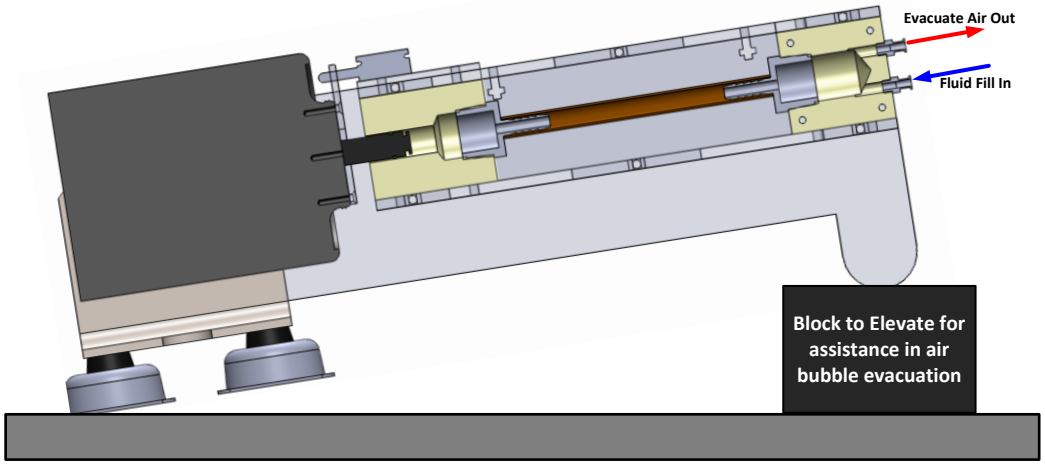

Figure 3.25. Illustration of filling procedure to replace all incompressible air with compressible saline.

The piston stroke of the EDS is programmatically controlled through the EDS with a maximum stroke of 12.7 mm. This change in stroke induces a change in internal fluid pressure to generate a desired dynamic pulse pressure waveform could be generated by adjusting the EDS piston stroke alongside the static internal pressure.

After distension testing, to efficiently drain the internal volume of the tubular test sample, the proximal end of the EVDSA is raised 65 mm to allow for the saline to be displaced with air. Both inlet and outlet stopcock valves are opened and air is injected into

the upper luer port. This declined orientation allows for the saline to drain from the lower open luer port. The internal volume is slowly filled with air using a 50 mL syringe, while gently squeezing the attached and sealed compliant tube to assist in the draining until the saline completely empties from the lower luer fitting (Figure 3.26).

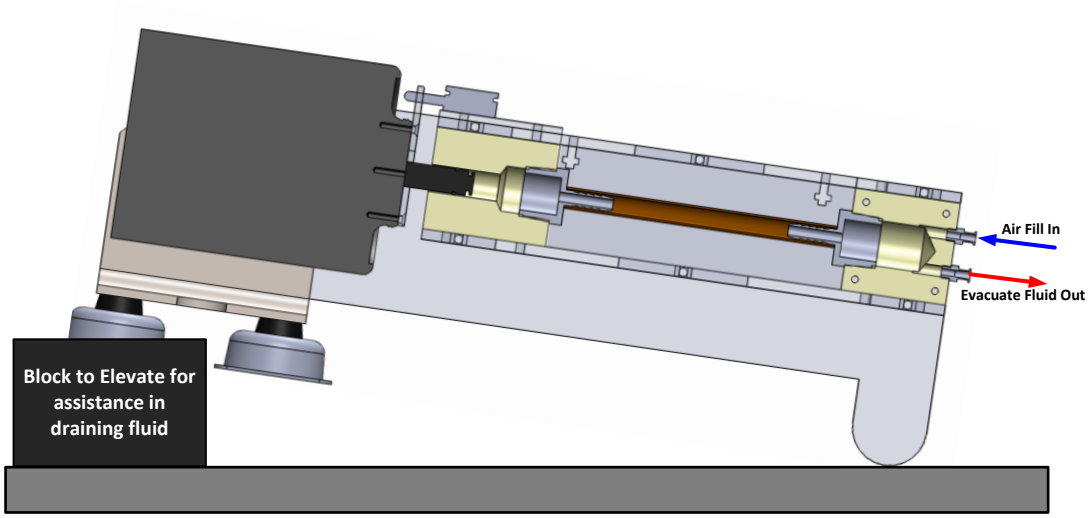

Figure 3.26. Illustration of filling procedure to replace all incompressible air with compressible saline.

3.2.3 Piezoelectric Poling System

Poling electrodes are designed and developed to ensure a consistent electric field is applied across a constant SFCS sample thickness of 2 mm. Generating an electric field strength up to 3 kV/mm. Figure 3.27 displays the polarization mold that is implemented in the poling of SFCS-ZnO blends, comprising of a 7 layered stacked assembly. Custom lasercut 80 X 80 X 6.3 mm acrylic base (a.) and top (g.) are used to ensure a uniform

clamping force of the mold. Custom Ø75 X 1.8 mm PCB electrodes (b. and f.) are milled using a CNC board milling machine. A custom lasercut 2 mm Delrin spacer (d.) is implemented to control the electrode gap thickness SFCS-ZnO during poling.

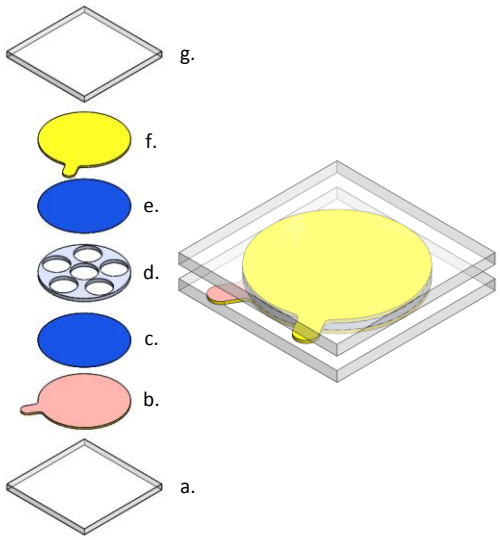

Figure 3.27. 3D rendering and exploded view of SFCS:ZnO polarization molds

There are two polarization configurations pursued in this investigation a low voltage (≤ 1 Kv via Keithley) and a high voltage (up to 6 Kv via Hipotronics). Figure 3.28 displays the complete polarization setup with the Keithley SMU atop an acrylic enclosure that is utilized as a protective shield during the high voltage poling procedures, the polarization mold is shown within the protective enclosure. Figure 3.29 displays the polarization configuration with the Hipotronics supply atop a benchtop fume hood with the acrylic enclosure placed inside to act as a secondary layer of protection against electrocution.

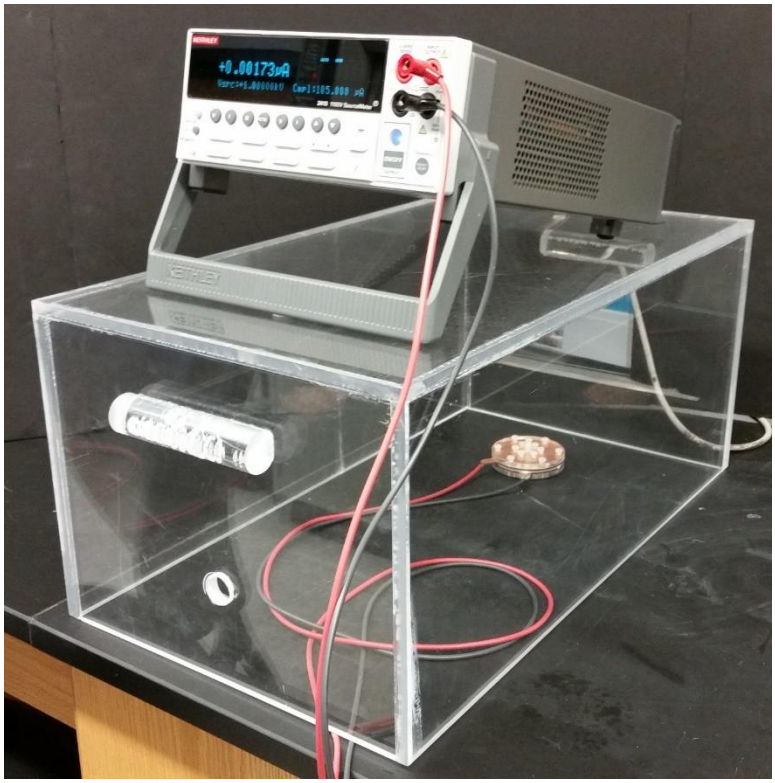

Figure 3.28. Keithley 2410 Sourcemeter sitting atop an acrylic enclosure with poling mold.

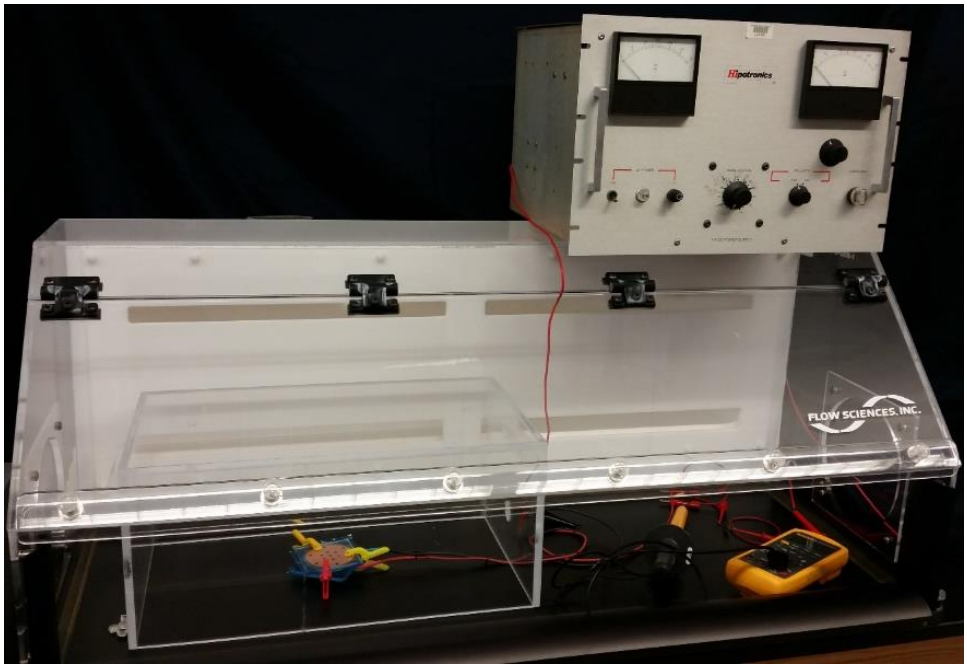

Figure 3.29. Hipotronics HV DC Power Supply sitting atop an acrylic enclosure with poling mold.

3.2.4 Custom Laser Cut Molds

Several custom laser cut molds are employed to assist in the fabrication of a multitude of sample geometries for the SFCS blends for all experimental testing required for this investigation. All of the planar molds were comprised of 1/8" thick acrylic and assembled with 8-32 socket head cap screws.

3.2.4.1 Porosity and Water Absorption Mold

The samples for the porosity and water absorption experiments required a smaller geometry to fit within the sample holders. In order to accommodate, a mold is fabricated

to make SFCS samples that are 10 mm X 18 mm X 3 mm. An array of 9 total cavities fit within the mold platform (Figure 3.30).

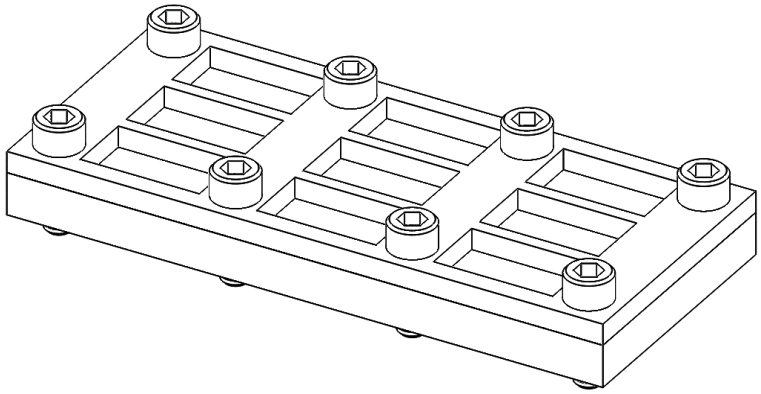

Figure 3.30. CAD rendering of coupon mold for porosity and water absorption samples

3.2.4.2 Shear Testing Mold

The samples for the electrical characterization via shear testing experiments require a flat geometry to fit within the parallel plate electrode geometry of the testing rig. Thus, a new disc mold is fabricated to make samples that have a diameter of 22 mm and 2 mm thick. An array of 3 total cavities fit within the mold platform (Figure 3.31).

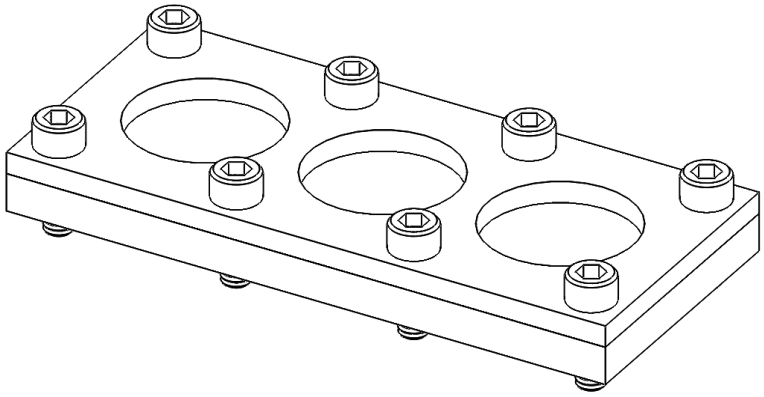

Figure 3.31. CAD rendering of disc mold for shear testing samples

3.2.4.3 Ring Test and Perivascular Band Mold

The samples for the mechanical testing and perivascular band experiments require an annular cylinder geometry to reduce the localized induced stresses caused by the grip area during mechanical testing while also making the band-like structure capable of being mounted to the simulated blood vessel. The samples dimensions are 20 mm outer diameter, 4 mm wall thickness, and 9.6 mm cylinder height. An array of 7 total cavities fit within the circular mold platform (Figure 3.32). The perivascular band mold is also designed to

accommodate for a stackable configuration. The circular mold is primarily developed so the stacked molds (up to 4) would fit within a lyophilizer vacuum jar (Figure 3.33).

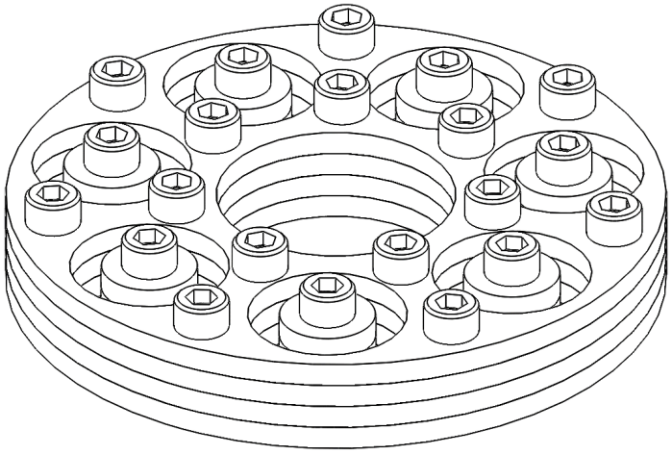

Figure 3.32. CAD rendering of ring mold for mechanical and distension testing samples

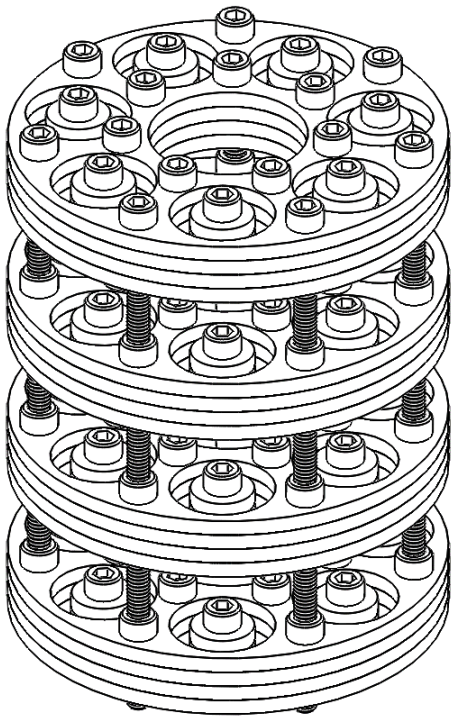

Figure 3.33. CAD rendering of ring mold in stacked configuration

The polymethylmethacrylate (PMMA) ring molds were successfully manufactured via lasercutting techniques and assembled using 8-32 fasteners. A series of assembled molds were stacked by inserting the threaded ends of the 1 inch 8-32 socket head cap screws into the hexagonal heads of the fasteners of the assembled mold below, as seen in Figure 3.34a. This assembled mold stack was easily inserted and removed from the lyophilizer vacuum jar and then separated to individual molds (Figure 3.34b).

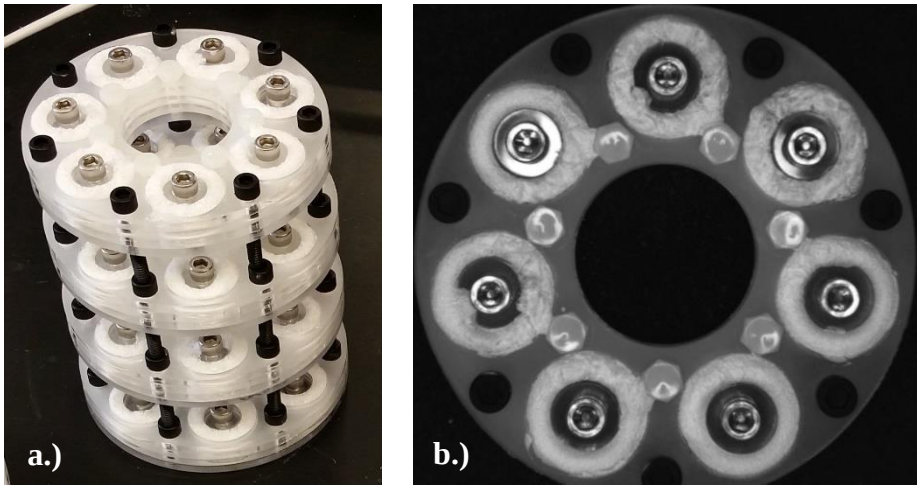

Figure 3.34. Left: Image of stacked configuration of ring molds, Right: Image of individual mold.

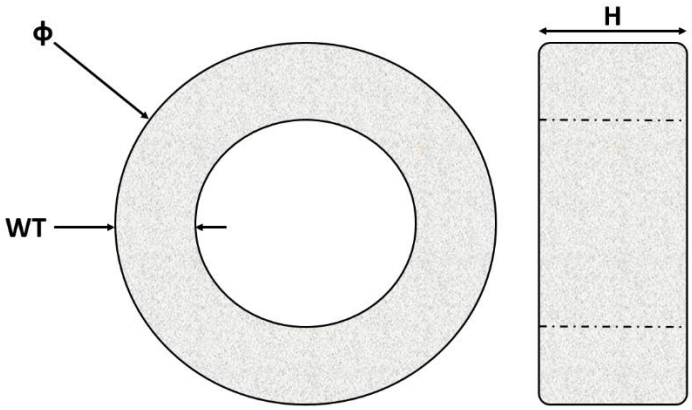

Figure 3.35. Illustration describing metrology metrics of molded SFCS-ZnO ring specimen.

Table 3.3 lists the critical feature specifications that the acrylic molds were manufactured to.

Table 3.3. List of featured designed dimensions within mold.

	Mold Specification (mm)
Outer Diameter (Ø)	20.0
Wall Thickness (WT)	4.25
Height (H)	9.5

3.2.4.4 Engineered Blood Vessel Mold

Due to the lack of available off-the-shelf tubing that effectively simulate blood vessel distension, primarily due to the tubing wall thickness and effective durometer values, a custom mold is fabricated. The simulated blood vessel has an exposed outer and inner diameter of 11mm and 7.75 mm, respectively, and an overall length of 95mm. The custom tube is comprised of DragonSkin®10 Fast (Smooth-On, Macungie, PA), having a ShoreA hardness of 10A, tensile strength of 475 PSI, and a 100% modulus of 22 PSI. This material is typically used as a blood vessel simulant for flow models and training of suturing techniques in cardiovascular surgery. Figure 3.36a illustrates the CAD model of the overall mold, where Figure 3.36b shows the cross section of the mold, displaying the inner channels that allow for the injection of the DragonSkin®. Figure 3.36c shows a rendering of the molded part with a partial cross section, exhibiting the inner channels that are cut away after the part has fully cured, leaving a simple tube of custom cross section that can be cut to any desired length for testing.

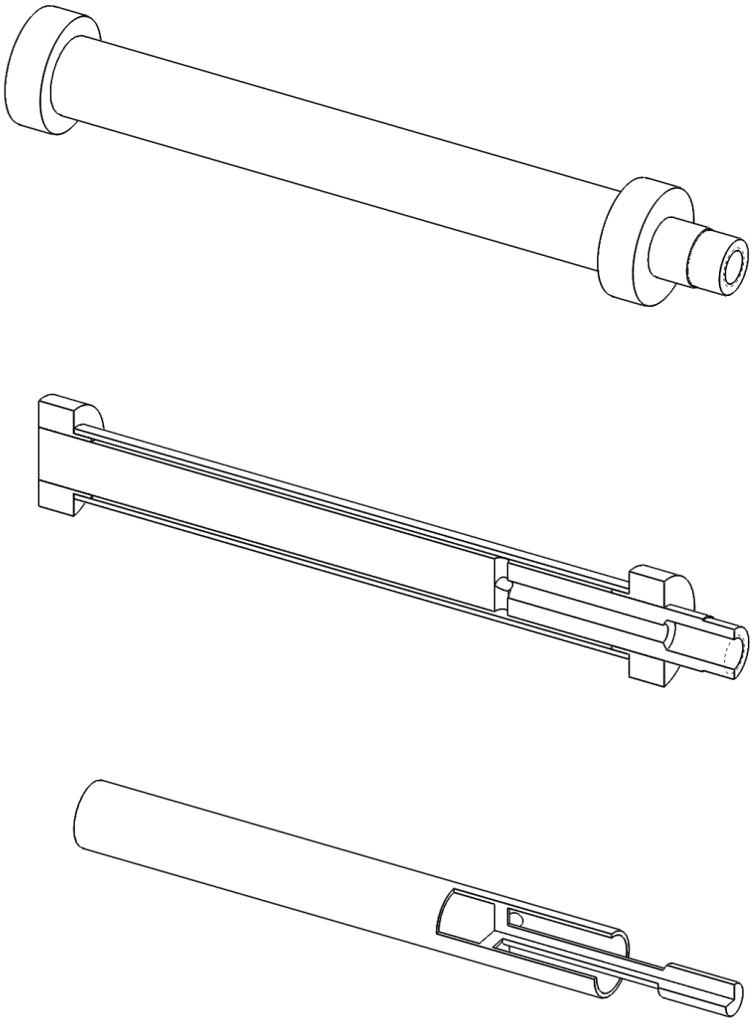

Figure 3.36. a. 3D CAD rendering of the assembled simulated blood vessel mold, b. a cross section view of said mold, and c. 3D CAD rendering of the molded vessel with cutaway view displaying the inner channel that flows elastomer resin into the annular region of the mold

3.2.5 Custom Amplification Electronics

A custom differential amplifier is developed to amplify the raw SFCS-ZnO sensor output voltage signal so that it is within the maximum measurement range yet above the minimum resolution of the A/D converter. A differential amplifier is an electronic amplifier that amplifies the difference between the positive and negative analog input voltages and can ideally be represented as;

$$V_{out} = A_D(V_{in}^{+} - V_{out}^{-}) \tag{16}$$

where A_D is the amplifier gain. The custom differential amplifier (schematic shown in Figure 3.37) developed for this investigation can be divided into 3 primary categories: amplification (Blue), gain adjustment (Red), and offset adjustment (Green).

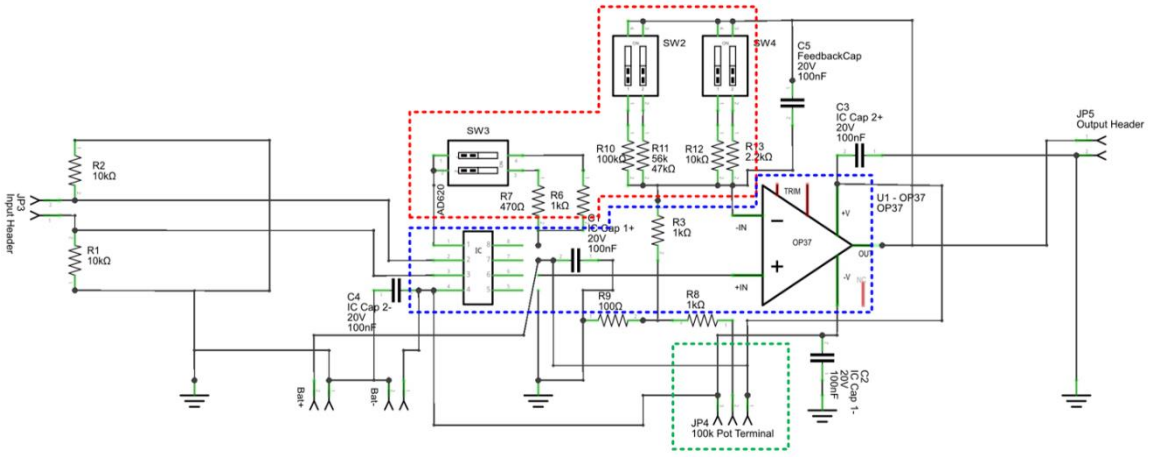

Figure 3.37. Schematic of differential amplifier

The amplification occurs across 2 stages: 1.) differential amplification and 2.) an operational amplifier. In the first stage, differential amplification employs an instrumentation amplifier (AD620, Analog Devices, Norwood, MA) as shown in Figure 3.38.

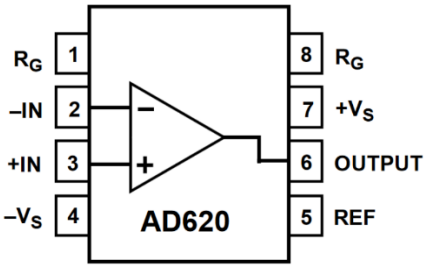

Figure 3.38. Illustration of connection pinout for the AD620 instrumentation amplifier.

where the theoretical gain (A_D) can be calculated using the relationship:

$$A_D = \frac{49400}{R_G} + 1 \tag{17}$$

where R_G is the gain resistor value that allows for the differential gain to be programmatically adjusted with fine-tuning of one externally connected resistor. The second stage employs an operational amplifier (TLC2201CP, Texas Instruments Inc.,

Dallas, TX) in the non-inverting configuration (Figure 3.39). The theoretical gain (A_O) can be calculated as:

$$A_O = \frac{R_2}{R_1} + 1 \tag{18}$$

where R_1 is the gain resistor value and R_2 is the feedback resistor value.

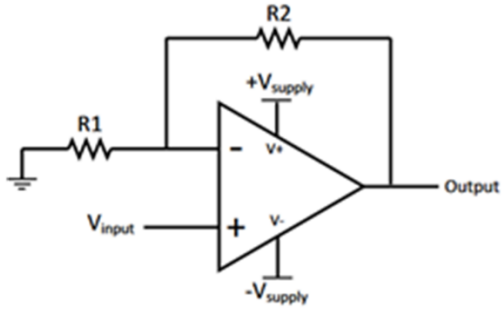

Figure 3.39. Schematic of the TLC2201CP operational amplifier.

To have some level of adjustability in the amplifier, gain adjustment switches are incorporated into the circuitry (red area in Figure 3.37). The differential amplification stage (1) had a 2-position switch accounting for 2 individual gain resistor values while the operational amplification stage (2) had a 4-position switch accounting for 4 individual gain

resistor values. To determine the overall theoretical gain of the circuit, the current gain values of each stage are in a cascaded series and are multiplied together as shown below;

$$A_{overall} = A_D \times A_o \tag{19}$$

Table 3.4 displays each theoretical gain setting for each stage switch position. The total theoretical gain is listed in the far right column.

Table 3.4. Listing of individual and overall gain settings for custom differential amplifier.

STAGE 1 DIP SWITCH POSITION	**STAGE 1 RESISTOR VALUE (Ω)**	**STAGE 1 GAIN SETTING**		**STAGE 2 DIP SWITCH POSITION**	**STAGE 2 RESISTOR VALUE (Ω)**	**STAGE 2 GAIN SETTING**		**OVERALL GAIN $A_{overall}$**
1	470	106.1		1	2200	3.2		340
1	470	106.1		2	10000	11		1167
1	470	106.1		3	56000	57		6048
1	470	106.1		4	100000	101		10717
2	1000	50.4		1	2200	3.2		161
2	1000	50.4		2	10000	11		554
2	1000	50.4		3	56000	57		2873
2	1000	50.4		4	100000	101		5090

A 100kΩ rotary potentiometer with linear output is implemented as the offset adjustment for the circuit (green area in Figure 3.37). This potentiometer is used to manually offset the stable static signal back to zero upon loading of a new sample between experiments.

The concept of the differential amplifier circuit is laid out on a virtual breadboard in a software package titled Fritzing (FHP, Fachhochschule Potsdam, Potsdam, Germany) prior to prototyping on an actual breadboard, which enables the "build" of the circuit virtually with actual off-the-shelf electronic components (Figure 3.40). The actual prototype breadboard is presented in Figure 3.41, with the 2 stage amplifiers (the two black DIP socket components), the gain adjustment switches for stage 1 (the red component with 2 position switches) and stage 2 (the blue component with 4 position switches), and the offset adjustment potentiometer (the large black knob) represented in the figure. The Fritzing software also converts the virtual breadboard layout to a PCB layout (Figure 3.42), so the designer can effectively click and drag to move the individual circuit components on the virtual PCB to generate an efficient and organized populated layout. The size of the PCB can be manually adjusted to suit the desired footprint of the circuit as well.

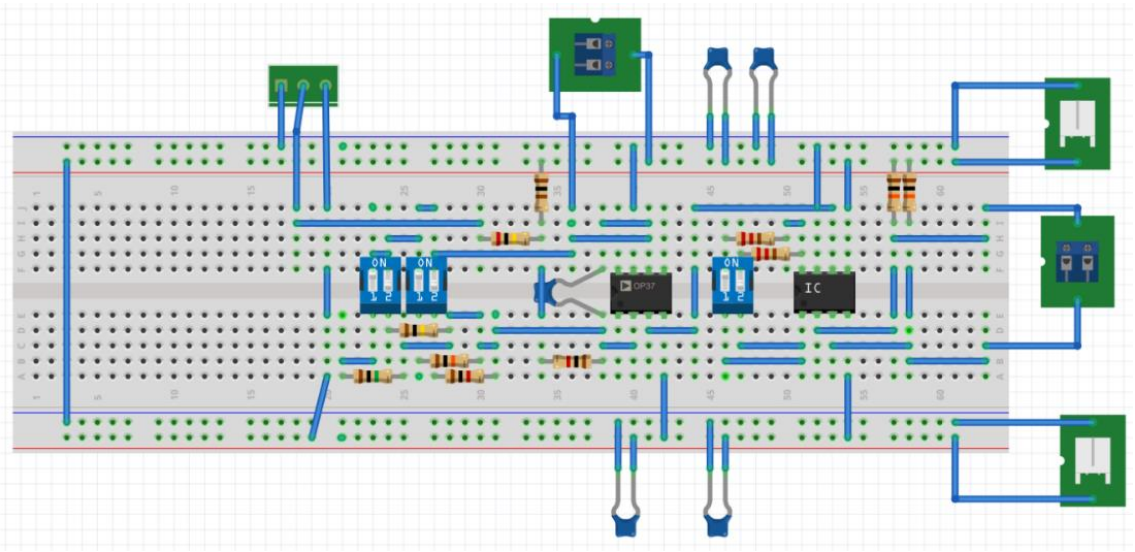

Figure 3.40. Rendering of layout for the breadboard configuration of the differential amplifier.

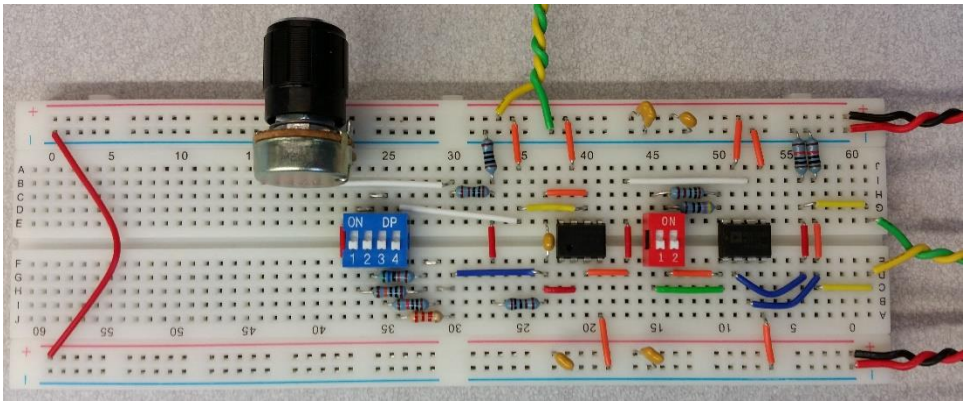

Figure 3.41. Differential amplifier in actual breadboard layout.

The Fritzing software also converts the virtual breadboard layout to a PCB layout (Figure 3.42). The designer can effectively click and drag to move the individual circuit components on the virtual PCB to generate an efficient and organized populated layout. The size of the PCB can be manually adjusted to suit the desired footprint of the circuit as well.

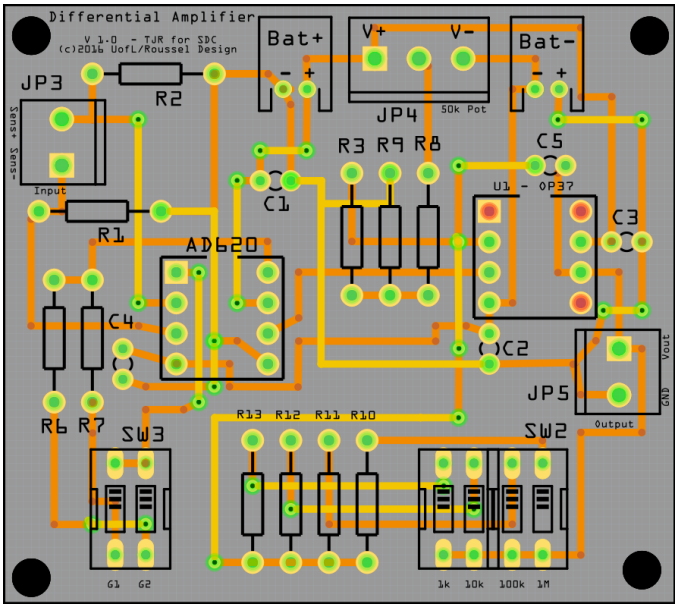

Figure 3.42. PCB layout of differential amplifier.

Following assembly, the amplifier was mounted to a laser-cut acrylic frame for stability and portability (Figure 3.43). The battery packs were then securely mounted to the frame via zip ties.

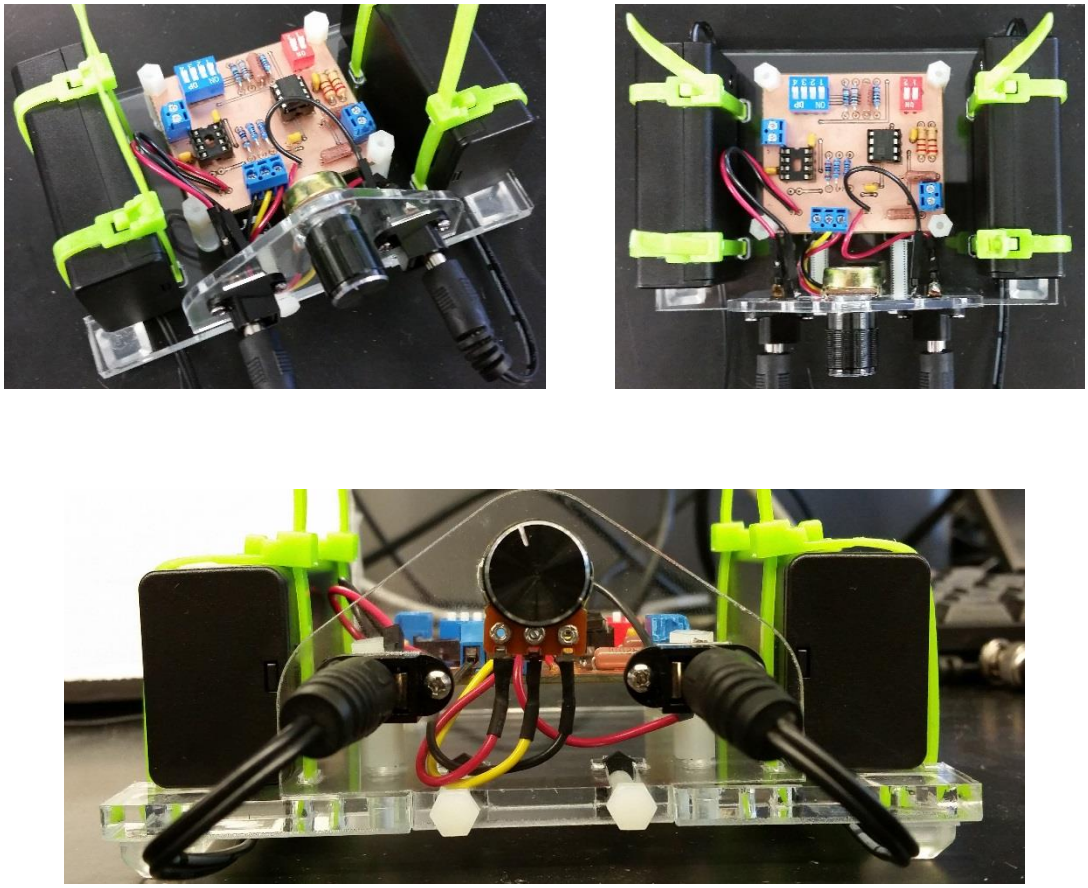

Figure 3.43. Images of differential amplifier, (Top Left) Isometric view, (Top Right) Top view, (Bottom) Front view

Actual gain values of the amplifier were determined via the following calibration procedure. A function generator, set to a voltage of 100 mV peak-to-peak and a frequency of 2 Hz, was wired into a dual stage voltage divider circuit consisting of two 1:10 divider

circuits in series that generated an overall theoretical 1:100 voltage division (Figure 3.44). This voltage divider was implemented to reduce the voltage output of the function generator to better emulate the low voltage signal (μV range) that the test specimen had outputted during preliminary experiments.

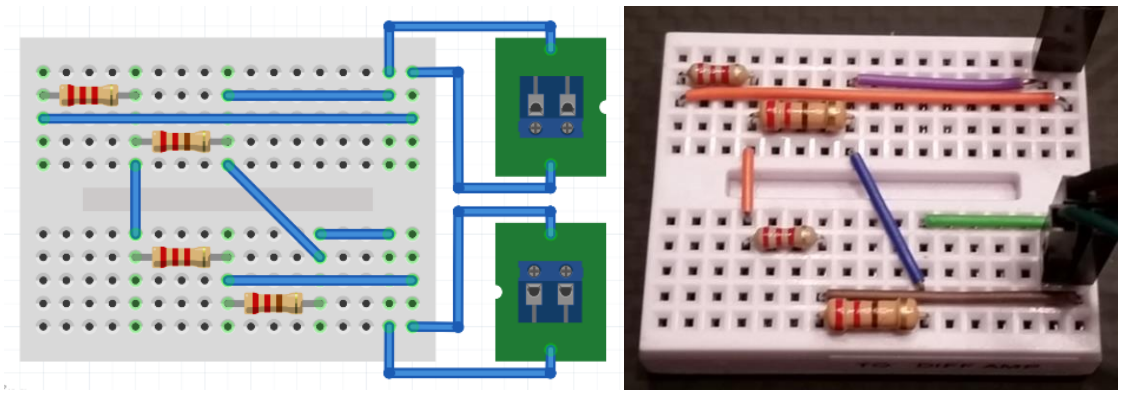

Figure 3.44. (Left) Rendering of voltage divider circuit for amplifier calibration drawn vie Fritzingand (Right) Populated breadboard

This circuit was then wired directly into an oscilloscope for measurement of the circuit output, reducing the input voltage of 100 mVpp through the divider down to 720 μV. This known circuit output was then inputted from the function generator into the differential amplifier circuit to confirm the designed gain settings. Prescribed gain resistors were adjusted via DIP switches on the amplifier and the actual voltage was measured (V_{MEAS}) via the oscilloscope and recorded. The actual gain settings of the amplifier were calculated via the following relationship:

$$G_{ACTUAL} = \frac{V_{MEAS}\ (V)}{720\ (\mu V)} \times 1000000 \quad (20)$$

The measured voltage values and calculated gains were listed in Table 3.5. The percent error was calculated and found to be within ±3.1% for each gain setting. This calibration method gives certainty to the measured electrical response of the SFCS-ZnO specimens that is amplified through the differential amplifier and recorded in LabVIEW.

Table 3.5. Theoretical and actual gain based on stage resistors and the measured voltage at the amplifier.

STAGE 1 DIP SWITCH POSITION	STAGE 2 DIP SWITCH POSITION	STAGE 1 RESISTOR VALUE (Ω)	STAGE 2 RESISTOR VALUE (Ω)	G_{THEOR}	V_{MEAS}	G_{ACTUAL}	% Error
1	1	470	2200	340	0.252	**350.0**	***3.1%***
1	2	470	10000	1167	0.816	**1133.3**	***-2.9%***
1	3	470	56000	6048	4.28	**5944.4**	***-1.7%***
1	4	470	100000	10717	7.52	**10444.4**	***-2.5%***
2	1	1000	2200	161	0.116	**161.1**	***-0.1%***
2	2	1000	10000	554	0.388	**538.9**	***-2.8%***
2	3	1000	56000	2873	2.02	**2805.6**	***-2.3%***
2	4	1000	100000	5090	3.56	**4944.4**	***-2.9%***

3.3 Methodology

3.3.1 Piezo Composite Formulation Using Tissue Scaffold Blends

3.3.1.1 Tissue Scaffold Blends

The tissue scaffold based piezo composite is comprised of silk fibroin, chitosan, and ZnO nanoparticles. Three blends of silk fibroin chitosan (SFCS) mixtures are investigated in this study, the SF and CS are mixed by volume to generate 70:30 (70%:30% by vol), 50:50 (50%:50% by vol) and 30:70 (30%:70% by vol) SF:CS. The SFCS blends are employed as the inactive component of the piezocomposite. The following procedures detail the overall processes for SF extraction and dissolution from Bombyx mori silk cocoons (Figure 3.45).

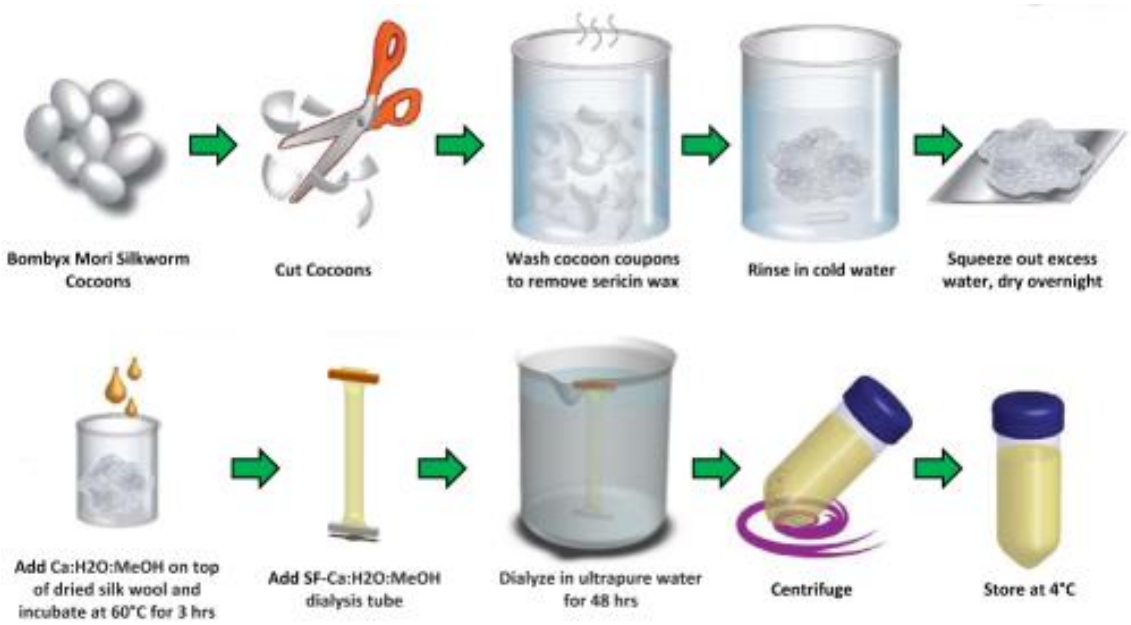

Figure 3.45. Illustration of silk fibroin extraction and dissolution process. (Redrawn from [44])

3.3.1.2 Silk Fibroin Extraction

The silk from the Bombyx Mori cocoon comprises of two key fibroin protein chains, light (25 kDa) and heavy (325 kDa) chains [44]. These essential protein chains are enclosed in sericin, a glue-like protein securing the fibroin chains together to form the cocoon – a composite fiber structure that protects the growing worm. To effectively process and extract the silk fibroin from the raw cocoons, the embedded sericin wax must be removed.

A 2-liter glass beaker is filled with 2 liters of ultrapure water, covered with aluminum foil and heated to a boil. Bombyx Mori cocoons are cut with scissors into dime-sized pieces and the residual silkworm waste within the cocoons is disposed. A 0.02 M solution of sodium carbonate (Na_2CO_3) is made by adding 4.24 grams of Na_2CO_3 to 2 L of boiling water to completely dissolve into solution. Subsequently, 5 grams of cocoon pieces is added to the boiling Na_2CO_3-water solution for 30 minutes and intermittently stirred with a glass stir bar to promote silk fibroin dispersion. After 30 minutes, the silk fibroin is promptly removed with a spatula and cooled under flowing ultrapure cold water. Excess water is then pressed out of the silk, placed in a 1-liter glass beaker filled with ultrapure water and soaked for 20 minutes. The rinse and soak procedure is repeated a total of three times. After the third wash, the silk is pressed to remove residual water and spread out onto a clean piece of aluminum foil and allowed to dry in a fume hood overnight. The 5 grams of cocoon pieces generates 3.3 grams of dry silk wool after the sericin wax has been fully washed away.

3.3.1.3 Fibroin Dissolution

The dried silk fibroin is added to a calcium nitrate tetrahydrate–methanol solution (molar ratio 1:4:2 Ca:H2O:MeOH) at a 10% weight-to-volume concentration (mg/mL) in a sealed container and placed in an oven at 65°C for 3 hours to fully dissolve with intermittent stirring. The fully dissolved fibroin solution (approximately 32 mL) is placed into a 22 mm diameter, 355 mm long dialysis tube with a molecular weight cut off of 7 kDa (Snakeskin #68700, Thermo Scientific, Rockford, IL) with 2 weighted clips on the bottom of the tube and 3 floating clips on top of the tube, and all air is evacuated from the tube. The clipped length of the dialysis tube is 305 mm. The dissolved silk fibroin is dialyzed against deionized water in a 2-liter graduated cylinder for 4 days, changing the water every 24 hours. The dialyzed SF solution is stored at 4°C until use.

3.3.1.4 Chitosan Dissolution

High molecular weight chitosan (419419, Sigma-Aldrich Co., St. Louis, MO) is dissolved at 3.66% (g/mL) in 2% acetic acid. Thoroughly mix the Chitosan blend for 15 minutes at approximately 2000 RPM using the custom material mixing system described above in Section 3.1.2. The fully blended chitosan is then stored at 4°C until use.

3.3.1.5 Blending of Silk Fibroin with Chitosan

Three solutions of silk fibroin and chitosan are blended by volume and characterized for this investigation (

Table 3.6). The typical volume of the blended SFCS solution regardless of concentration is 50 mL; therefore, known volumes of each material blend are utilized in each experiment. The blended SFCS solution is thoroughly mixed using the custom material mixing system for 15 minutes at approximately 2000 RPM.

Table 3.6. List of SFCS blends and corresponding volumes for 50 mL solution.

SFCS Blend	**% SF**	**% CS**	**SF (V) {mL}**	**CS (V) {mL}**
30:70	30	70	15	35
50:50	50	50	25	25
70:30	70	30	35	15

The blended solution is then equally divided (25 mL) and placed into two 22mm diameter, 250 mm long – 7 kDa dialysis tubes with 1 weighted clip on the bottom of the tube and 2 floating clips on the top of the tube, and all air is evacuated. The clipped length is approximately 200 mm. The blended SFCS is dialyzed against deionized water in a 7.5-liter tub for 3 days with the water being changed every 24 hours. Subsequently, the clear and homogeneous aqueous solution is stored at 4°C until use.

3.3.1.6 Blending of SFCS with Zinc Oxide Nanoparticles

ZnO nanoparticles (US Research Nanomaterials, Inc., Houston, TX) of 30 nm, 45 nm and 200 nm average particle size are selected as the active phase of the piezocomposite. The ZnO nanoparticles for each respective size are ultrasonically dispersed in deionized water at a concentration of 250 mg/mL. The final form of the piezocomposite tissue scaffolds is prepared using the process described next.

3.3.1.7 Silk Fibroin - Chitosan - ZnO Blend Scaffold Preparation

The ZnO dispersions are combined with the SFCS blends to reach the desired weight fractions (2%, 5% and 10%) of SFCS:ZnO composite using a drip method while being stirred at 500 RPM on the custom material mixing system. The ZnO:SFCS blends are injected into the laser cut acrylic molds described above via 5 mL pipetter and frozen in a -80°C freezer overnight. The next day, the samples are lyophilized for 24 hours. The dried samples are then removed from the molds and treated with 50:50 (v/v) MeOH:NaOH (1N) solution for 15 min, to crystallize the silk content and neutralize the chitosan content. The MeOH:NaOH solution is replaced with 1N NaOH solution and the samples are then treated for 12 hours. The samples are promptly removed from the NaOH solution and immediately placed in a 1X phosphate buffered saline solution at 37°C to leach out the NaOH. The phosphate buffered saline solution is changed every 4 hours until the solution pH has equilibrated to 7.4.

3.3.1.8 Tissue Scaffold Porosity

Tissue scaffolds containing a 3D porous matrix provide mechanical stability to support cell adhesion and expansion while allowing integration at a rate analogous with new tissue growth. Porosity is also critical to provide sufficient opportunity for cell migration, adhesion, and expansion while sustaining adequate transport for nutrient and gas exchange [45] [46] [47]. The lyophilized SFCS tissue scaffolds typically have a high porosity and interconnected pores. The addition of ZnO nanoparticles to the blended SFCS may affect the porous nature of the scaffold; thus, porosity characterization must be conducted.

The following procedure is performed to obtain the pore and apparent scaffold volume. Next, the effective porosity of SFCS-ZnO samples is calculated by means of the fluid re-saturation method [47]. Specifically, pore volume is calculated using the relationship:

$$V_1 = \frac{(M_a - M_b) - M_0}{\rho} \tag{21}$$

where M_0 is the dry mass of the lyophilized SFCS samples. M_a is the mass of 2 mL of 100% ethanol (ρ = 789 kg/m³) dispensed into a glass weighing dish with the dry SFCS samples fully immersed and saturated. The saturated SFCS sample is then removed and the weighing dish is reweighed giving the mass M_b. The change in mass divided by the density of the ethanol results in the pore volume.

A 10 mL pycnometer (Figure 3.46) is filled with ethanol, weighed and recorded as M_1. The ethanol is poured out and the wet scaffold, previously soaked in ethanol within the weighing dish, is placed in the pycnometer, and ethanol is added until the pycnometer is once again properly filled. The pycnometer is reweighed with the added SFCS sample and the mass denoted as M_2. The apparent scaffold volume is then calculated using:

$$V_2 = \frac{(M_a - M_b) - (M_2 - M_1)}{\rho} \tag{22}$$

The effective porosity of the SFCS samples is calculated according to the following equation:

$$\varepsilon = \left(\frac{V_1}{V_2}\right) \times 100\% = \left(\frac{M_a - M_b - M_0}{(M_a - M_b) - (M_2 - M_1)}\right) \times 100\% \tag{23}$$

where porosity is the ratio of the pore volume (V_1) to effective scaffold volume (V_2).

Figure 3.46. Image of 10 mL pycnometer.

3.3.1.9 Tissue Scaffold Water Absorption

A critical aspect of an engineered tissue scaffold is the capability of storing water, an essential characteristic for the support of a multitude of cellular functions by allowing ease of diffusion for cell nutrients and waste [37] [40] [48]. Thus, water absorption experiments are conducted on the SFCS scaffolds. The scaffolds are again freeze dried via lyophilization and weighed (W_{dry}). The samples are placed in saline and then placed in a heated water bath at 37°C. The samples are removed from the bath at prescribed time intervals of 30, 60, 90, 120, 180, and 240 minutes and the mass is recorded. Before the mass measurements are recorded, the SFCS samples are blotted to remove any excess water. Water absorption is calculated according to the following equation:

$$WA\% = \frac{W_{wet} - W_{dry}}{W_{dry}} \times 100 \quad (24)$$

where W_{dry} is the dry mass of the lyophilized SFCS samples and W_{wet} is the final measured mass of the wet sample after soaking in saline for 240 minutes.

3.3.2 Mechanical characterization of biocompatible piezo-composites

3.3.2.1 Dimensional Characteristics

SFCS-ZnO blends are mixed and then injected into the ring-shaped molds. A pipette is employed to dispense 1.5 mL of the SFCS-ZnO blend into each mold cavity. After curing, the SFCS-ZnO blends are removed from the mold and washed in MeOH/NaOH solutions. Finally, the blends are stored in 1X PBS and the outer diameter (OD), wall thickness (WT), and height (H) of the ring samples are measured with a pair of digital calipers and recorded. These dimensions alongside the measured porosity of each blend are used to determine the actual cross sectional area of each sample blend.

3.3.2.2 Mechanical characteristics

3.3.2.2.1 Uniaxial Tensile Testing

Mechanical and viscoelastic characteristics for all the SFCS-ZnO blends are evaluated in this study. Uniaxial tensile, stress relaxation and creep tests are performed

using the ring-shaped samples. The selected geometry of the ring-shaped samples alleviated any experimental error due to localized failure via inappropriate clamping of the specimens as seen with the traditional dog-bone type tensile specimens. Slippage and unwanted premature failure near the clamp grips are also common modes of failure and stress measurement uncertainty [49]. Specimen failure is defined as a complete breakage of the ring sample. Several metrics are extracted from the uniaxial tensile test data such as modulus of elasticity, ultimate strength, yield strength, and elongation at break. The modulus of elasticity of the material is defined as the slope of the linear portion of the stress-strain curve, is illustrated as the triangle in Figure 3.47 and is also represented as:

$$E = \frac{\Delta\sigma}{\Delta\varepsilon} \tag{25}$$

The gray hatched areas also represent the linear region of the stress-strain curve. The ultimate strength is represented as the maximum stress prior to failure of the specimen (Red **X** in Figure 3.47). The yield point or yield strength (Green $+$ in Figure 3.47) is defined as the point at which the linear region began to change by at least 10% [49]. The SFCS-ZnO ring samples are subjected to tensile testing on the Admet Uniaxial Microtester 4000 describe above. The constructs are mounted between two custom fabricated hooks adapted to securely mount to the mechanical tester, as shown in Figure 3.48.

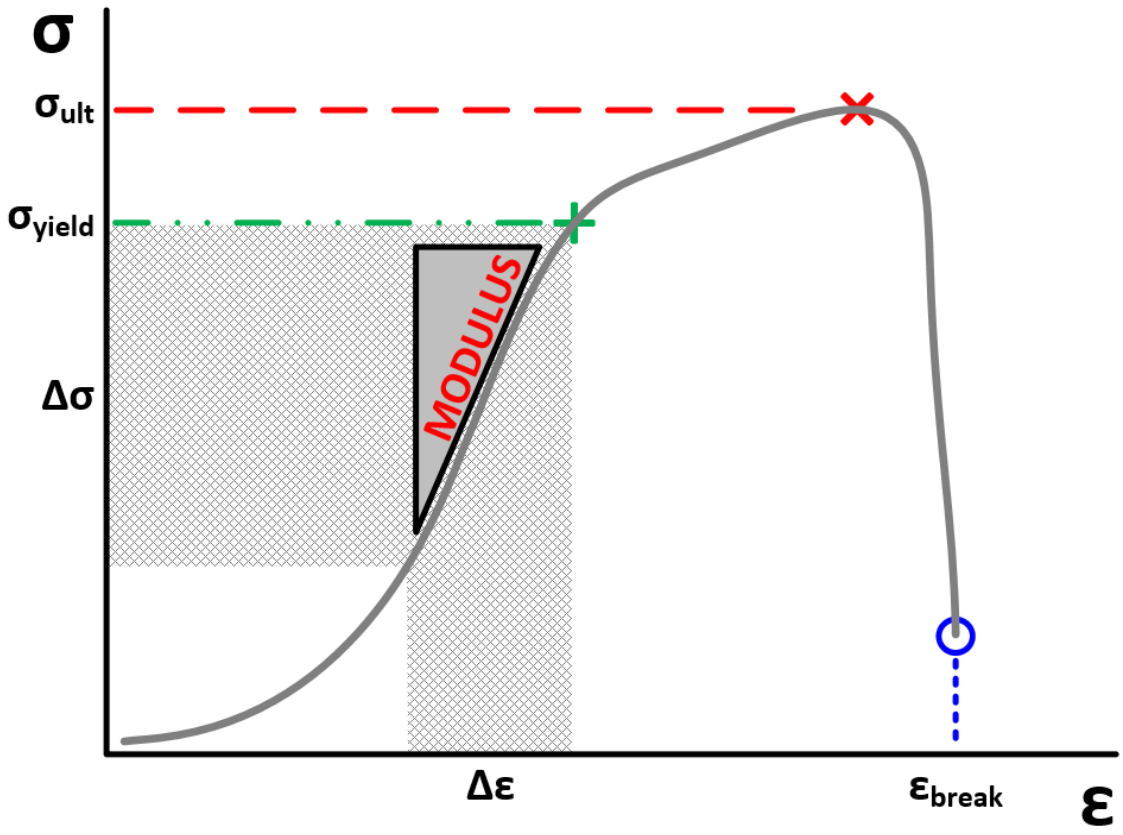

Figure 3.47. Graph representing a typical stress-strain relations of a SFCS-ZnO specimen, in which the modulus, yield stress, ultimate stress, and elongation at break are defined.

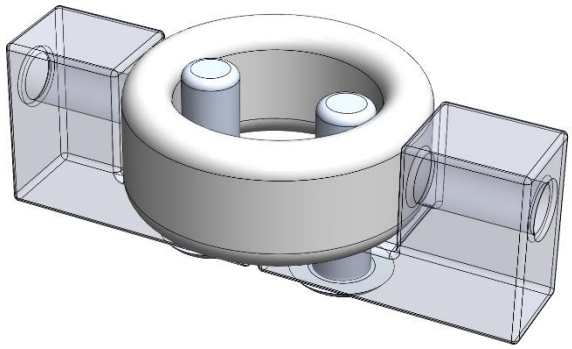

Figure 3.48. 3D rendering of custom "hook type" fixture to effectively grip the fabricated ring devices.

The center-to-center distance of the hook type fixture is set as the gauge length of the samples. The rings are loaded at a displacement rate of 50 mm/min and preconditioned with 10 cyclic loading sequences and a displacement estimated at 25% of failure strain before performing the tensile test to failure, as shown in the programmed testing sequence in Figure 3.49. Ultimate tensile strength (σ_{UTS}) and elongation at break (ε_B) are defined by the peak stress experienced by the sample and maximum strain at failure by the samples, respectively. Engineering stresses are calculated by dividing the recorded loads by the cross-sectional area of the SFCS-ZnO sample using the initial measured construct dimensions, while also compensating for material porosity. Engineering strain is used to measure the deformation of the vascular constructs. Stress-strain curves are plotted and analyzed using a Microsoft Excel script to calculate the tensile parameters.

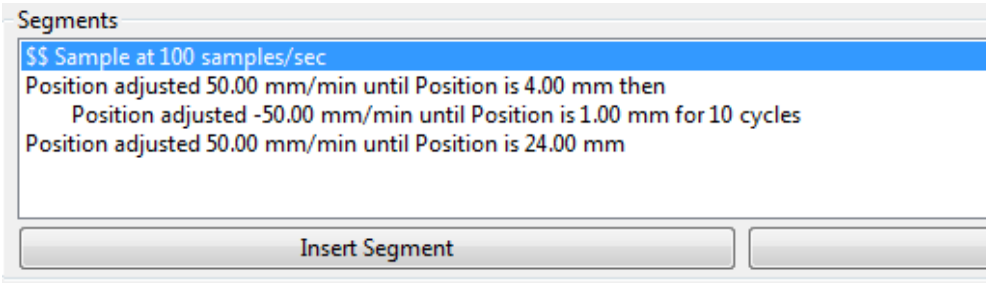

Figure 3.49. Inset of Testing Procedure from the Admet MTESTQuattro software.

3.3.2.3 Viscoelastic characteristics

Biomaterials, such as tissue scaffolds, in particular the SFCS-ZnO composite, have a time dependent or viscoelastic behavior. This time dependence is due to the distinct molecular structure of polymeric materials [50] [51] [52].

3.3.2.3.1 Stress Relaxation

One essential technique for characterizing the viscoelastic time dependent behavior of a material is a stress relaxation test. With this test, a constant strain is suddenly applied to a sample, being rapidly stretched at 50 mm/min to the new strained position and held for a prescribed time period (Figure 3.50 (left)). The Relaxation Modulus is given by:

$$E(t) = \frac{\sigma(t)}{\varepsilon_0} \tag{26}$$

where $\sigma(t)$ is the stress and ε_0 is the constant strain value. The stress is calculated from the recorded force value that is needed to maintain the constant strain input, which decreases with time (Figure 3.50 (right)). Since stress is a function of time, the Relaxation Modulus at a constant strain will also vary with time. Equation () demonstrates the uniaxial stress-strain relation for a viscoelastic material that is analogous to Hooke's Law for a case of a constant strain input.

The Initial Modulus at a time of t = 0 seconds is given by:

$$E(t=0) = \frac{\sigma(t=0)}{\varepsilon_0} = E_0 \tag{27}$$

where σ_0 is the peak stress experienced by the sample upon application of constant strain. Similarly, the Equilibrium Modulus at a time of $t = \infty$ is given by:

$$E(t=\infty) = \frac{\sigma(t=\infty)}{\varepsilon_0} = E_\infty \tag{28}$$

where σ_∞ is the relaxed stress experienced by the sample after of constant strain.

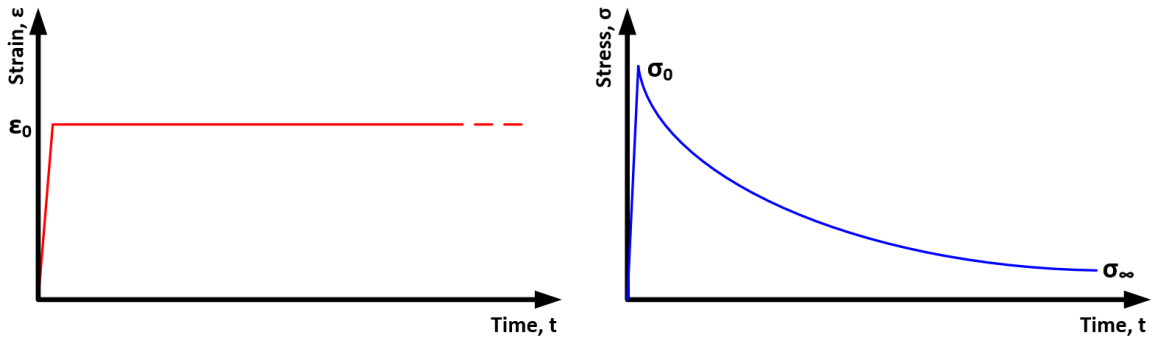

Figure 3.50. Illustration of Relaxation Test: Constant strain input (left) and representative stress output (right).

Stress-relaxation testing of the different SFCS-ZnO constructs is performed as described by others [53]. Like the uniaxial tensile testing, the SFCS-ZnO ring samples are molded, processed and then mounted between the two adapted hooks of the hook type fixture which is placed in the previously stated mechanical tester. These tests require an extended timeframe; therefore, a heated bath is utilized to maintain the ring samples at a constant temperature (37°C) in saline during the entire programmed test. The ring samples

are loaded at a displacement rate of 50 mm/min until an initial displacement value of 3.00 mm is reached and held at this displacement value for 240 seconds. Then, the ring samples are subjected to five rapid incremental displacement steps of 0.5 mm and held for a period of 120 seconds for each incremental step to allow the SFCS-ZnO sample to reach equilibrium. Initial modulus, denoted as the maximum stress value recorded for each relaxation cycle. Whereas, the equilibrium modulus, denoted as the minimum stress recorded at the end of each relaxation cycle. Stress-relaxation data are plotted and analyzed using a custom Microsoft Excel script, allowing for the detection of peak and equilibrium values as well as calculation of the initial and equilibrium moduli.

3.3.2.3.2 Creep

An additional method for characterizing the viscoelastic time dependent behavior of a material is using a creep test. A sudden stress is applied to the sample at a rate 50 mm/min and maintained to a constant value. Strain under constant load increases with time and the below mentioned test defines a quantity called Creep Compliance that is given by:

$$D(t) = \frac{\varepsilon(t)}{\sigma_0} \tag{29}$$

where ε(t) is time dependent strain and σ_0 is the applied constant stress value. Strain is calculated from the recorded displacement necessary to maintain the constant stress input, which increases with time (Figure 3.51 (top)). Point 1 in the bottom of Figure 3.51 represents the end of the linear elastic strain region of the sample during sudden loading and the start of the viscoelastic creep region at a specific constant stress. Point 2 represents

the end of the creep region for the specified 720 second creep test duration and the start of the sudden return to the sample zero stress state. Point 3 represents the end of the sudden reduction of elastic strain induced by returning the material to a zero stress state as seen in the upper stress plot and the start of the creep recovery where the material attempts to return to the unloaded recovered position. Point 4 represents the end of the creep recovery region for the specified 720 second creep recovery test duration, if this point is above a zero-strain state then a residual strain has been induced via the creep test.

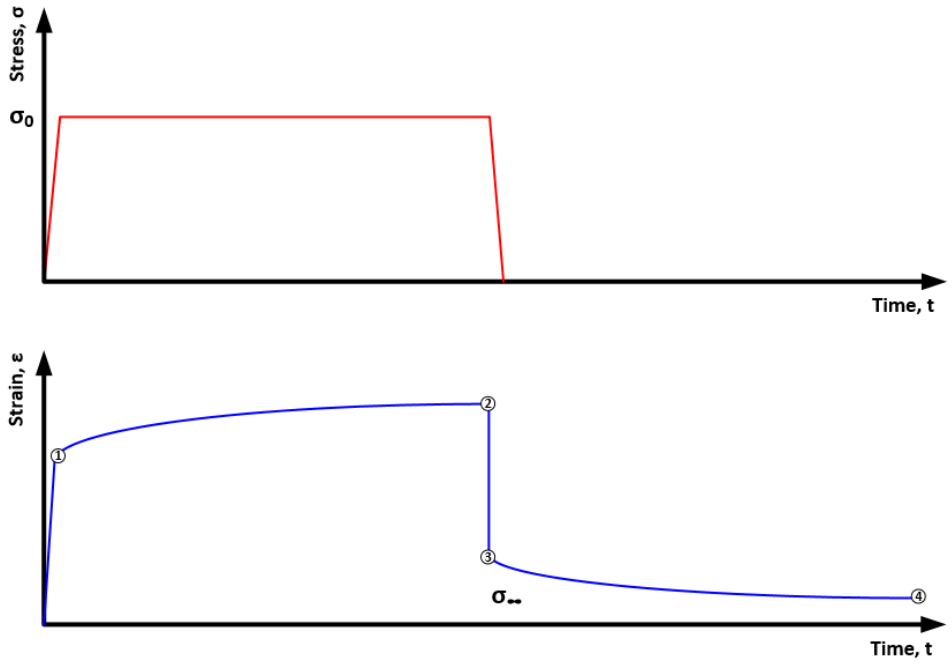

Figure 3.51. Illustration of Creep Test: Constant stress input (top) and representative strain output (bottom).

3.3.2.3.2.1 Linear Viscoelastic Behavior via Isochronous Stress-Strain Relationship

One method to determine linearity is by conducting creep tests at different stress levels and obtaining the creep compliance at constant times as well as generating the

"isochronous" stress-strain diagram. If this isochronous variation of the stress versus strain plot is linear at any recorded time, then the material demonstrates linear tendencies (Figure 3.52). If the variation in the plot is nonlinear, the material demonstrates nonlinear viscoelastic tendencies. Linearity of the isochronous stress – strain plot derives from the fact that the ratio of the strain to stress at a given time, t_i, from each stress level must be identical if the material is to be linear. That is, for t_1 we have

$$D(t = t_1) = \frac{\varepsilon_a(t=t_1)}{\sigma_0|_a} = \frac{\varepsilon_b(t=t_1)}{\sigma_0|_b} = \frac{\varepsilon_c(t=t_1)}{\sigma_0|_c} \tag{30}$$

which means that the compliance $D(t = t_1)$ is independent of stress level.

Similarly

$$D(t = t_2) = \frac{\varepsilon_a(t=t_2)}{\sigma_0|_a} = \frac{\varepsilon_b(t=t_2)}{\sigma_0|_b} = \frac{\varepsilon_c(t=t_2)}{\sigma_0|_c} \tag{31}$$

and

$$D(t = t_3) = \frac{\varepsilon_a(t=t_3)}{\sigma_0|_a} = \frac{\varepsilon_b(t=t_3)}{\sigma_0|_b} = \frac{\varepsilon_c(t=t_3)}{\sigma_0|_c} \tag{32}$$

The conditions above can be deduced from the requirement that the creep compliance is only a function of time (D(t)), and not a function of stress level (D(t,σ)), for a linear material.

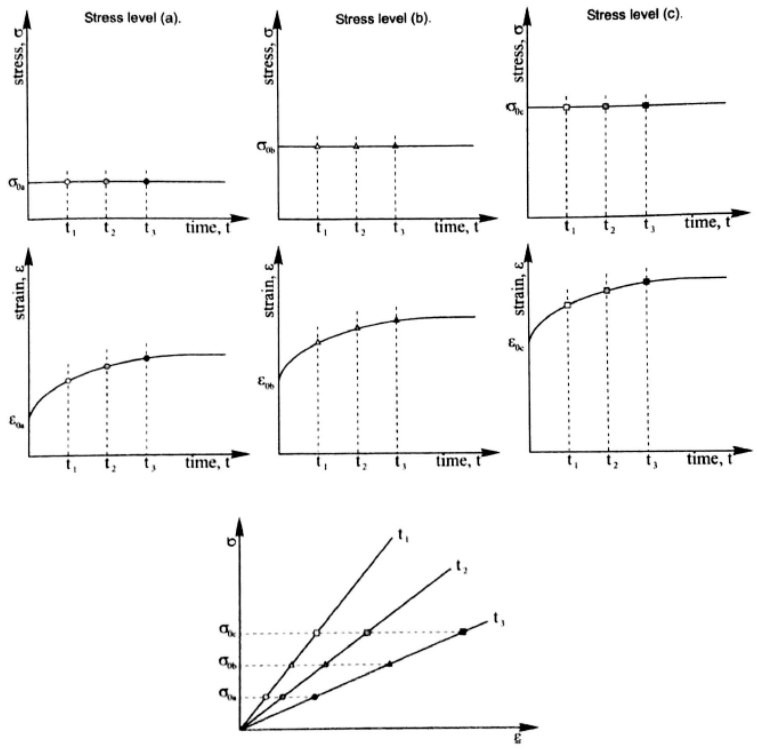

Figure 3.52. Linearity illustrated by an isochronous stress-strain plot at constant times from creep tests [50].

Creep testing of the different SFCS-ZnO constructs is performed as described by others [53]. Similar to the uniaxial tensile and stress relaxation testing, the SFCS-ZnO ring samples are molded, processed and then mounted between the two adapted hook type fixtures which is placed in previously stated mechanical tester. These tests also require an extended timeframe; therefore, a heated bath is utilized to maintain the ring samples at a constant temperature (37°C) in saline during the entire programmed test. The rings are loaded at a displacement rate of 50 mm/min until the initial creep force value of 5.00 grams is reached and then held within ±1% of the nominal force value for 720 seconds. The force is then returned to near 0 grams for another 720 seconds allowing the material to recover.

This 1440 second cycle is followed by 2 additional creep and creep recovery cycles in incremental force steps of 2.5 grams for each additional step to allow the SFCS-ZnO sample to reach equilibrium. The creep data is plotted and analyzed using a custom Microsoft Excel script, allowing the manual detection of points for the elastic strain (1), creep strain (2), elastic recovery (3), creep recovery (4), and residual strain (5) values.

3.3.2.3.3 Compliance and Circumferential Strain Testing

The compliance and circumferential strain of the engineered tube and actual porcine aortic tissue was determined using the imaging rig shown in Figure 3.53. The vessel was mounted in the custom distension unit and filled with saline. A wireless 1080P camera (Hero 3+ Silver Edition, GoPro, Inc., San Mateo, CA) with attached microscope LED array ring light (LED-144A, Amscope, Irvine, CA) was employed to capture images of the distended state of the mounted vessel at internal pressures ranging from 70 mmHg up to 140 mmHg.

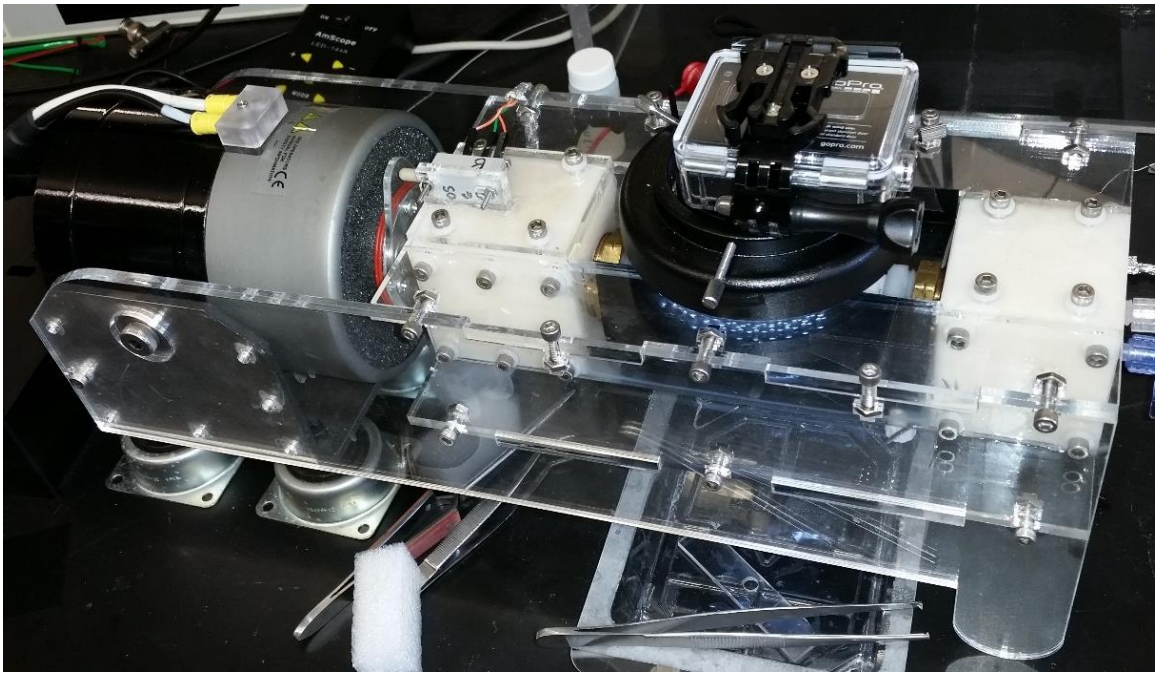

Figure 3.53. Image of the camera setup for capturing vessel diameters at varying static pressures.

The captured images were imported into an image processing and analysis software (ImageJ, National Institutes of Health, Bethesda, MD) and the outer diameter was measured. Figure 3.54(a.) – f.)) Figure 3.55 (a.) – f.)) demonstrate static vessel distension of the engineered elastomeric tube and descending porcine aorta, respectively. The applied internal pressures ranged from 70 mmHg to 140 mmHg.

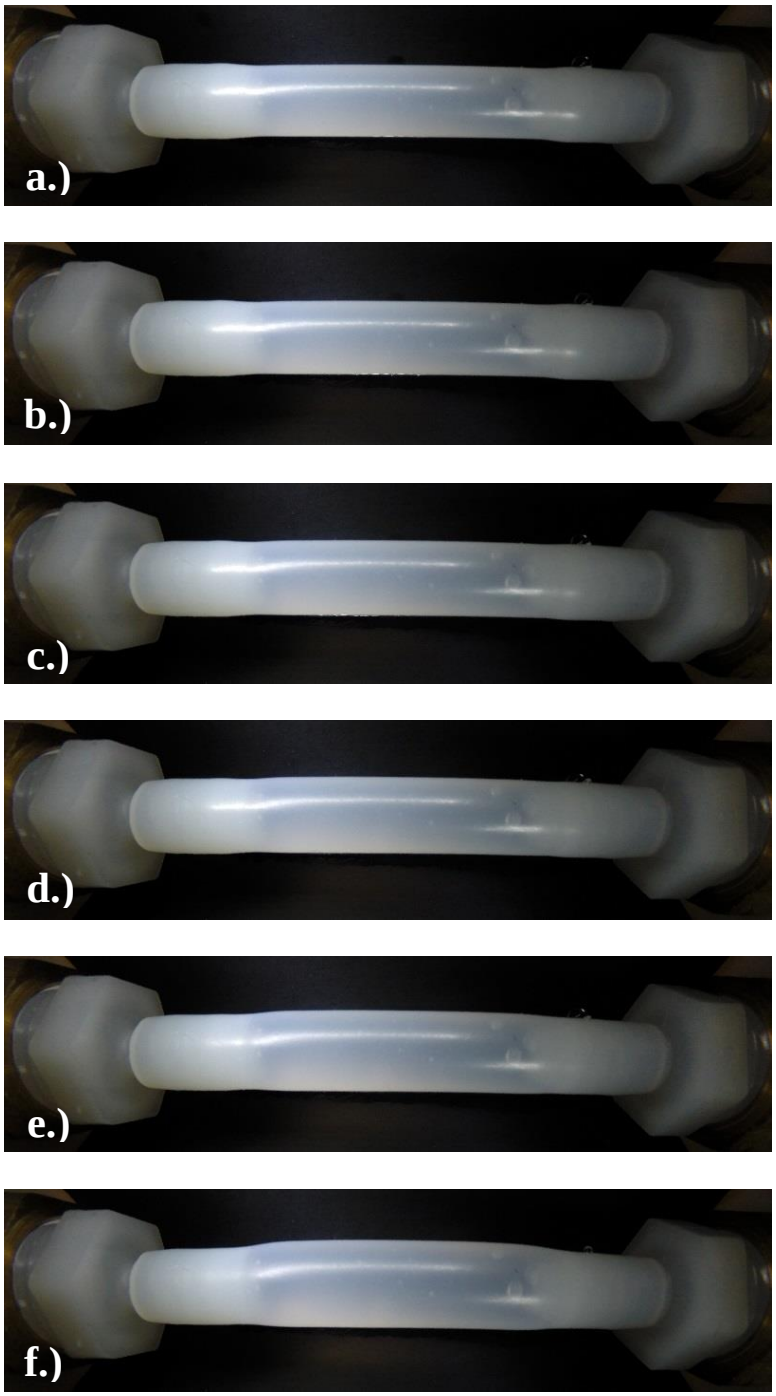

Figure 3.54. Series of images taken at internal vessel pressures at a.) 70mmHg, b.) 80 mmHg c.) 90 mmHg, d.) 100 mmHg, e.) 120 mmHg, and f.) 140 mmHg

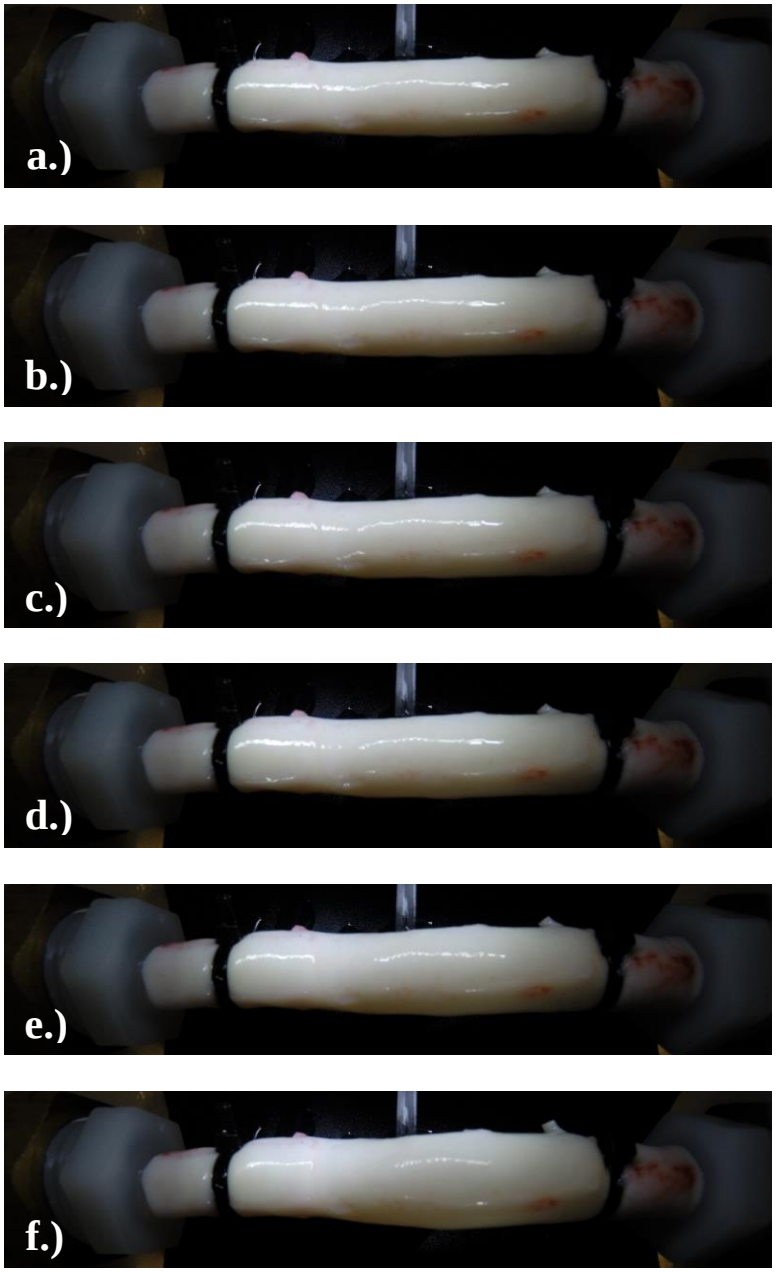

Figure 3.55. Series of images taken at internal vessel pressures at a.) 70 mmHg, b.) 80 mmHg, c.) 90 mmHg, d.) 100 mmHg, e.) 120mmHg, and f.) 140mmHg

3.3.3 Electrical characterization of Biocompatible Piezo-Composites

Electrical characteristics for select SFCS-ZnO blends are evaluated in this study. Electrical response to shear stress and vessel distension are performed by means of the disc shaped (cookie) and ring-shaped (donut) samples, respectively.

3.3.3.1 Shear Testing

Shear testing is performed on all SFCS-ZnO blends by employing the custom shear testing apparatus as described in Section 3.2.1. The 2-mm thick SFCS-ZnO disk sample is mounted between the fixed and movable electrode plates (as shown in Figure 3.56). A series of programmed displacements are applied to the disk samples.

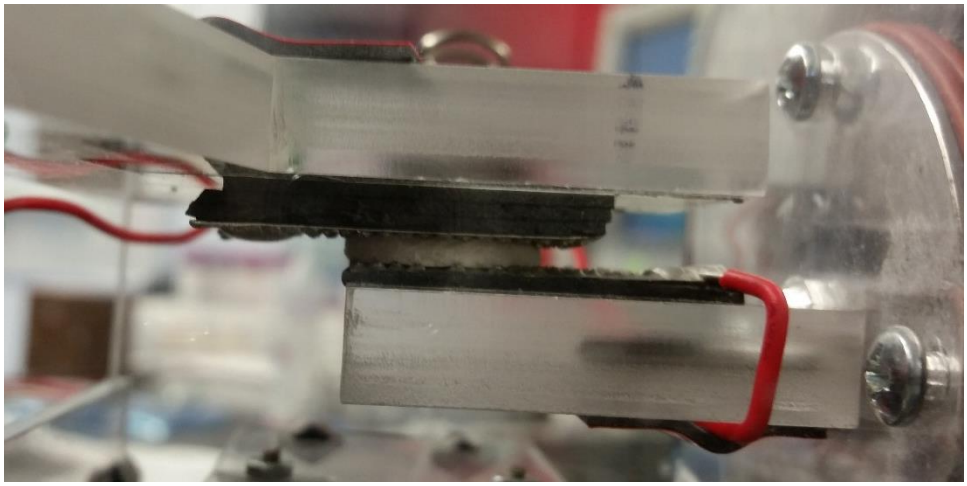

Figure 3.56. Image of shear testing fixture with sample loaded and prepared for the test.

The programmed displacements and the calculated real shear strain are shown in Table 3.7. Permutations of the stated strain cycles were input thru a control and data acquisition software package (LabView, National Instruments Corp., Austin, TX) at three prescribed frequencies, 0.6, 1.2 and 2.4 Hz. Table 3.8 represents the total number of strain/frequency permutations applied the samples during the shear tests. The measured shaker displacement and SFCS-ZnO sample electrical response is recorded for each experiment.

Table 3.7. Applied shear strain to samples

Shaker Displacement (μm)	**Shear Strain**
100	5.0%
200	10.0%
500	25.0%

Table 3.8. Permutations of programmed strains and frequencies applied during typical electrical test.

	Set 1			**Set 2**			**Set 3**		
Strain Amplitude (%)	5			10			25		
Frequency (Hz)	0.6	1.2	2.4	0.6	1.2	2.4	0.6	1.2	2.4

The primary purpose of these sets of experiments was to identify which blends generate the highest response to an applied strain to reduce the number of blends investigated in the distension testing trials. The results will assist the investigator in narrowing the field of test samples to up to four independent blends that generate significantly higher response than others. The four blend candidates with the highest electrical response will then be advanced into the vessel distension investigation for further study.

3.3.3.2 Vessel Distension Testing

Vessel distension testing is performed on select SFCS-ZnO blends by employing the EVDSA as described in Section 3.2.2. The SFCS-ZnO ring sample is mounted onto the vessel as shown in Figure 3.57 by sliding the sample over the cut ends prior to placement in EVDSA. Table 3.9 represents the total number of pressure/frequency permutations applied to the samples during the distension tests. The measured shaker displacement, internal vessel pressure, and SFCS-ZnO sample electrical response is recorded for each experiment.

Figure 3.57. Image of mounted ring sample on aorta.

Table 3.9. Permutations of pressures and frequencies applied during typical vessel distension test.

	Set 1			**Set 2**			**Set 3**		
Strain Amplitude (%)	100/70			120/70			140/70		
Frequency (Hz)	0.6	1.2	2.4	0.6	1.2	2.4	0.6	1.2	2.4

3.3.3.3 Determination of Electrode Placement for Vessel Distension Study

Placement of the wire electrodes may affect electrical response of the SFCS-ZnO sample. Determining the optimal electrode location is investigated via testing six configurations. Three positions with the electrode wires are aligned in the axial direction, with respect to the centerline of the distended vessel, at 45˚, 90˚, and 180˚ between them (Figure 3.58 a.), c.), and e.), respectively). While the other three positions are aligned to the radial direction, also at 45˚, 90˚, and 180˚ between them (Figure 3.58 b.), d.), and f.), respectively). The electrode placement investigation is performed on a single SFCS-ZnO blend, one of the four selected with significantly higher response from the shear testing

investigation. The noted electrodes are 26G tinned copper wire (0.405 mm in diameter) with insulation. The wires terminate directly into the inputs channels of the differential amplifier described in Section 3.2.5. Figure 3.59 demonstrates the actual placement of the electrode wires in an SFCS-ZnO ring sample.

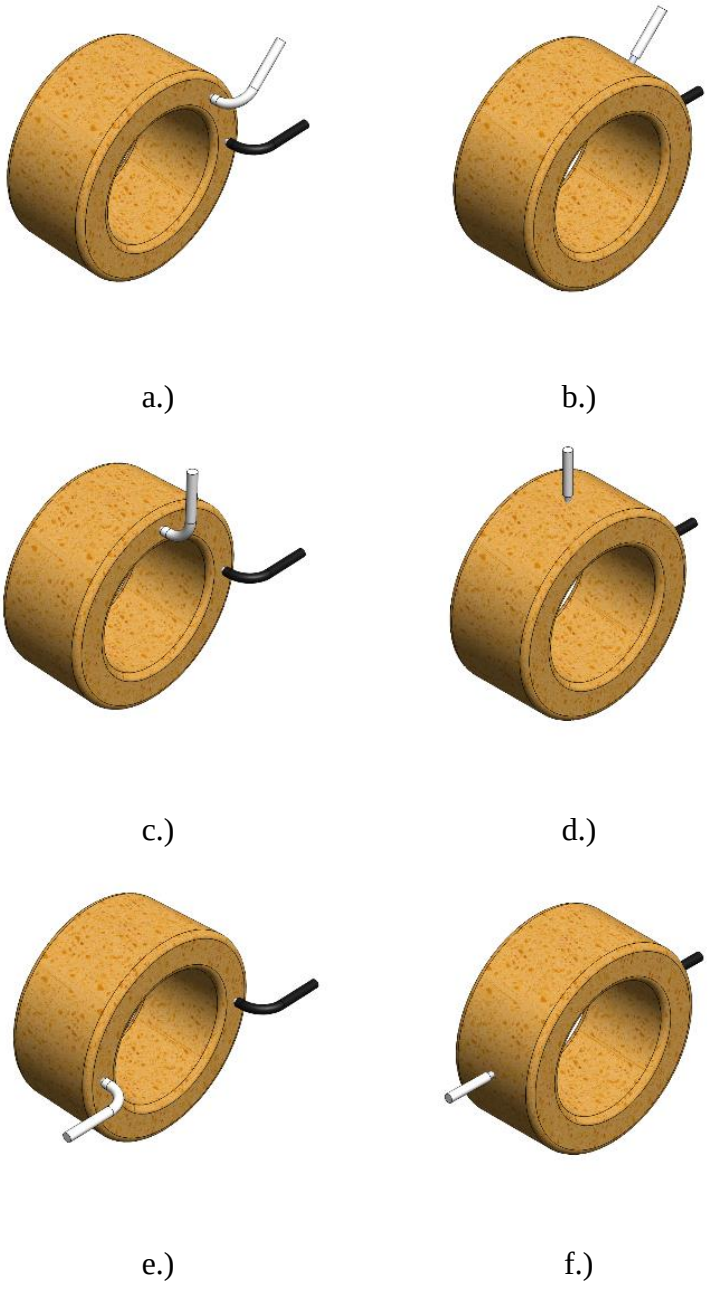

Figure 3.58. CAD rendering illustrating location of wire electrodes placed at 45˚ (a. and b.), 90˚ (c. and d.), and 180˚ (e. and f.) oriented in both axial and radial configurations with respect to the vessel geometry.

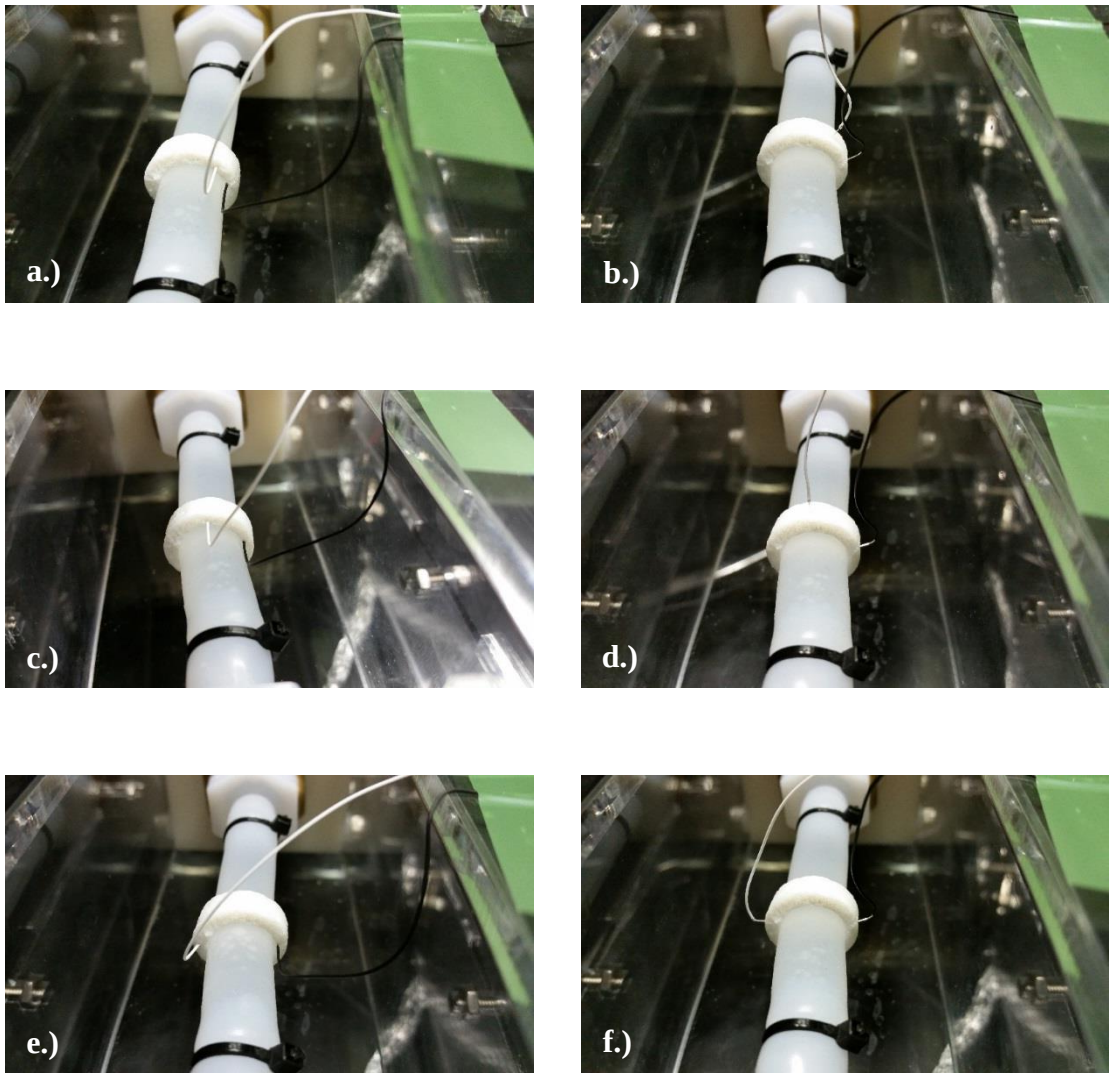

Figure 3.59. Images of actual electrode placement at 45˚, 90˚, and 180˚ oriented in both axial and radial configurations with respect to the vessel geometry.

Figure 3.60 demonstrates the typical placement of the tested samples with attached electrodes on the excised descending aorta.

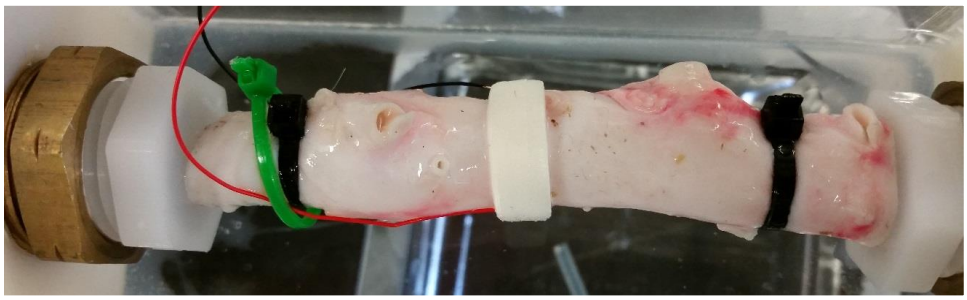

Figure 3.60. Image of SFCS-ZnO ring sample mounted onto an excised descending aorta with electrode mounted in 180˚ axial orientation.

3.3.4 Summary

The sections in this chapter have outlined the details taken to fabricate tissue scaffolds comprised of silk fibroin, chitosan, and zinc oxide nanoparticles. Metrics such as porosity and water absorption are measured for scaffold performance to take up water and potentially nourish surrounding tissue upon potential implantation. Mechanical and viscoelastic characteristics are established via uniaxial tensile, stress relaxation and creep testing, respectively. Electrical response of the SFCS-ZnO samples is experienced and recorded from mechanical shear strain and circumferential strain via vessel distension. The development of the blending techniques to the testing of a proof of concept perivascular band for measuring arterial distension will be discussed.

CHAPTER 4: RESULTS AND DISCUSSION

In this chapter, the results associated with the specific aims outlined in the introduction chapter will be examined. The results of the biocompatible piezo composite formulation will be presented and metric data analyzed. The mechanical and viscoelastic properties of the composite materials will then be presented and evaluated. The piezoelectric properties of the composite scaffold are then presented. Finally, the electrical response of the piezo-composite will be analyzed while experiencing circumferential strain via distension of an engineered blood vessel and one extracted from an animal.

4.1 Formulation of Biocompatible Piezo-Composites

4.1.1 SFCS-ZnO Blend Viscometry

The shear viscosity of the SFCS-ZnO blends was measured prior to the lyophilization step of the scaffold fabrication process using the cone-and-plate viscometer described in Section 3.1.3. However, prior to measuring the shear viscosities of three SFCS-ZnO blends, the shear viscosities of the SFCS scaffolds at the three blended concentrations (30:70; 50:50 & 70:30) without ZnO nanoparticles were determined (Figure 4.1). Non-Newtonian thixotropic or shear thinning behavior was observed with each SFCS blend, demonstrating a reduction in shear viscosity as the shear strain increased. The non-Newtonian shear thinning behavior was anticipated since both SF and CS natively

demonstrate this phenomenon, due to the alignment of molecules and resistance to friction between adjacent fibers within the blend as the shear rate is increased [54].

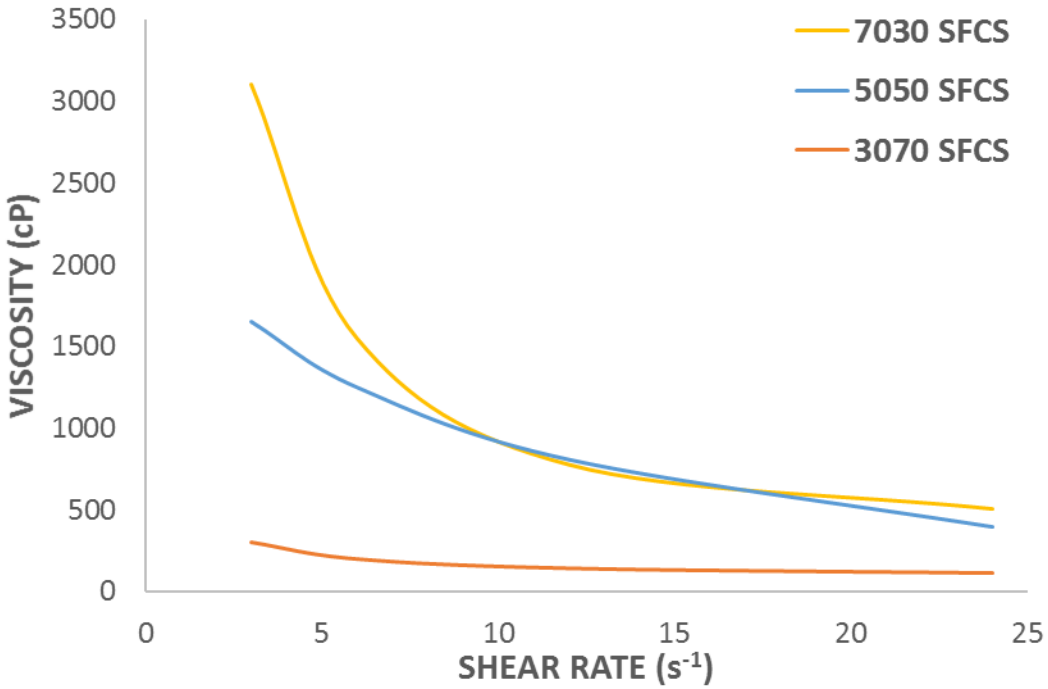

Figure 4.1. Viscosity Measurements of SFCS composites absent of ZnO nanoparticles

Subsequently, shear viscosity of the SFCS scaffolds with ZnO nanoparticles were measured for each ZnO nanoparticle size (30 nm, 45 nm & 200 nm) at the three different nanoparticle concentrations (2%, 5% & 10% nanoparticles by vol.) While viscosity measurement experiments were conducted on all the blends, many of the blends were unable to yield reliable or accurate values due to torque overload on the cone and plate viscometer caused by shear-induced coagulation of the nanoparticles (Table 4.1). Shear-induced coagulation has been reported to occur when particle-to-particle interaction increases with smaller particle size at constant weight fractions [55] [36]. This behavior

was observed in the SFCS-ZnO blends listed in (Table 4.1), so these blends were unable to yield accurate shear values and were eliminated from further investigation.

Table 4.1. List of blends that yielded accurate (successful blends) and inaccurate (unsuccessful blends) viscosities..

Unsuccessful Blends	**Successful Blends**
3070-30nm-10%	3070-30nm-2%
3070-45nm-10%	3070-30nm-5%
5050-30nm-10%	3070-45nm-2%
5050-45nm-5%	3070-45nm-5%
5050-45nm-10%	3070-200nm-2%
5050-200nm-5%	3070-200nm-5%
7030-30nm-2%	3070-200nm-10%
7030-30nm-5%	5050-30nm-2%
7030-45nm-2%	5050-30nm-5%
7030-45nm-5%	5050-30nm-10%
7030-200nm-2%	5050-45nm-2%
7030-200nm-5%	5050-45nm-5%
	5050-200nm-2%

Figure 4.2. Image of shear induced coagulation of ZnO nanoparticles in SFCS composite for a 2 mL SFCS-ZnO sample after exposed to shear via the cone and plate viscometer. Particle coagulation was clearly present. (Additional images of unsuccessful blends are shown in Appendix 2.)

Just as observed with the SFCS only blends, non-Newtonian shear thinning was seen with each SFCS-ZnO blend with the viscosity decreasing as the strain rate increased (Figure 4.3). This plot displays the 30:70 blends with 200 nm ZnO particles at all three weight fractions (WF) and represents a typical trend for all blends. It is evident that the shear viscosity increases with WF.

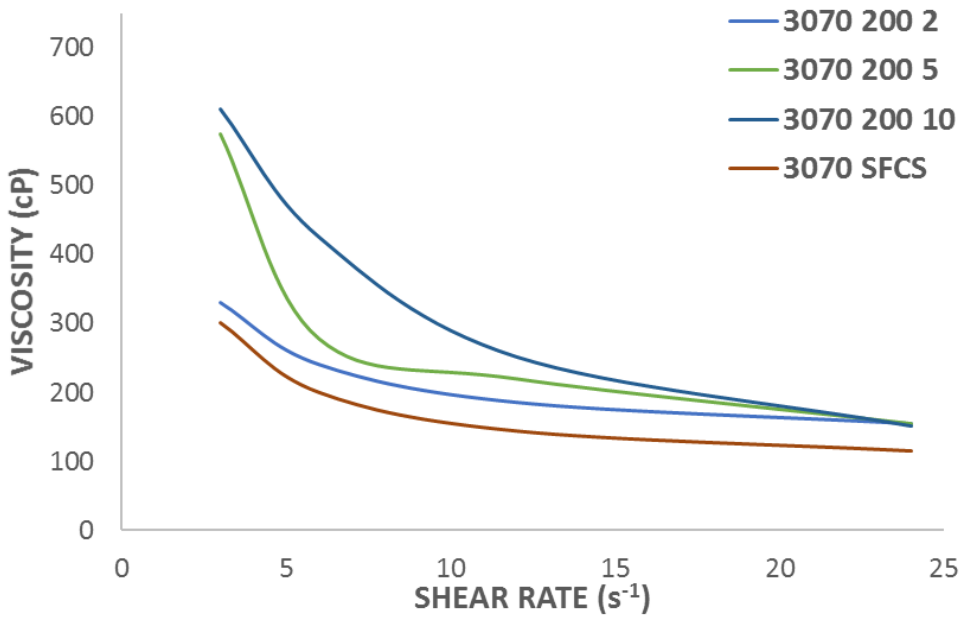

Figure 4.3. Plot of Viscosity vs. Shear Rate for 30:70 SFCS blends with 200 nm particles at varying concentrations.

4.1.2 pH Measurement of Composite Blends

The pH of each SFCS-ZnO scaffold blend was measured using the Beckman Coulter pH and Electrochemistry Meter. The pH of the SFCS blends only (no ZnO nanoparticles) displayed a near neutral pH of approximately 6.5 with no significant difference in pH between each blend type (Table 4.2). While for the aqueous ZnO solutions (0.25 g/mL concentration), the pH was found to be of high alkalinity of approximately 9.5 (Figure 4.4) and there was a significant difference in pH between the 30 nm and 45 nm ($\rho^* = 0.003$) and 30 nm and 200 nm ($\rho^{**} = 0.016$) solutions, while the pH values were insignificant between the 45 nm and 200 nm ($\rho = 0.098$).

Table 4.2. pH of SFCS composites without embedded ZnO nanoparticles

Blend	Average pH	Standard Deviation
30:70	6.49	0.04
50:50	6.44	0.05
70:30	6.46	0.08

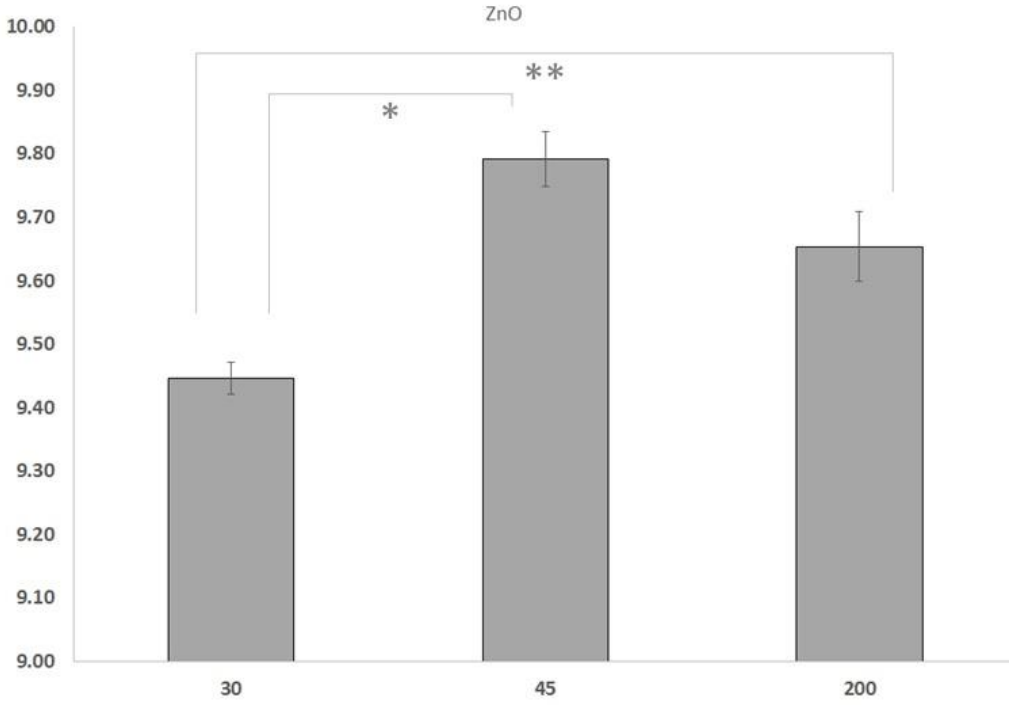

Figure 4.4. Bar chart of pH of aqueous dispersion ZnO nanoparticle.

The pH of each of the SFCS-ZnO blends were measured and an increase in pH was observed for the individual blends of SFCS-ZnO from 2% up to 10% (Figure 4.5), albeit not significant. An analysis of variance (ANOVA) was performed to determine significance of individual factors, SFCS Blend (30:70, 50:50, 70:30), ZnO Particle Size (30 nm, 45 nm, 200 nm), and ZnO weight percent (2%, 5%, 10%). Some significant differences were found for pH values between specific blend combinations; however, no general significant trend was seen.

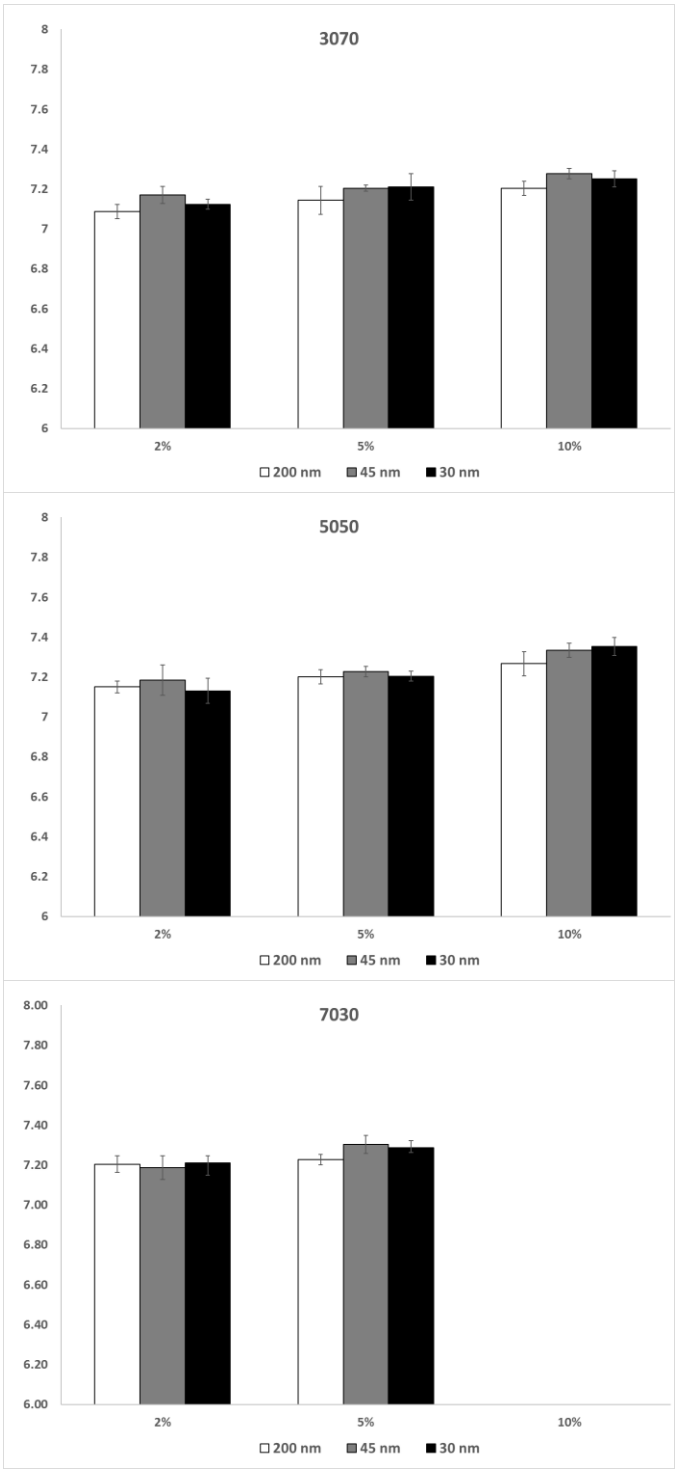

Figure 4.5. Bar chart illustrating average pH of SFCS-ZnO blends with standard deviation.

4.1.3 Water Absorption

As described in chapter 3, the total mass of the engineered SFCS-ZnO blended scaffolds soaked in water were recorded at prescribed time intervals (0 (dry), 30, 60, 90, 120, 180, and 240 minutes). The average change in the dry mass versus wet mass for each of the pure SFCS blends were plotted (Figure 4.6). At the 240-minute interval, the 30:70, 50:50, and 70:30 blends were all significantly different. It was noted that increasing amounts of chitosan resulted in significantly higher mass due to chitosan's ability to "take up" water more efficiently [37]. The average change in mass for each of the SFCS-ZnO blends was also found to significantly increase as the concentration of zinc oxide nanoparticles increased (Figure 4.7, Figure 4.8, Figure 4.9).

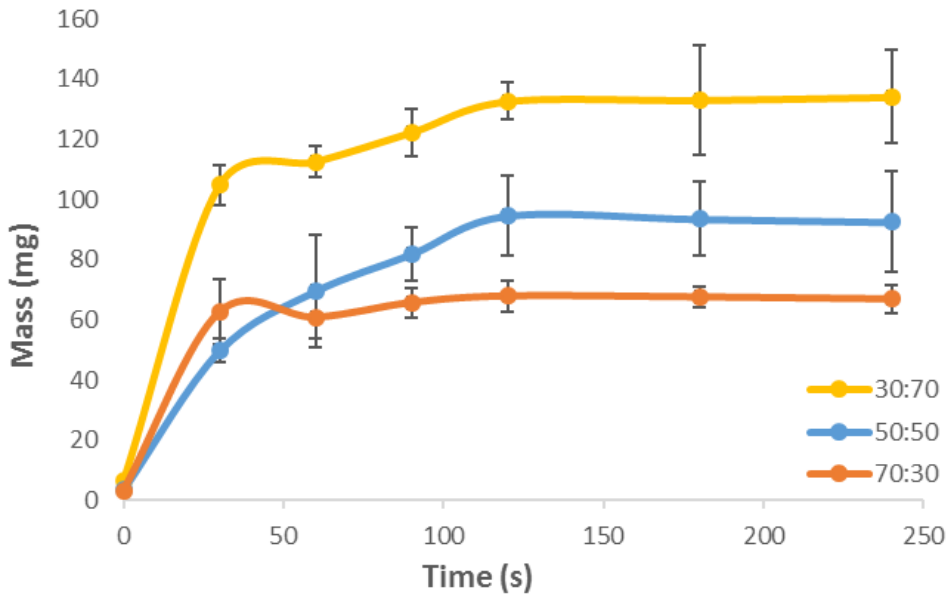

Figure 4.6. Mass properties of pure SFCS blended scaffolds.

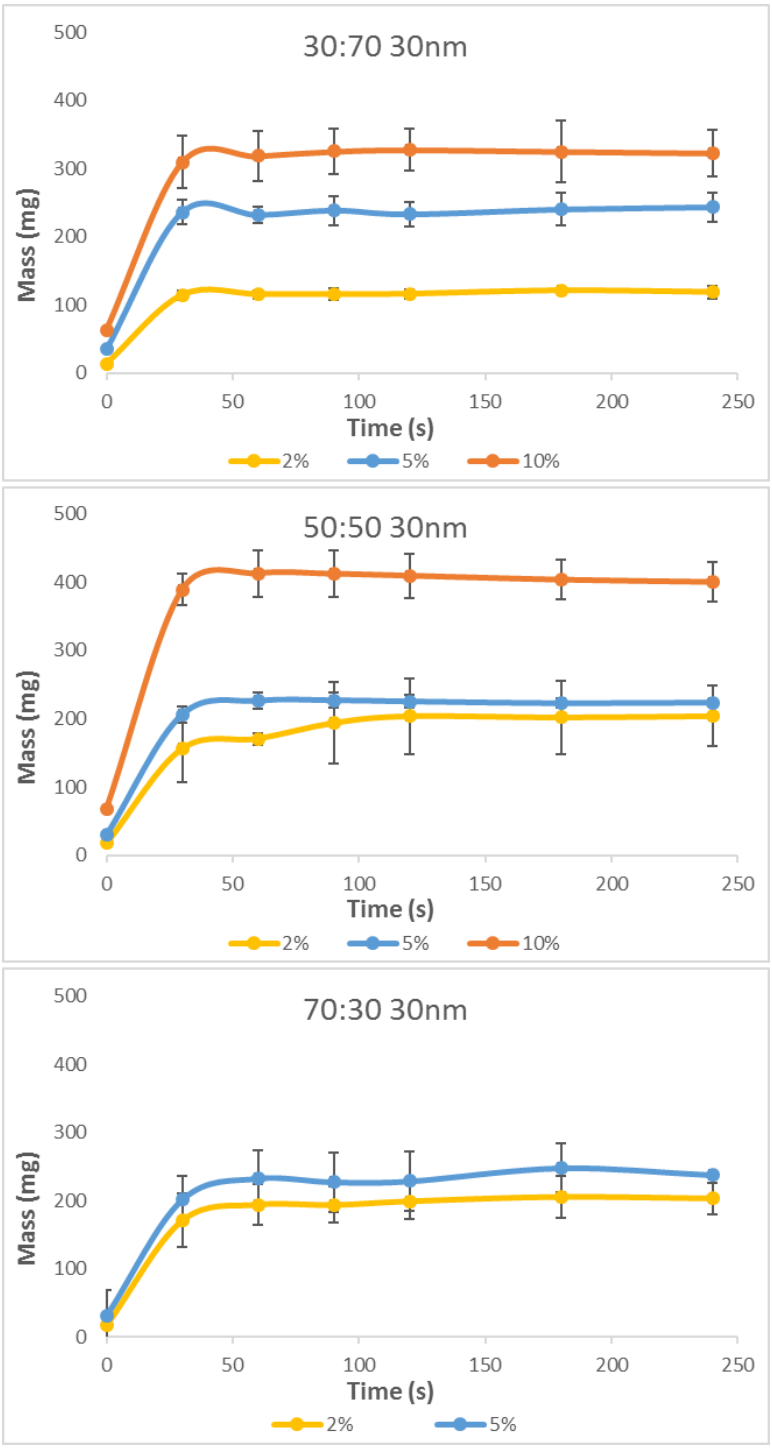

Figure 4.7. Average change in mass for each of the SFCS-ZnO blends with 30 nm particles. Note: The 70:30, 30 nm, 10% by weight is not shown due to inability to mix the particular blend.

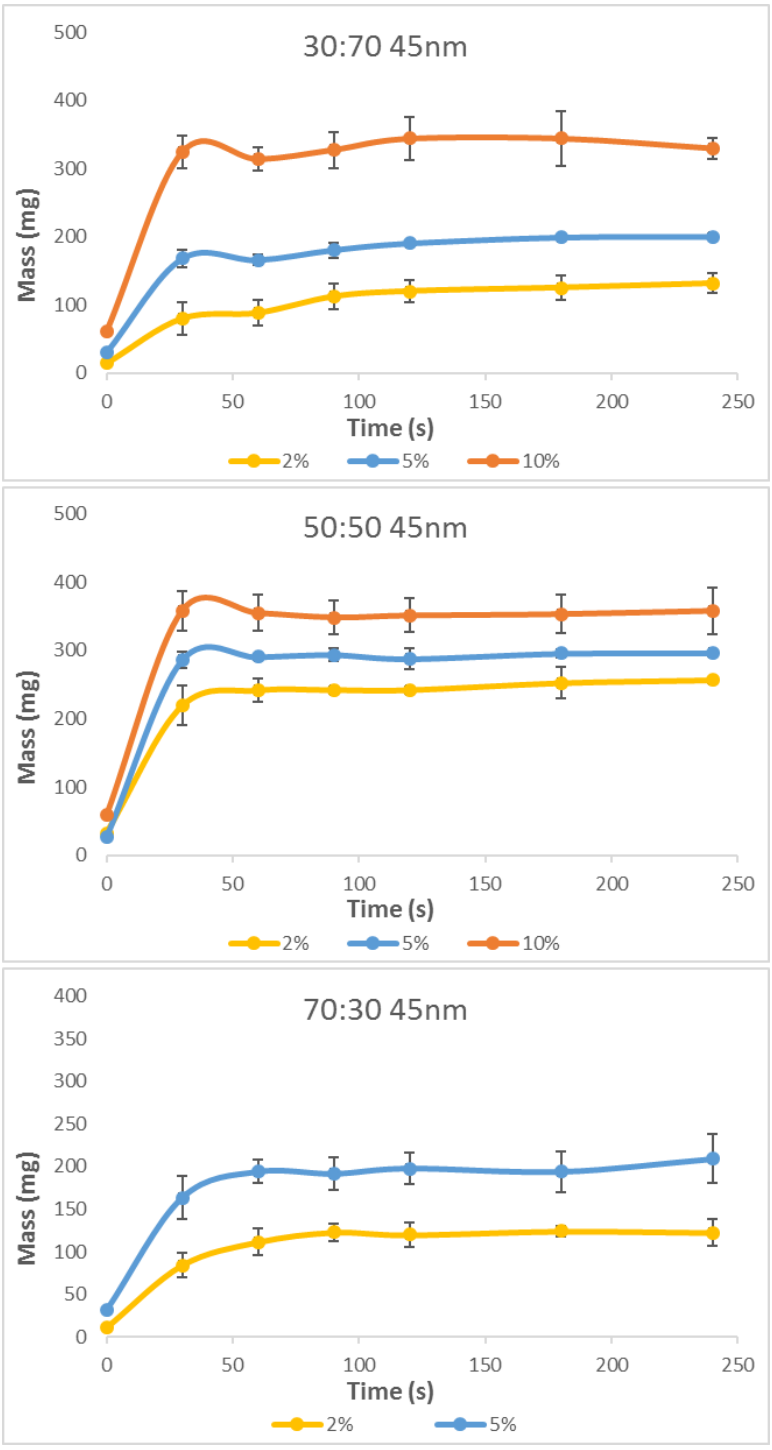

Figure 4.8. Average change in mass for each of the SFCS-ZnO blends with 45 nm particles. Note: The 70:30, 45 nm, 10% by weight is not shown due to inability to mix the particular blend.

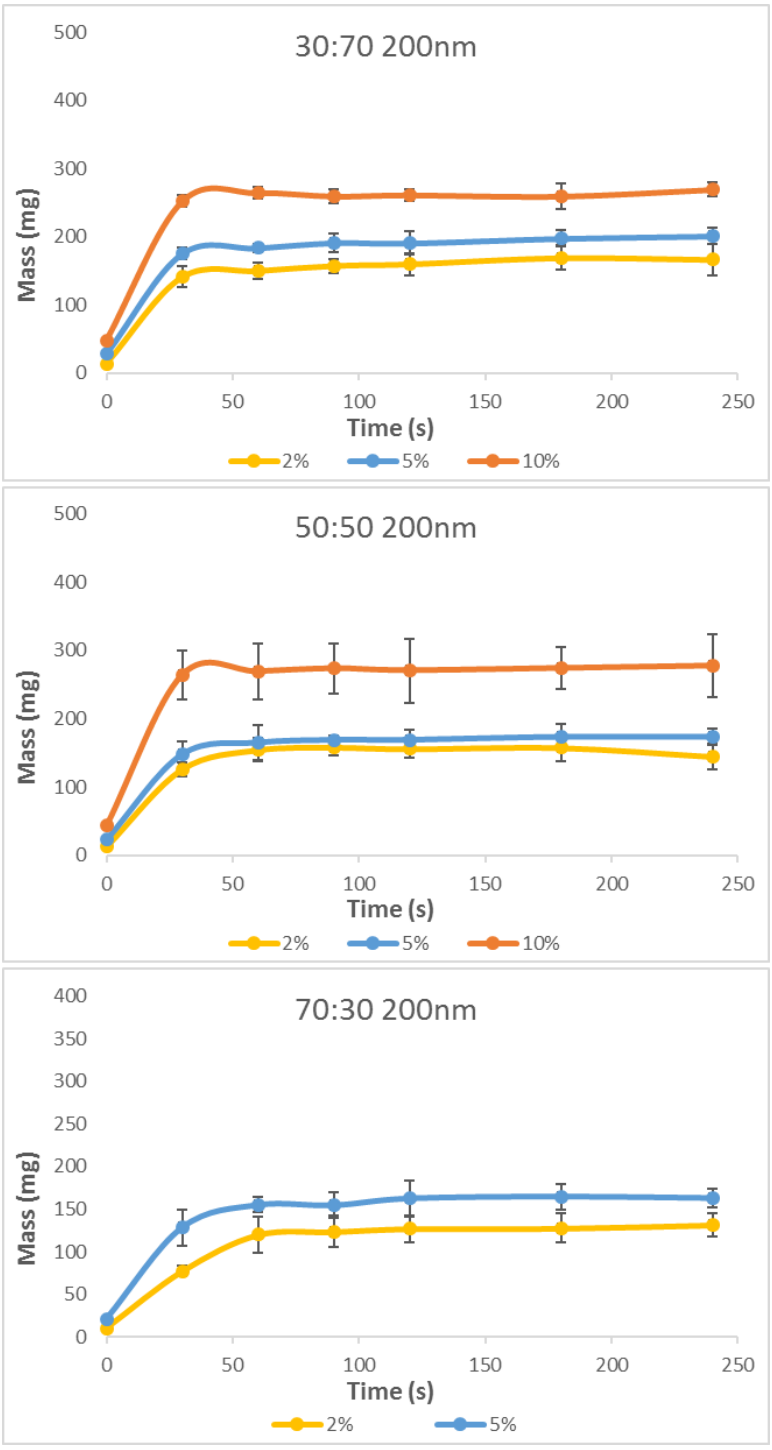

Figure 4.9. Average change in mass for each of the SFCS-ZnO blends with 200 nm particles. Note: The 70:30, 200 nm, 10% by weight is not shown due to inability to mix the particular blend.

Water absorption was calculated to delineate the effects of an increase in mass due to the addition of zinc oxide and the scaffold's natural capability for absorbing water. The capacity of each SFCS-ZnO blend to absorb water was calculated via Equation (33) and plotted at 30, 60, 90, 120, 180, and 240 minute intervals (Figure 4.10). Measurements were concluded at the 240-minute interval due to all samples reaching steady state with an average percent change, %Δ, of:

$$\%\Delta = \frac{A_{240} - A_{180}}{A_{180}} \times 100\% \tag{33}$$

where A_{240} and A_{180} were the measured water absorption values at the corresponding time intervals. The average percent change among all datasets of the SFCS only blends was 2.45%, therefore water absorption was determined to reach steady state. The water adsorption data for the SFCS only blends was found to follow the same trend as Figure 4.7, Figure 4.8, Figure 4.9, where the scaffolds with higher chitosan content also exhibited a higher affinity for water absorption.

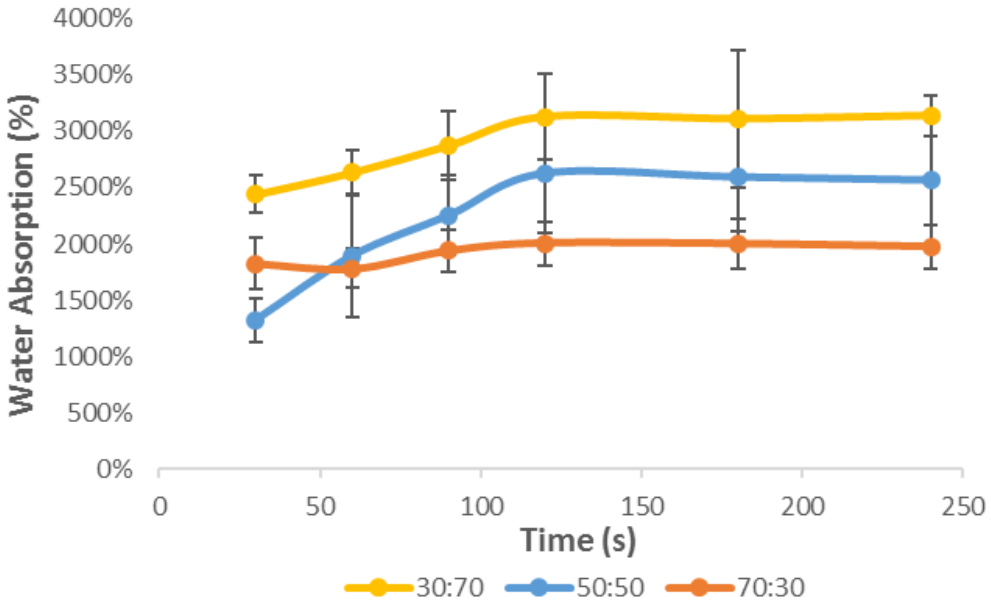

Figure 4.10. Water absorption of pure SFCS blended scaffolds up to a time interval of 4 hours.

Similarly, the capacity of each SFCS-ZnO blend to absorb water was calculated and plotted at 30, 60, 90, 120, 180, and 240 minute intervals (Figure 4.11, Figure 4.12, Figure 4.13). The data demonstrated that a higher ZnO content for any particular SFCS blend reduced the capacity of the scaffold to absorb water. Furthermore, as the ZnO weight concentration increased, the blended sample's ability to absorb water significantly decreased (Figure 4.14). This phenomenon was due to ZnO having a natural hydrophobicity [56] [57], which counteracted the hydrophilicity and natural ability of pure SFCS blends to take up water at higher concentrations, in addition to the nanoparticles physically occupying the spaces in the scaffold pores or matrix where the water would potentially reside.

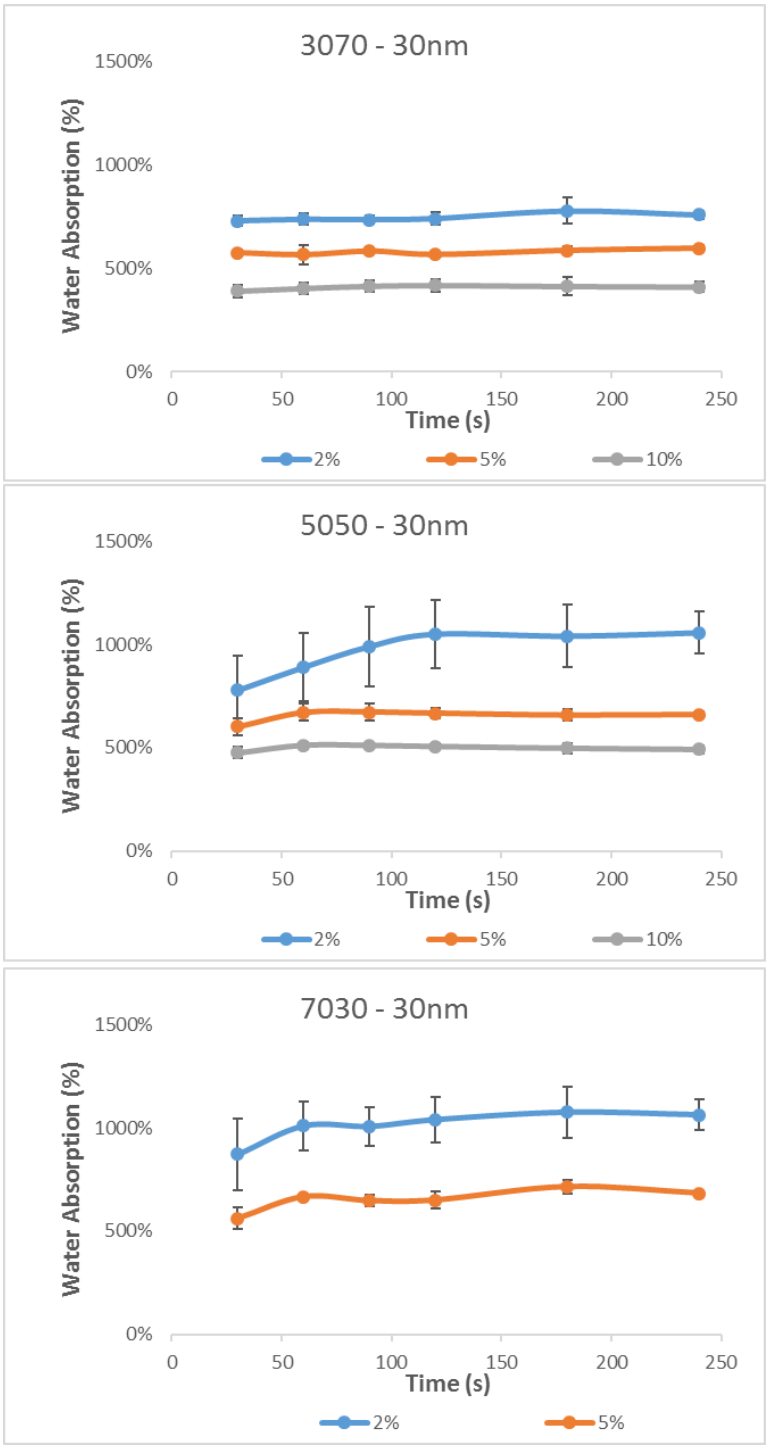

Figure 4.11. Average water absorption data for SFCS-ZnO blends with 30 nm particles representing collection intervals up to 240 minutes. Note: The 70:30, 30 nm, 10% by weight is not shown due to inability to mix the particular blend.

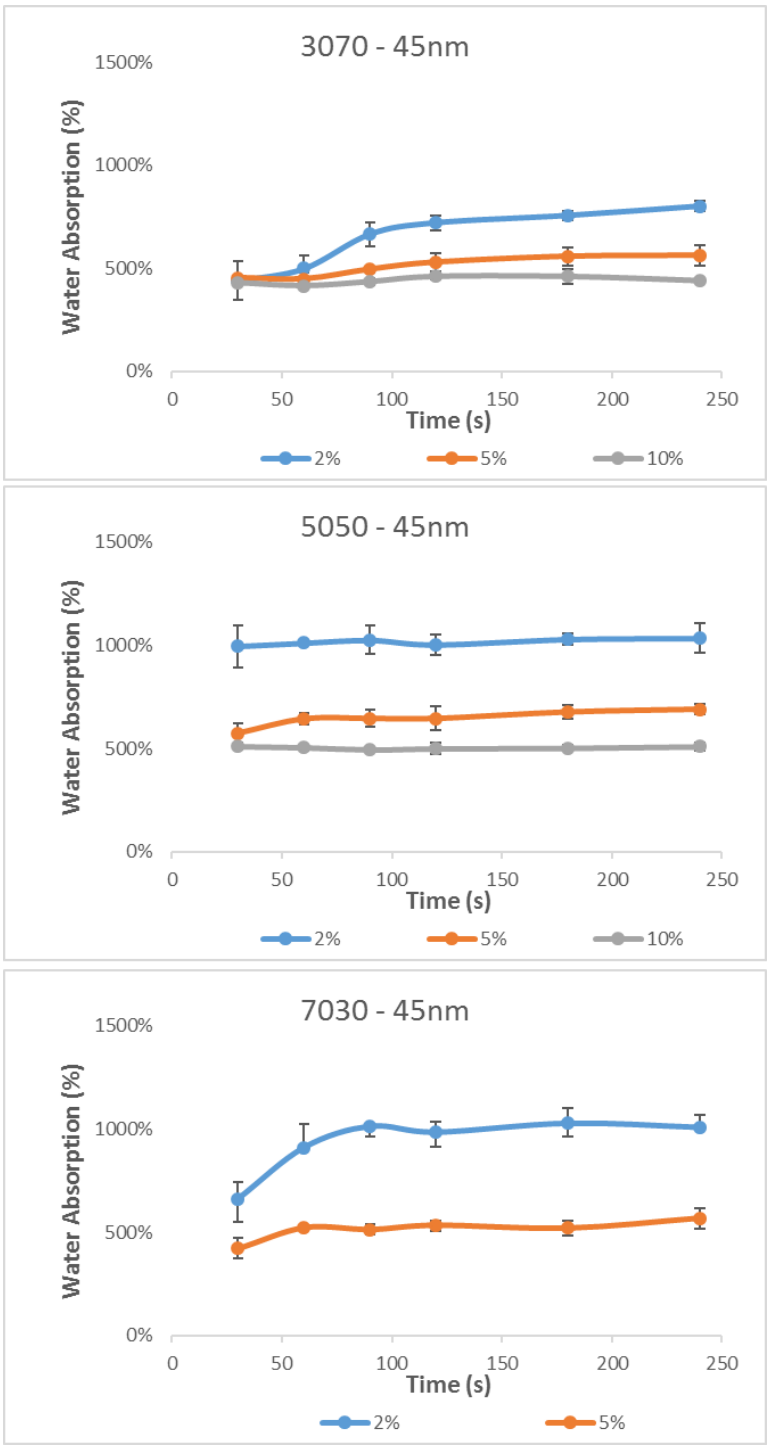

Figure 4.12. Average water absorption data for SFCS-ZnO blends with 45 nm particles representing collection intervals up to 240 minutes. Note: The 70:30, 45 nm, 10% by weight is not shown due to inability to mix the particular blend.

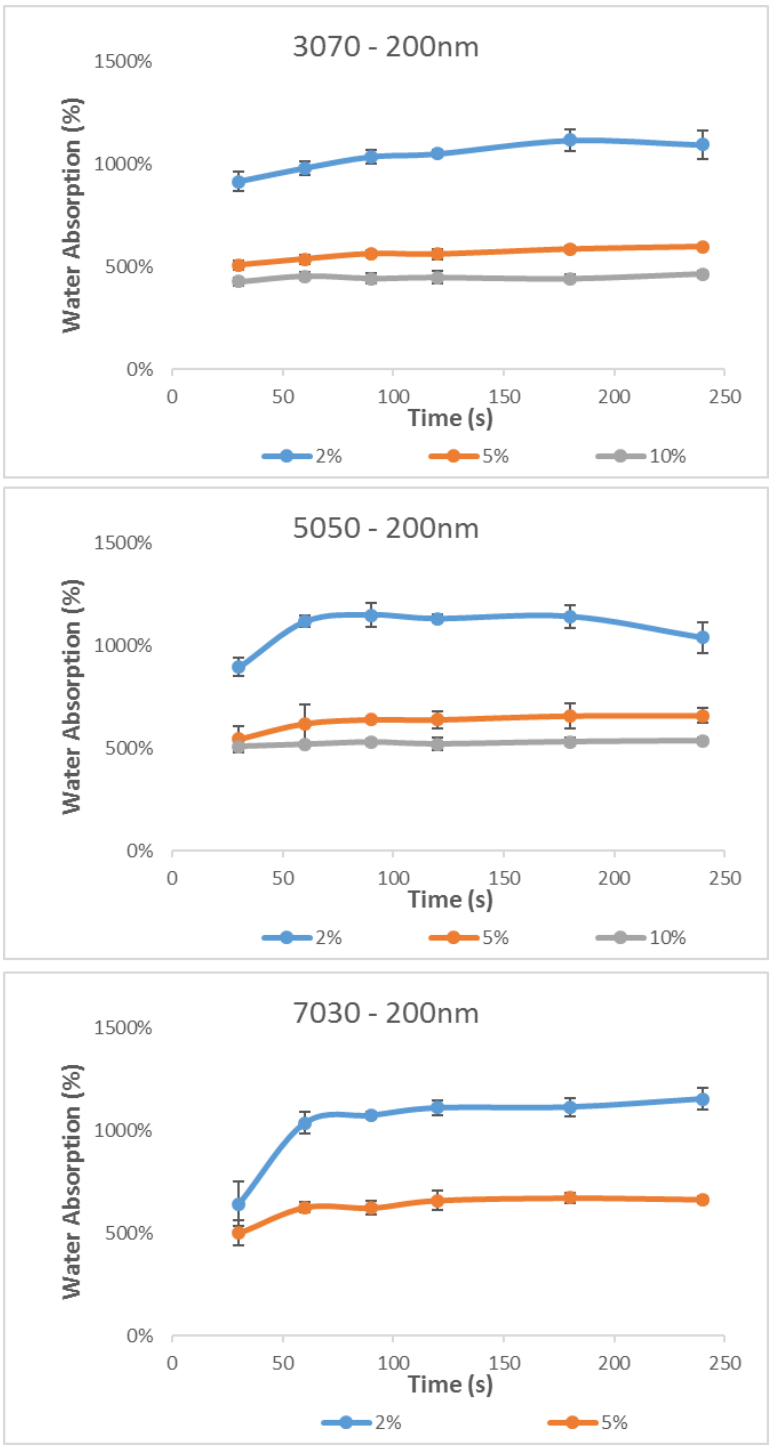

Figure 4.13. Average water absorption data for SFCS-ZnO blends with 200 nm particles representing collection intervals up to 240 minutes. Note: The 70:30, 200 nm, 10% by weight is not shown due to inability to mix the particular blend.

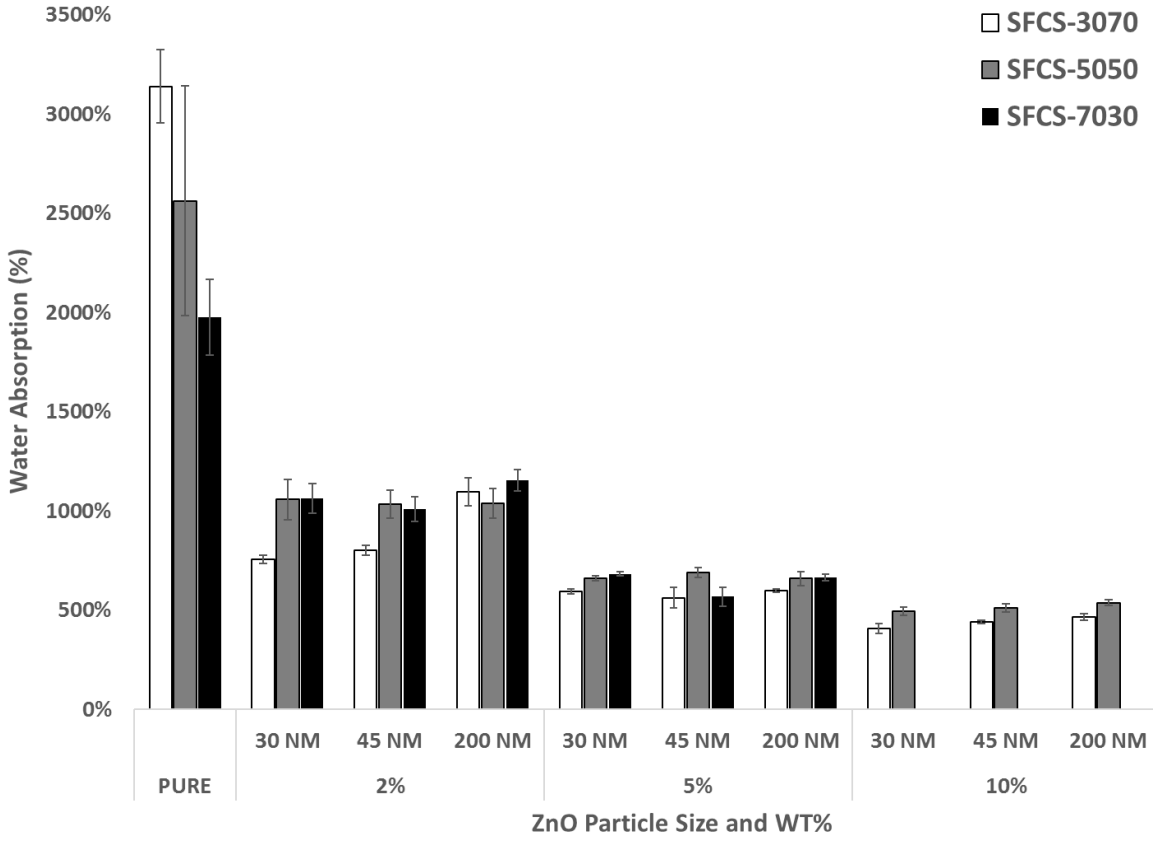

Figure 4.14. Bar chart illustrating differences water absorption between SFCS-ZnO blends.

4.1.4 Scaffold Metrology

Basic metrology was performed on the SFCS-ZnO ring specimens after being processed through the post lyophilization crystallization and neutralization process with MeOH:NaOH as described in Section 3.3.1. Three samples from each blend were extracted from the PBS storage solution and the outer diameter (ϕ), wall thickness (WT) and the height of the ring (H) were recorded using a set of 6-inch digital calipers.

The dimensional data was analyzed to determine whether SFCS blend, ZnO particle size, or ZnO concentration affected the overall dimensions of the fabricated rings within

the mold due to material shrinkage during the lyophilization, crystallization and neutralization processes. The SFCS blend was found to significantly affect ($p < 0.05$) the outer diameter, wall thickness, and height values of the SFCS-ZnO rings (Table 4.3). On the other hand, the particle size was found to have no significant effect ($p > 0.05$) on the outer diameter, wall thickness, and height of the SFCS-ZnO ring assemblies shown in Table 4.4. Similar to the SFCS blend, the ZnO concentration was found to significantly effect ($p < 0.05$) the outer diameter, wall thickness, and height values of the SFCS-ZnO rings shown in Table 4.5.

Table 4.3. Average outer diameter (Ø), wall thickness (WT), and height (H) of each SFCS-ZnO blend with respect to SFCS Blend.

SFCS BLEND	Ø (mm) Average ± Std. Dev.	WT (mm) Average ± Std. Dev.	H (mm) Average ± Std. Dev.
3070	16.179 ± 0.704	3.436 ± 0.117	7.679 ± 0.498
5050	15.820 ± 0.262	3.400 ± 0.090	7.430 ± 0.425
7030	15.741 ± 0.536	3.186 ± 0.150	7.299 ± 0.541

Table 4.4. Average outer diameter (Ø), wall thickness (WT), and height (H) of each SFCS-ZnO blend with respect to Particle Size (nm).

PARTICLE SIZE (nm)	Ø (mm) Average ± Std. Dev.	WT (mm) Average ± Std. Dev.	H (mm) Average ± Std. Dev.
30	15.995 ± 0.471	3.298 ± 0.124	7.459 ± 0.402
45	16.035 ± 0.491	3.357 ± 0.199	7.351 ± 0.630
200	15.773 ± 0.683	3.425 ± 0.111	7.662 ± 0.405

Table 4.5. Average outer diameter (Ø), wall thickness (WT), and height (H) of each SFCS-ZnO blend with respect to ZnO Concentration.

ZnO CONC.	Ø (mm) Average ± Std. Dev.	WT (mm) Average ± Std. Dev.	H (mm) Average ± Std. Dev.
2%	15.458 ± 0.394	3.311 ± 0.141	7.157 ± 0.403
5%	16.100 ± 0.261	3.367 ± 0.191	7.503 ± 0.435
10%	16.402 ± 0.536	3.422 ± 0.089	7.973 ± 0.222

After the MeOH/NaOH crystallization and neutralization wash, the measured SFCS-ZnO scaffolds had a global average shrinkage value of 20.8% ± 1.9% for all 3 critical dimensions with respect the mold dimensions. The methanol treatment of the SFCS-ZnO specimens induces the transition of random coil conformation to β-sheet structure of the silk fibroin which results in the shrinkage of materials [58]. Surface tension of the SFCS material itself contributed to the compacting of the overall porous structure, which resulted in the dimensional changes between the mold and final ring scaffolds. Gobin et al. [37] also observed shrinkage, with up to a 75% dimensional change. The design of a mold affects the scaffold architecture and the amount of shrinkage that the sample experiences; this is a common occurrence among any engineered part that is injection molded.

4.1.5 Imaging

Metrology was performed on the SFCS-ZnO blended specimens via the LEO Supra 35 VPSEM. Images of the ZnO nanoparticles that were employed within the blended scaffolds were also recorded, shown in Figure 4.15. A droplet (50 µL) of each aqueous ZnO solution (50 uL of 0.25 g/mL into 10 mL water) was dispensed onto a separate glass slide via a micropipettor and allowed to dry. The dried sample was then placed within the SEM for imaging.

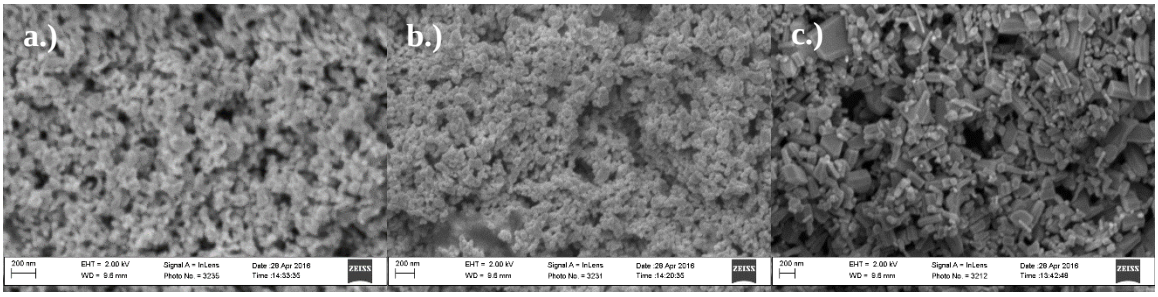

Figure 4.15. SEM image of a.) 30nm ZnO nanoparticle, b.) 45nm ZnO nanoparticle, and c.) 200nm ZnO nanoparticle

The scaffold cross-sectional morphology was imaged via scanning electron microscopy after crystallization, neutralization and a secondary lyophilization process to ensure the samples were dry for imaging. Large β-sheets were observed in near parallel formation, for each blend of the pure SFCS (Figure 4.16, Figure 4.17, Figure 4.18). The addition of ZnO nanoparticles did not affect the β-sheet formation in any of the blends for any of the ZnO WT% (Figure 4.19, Figure 4.20, Figure 4.21). Also, as the WT% increased, the nanoparticles were clearly visualized on the β-sheets. All other SEM images of SFCS-ZnO blends displaying nanoparticles can be found in Appendix 3.

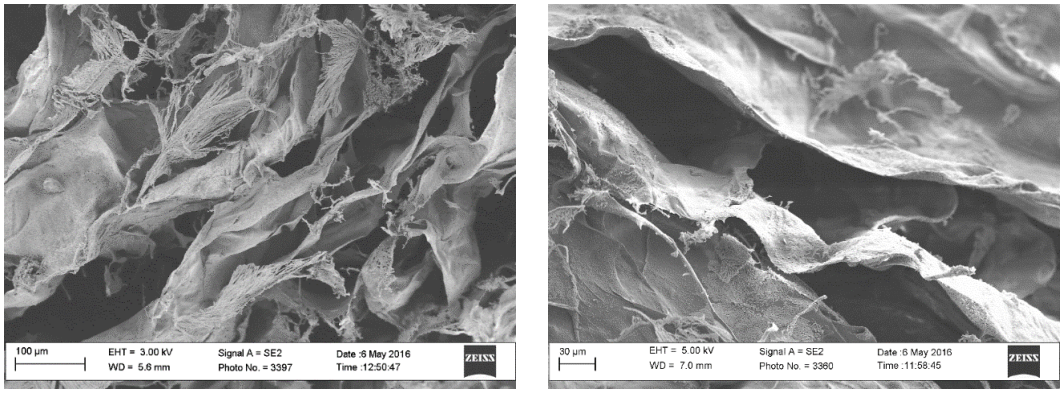

Figure 4.16. SEM images of pure 3070 SFCS tissue scaffold

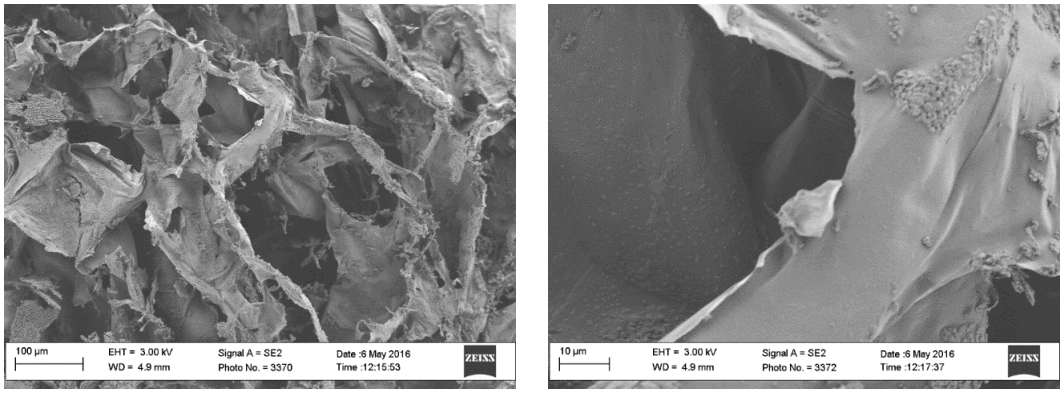

Figure 4.17. SEM images of pure 5050 SFCS tissue scaffold

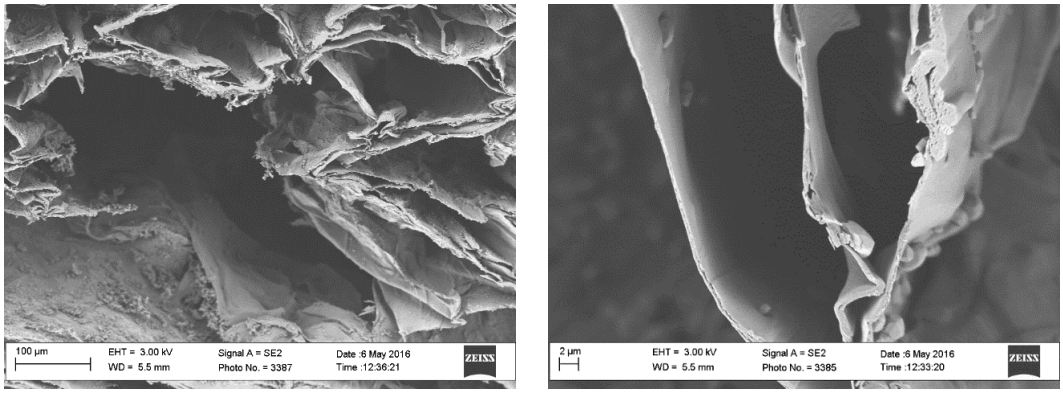

Figure 4.18. SEM images of pure 7030 SFCS tissue scaffold

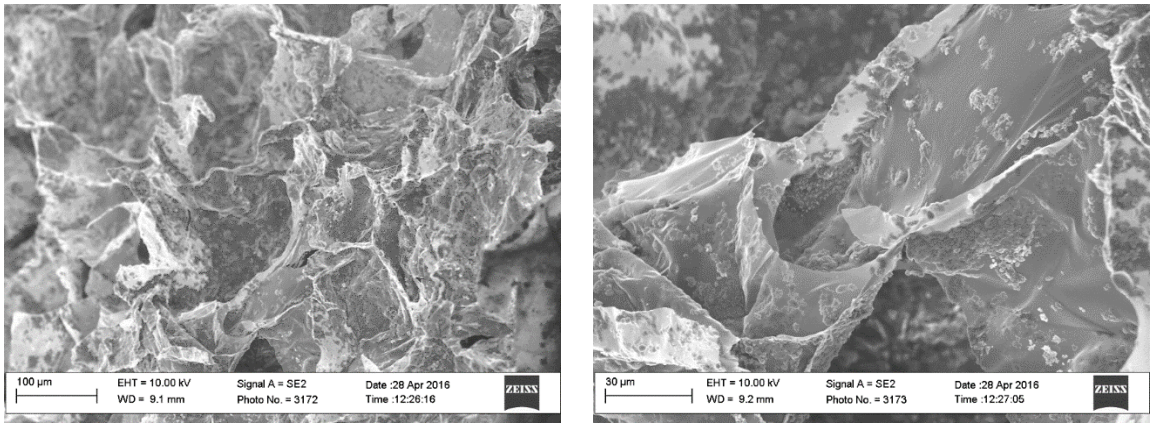

Figure 4.19. Low and high magnification SEM image of a cross section of 30:70 – 45nm – 2% SFCS-ZnO tissue scaffold.

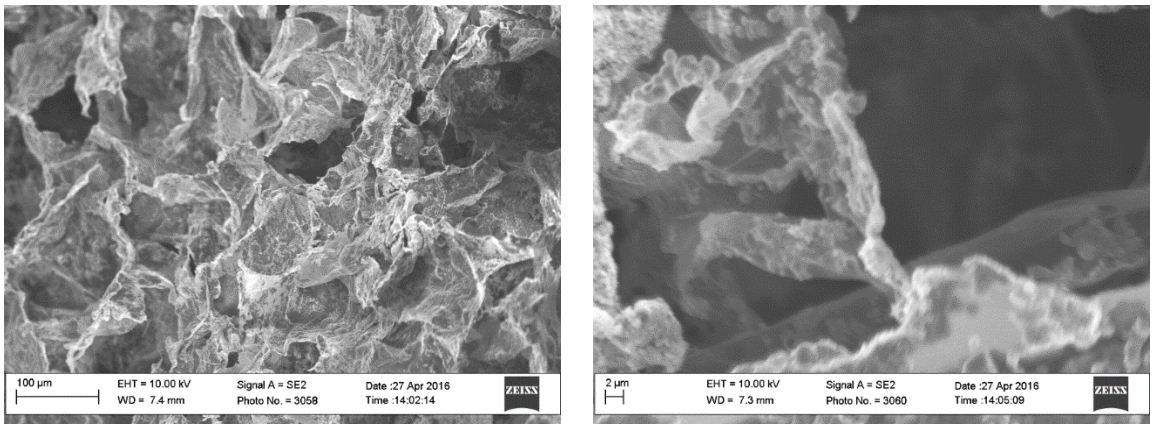

Figure 4.20. Low and high magnification SEM image of a cross section of 30:70 – 45nm – 5% SFCS-ZnO tissue scaffold.

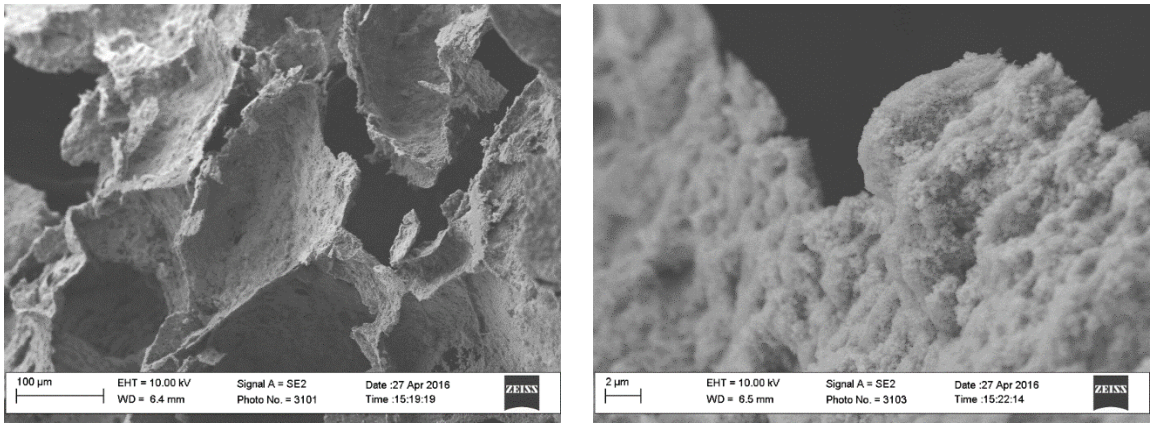

Figure 4.21. Low and high magnification SEM image of a cross section of 30:70 – 45nm – 10% SFCS-ZnO tissue scaffold.

4.1.6 Porosity Measurement

The resaturation technique was implemented to determine the porosity of each of the SFCS-ZnO blends and the blends were processed through the protocol stated in Section 3.3.2. The pure SFCS blends had an average porosity of 92% ± 1.3%, 93% ± 1.2%, and 91% ± 4.4% for the 30:70, 50:50, and 70:30 SFCS blends, respectively, with no significance difference between blend ratios (Figure 4.22). These highly porous blends corresponded well with the constructs produced by Zeng et. al [47] and She et. al [46], both reported an ~95% porosity for SFCS blends of similar ratios, employing the resaturation method and mercury intrusion porosimetry methods, respectively. However, with the addition of the ZnO nanoparticles, the average porosity decreased significantly ($p < 0.05$) with respect to the pure SFCS blends (Figure 4.22). Additionally, inconsistencies were noted in the porosities of the SFCS-ZnO blends, which ranged from 24%±3.8% up to 78%±7.0%. Thus, while the blends with ZnO nanoparticles showed a decrease in the porosity as the concentration of nanoparticles increased; however, these trends were not significantly different ($p > 0.05$). The decrease in the porosity was most likely to the ZnO nanoparticles filling the voids in the SFCS scaffold matrices; thereby, decreasing the porous nature of the scaffold. Although the resaturation technique produced effective porosities for each SFCS-ZnO blends, complete specimen saturation was difficult to achieve. As a result, the porosities obtained in this study were probably lower than those determined by other methods such as mercury intrusion porosimetry [59]. The latter porosity measurement technique was not pursued for this investigation due to the lack access to the equipment necessary to perform these measurements at or near the university.

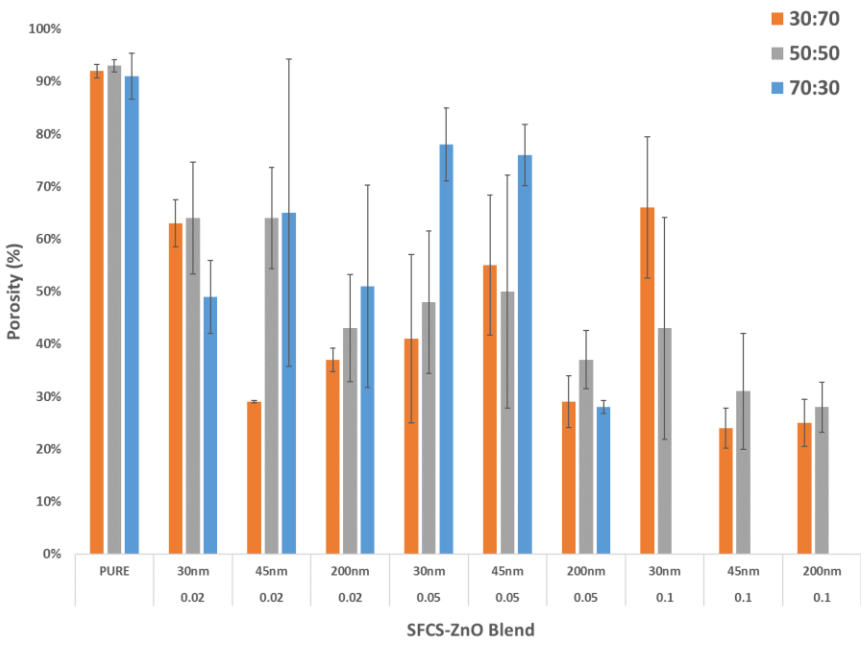

Figure 4.22. Bar chart exhibiting average porosity of all individual SFCS-ZnO blends

4.2 Mechanical Characterization of Biocompatible Piezo-Composites

Mechanical and viscoelastic properties of the SFCS-ZnO blends were evaluated and analyzed. Uniaxial tensile, stress relaxation and creep tests were performed on the SFCS-ZnO blends all at 37°C. The ring shaped specimens were placed in the 37°C water bath and allowed to acclimate for 5 minutes before being mounted in the custom ring testing fixture shown in Figure 4.23 before commencing with the testing procedure. A total of 3 rings per SFCS-ZnO blend group were tested.

Figure 4.23. Image of SFCS-ZnO sample mounted in custom ring testing fixture

4.2.1 Uniaxial Tensile Testing

The tensile properties of the SFCS-ZnO blended scaffolds were determined via uniaxial tensile testing while the samples were submersed in the water bath. Prior to testing, each tensile sample was preconditioned, by completing 10 loading-unloading cycles at a constant strain rate of 50 mm/min, to minimize the viscoelastic effects of the material during the material characterization process and obtain consistent, repeatable stress-strain curves. Thereafter, uniaxial tensile testing was performed on the samples using a continuous sampling rate of 100 Hz for collecting the tensile force data and a crosshead position at the strain rate of 50 mm/min Figure 29 shows a typical stress-strain plot of the preconditioning process for an SFCS-ZnO specimen (30:70 – 30 nm – 2%) during the 10 applied loading cycles. The hysteresis loop shifts during the cyclic loading and eventually converges to a deformed state with lower hysteresis. Figure 4.24 displays the loading-unloading hysteresis cycle in a stress-time plot that demonstrates that the measured stress converges within 10 preconditioning cycles.

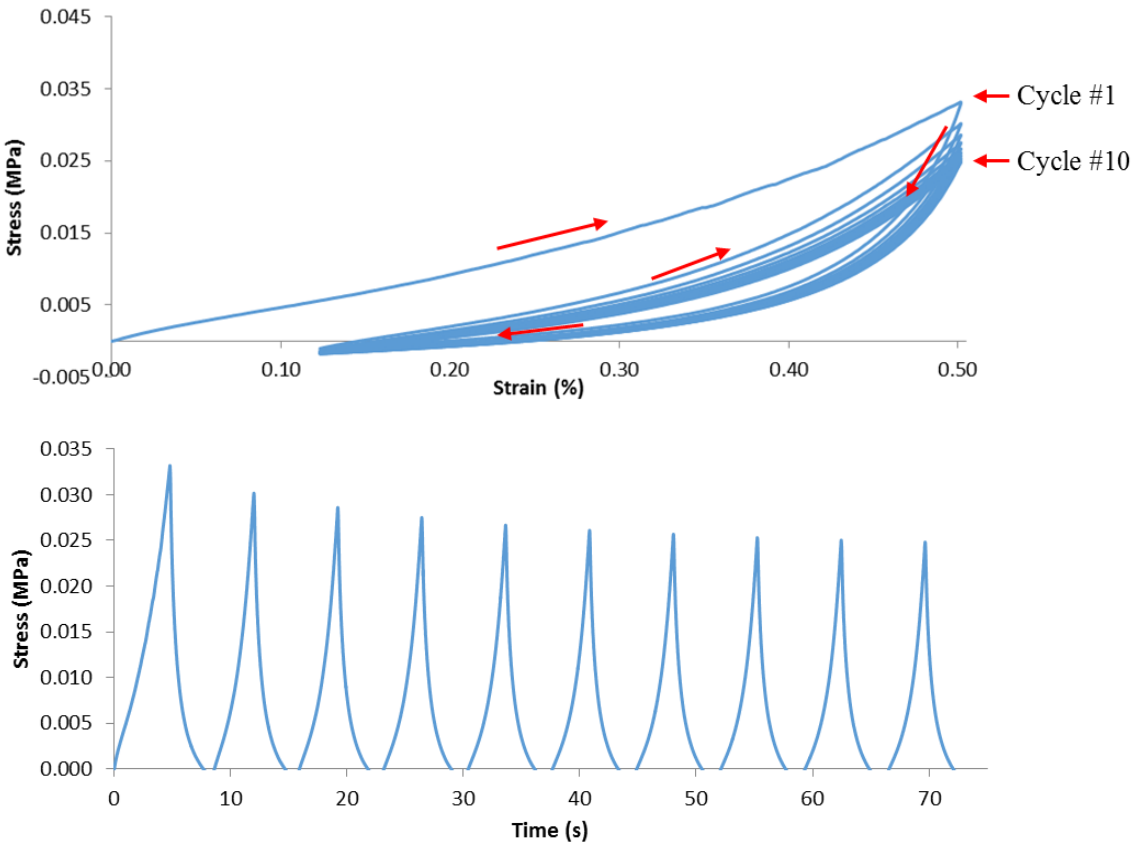

Figure 4.24. (Top) Stress – Strain and (Bottom) Stress – Time plot demonstrating sample preconditioning up to 50% strain in a typical SFCS-ZnO blend (30:70 – 30 nm – 2%)

The data collected from the acquisition system of the Admet Microtester were used in conjunction with the cross sectional dimensions and individual porosity data to calculate the stress of each specimen. These values were combined with the strain data and plotted to produce the stress-strain curves similar to those shown in Figure 4.25. Figure 4.26, Figure 4.27, and Figure 4.28 display the stress – strain relationship for a single sample of each SFCS-ZnO blend.

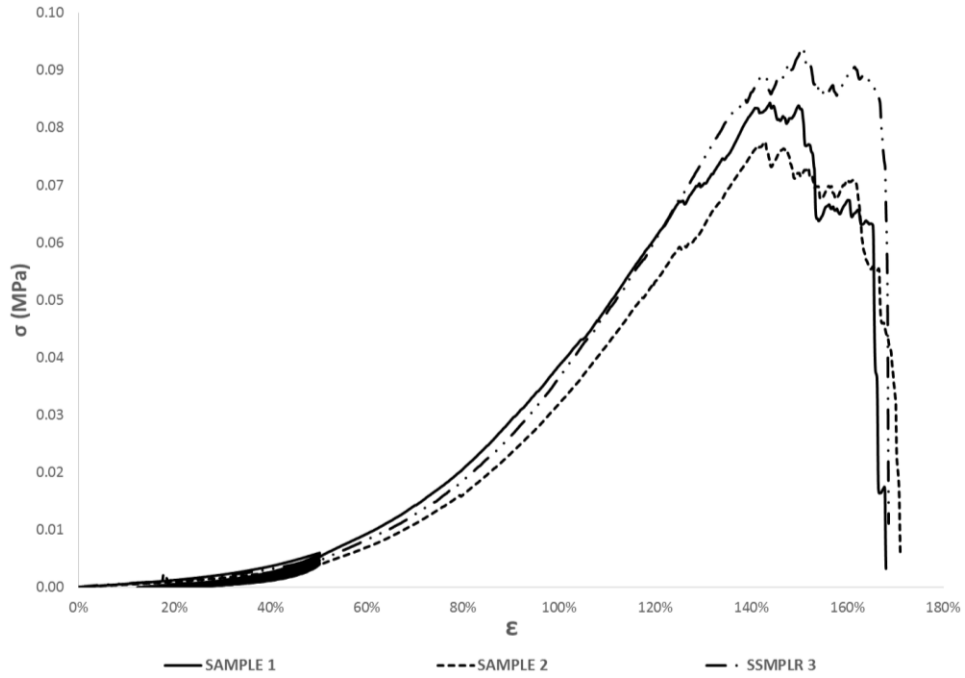

Figure 4.25. Stress versus strain plot for three 70:30 – 45 nm – 5% SFCS-ZnO samples.

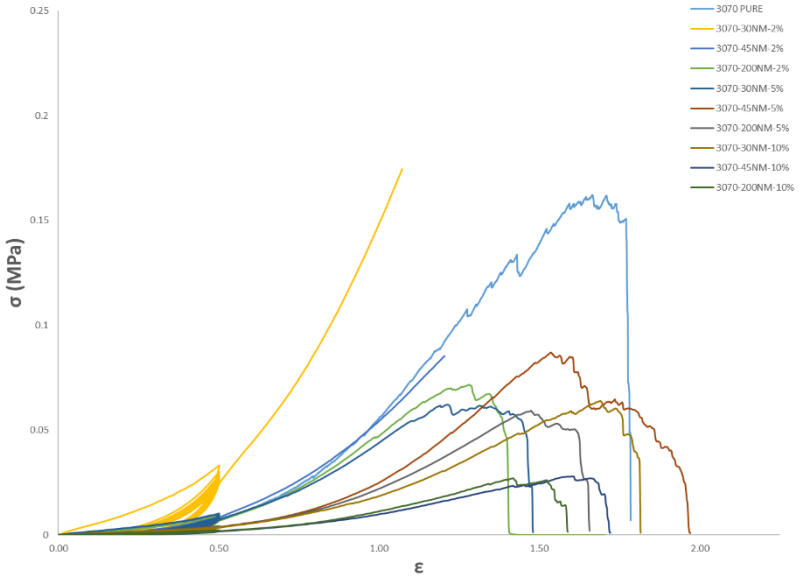

Figure 4.26. Stress versus strain plot for one sample of each ZnO composition in 30:70 blend.

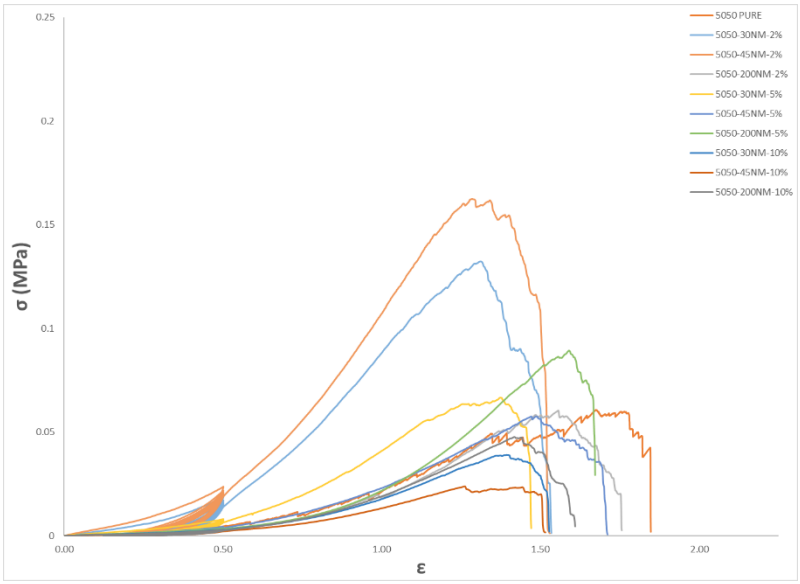

Figure 4.27. Stress versus strain plot for one sample of each ZnO composition in 50:50 blend

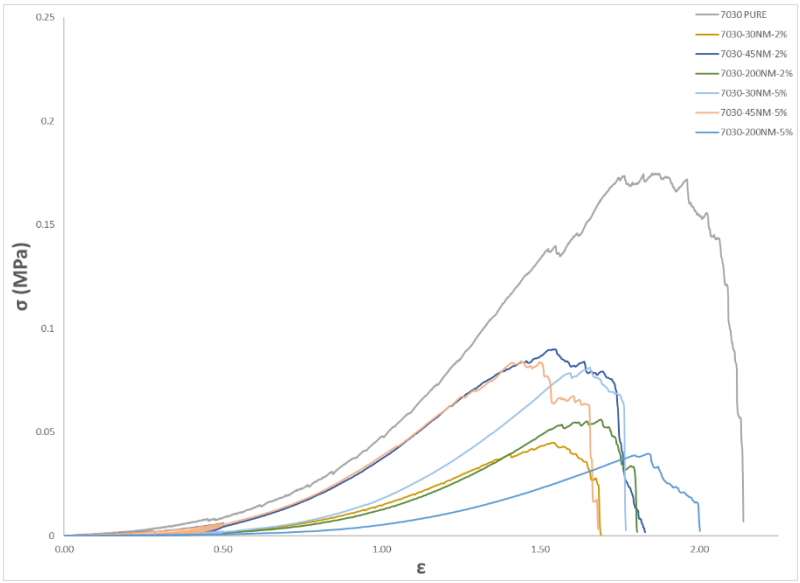

Figure 4.28. Stress versus strain plot for one sample of each ZnO composition in 70:30 blend

The ultimate tensile strength (σ_{ULT}), modulus of elasticity (E), and percent elongation were determined from the acquired data. Ultimate tensile strength was measured as the maximum stress that the specimen can endure while elongated prior to fracture. Figure 4.29 represents the average ultimate tensile strength of each individual SFCS-ZnO blend, where the data shows a trend of a reduction in tensile strength with the increase in ZnO nanoparticle concentration. Figure 4.30 demonstrates that the pure SFCS blends exhibited significantly higher tensile strength ($p^{*,**} < 0.05$) in comparison to the 5% and 10 % SFCS-ZnO blends. The 2% and 5% SFCS-ZnO blends also displayed a significantly higher tensile strength ($p^{+,-} < 0.05$) than that of the 10% blends as well. This trend was probably due to the number of potential dislocation sites within the SFCS-ZnO scaffold sample increasing as the ZnO WT% increases. Thus, the higher the number of inclusions generated by the addition of particles within the matrix gives a higher likelihood of premature failure, which is observed in Figure 4.29 and Figure 4.30.

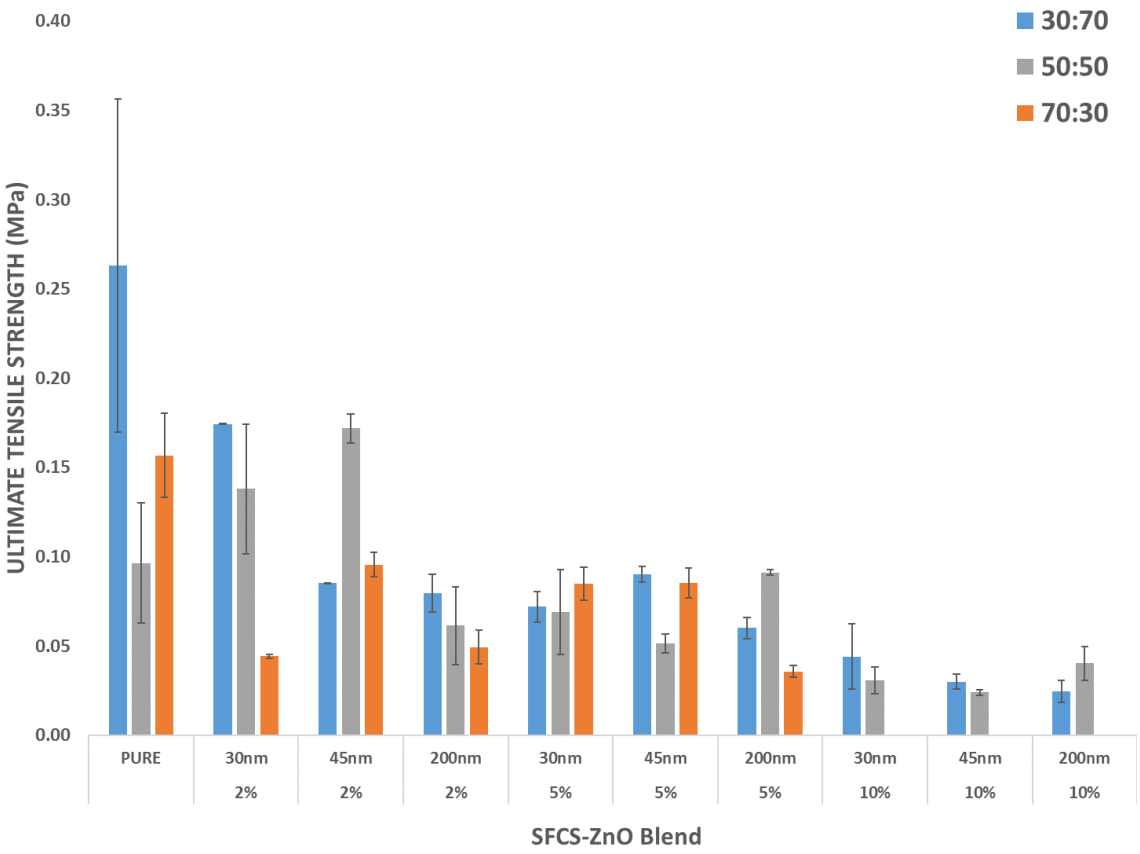

Figure 4.29. Bar chart exhibiting average ultimate tensile strength of all individual SFCS-ZnO blends

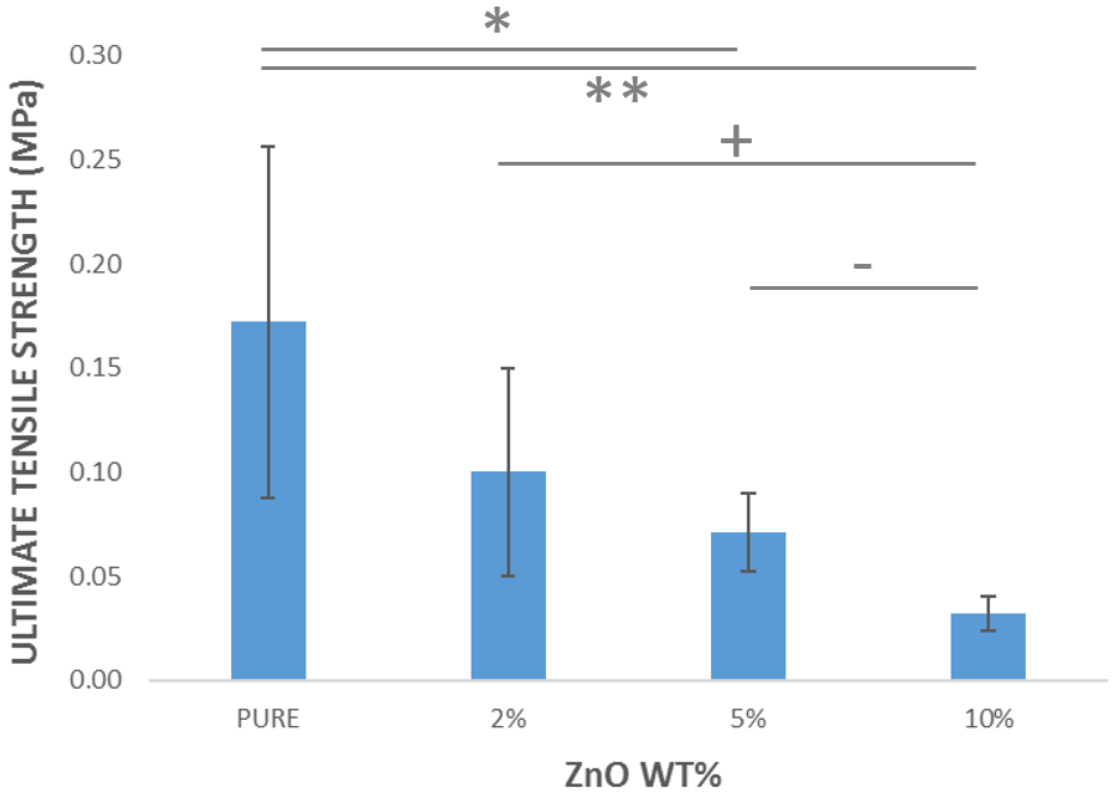

Figure 4.30. Barchart illustrating differences in average ultimate strength among SFCS-ZnO blends of known ZnO weight percent.

During SFCS-ZnO scaffold preparations, microcracks and fractures may have formed within the ring structure due to the removal of the extremely fragile ring specimens after the lyophilization process. Unfortunately, the freeze-dried specimens did not simply fall out of the mold upon removal, the mold required separation to ensure any damage to samples was minimized. The inner mold cores required subtle removal steps to near surgical precision to separate them from the internal diameter of the ring specimen to ensure minimal damage. Upon removal from the molds, the fragility of the freeze-dried samples noticeably increased with the higher concentrations of ZnO nanoparticles. This would further strengthen the increased deviation of the average tensile strength values for

the pure SFCS blends, possibly increasing the number of microcracks and fractures introduced during demolding. In a uniaxial tensile test where the specimen is stretched, the much weaker scaffold matrix experiences most the load while the particles separate away from one another. However, if agglomeration occurs with an increase in ZnO particle concentration, this behavior will be even more prominent.

Elastic modulus was calculated from the selected points of the linear region of the stress-strain plot and placed into Equation (18). Figure 4.31 represents the average elastic modulus of each individual SFCS-ZnO blend, where the data shows a trend of a reduction in elasticity with the increase in ZnO nanoparticle concentration. Figure 4.32 reveals that the pure SFCS blends exhibited significantly higher elasticity ($p < 0.05$) in comparison to the 5% and 10 % SFCS-ZnO blends. The 2% and 5% SFCS-ZnO blends also show a significantly higher elasticity ($p^{+,-} < 0.05$) than that of the 10% blends as well. Gupta et al. [60] experienced a similar moduli reduction phenomenon with their SFCS scaffolds with dispersed emodin based nanoparticles ranging from 40 nm to 100 nm in size after sonication.

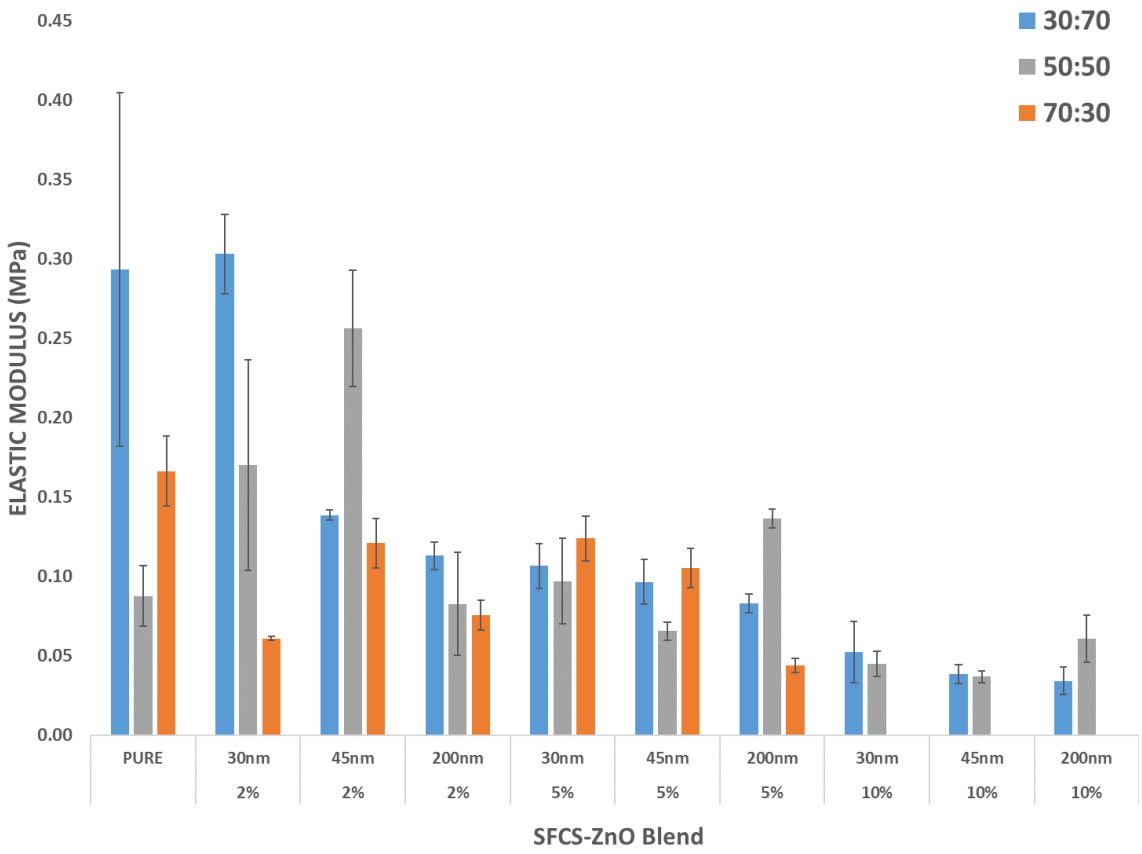

Figure 4.31. Bar chart exhibiting average elastic modulus of all individual SFCS-ZnO blends

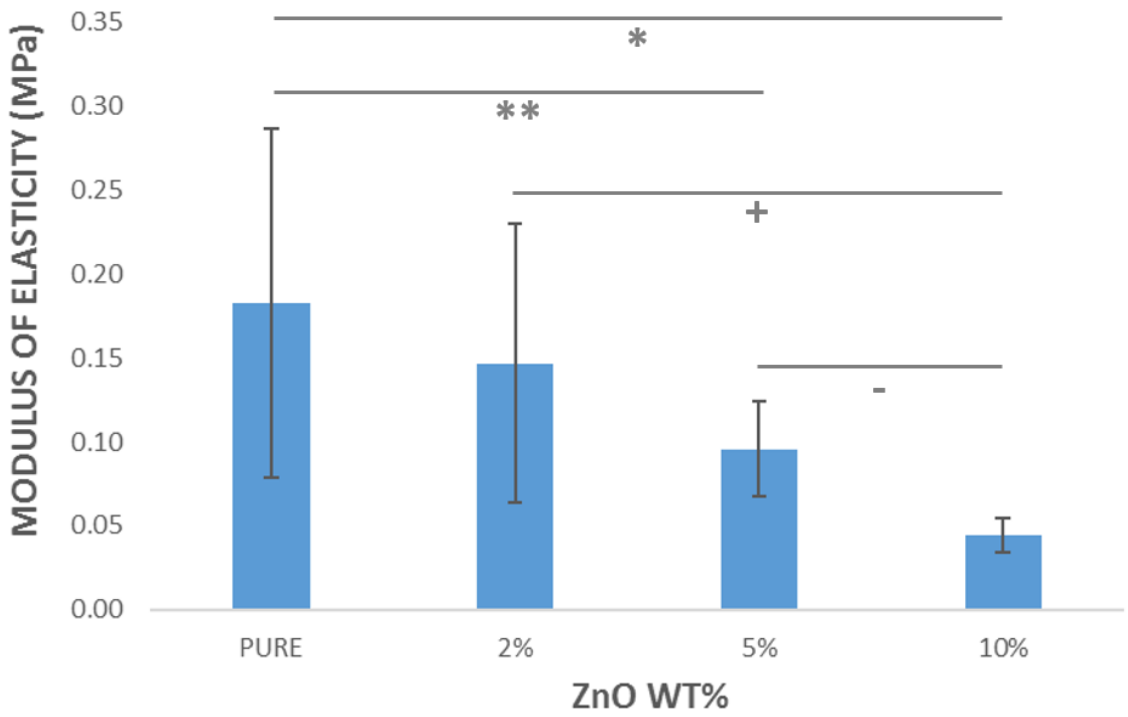

Figure 4.32. Barchart illustrating differences in average elasticity among SFCS-ZnO blends of known ZnO weight percent.

Elongation at failure was calculated from the collected stress-strain data, representing the ratio between final length and initial length at failure of the SFCS-ZnO specimen. Figure 4.33 represents the average elongation at failure of each individual SFCS-ZnO blend. The individual data does not tend to show any trend in elongation with the increase in ZnO nanoparticle concentration.

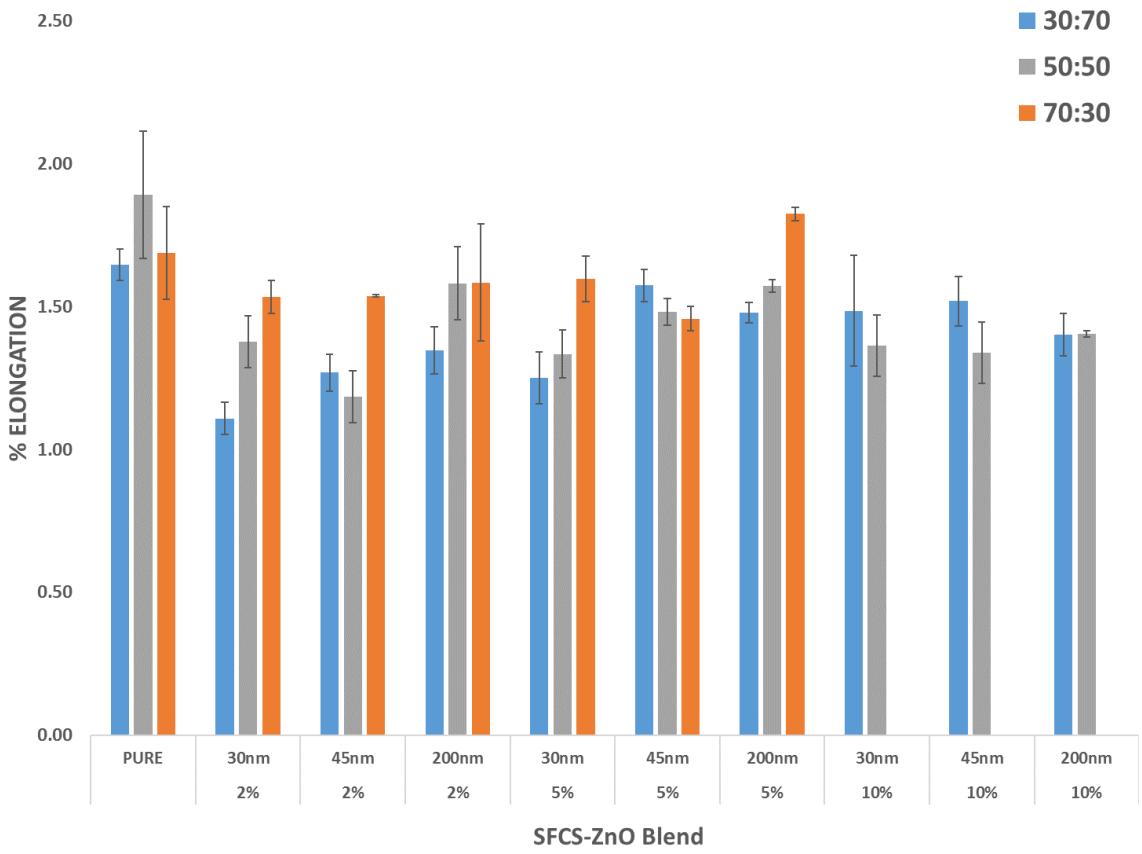

Figure 4.33. Bar chart exhibiting average % elongation of all individual SFCS-ZnO blends

Figure 4.34 reveals that the pure SFCS blends exhibited significantly higher elongation ($p < 0.05$) in comparison to the 2%, 5% and 10 % SFCS-ZnO blends. Elongation at break and ultimate tensile strength of the biocomposites demonstrated a reduction with an increase in the ZnO nanoparticle filler concentration. Again, this is due to the increase in defect sites with an increase in nanoparticle concentration. The pure SFCS blends display a significantly higher elongation at break than the blends with ZnO nanoparticles. Specifically, blends within the 2% and 5% WT%, show a general trend of an increase in elongation at the 200-nm particle size and decreases with the 45 nm and 30 nm particles,

respectively. A blend of 200 nm particles at a fixed WT% compared to 30 nm particles will have far less potential defect sites due to the nominal number of actual particles dispersed throughout the sample.

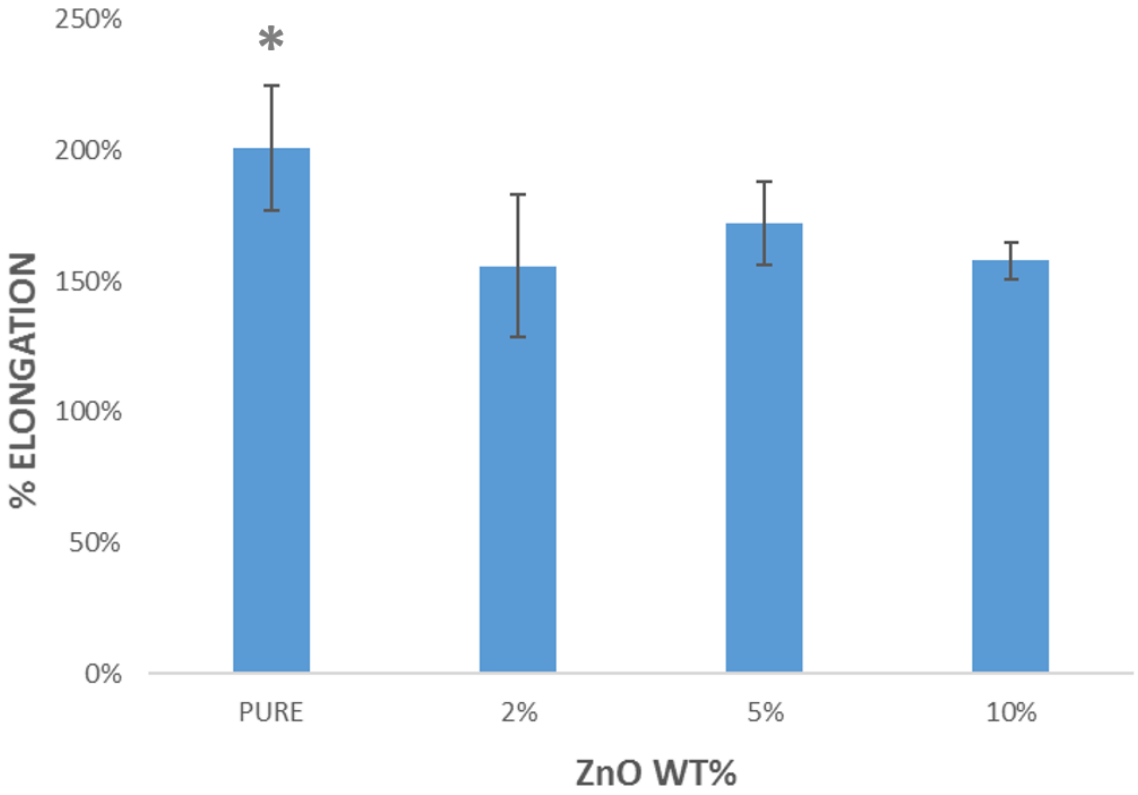

Figure 4.34. Barchart illustrating differences in average elongation among SFCS-ZnO blends of similar ZnO weight percent.

4.2.2 Viscoelastic Testing

All materials exhibit some viscoelastic behavior. Metals typically display purely elastic response at small deformations and plastically deform under large deformations, which is commonly independent of time. By contrast, materials such as synthetic

polymers, wood, and human tissue and engineered biomaterials exhibit significant viscoelastic effects at small and large deformations [61]. The SFCS-ZnO composite blends demonstrated time dependent or viscoelastic response. This time dependence is primarily due to the distinct molecular structure of the SF and CS biomaterials [50] [51] [52].

4.2.2.1 Stress Relaxation

A technique for characterizing the viscoelastic time dependent behavior of a material is the stress relaxation test, where a constant strain is applied to an SFCS-ZnO sample, at a rate 50 mm/min to constant strain values of 37.50%, 43.75%, 50.00%, 56.25%, and 62.50% and held statically for the prescribed times noted in Section 3.3.4 (Figure 4.35 (Top)), with a typical resultant stress response is shown in Figure 4.35 (bottom). It is noted that the induced stress of the SFCS-ZnO blended materials increases with an increase in applied strain, but relaxes over time while held at a constant strain.

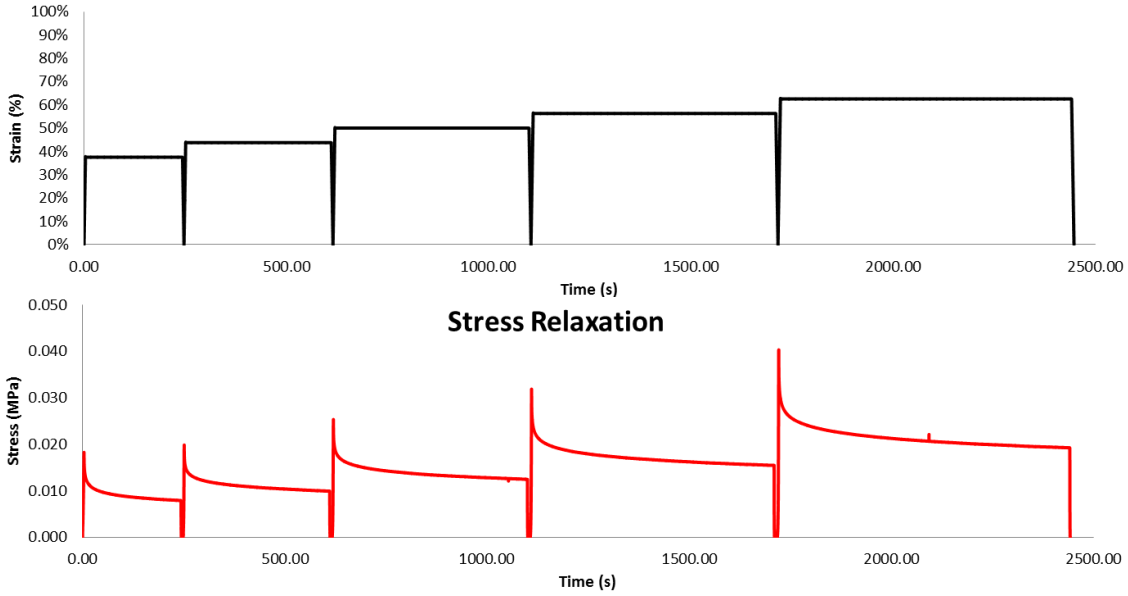

Figure 4.35. Representative plot of (Top) Strain – Time of the controlled cross head and (Bottom) a typical stress – time plot of a SFCS-ZnO blended sample (30:70 – 30 nm – 2%).

Figure 4.36 represents the data shown in Figure 4.35 (bottom) as a stacked plot with the maximum stress for each cycle at time zero. There are three viscoelastic phenomena occurring within this plot that will be presented and discussed within the investigation; 1.) The initial stress in the specimen induced by the rapid increase in strain during the experiment, 2.) the rate at which the SFCS-ZnO blends relax while under a constant static strain and 3.) the equilibrium stress at which the specimen reaches while under that constant static strain.

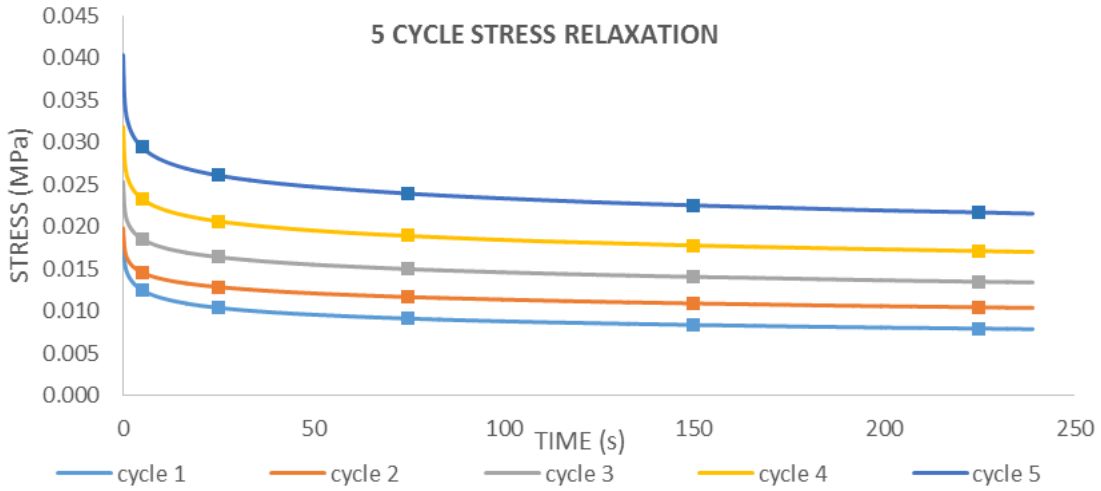

Figure 4.36. Plot of stress relaxation versus time of a 3070-30nm-2% blended sample.

4.2.2.1.1 Initial Stress

The maximum stress experienced by the SFCS-ZnO blended specimen for each constant strain cycle is termed the initial stress. Figure 4.37 represents the average initial stress for each blend consolidated into 3 bar charts, representing the initial stress of the SFCS-ZnO blends with respect to ZnO WT%, ZnO particle size, and SFCS blend, respectively. ANOVA was performed on the initial modulus data demonstrating that ZnO WT% and ZnO particle size significantly affected the initial stress where $p_{WT\%}$ = 0.05, 0.044, 0.037, 0.033, and 0.028; p_{size} = 0.01, 0.006, 0.005, 0.004, and 0.004 for each strain cycle, respectively. SFCS blend demonstrated no significance with respect to initial modulus ($p >> 0.05$). Similar to the mechanical testing, the nanoparticles WT% and size tend to have more of an affect on material performance.

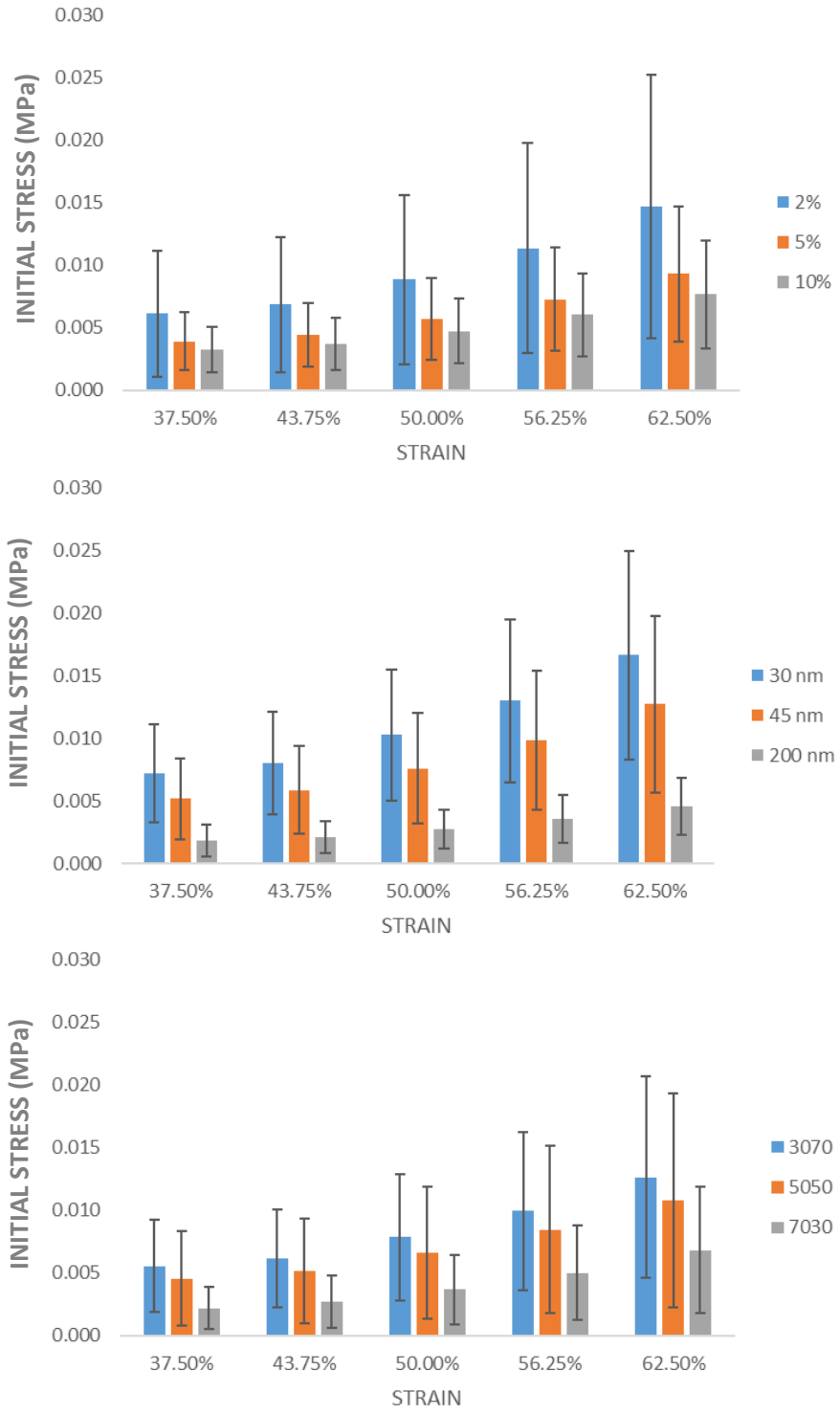

Figure 4.37. Consolidated plots of initial modulus versus applied strain with respect to (Top) ZnO WT%, (Middle) ZnO Size, and (Bottom) SFCS blend

4.2.2.1.2 Relaxation Rate

When the presented Stress – Time data is plotted on a log-log scale (Figure 4.38), the results demonstrate a linear trend, indicating that the relaxation curves can be approximated via the power law equation

$$y = At^n \tag{34}$$

where the slopes of the relaxation data curves are indicated by the power (n) of the data. Thus, the magnitude of n indicates the rate of relaxation with respect to time and when the data is fitted to a power trend line, a strong correlation is achieved (R^2 > 99%) for each applied strain case.

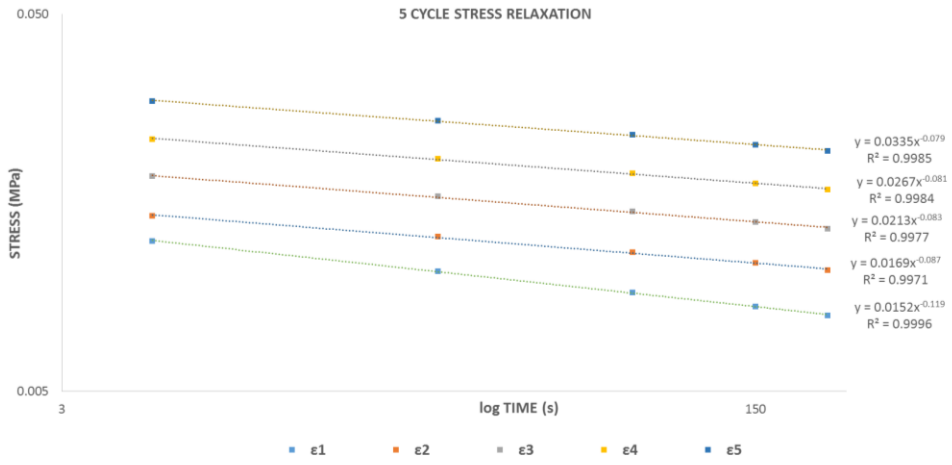

Figure 4.38. A log – log plot of stress relaxation versus time of 3070-30nm-2% blend.

Figure 4.39 represents the average relaxation rate for each blend consolidated into 3 bar charts, Figure 4.39a, b and c represents the relaxation rate of the SFCS-ZnO blends with

respect to ZnO WT%, ZnO particle size, and SFCS blend, respectively. ANOVA was performed on the relaxation rate data demonstrating that there was no significant difference in relaxation rate between ZnO WT% ($p >> 0.05$), ZnO particle size ($p >> 0.05$), and SFCS blends ($p >> 0.05$). There was a significant difference in relaxation rate between the first constant strain cycle (37.50%) and the other test cycles ($p < 0.001$). This difference is due to the lack of material preconditioning for this experiment due to the MQuattro Controller's inability to programmatically handle the number lines of input for the multicycle relaxation test preceded by the preconditioning cycle. By performing preconditioning on the test specimens, the difference in relaxation rate may have been mitigated. This phenomenon was observed by all tested samples. The relaxation rate stabilized for each subsequent strain cycle after the first at the lowest applied strain. The relaxation rate essentially remains linear throughout the tested strain range of 37.5% up to 62.5%, this is well above the normal circumferential strain experienced by the pulmonary artery during distension in a healthy individual. Thus, demonstrating viable functionality.

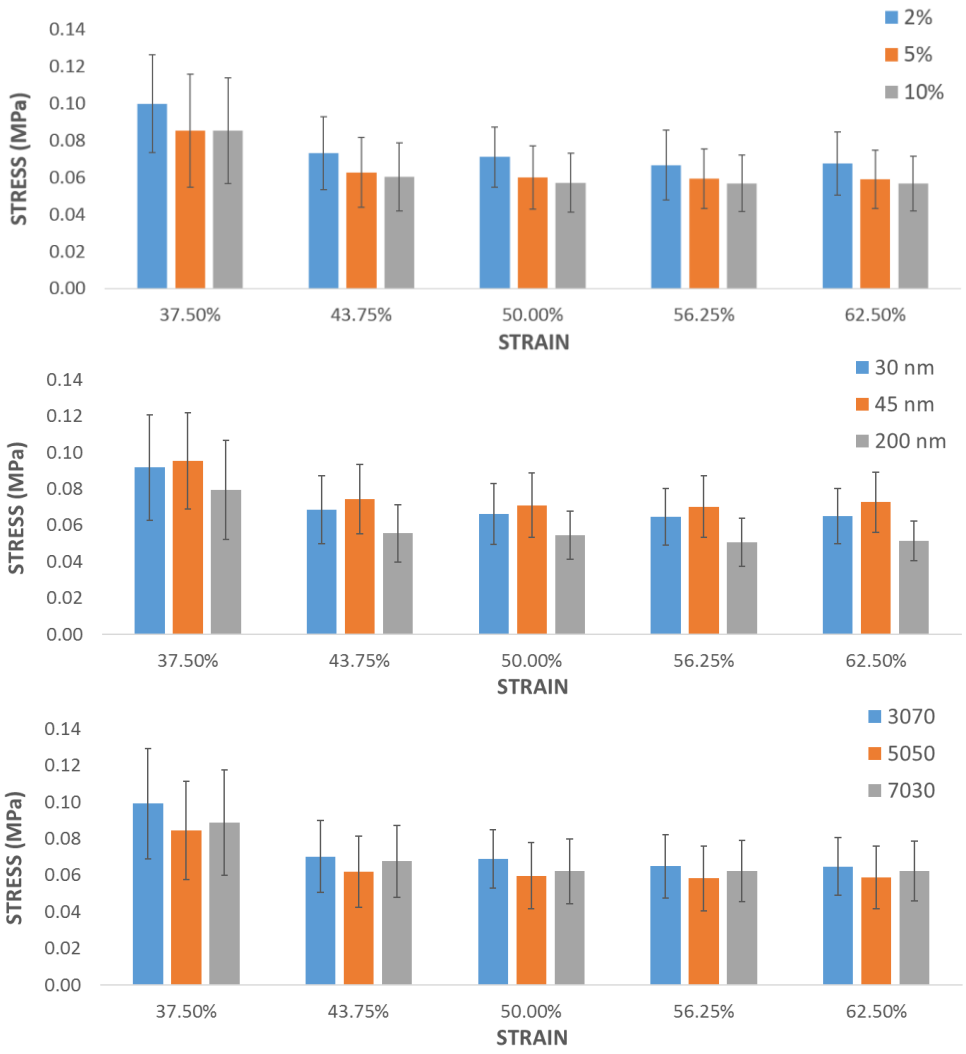

Figure 4.39. Consolidated plots of relaxation rate versus applied strain with respect to (Top) ZnO WT%, (Middle) ZnO Size, and (Bottom) SFCS blend

4.2.2.1.3 Equilibrium Stress

The relaxation or equilibrium stress experienced by the SFCS-ZnO blended specimen for each constant strain cycle is shown in Figure 4.40, which represents the average initial stress for each blend was also consolidated into is also presented in 3 bar charts. The equilibrium stress of the SFCS-ZnO blends with respect to ZnO WT%, ZnO

particle size, and SFCS blend, respectively, are presented. An ANOVA was performed on the equilibrium stress data demonstrating that ZnO WT% and ZnO particle size significantly affected the initial modulus where $p_{WT\%}$ = 0.05, 0.044, 0.039, 0.031, and 0.025; p_{size} = 0.003, 0.003, 0.003, 0.002, and 0.002 for each strain cycle, respectively. SFCS blends demonstrated no significance with respect to initial modulus ($p >> 0.05$). Similar to the initial stress data, as the applied strain increased as did the stress. Since the relaxation rate is essentially linear and equal across all recorded samples, the equilibrium stress also follows that trend of increasing with respect to applied strain cycle.

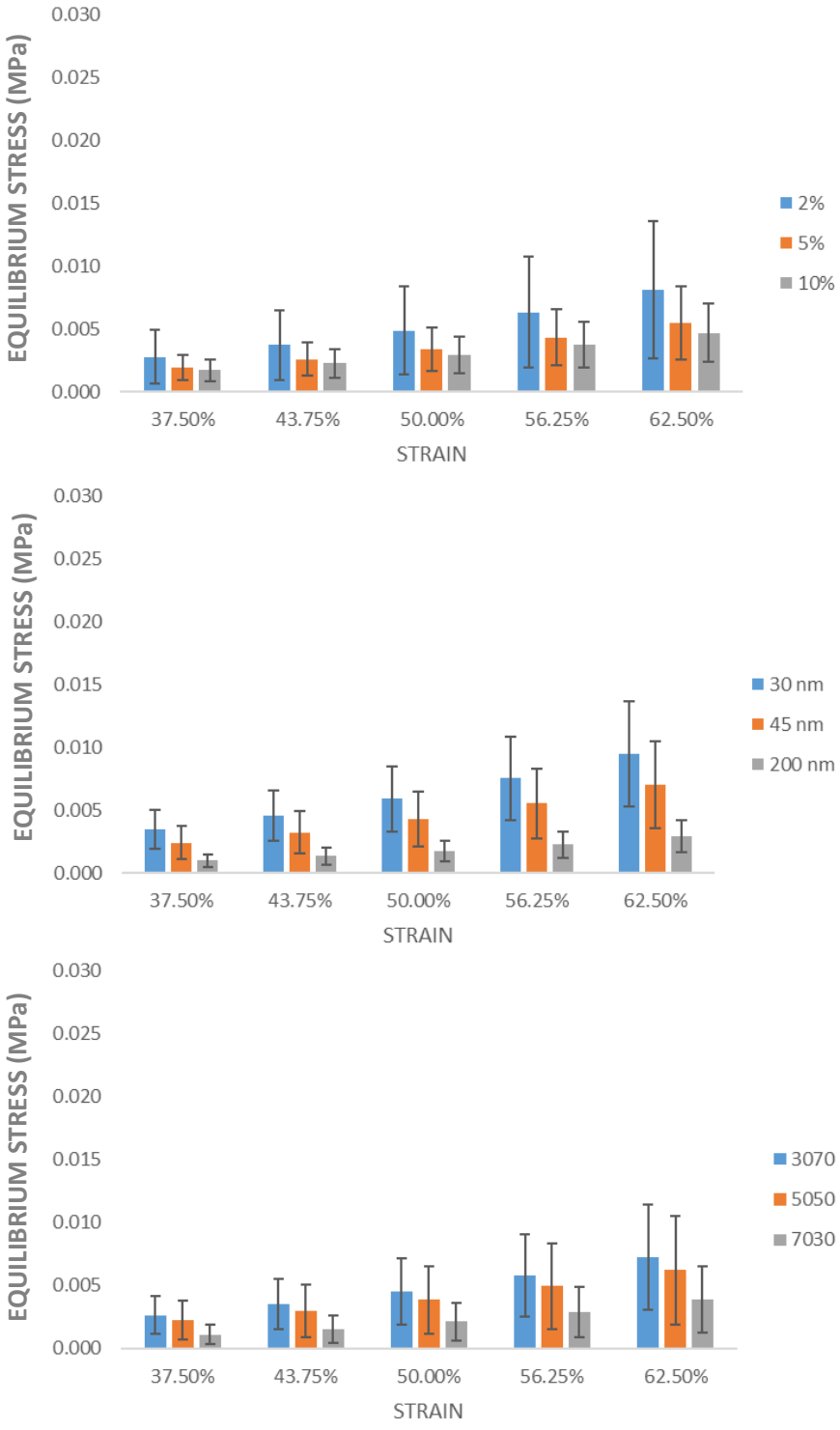

Figure 4.40. Consolidated plots of equilibrium modulus versus applied strain with respect to (Top) ZnO WT%, (Middle) ZnO Size, and (Bottom) SFCS blend

4.2.2.2 Creep Testing

Other techniques for characterizing the viscoelastic time dependent behavior of the SFCS-ZnO blended materials are creep and creep recovery tests, where a constant force is applied to the SFCS-ZnO sample, at a rate 50 mm/min to constant force values of 5.0, 7.5 and 10.0 grams and held statically for the prescribed times noted in Section 3.3.5 (Figure 4.41 (Top)) with a typical strain response shown in Figure 4.42 (bottom). The induced strain of the SFCS-ZnO blended materials increases as the applied stress increases over time while held at the constant force.

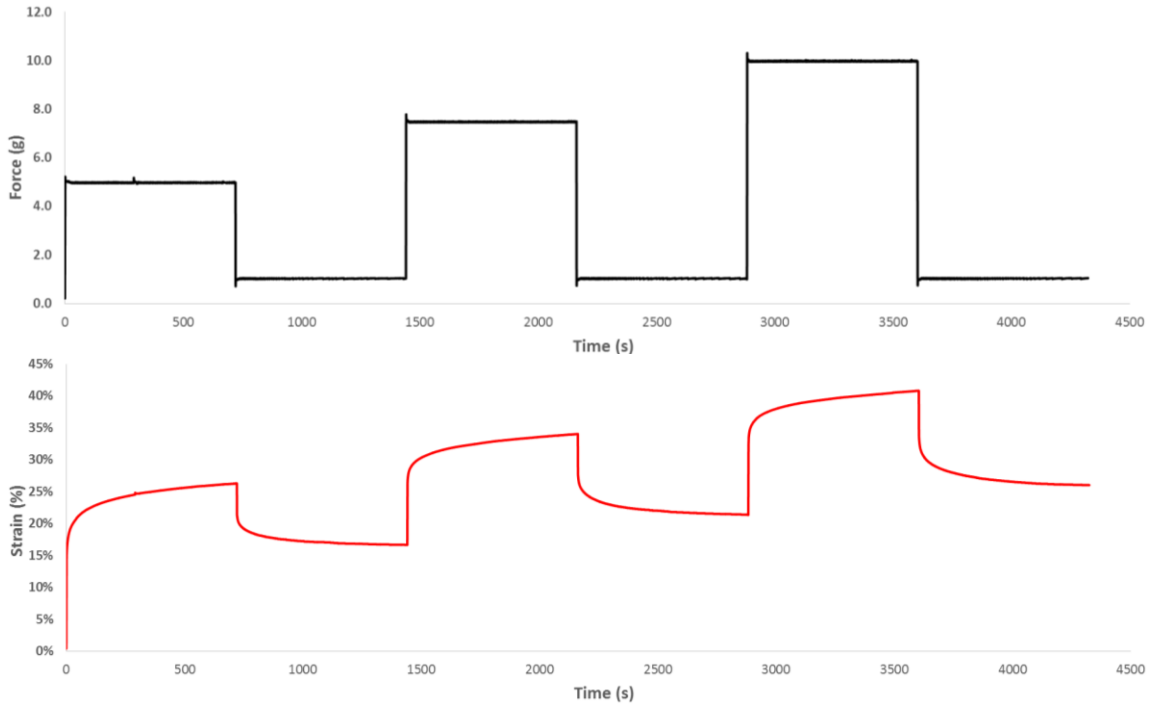

Figure 4.43. Representative plot of (Top) Stress – Time and (Bottom) a typical strain – time plot of a SFCS-ZnO blended sample (SFCS-3070-30NM-2%)

Figure 4.44 and Figure 4.45 present stacked plots of the creep and creep recovery data for the induced strain data shown in Figure 4.43 (bottom) with the initial induced strain for each cycle at time zero. It is noted that there are four viscoelastic phenomena occurring within this plot; 1.) The creep strain induced by the application of the constant force during the experiment for each cycle, 2.) The creep recovery strain induced by the removal of the applied constant force during the experiment, 3.) The rate of creep and rate of creep recovery the SFCS-ZnO blends creep while under said constant force and upon removal, 4.) The residual strain within the SFCS-ZnO sample after the removal of the applied force.

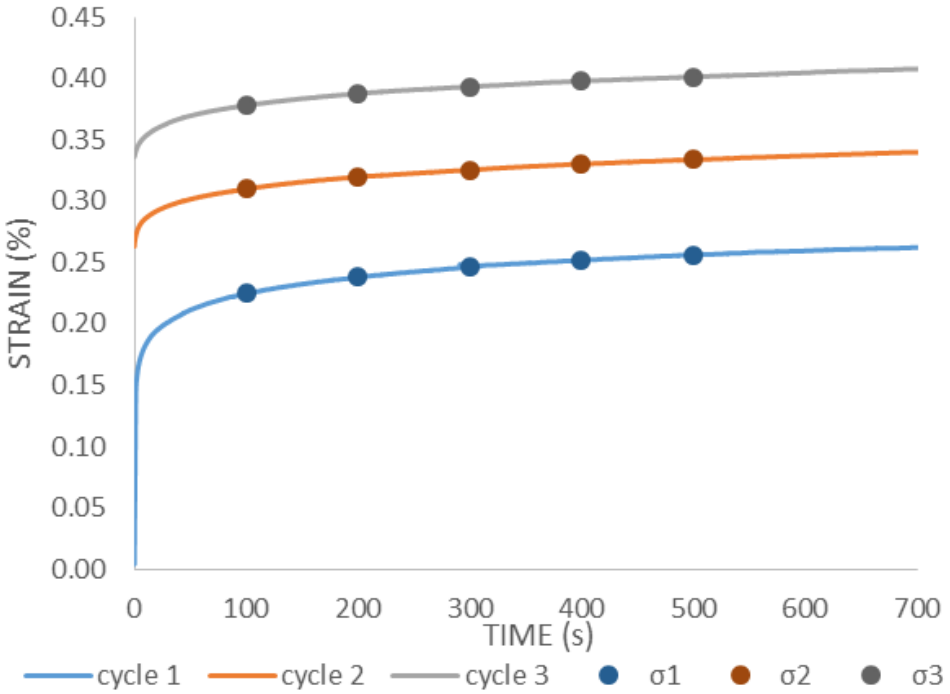

Figure 4.44. Plot representing creep of a 3070-30NM-2% blended SFCS-ZnO sample

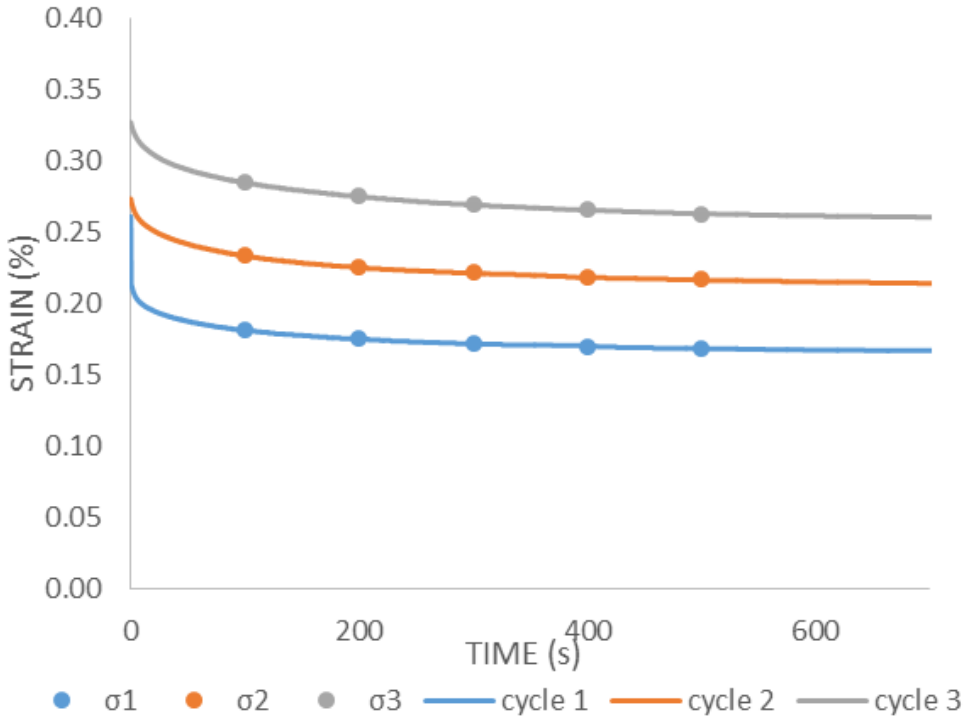

Figure 4.45. Plot representing creep recovery of a 3070-30NM-2% blended SFCS-ZnO sample

4.2.2.2.1 Creep Strain

The average creep experienced by the SFCS-ZnO blended specimens for each constant force cycle is represented in 3 bar charts (Figure 4.46), which representing the strain responses of the SFCS-ZnO blends with respect to ZnO WT%, ZnO particle size, and SFCS blend, respectively. An ANOVA was performed on the creep strain data demonstrating that ZnO WT%, ZnO particle size, and SFCS blend demonstrated no significance with respect creep strain ($p >> 0.05$). Similar to the stress relaxation tests, the first constant stress cycle resulted in a higher average strain value than that of the latter two cycles due to the lack of preconditioning experienced by the sample due to the MQuattro Controller's inability to programmatically handle the number lines of input for the

multicycle creep test preceded by the preconditioning cycle. This data shows that while under a constant load a sample regardless of SFCS-ZnO blend can handle a maximum induced strain of nearly 50%.

Creep resistance can be defined as a material's ability to resist any kind of distortion when under a constant load over time. Ultimately, for optimum performance and maximum lifetime of the SFCS-ZnO sample should have a high creep resistance (i.e. low deformation under constant load). As seen in Figure 4.46, all samples tend to show similar resistance to creep.

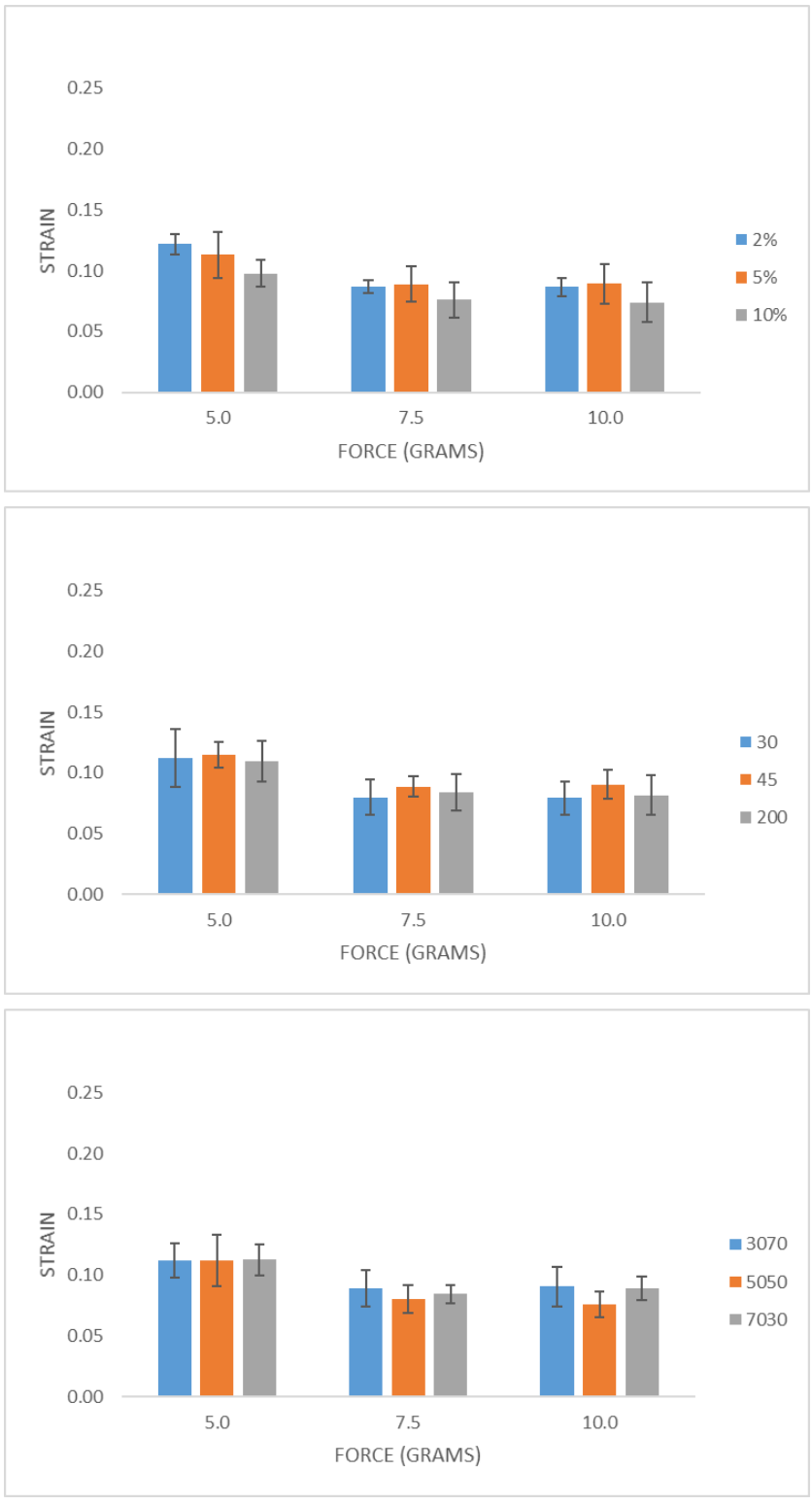

Figure 4.46. Plot of creep strain with respect to (Top) ZnO WT%, (Middle) ZnO Size, and (Bottom) SFCS blend

4.2.2.2.2 Creep Recovery

The creep recovery strain experienced by the SFCS-ZnO blended specimens upon the removal of each constant force cycle is also represented in 3 bar charts (Figure 4.47) with the strain responses of the SFCS-ZnO blends presented as ZnO WT%, ZnO particle size, and SFCS blend, respectively. An ANOVA was performed on the creep recovery strain data demonstrating that the SFCS blend significantly affected the specimen recovery where the p-values were $p_{BLEND} = 0.037$, 0.035, and 0.010; for each force cycle. ZnO WT% and ZnO particle size demonstrated no significance with respect creep recovery strain ($p >> 0.05$). This significance with respect to the SFCS blend is expected since the supporting matrix is the SFCS scaffold with a dispersion of ZnO nanoparticles that when under tension will typically separate. The SFCS matrix will induce contraction of the ring upon reduction of the load allowing for recovery.

Figure 4.47. Plot of creep recovery strain with respect to (Top) ZnO WT%, (Middle) ZnO Size, and (Bottom) SFCS blend

4.2.2.2.3 Creep Rate and Creep Recovery Rate

When the Strain – Time data from the creep experiments is plotted on a log Strain – log Time scale (Figure 4.48 and Figure 4.49), the curves are linear, similar to the stress relaxation data curves presented previously, indicating that the creep and recovery curves can also be approximated with the power law equation. Thus, the slopes of the creep and creep recovery data fitted to a power trend line show a strong correlation, with an $R^2 > 99\%$ for each applied force case for creep and an $R^2 > 94\%$ for each applied force case for creep recovery.

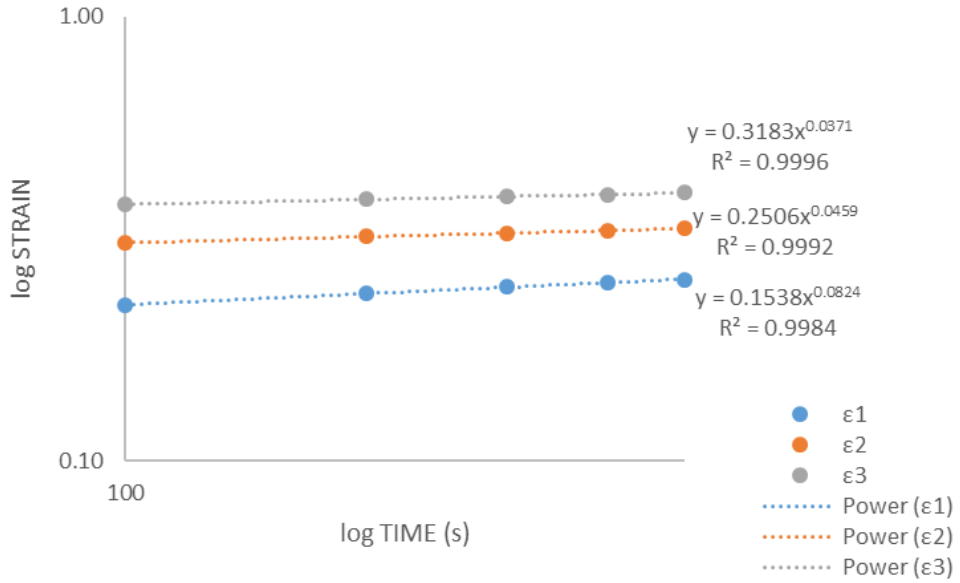

Figure 4.48. A representative log – log plot of Strain – Time of a single creep strain data set of 3070-30nm-2% blend.

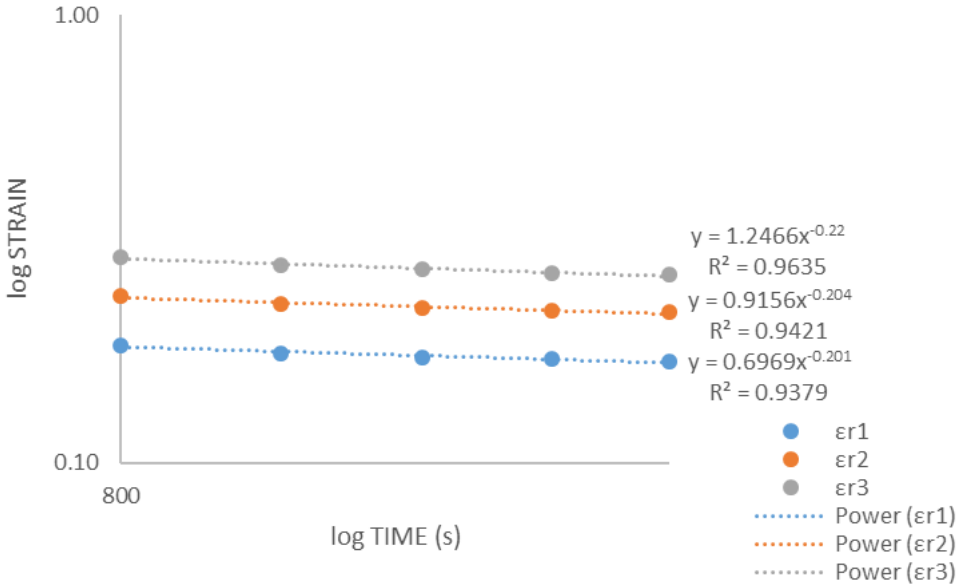

Figure 4.49. A representative log – log plot of Strain – Time of a single creep recovery strain data set of 3070-30nm-2% blend.

Figure 4.50 represents the average rate of creep for each blend in 3 bar charts, representing the rate of creep of the SFCS-ZnO blends with respect to ZnO WT% (Figure 4.50 (Top)), ZnO particle size (Figure 4.50 (Middle)), and SFCS blend (Figure 4.50 (Bottom)), respectively. An ANOVA was performed on the creep rate data demonstrating that ZnO WT% significantly affected the specimen rate of creep where the p-values were $p_{ZnO\text{-}WT\%}$= 0.016, 0.004, and 0.005 for each force cycle; while SFCS blend significantly affected the specimen for the 7.5 and 10 gram cycles (p_{blend} = 0.020 and 0.022) respectively. The ZnO particle size demonstrated no significant difference with respect to creep recovery strain (p_{size} = 0.480, 0.324, and 0.297).

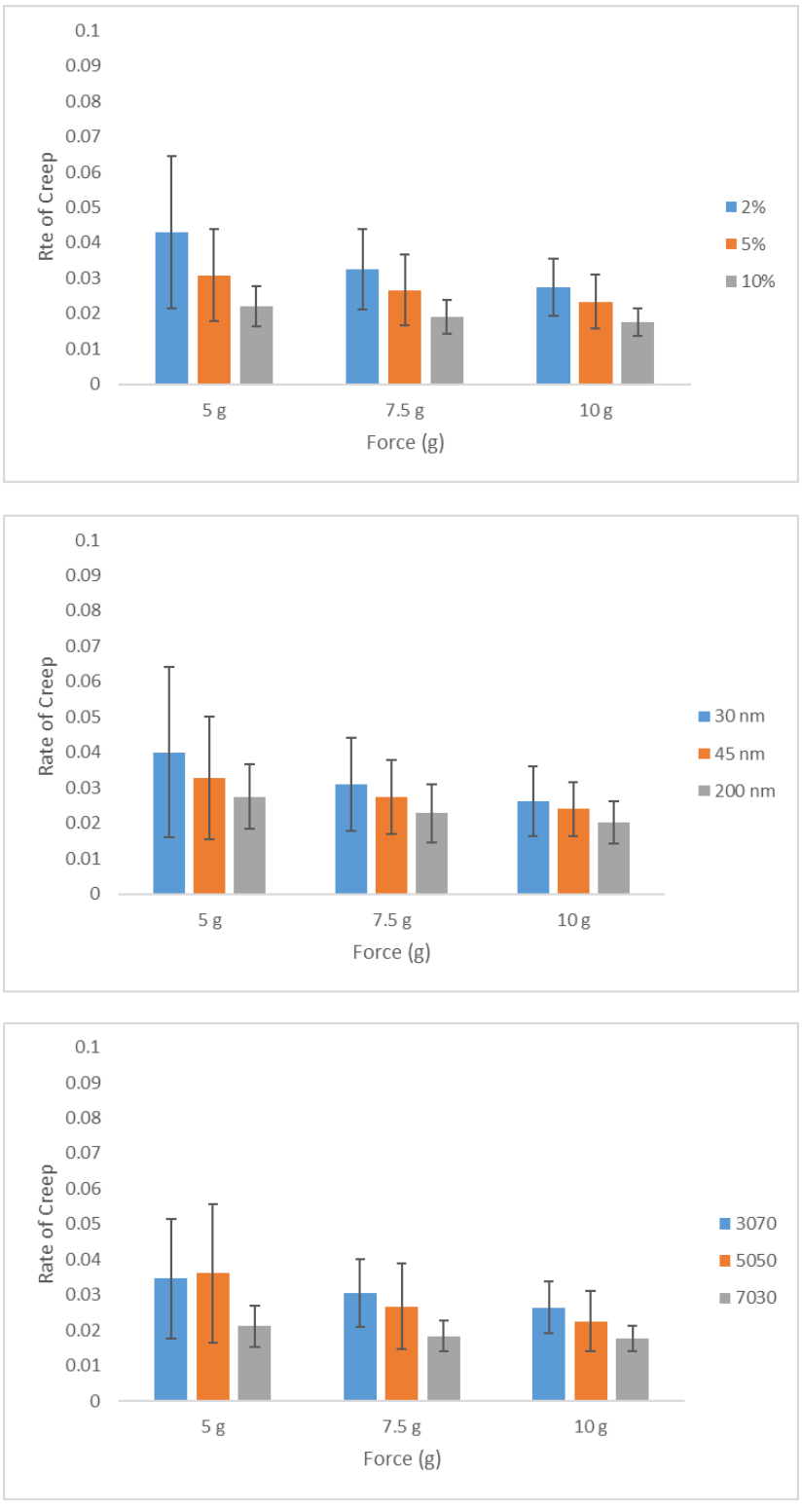

Figure 4.50. Plots of rate of creep with respect to (Top) ZnO WT%, (Middle) ZnO Size, and (Bottom) SFCS blend

Figure 4.51 presents the average rate of creep recovery for each blend in 3 bar charts, representing the rate of creep recovery of the SFCS-ZnO blends with respect to ZnO WT% (Figure 4.51 (Top)), ZnO particle size (Figure 4.51 (Middle)), and SFCS blend (Figure 4.51 (Bottom)), respectively. An ANOVA was performed on the data demonstrating that ZnO WT% and SFCS blend significantly affected the rate of creep recovery where the p-values were $p_{ZnO\text{-}WT\%}$= 0.031, 0.016, and 0.011 and p_{BLEND} = 0.006, 0.003 and 0.022 for each force cycle, respectively. The ZnO particle size demonstrated no significance with respect creep recovery strain (p_{size} = 0.763, 0.529, and 0.506).

Both rate of creep and rate of creep recovery were significantly affected by SFCS blend and ZnO concentration. The underlying support matrix is the blended SFCS with a dispersion of ZnO nanoparticles that when under tension will typically separate. When stretched the SFCS matrix will induce contraction of the ring upon a reduction in the load allowing for recovery.

When comparing the rate of creep to the rate of creep recovery, one observes that the rate of creep recovery is approximately 5 times greater than that of the rate of creep. This indicates that the sample returns to its initial unstressed state up to 5 times faster than when it is under a constant load. This is an optimal situation for this device, when comparing the loading scenario to vessel distension. The sample should recover from the vessel distension to rapidly accommodate change to the near unstressed state.

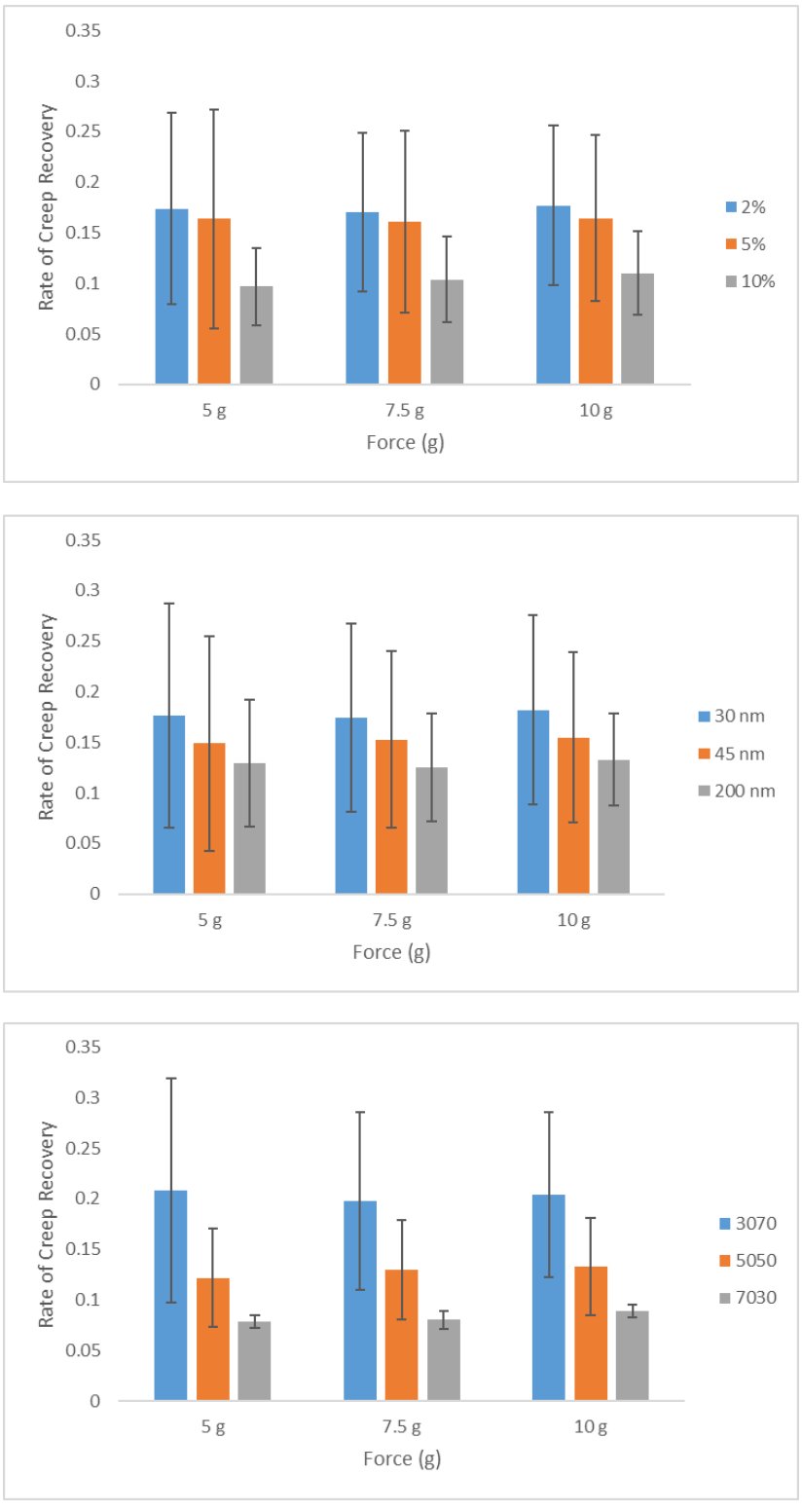

Figure 4.51. Plots of rate of creep recovery with respect to (Top) ZnO WT%, (Middle) ZnO Size, and (Bottom) SFCS blend

4.2.2.2.4 Residual Creep Strain

The residual creep strain experienced by the SFCS-ZnO blended specimens upon the removal of each constant force cycle is also represented and consolidated into 3 bar charts (Figure 4.46) with the strain responses for the SFCS-ZnO blends presented as ZnO WT%, ZnO particle size, and SFCS blend, respectively. An ANOVA was performed on the residual strain data demonstrating that the ZnO WT% and SFCS blend significantly affected the specimen recovery where the p-values were $p_{ZnO\%}$ = 0.011, 0.017, and 0.028 and p_{BLEND} = 0.000, 0.000, and 0.000; for each force cycle, respectively. The ZnO particle size demonstrated no significance with respect creep recovery strain (p_{SIZE} = 0.436, 0.344, 0.297) for each force cycle.

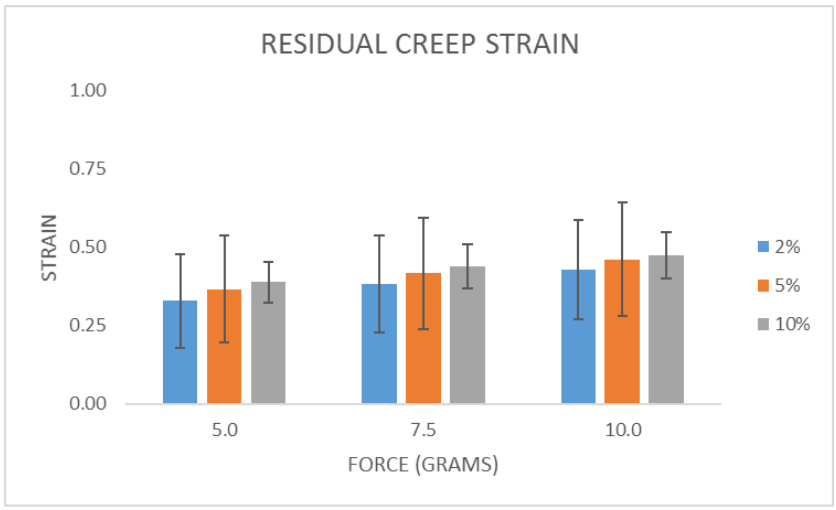

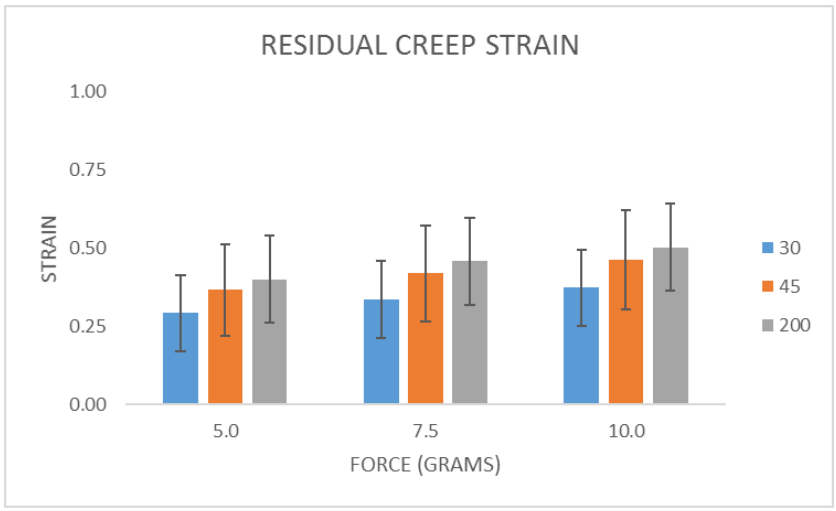

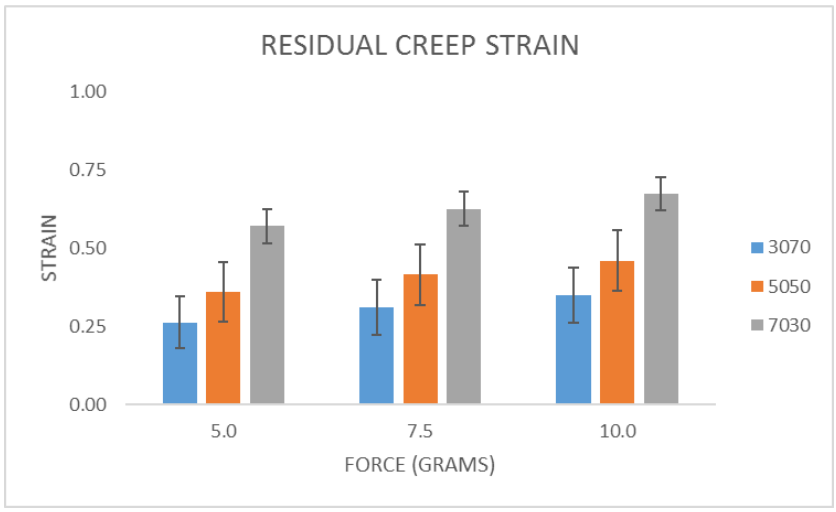

Figure 4.52. Plot of residual creep strain with respect to (Top) ZnO WT%, (Middle) ZnO Size, and (Bottom) SFCS blend

4.3 Electrical characterization of biocompatible piezo-composites

4.3.1 Shear Testing

Electrode displacement and SFCS-ZnO sample response was recorded for each test. Three samples were tested from each SFCS blend (27 blends in total, excluding 70:30 – 10% ZnO, due to previously stated mixing issues). The test samples were 20 mm round disks that were 2 mm in thickness. Figure 4.53 demonstrates what a typical SFCS-ZnO Response – Displacement plot resembled. This particular plot represents a 70:30 SFCS blend with 30 nm ZnO particles at 2% weight concentration.

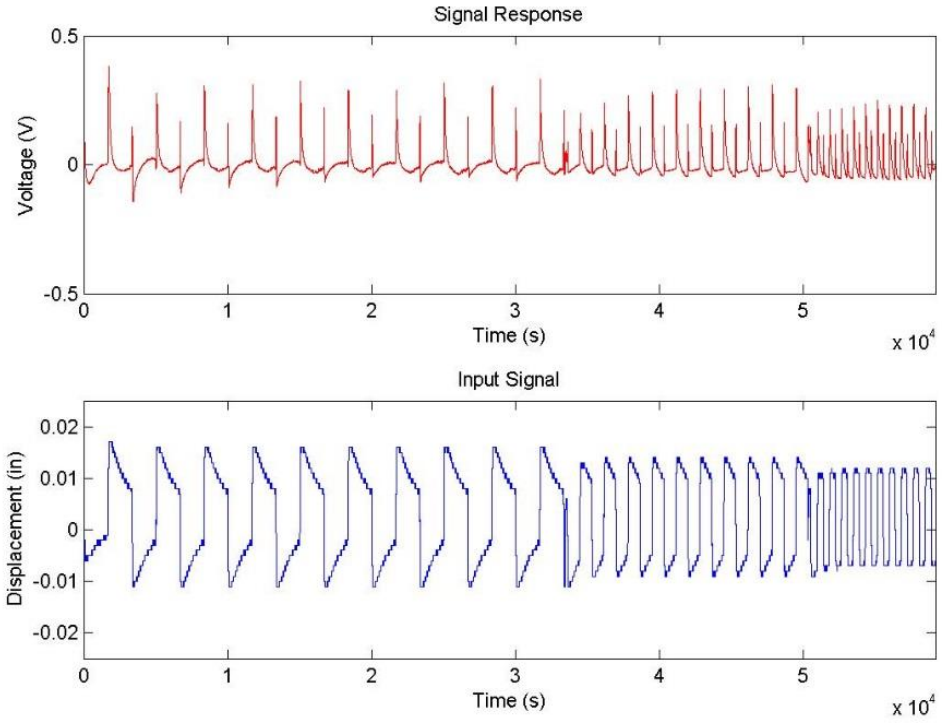

Figure 4.53. Plot illustrating (Bottom) Electrode displacement (25% strain) and the (Top) Response of a SFCS-ZnO blend (70:30 with 30 nm at 2% ZnO)

All three frequency parameters were tested in sequence at a constant 25% strain, starting from 0.6 Hz (left side of plot) to 1.2 Hz (middle of plot) to 2.4 Hz (right of plot). Similar data was recorded and plotted for each strain permutation (5% and 10%) as well. The voltage vs. time plot above clearly displays an electrical response induced by a change in strain at each frequency. Kwon et. al. [61], Chen et. al. [62], and Park et. al. [63] fabricated piezoelectric substrates consisting of PZT film, PZT nanorod and ZnO nanoparticle dispersion in PDMS (0-3), respectively, which yielded similar results. Specifically, Kwon et. al. exposed their developed thin film device to compression to generate the electrical response shown in Figure 4.54, experiencing a sharp peak upon application of the load and then release. While Chen et. al. and Park et. al. exposed their developed nanorod device and 0-3 soft nanoparticle device, respectively, to bending for generating the electrical responses shown in Figure 4.55 and Figure 4.56, which also yielded a sharp peak upon application of the load and then release. The response of the SFCS-ZnO blends have similarities to the aforementioned piezoelectric devices which demonstrates the efficacy of the soft bio-device.

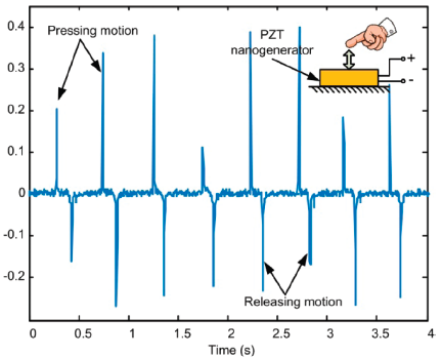

Figure 4.54. Piezoelectric response to of a flexible film device comprised of PZT [61]

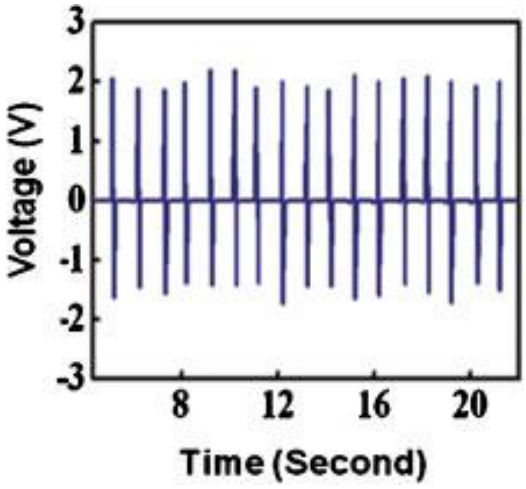

Figure 4.55. Piezoelectric response to bending nanorod device comprised of PZT [62].

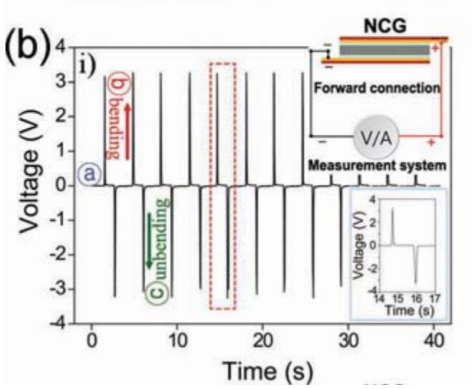

Figure 4.56. Piezoelectric response to bending a 0-3 nanoparticle composite based device comprised of ZnO dispersed within PDMS [63]

The Strain-Response data was compiled in a custom MatLab Peak Detection script (Appendix C.2) that would detect the average Peak-to-Peak value for each set of strain data at each individual frequency. This average peak-to-peak data was then inputted into a Microsoft Excel script for further analysis and plotted for side-by-side comparison to the other blends.

Plots shown in Figure 4.57 through Figure 4.65 display the actual electrical responses of the SFCS-ZnO blends with no gain used at all frequency and strain permutations. For each SFCS-ZnO blend, an increase in the strain experienced by the blend generated an increase in specimen response. Of the 27 total blends that were tested in this study, only 4 demonstrated a significantly higher response to the applied strain. As shown in Figure 4.58 and Figure 4.61, the 5% weight concentrations for the 30:70 and 50:50 blends comprised of 30 and 45 nm ZnO nanoparticles exhibited a higher response to the applied strain than any of the other SFCS-ZnO blends, including the control pure SFCS blends. A goal of this specific experiment was to narrow down which blends have the highest response to strain in order to reduce the number of blends included in the distension tests.

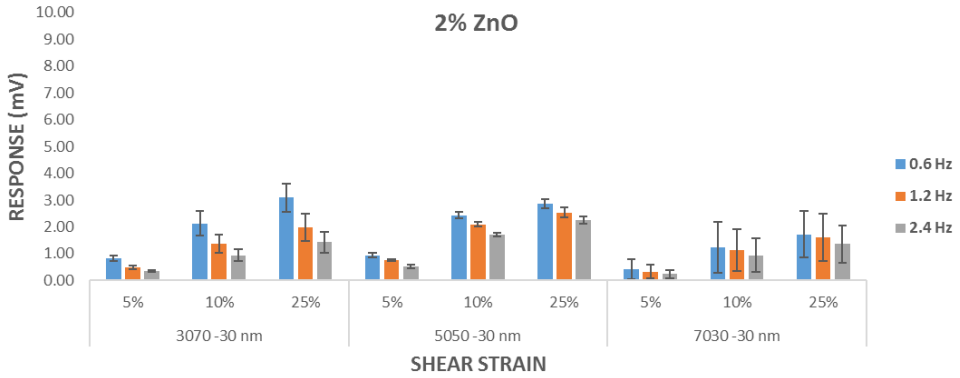

Figure 4.57. Barchart of 2%-30 nm SFCS-ZnO response to 5%, 10%, and 25% shear strain at 0.6, 1.2 and 2.4 Hz.

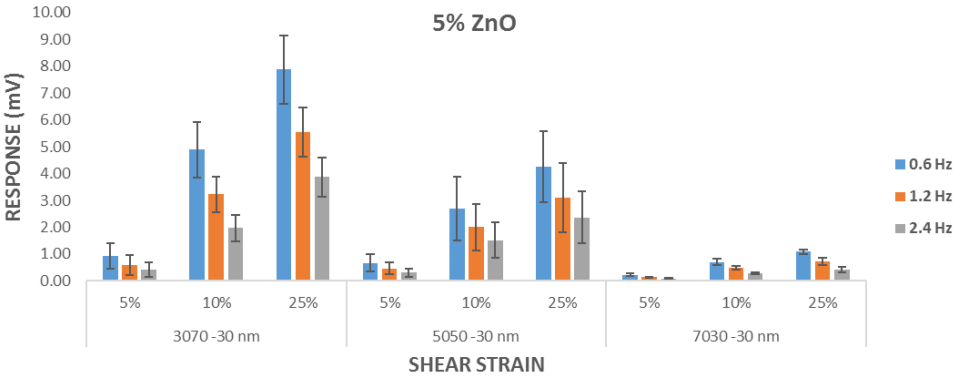

Figure 4.58. Barchart of 5%-30 nm SFCS-ZnO response to 5%, 10%, and 25% shear strain at 0.6, 1.2 and 2.4 Hz.

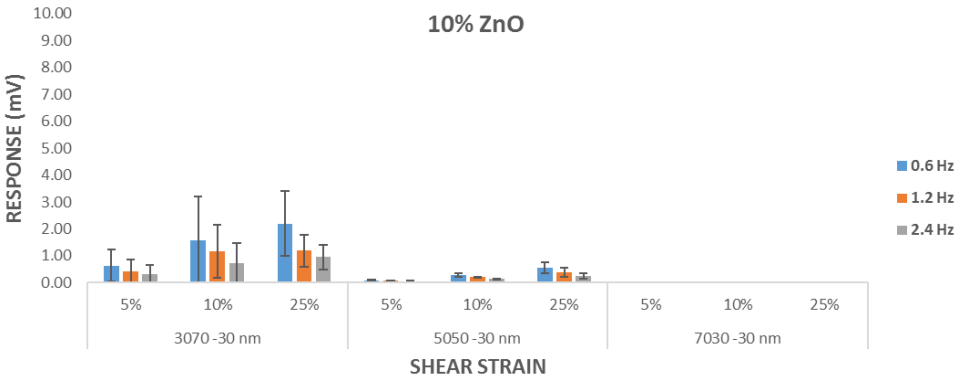

Figure 4.59. Barchart of 10%-30 nm SFCS-ZnO response to 5%, 10%, and 25% shear strain at 0.6, 1.2 and 2.4 Hz.

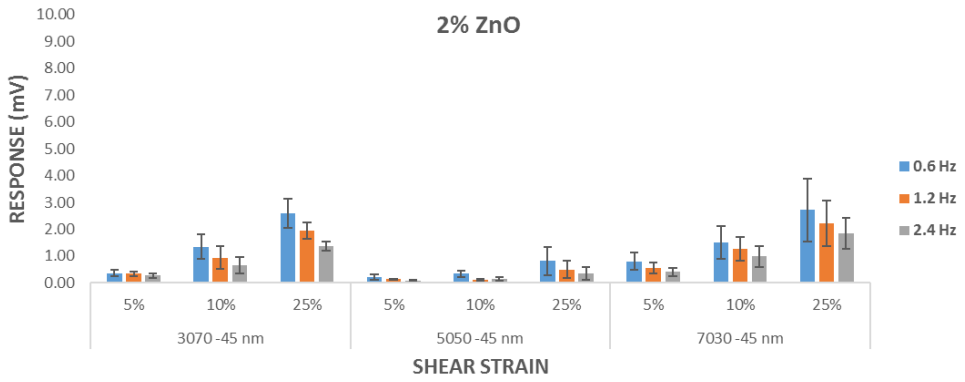

Figure 4.60. Barchart of 2%-45 nm SFCS-ZnO response to 5%, 10%, and 25% shear strain at 0.6, 1.2 and 2.4 Hz.

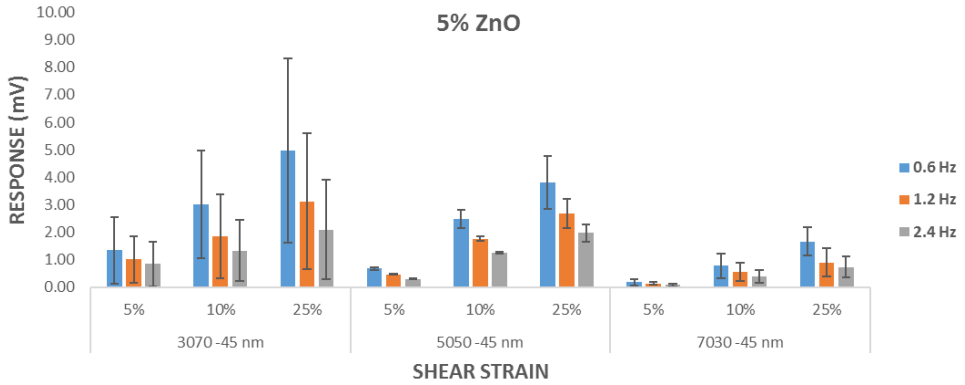

Figure 4.61. Barchart of 5%-45 nm SFCS-ZnO response to 5%, 10%, and 25% shear strain at 0.6, 1.2 and 2.4 Hz.

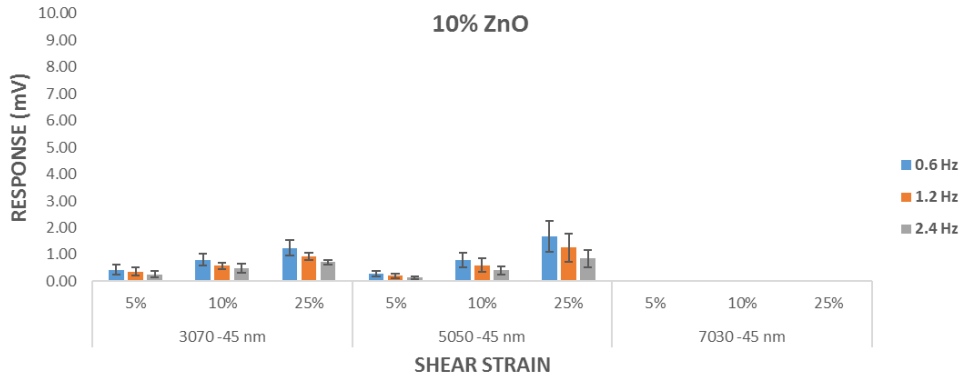

Figure 4.62. Barchart of 10%-45 nm SFCS-ZnO response to 5%, 10%, and 25% shear strain at 0.6, 1.2 and 2.4 Hz.

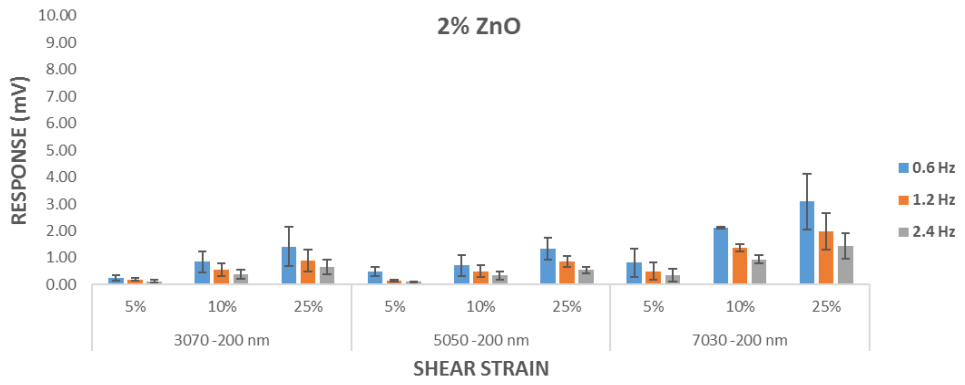

Figure 4.63. Barchart of 2%-200 nm SFCS-ZnO response to 5%, 10%, and 25% shear strain at 0.6, 1.2 and 2.4 Hz.

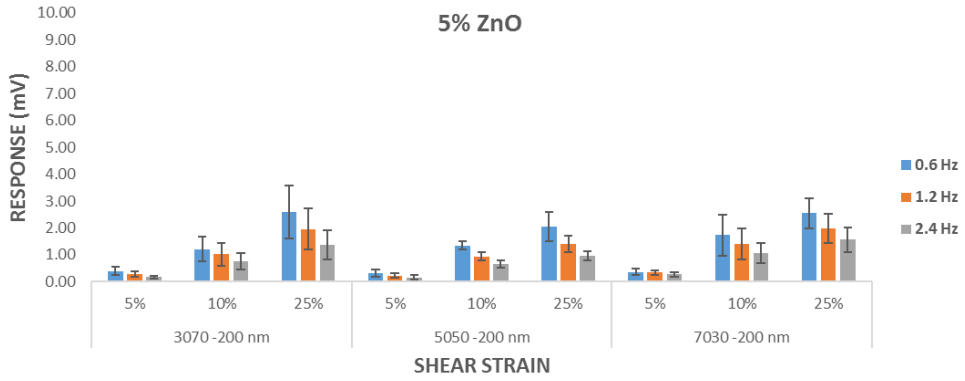

Figure 4.64. Barchart of 5%-200 nm SFCS-ZnO response to 5%, 10%, and 25% shear strain at 0.6, 1.2 and 2.4 Hz.

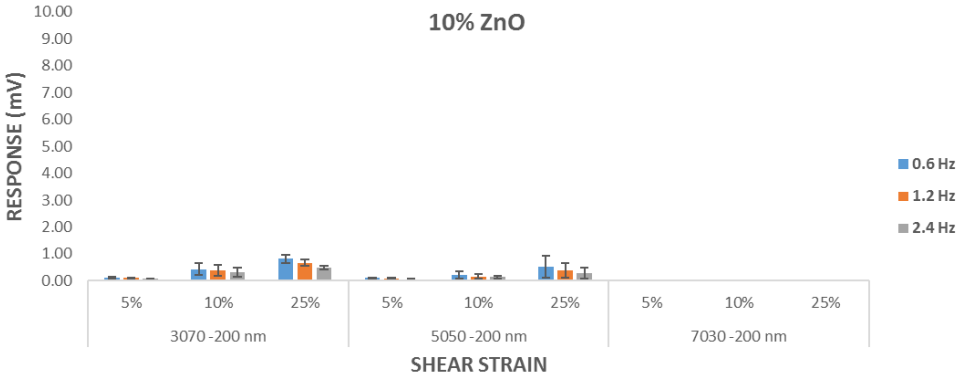

Figure 4.65. Barchart of 10%-200 nm SFCS-ZnO response to 5%, 10%, and 25% shear strain at 0.6, 1.2 and 2.4 Hz.

Figure 4.66 displays the actual electrical response of the pure SFCS blends at all frequency and strain permutations. The maximum response for any of the pure blends did not exceed 750 µV. Silk fibers and silk fibroin are naturally piezoelectrics, as are many other naturally occurring materials, such as quartz and bone. Under well controlled testing conditions with high precision measurement equipment, natural silk fibers can generate a voltage difference of up to 20 millivolts when stressed [64]. The electrical response of the pure SFCS blends were lower than that of most SFCS-ZnO blends tested in this investigation, especially the 4 selected for the distension trials.

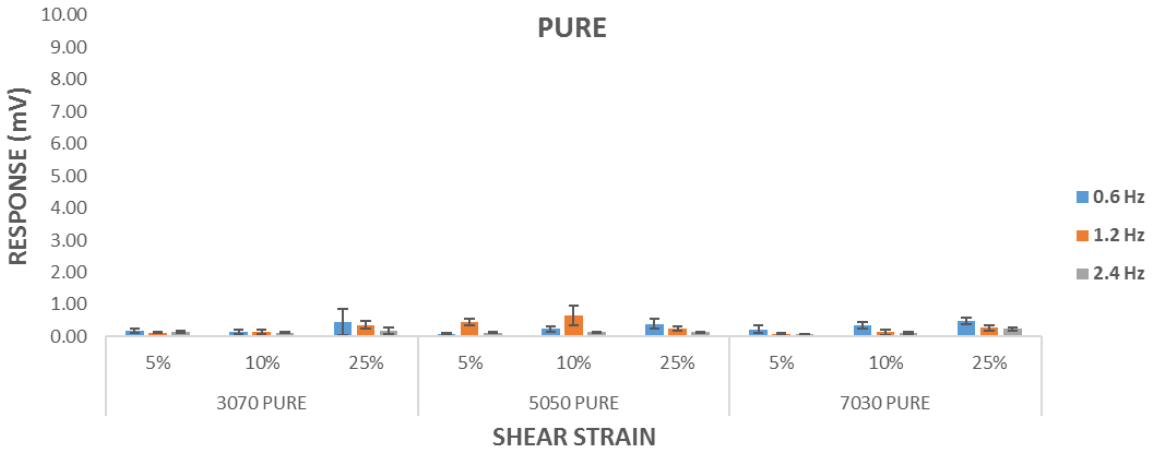

Figure 4.66. Barchart of pure SFCS sample response to 5%, 10%, and 25% shear strain at 0.6, 1.2 and 2.4 Hz.

4.3.1.1 Frequency Dependence

There is a noticeable effect of the measured SFCS blend sample response with respect to the applied shaker frequency. The output voltage amplitude is reduced when the applied frequency increases. This effect is due to the soft SFCS- blended samples' inability

to respond at the same rate as the applied external mechanical strain, which dampens the overall magnitude of the external force. Xu et al. [65] experiences this same phenomenon with PZT nanowire arrays within an epoxy matrix which they employed for energy scavenging at considerably low frequencies. An additional possibility of this frequency dependent response may be due to the tested material experiencing mechanical preconditioning as the sample is being tested. With each increase in frequency, the sample experiences an additional level of mechanical conditioning. This phenomenon in alongside the structural latency of the scaffold matrix contribute to the reduction in output of the sample.

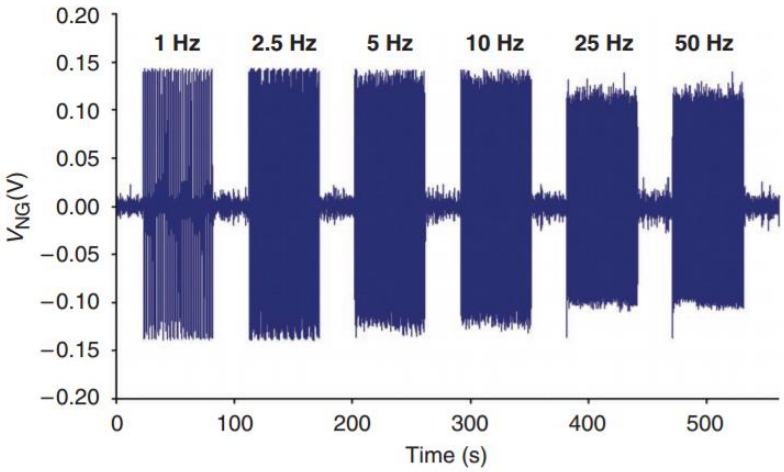

Figure 4.67. Plot representing frequency dependent reduction in electrical response [65]

4.3.1.2 Poling Study

A study of poling of the SFCS-ZnO blended materials and its effectiveness was performed to assess whether the procedure would affect electrical response of the selected materials from the study performed in Section 4.3.1. The poling electrodes were fabricated

and assembled with all components described in Section 3.2.3. The gap between the electrodes was set to 2 mm. The wet SFCS-ZnO samples were placed equidistant from one another in the poling assembly, loading no more than 3 samples per poling procedure, and allowing for a center-to-center spacing of approximately 30 mm between samples. Around 15 minutes into the poling procedure stated in Chapter 3, arcing across the electrodes would occur at driving voltages as low as 2 kilovolts. Damage to the specimen, poling electrode assembly, and high voltage power supply occurred during the poling process. Figure 4.68 demonstrates the damage that occurred on the electrode (upper inset) and the specimen (lower inset). To prevent a total loss of the piece of equipment, testing was halted due to excessive damage to the high voltage power supply resulting in substantial repairs to the internal instrumentation by the investigator and resident experts.

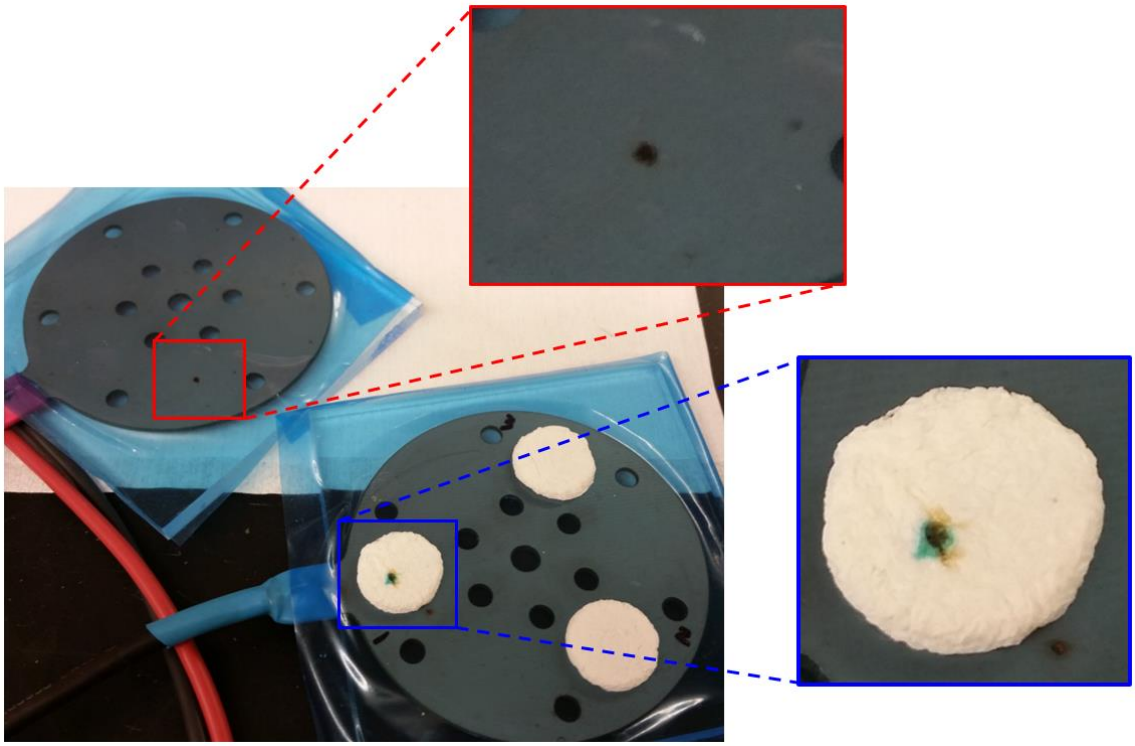

Figure 4.68. Image of damage resulted via applying a high voltage to the poling electrode assembly.

4.3.2 In Vitro Testing of SFCS-ZnO Blends in Mock Vessel Models

4.3.2.1 Compliance and Circumferential Strain Testing

Mechanical characteristics such as compliance and circumferential strain were calculated from the recorded diameters of porcine aorta tissue and the engineered analog tubes constructed from an elastomeric polymer (DragonSkin®). These values were critical in determining the relationship between the applied pressure via the Custom Electrodynamic Vessel Distension Simulation Apparatus to determine the required platen

stroke to achieve the desired pulse pressure ranges. Table 4.6 and Table 4.7 present the calculated compliance and circumferential strains attained in response to simulated diastolic and systolic pressures. Three different systolic pressures were applied to the elastomeric tubes and porcine aortas with the diastolic pressures held constant. Varying the systolic pressure and leaving the diastolic pressure at a constant 70 mmHg for each test set was determined to be the simplest method since it was easier to increase the systolic pressure within the vessel by changing the stroke of the EDS, while maintaining the baseline diastolic pressure that was driven by the initial injection of saline into the VAS. The relationship between the applied pressure and the compliance and circumferential strain were critical in determining the required platen stroke for achieving the desired pulse pressure ranges of the EVDSA.

Table 4.6. List of compliance and circumferential strain data calculated from measured vessel diameters from an engineered tube comprised of DragonSkin®.

Applied Pressure		**Measured Diameter**		**Compliance**	**Circumferential Strain**
P_{sys}	**P_{dia}**	**D_{sys}**	**D_{dia}**	**C**	**ε_D**
(mmHg)	**(mmHg)**	**(mm)**	**(mm)**	**($mmHg^{-1}$)**	**(mm/mm) %**
140	70	13.30	11.2	0.0027	21%
120	70	12.32	11.2	0.0020	11%
100	70	11.74	11.2	0.0016	5%

Table 4.7. List of compliance and circumferential strain data calculated from measured vessel diameters from a 15 kg pig aorta.

Applied Pressure		**Measured Diameter**		**Compliance**	**Circumferential Strain**
P_{sys}	**P_{dia}**	**D_{sys}**	**D_{dia}**	**C**	**ε_D**
(mmHg)	**(mmHg)**	**(mm)**	**(mm)**	**($mmHg^{-1}$)**	**(mm/mm) %**
140	70	14.02	11.45	0.0032	23%
120	70	12.80	11.45	0.0024	12%
100	70	12.30	11.45	0.0024	7%

The changes in diameter due to vessel pressure were plotted for both the engineered Dragonskin® tube and the descending aorta of the 15 kg pig (Figure 4.69). The applied pressure ranged from 70 to 140 mmHg that resulted in a change in diameter of 2.58 mm

and 2.10 mm for the porcine aorta and Dragonskin®, respectively. The goal was to mimic the mechanical behavior of the aortic tissue during distension with the more accessible off the shelf Dragonskin® resin. The distinct difference between the two vessels is the difference in diameters at each applied pressure value (Figure 4.69). The engineered vessel was fabricated within a mold with a nominal diameter of 10 mm, which was the inner diameter of an off the shelf tube that was cheap and readily available for use. This dimension could not be easily changed without the use of a custom manufactured mold. The aorta was on average 13.6±0.8% larger in diameter at each applied pressure, primarily because the aorta was larger in diameter. Notice the undulations in the aorta curve versus the engineered tube. This was due to the aorta not having homogenous material properties throughout its length or circumference, whereas, the elastomeric tube had a much higher level of homogeneity throughout, generating a smoother curve. Also, the slope of each curve is quite similar as well, 0.030x and 0.035x for the Dragonskin and aorta, respectively, with both having an R^2 = to 95.5%.

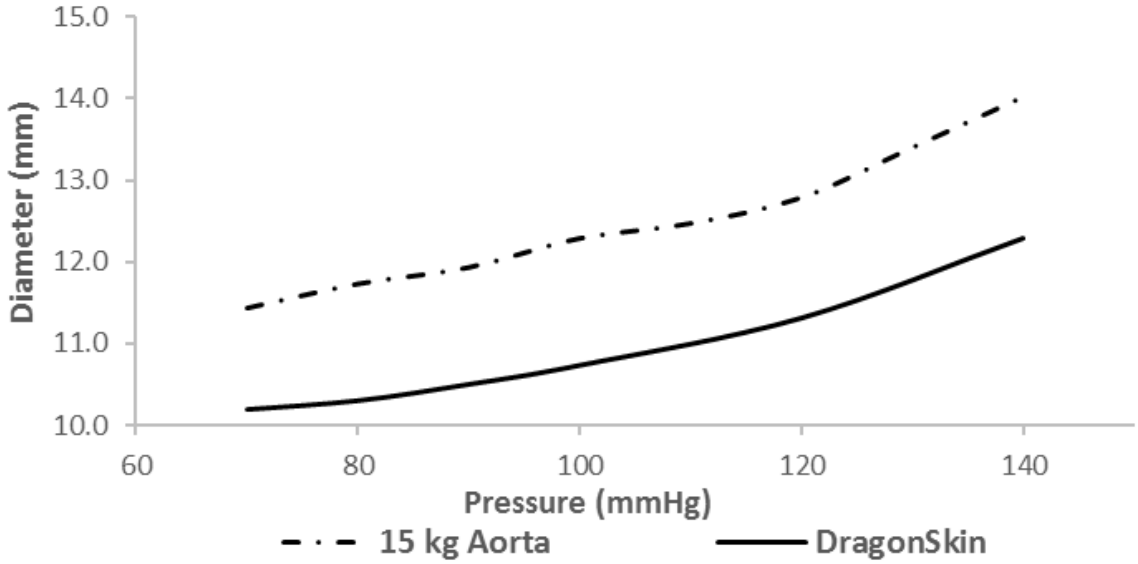

Figure 4.69. Diameter – Pressure plot of engineered Dragonskin vessel and a 15 kg porcine aorta.

Figure 4.70 demonstrates the similarities in changes in circumferential strain due to vessel pressure between the engineered Dragonskin® tube and the descending aorta of the 15 kg pig. The applied pressure ranged from 70 to 140 mmHg for the porcine aorta and Dragonskin®, respectively. The curves have striking similarities with respect to circumferential strain and nearly overlap one another; indicating how well the engineered tube approximated the mechanical behavior of the porcine aorta. Thus, the DragonSkin® vessels were used for initial testing of the ring samples in order to determine the optimum placement of the electrodes in the SFCS-ZnO ring samples before performing the porcine aorta tests.

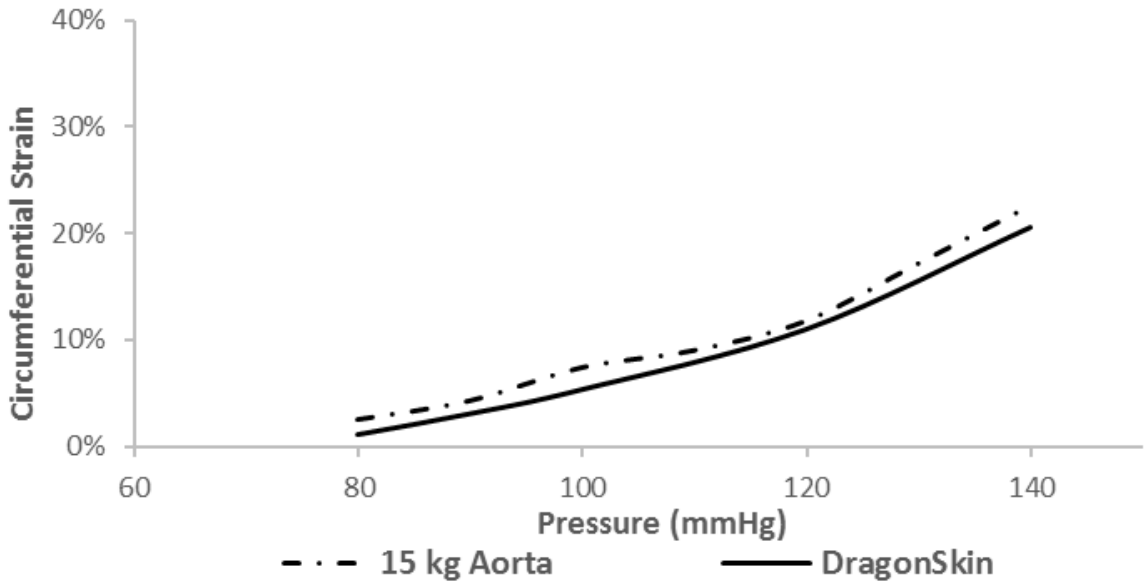

Figure 4.70. Circumferential Strain – Pressure plot of engineered Dragonskin vessel and a 15 kg porcine aorta.

4.3.2.2 Electrode Placement Investigation

Upon completion of the shear testing and identification of the 4 top performing SFCS-ZnO blends, the ring-shaped samples were placed on the DragonSkin® vessels. Three samples of the 50:50 SFCS-ZnO blend with 45 nm particle at a 5% concentration were used to identify the optimum electrode placement by investigating 6 different electrode positions and configurations, as previously described in Section 3.3.3.3. Electrode placement and SFCS-ZnO sample response was recorded for each test. The EDS platen stroke, internal vessel pressure induced by said change in platen stroke, and the measured voltage generated by the distended SFCS-ZnO sample were plotted (Figure 4.71). The programmed square wave input into the EDS controller-amplifier induced a square wave pressure response profile. The initial impulse experienced by the pressure

sensor was a rapid increase that resulted in an overshoot in the pressure. This overshoot was likely due to the small internal closed volume of the test apparatus and the pressure waves irradiating from the piston and traveling along the inner volume of the tube, induced by the rapid change in stroke. The change in SFCS-ZnO response corresponded to the change in pressure, whereas the vessel distended, and the ring sample experienced an increased state of tension. The electrical response of the samples, while in the state of tension resulted in a negative peak due the local polarization of the SFCS-ZnO sample that was loaded. ZnO was naturally polarized, therefore it did not require high voltage polarization to generate a piezoelectric output. If the natural polarization negates the applied force then the resultant output will have a negative charge. Alternatively, when the vessel returns to its diastolic state via rapid reduction in applied pressure, the ring experiences compression during the rapid return to its original state and a positive electrical output peak was observed. The highly porous nature of the SFCS scaffold and the low stiffness made the 0-3 piezocomposite tend to have a higher affinity for compressive loads. As the scaffold was stretched via tensile forces the intricate matrix elongated; thus, it was difficult to apply a tensile force directly onto the nanoparticles themselves due to the weak to no binding between the SFCS matrix and the nanoparticles. Whereas, when under a compressive load, the porous matrix collapses, the SFCS scaffold which then exuded a direct compressive load onto the nanoparticles as well as increased the particle-to-particle interaction of the ZnO. This type of result was also experienced by [63] through the continual stretching and relaxing of 0-3 type piezoelectric materials. As seen in the shear testing data from Section 4.3.1, a reduction in electrical response was observed as frequency increased.

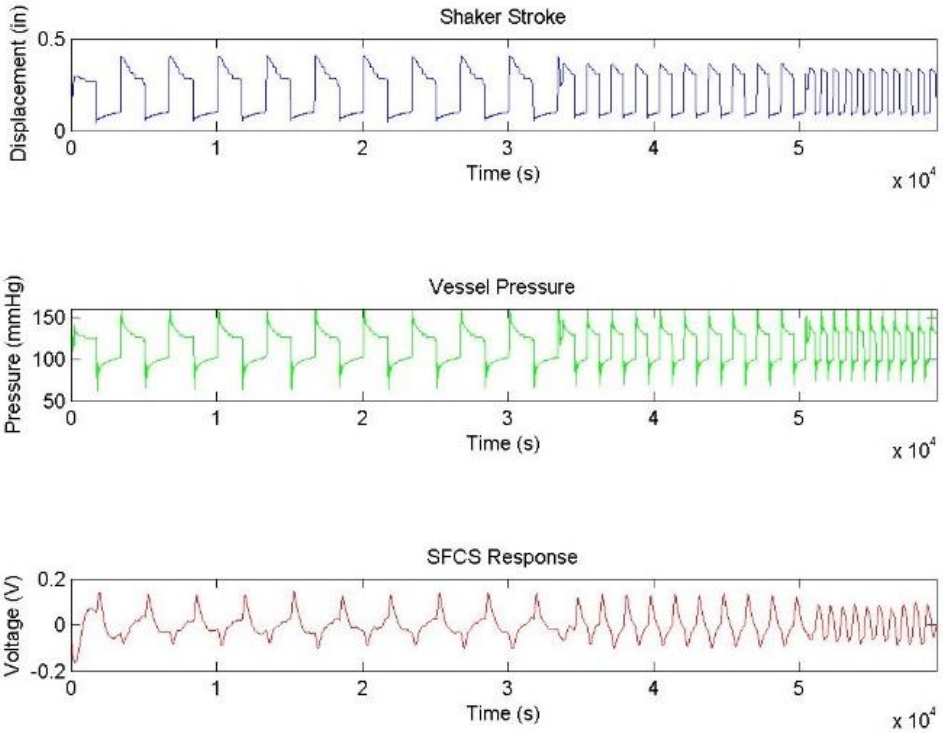

Figure 4.71. 5050-45nm-2%, 180 degree axial position, with amplification.

As mentioned previously, SFCS-ZnO ring sample response with respect to electrode position, pulse pressure range, and frequency were also investigated (Figure 4.72). The data demonstrated that the 180˚ axial electrode configuration had a higher response compared to the other two axial configurations (with angular positions 45˚ and 90˚) and radially (at 180˚ position) configured electrodes. The 180˚ position accounted for a nominal electrode distance of approximately 22.0 mm. The change in the noted variables accounted for the reduction in electrical response. The angular distance between the wire electrodes for the 180˚ axial position generated the highest due to the greater number of piezoelectric nanoparticles between the electrodes. Whereas, the 45˚ and 90˚ configurations would, in theory, have had 25% and 50% less nanoparticles, respectively, due to the shorter distance between the electrodes. Additionally, the orientation of the wire

while inserted into the SFCS-ZnO sample influenced the response of the sample as well. Specifically, the axial orientation effectively had double the contact surface area (12.56 mm^2) for the electrode within the SFCS-ZnO sample in comparison to the radial orientations (6.28 mm^2). This point was further supported by the output response results where the radial orientation displayed a lower response than the axial orientation, albeit not significant.

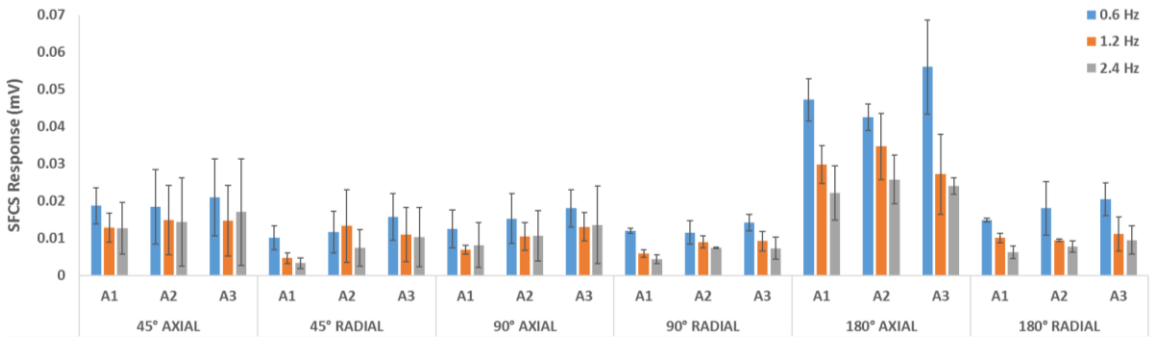

Figure 4.72. Bar chart demonstrating output of SFCS ring samples wire electrodes placed at 45˚, 90˚, and 180˚ oriented in both axial and radial configurations with respect to the vessel geometry.

4.4 Ex vivo testing of SFCS-ZnO samples on excised porcine aorta

Upon completion of the electrode placement investigation, the 4 top performing SFCS-ZnO blends were then placed on excised descending aortas from 15 kg Yorkshire/Landrace pigs. The electrode wires were oriented in the 180˚ axial position. Similar to the electrode placement studies, the EDS platen stroke, measured internal vessel

pressure, and the measured output voltage generated by the distended SFCS-ZnO blends data was recorded and plotted. Like the in vitro elastomer-based tubes, the change in SFCS-ZnO response corresponded to the change in pressure (Figure 4.73). In addition, the peak-to-peak response data for the SFCS-ZnO ring samples with respect to electrode position, pulse pressure range, and frequency were plotted (Figure 4.74). Of the 4 SFCS-ZnO blends tested, the observed data demonstrated that the 3070 SFCS blend with the 30 nm ZnO nanoparticles at a ZnO concentration of 5% by weight exhibited the highest response during distension. The average Elastic Modulus of the 4 tested SFCS-ZnO candidates was also presented in Figure 4.74, shown as large black circles with the error bars denoting standard deviation. This demonstrated a correlation between the mechanical stiffness of the SFCS-ZnO matrix and the electrical response of the material. Thus, this final experiment proved that the SFCS tissue scaffolds with embedded ZnO nanoparticles do provide the capability to act as a piezoelectric pressure sensor under cardiovascular physiological conditions.

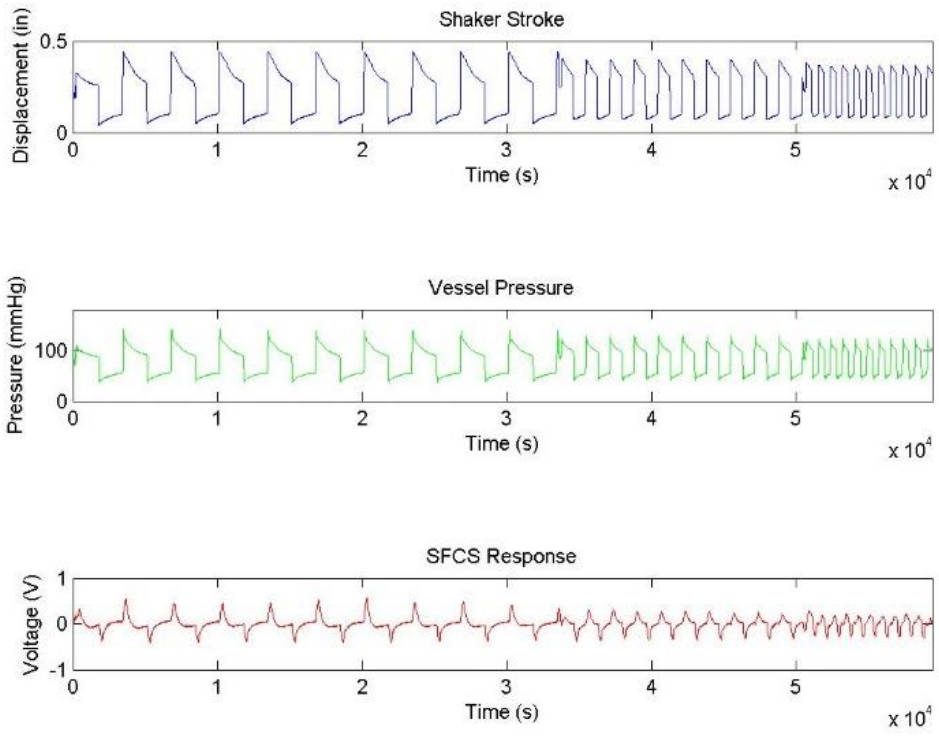

Figure 4.73. Plot of shaker stroke (Top), vessel pressure (Middle), and SFCS response (Bottom) for a 3070-45nm -5% sample

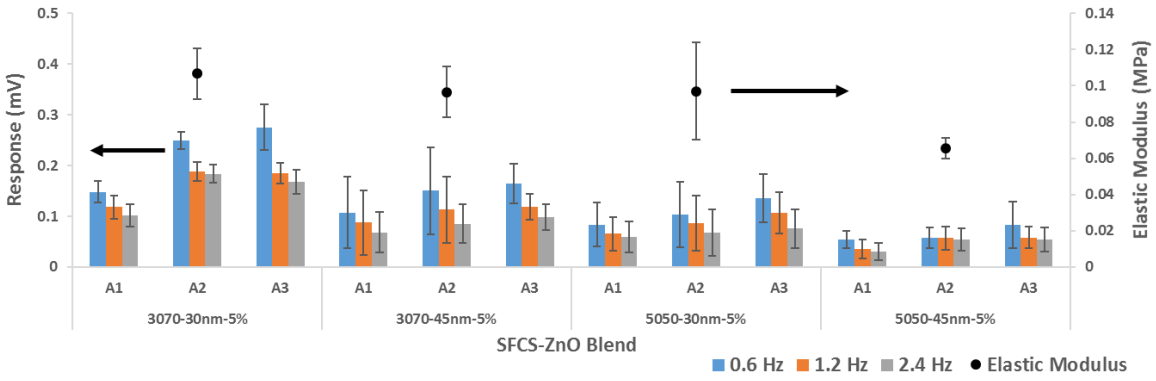

Figure 4.74. Bar chart demonstrating output of SFCS ring samples when mounted to porcine aortic tissue and distended.

CHAPTER 5: CONCLUSIONS

The goal of this project was to develop and create prototype biocompatible and bioresorbable electroactive perivascular bands comprised of several permutations of SFCS blends, ZnO nanoparticle size and ZnO nanoparticle concentrations. Mechanical and electrical studies were performed to determine the optimal blend of scaffold with respect to ZnO nanoparticle concentration. Demonstration and advancement of said prototypes would not have been possible without the development of:

- Molds for production of all SFCS-ZnO test samples
- A custom-designed differential amplification circuit with electronics chosen for easy gain adjustment and low-noise
- Supporting data acquisition and analysis software to set the response offsets, control sampling, and record the experimental data
- A custom dynamic material shearing unit
- A custom dynamic distension unit

Collectively, the aforementioned individual components provided experimental platforms to explore the mechanical and electrical performance of the SFCS-ZnO blends. Evaluation of the electronics indicated that the performance of the amplification circuit fell within specifications and functioned as designed. The data acquisition and analysis software developed was an essential component for both experimental control as well as

post experiment data processing methods. The custom dynamic shearing and distension units proved vital in the determination of electrical response of the SFCS-ZnO samples when exposed to mechanical shear strains and circumferential strains induced via vessel distension. This investigation established that a fully functional biocompatible material can be doped with a biocompatible piezoelectric nanoparticle and demonstrate a means of converting mechanical strain into a measurable electrical signal output without the need of power or external wiring of any kind.

Based on the present investigation and current understanding of the functionality of the newly developed tissue engineered perivascular sensor, the following recommendations are made with respect to future work:

1. Take a deeper look into the actual piezoelectric characteristics of the device. Potentially determining and gaining a greater understanding of the principles behind the scenes.
2. Develop a perivascular band that goes beyond the proof of concept solid ring structure which currently cannot be surgically placed around a desired blood vessel. A method of securely wrapping a flat strap band design, similar to a wristwatch band, would be required for proper surgical installation of the device.
3. Develop an implantable electrode that interfaces with the tissue engineered scaffold more effectively than the current simple electrode wire approach used in this study.
4. Perform an acute in vivo animal experimentation to confirm device robustness to survive surgical implantation and short term efficacy of the device. Determine whether the device functions while under normal physiological conditions in vivo.

Perform a chronic in vivo animal experimentation to determine long term efficacy of the device. This study would 1.) determine the body's response to the implanted device over time and 2.) discover whether the electrical response degrades or improves as the body incorporates the tissue scaffold into the vessel wall.

REFERENCES

[1] D. M. V. L. R. E. J. B. J. D. B. W. B. B. e. a. A. S. Go, ""Heart Disease and Stroke Statistics—2013 Update: A Report From the American Heart Association,"," *Circulation, vol. 127,* pp. pp. e6-e245, 2013.

[2] M. G. L. E. P. L. A. B. R. B. D. W. B. K. e. a. D. M. Lloyd-Jones, ""Lifetime risk for developing congestive heart failure - The Framingham Heart Study,"," *Circulation, vol. 106,* pp. pp. 3068-3072, 2002.

[3] E. B. a. R. O. Bonow, Braunwald's heart disease : a textbook of cardiovascular medicine, 9th ed., Philadelphia: Saunders, 2012.

[4] "Underlying Cause of Death 1999-2013," 3 February 2015. [Online]. Available: http://wonder.cdc.gov/ucd-icd10.html.

[5] L. J. S. C. A. A. T. a. S. L. M. G. George, ""Pulmonary Hypertension Surveillance United States, 2001 to 2010"," *Chest,* vol. 146, pp. pp. 476-495, 2014.

[6] P. B. A. R. C. B. M. F. A. M. R. C. L. W. S. e. a. W. T. Abraham, "Wireless pulmonary artery haemodynamic monitoring in chronic heart failure: a randomised controlled trial,"," *Lancet,* vol. 377, pp. pp. 658-666, 2011.

[7] M. e. a. George, ""Pulmonary Hypertension Surveillance United States, 2001 to 2010," *Chest,* vol. 146, pp. 476-495, 2014.

[8] J. Booth, "A Short History of Blood Pressure Measurement," *Proceedings of the Royal Society of Medicine,* vol. 70.11, pp. 793-799, 1977.

[9] J. E. H. L. J. A. B. E. F. J. G. M. N. H. e. a. T. G. Pickering, ""Recommendations for blood pressure measurement in humans and experimental animals: part 1: blood pressure measurement in humans: a statement for professionals from the Subcommittee of Professional and Public Education of the American Heart Association Co," *Circulation,* vol. 111, pp. 697-716, 2005..

[10] J. S. P. A. S. M. A. H. R. M. S. a. B. S. J. Y. Wagner, ""Noninvasive continuous versus intermittent arterial pressure monitoring: evaluation of the vascular unloading technique (CNAP device) in the emergency department"," *Scand J Trauma Resusc Emerg Med,* vol. 22, p. 8, 2014.

[11] J. T. M. A. B. P. E. P. K. M. M. J. G. B. e. a. R. J. Roeleveld, ""A comparison of noninvasive MRI-based methods of estimating pulmonary artery pressure in pulmonary hypertension"," *J Magn Reson Imaging,* vol. 22, pp. 67-72, 2005.

[12] W. J. Germann and C. L. Stanfield, Principles of human physiology, San Francisco: Pearson Education/Benjamin Cummings, 2001.

[13] A. C. G. a. J. E. Hall, Textbook of medical physiology, 9th ed.:, Philadelphia: W.B. Saunders, 1996.

[14] P. E. a. R. J. M. Caccamo, ""Current state of ventricular assist devices"," *Curr Heart Fail Rep,* vol. 8, pp. 91-98, 2011.

[15] M. M. Givertz, ""Ventricular Assist Devices Important Information for Patients and Families"," *Circulation,* vol. 124, pp. E305-E311, 2011.

[16] P. H. a. L. Kuppurao, ""Ventricular assist devices"," *Continuing Education in Anaesthesia, Critical Care & Pain,* vol. 12, pp. 145-151, 2012.

[17] M. M. G. G. C. S. a. G. H. M. S. R. Wilson, ""Ventricular Assist Devices The Challenges of Outpatient Management,"," *Journal of the American College of Cardiology,* vol. 54, pp. 1647-1659, 2009.

[18] A. C. Guyton and J. E. Hall, Textbook of medical physiology, Philadelphia: W.B. Saunders, 1996.

[19] E. H. J, "S. Laurent, J. Cockcroft, L. Van Bortel, P. Boutouyrie, C. Giannattasio, D. Hayoz, et al., "Expert consensus document on arterial stiffness: methodological issues and clinical applications,"," *Eur Heart J,* vol. 27, pp. 2588-605, 2006.

[20] M. K. S. D. S. P.-G. M. J. G. V. F. e. a. J. Sanz, ""Evaluation of pulmonary artery stiffness in pulmonary hypertension with cardiac magnetic resonance,"," *JACC Cardiovasc Imaging,,* vol. 2, pp. 286-95, 2009.

[21] L. T. a. N. C. Chesler, ""In vivo and in vitro measurements of pulmonary arterial stiffness: A brief review,"," *Pulm Circ,* pp. 505-17, 2012.

[22] A. M. C. Vaiss, ""Technical aspects of compliance assessment,"," *Arch Mal Coeur Vaiss,* vol. 84, pp. 77-81, 1991.

[23] J. J. M. F. P. H. R. B. a. M. A. Y. Tardy, ""Non-invasive estimate of the mechanical properties of peripheral arteries from ultrasonic and photoplethysmographic measurements,"," *Clin Phys Physiol Meas,* vol. 12, pp. 39-54, 1991.

[24] M. J. K. H. A. B. a. H. A. S. B. L. M. Van Bortel, ""Effects of antihypertensive agents on local arterial distensibility and compliance"," *Hypertension,* vol. 26, pp. 531-4, 1995.

[25] R. G. G. a. M. M. Budge, ""Terminology for describing the elastic behavior of arteries"," *Hypertension,* vol. 41, pp. 1180-2, 2003.

[26] R. C. A. G. M. D. a. G. M. G. Parati, ""Comparison of Finger and Intra-Arterial Blood-Pressure Monitoring at Rest and during Laboratory Testing"," *Hypertension,* vol. 13, pp. 647-655, 1989.

[27] W. H. K. a. D. J. Y. P. Cong, ""Wireless Implantable Blood Pressure Sensing Microsystem Design for Monitoring of Small Laboratory Animals,"," *Sensors and Materials,* vol. 20, pp. 327-340, 2008.

[28] W. H. K. a. D. J. Y. P. Cong, ""Wireless Batteryless Implantable Blood Pressure Monitoring Microsystem for Small Laboratory Animals,"," *Ieee Sensors Journal,* vol. 10, pp. 243-254, 2010.

[29] J. T. M. A. B. P. E. P. K. M. M. J. G. B. e. a. R. J. Roeleveld, ""A comparison of noninvasive MRI-based methods of estimating pulmonary artery pressure in pulmonary hypertension"," *J Magn Reson Imaging,* vol. 22, pp. 67-72, 2005.

[30] V. Y. T. a. C. R. Bowen, Electromechanical properties in composites based vsculature on ferroelectrics, London: Springer, 2008.

[31] D. P. S. a. L. E. C. R. E. Newnham, ""Connectivity and Piezoelectric-Pyroelectric Composites"," *Materials Research Bulletin,* vol. 13, pp. 525-536, 1978.

[32] K. Uchino, Advanced piezoelectric materials : science and technology., Philadelphia: Woodhead Publishing, 2010.

[33] A. I. Ltd., Piezoelectric ceramics : principles and applications, 2nd ed., Mackeyville: APC International, 2011.

[34] S. J. Hollister, ""Porous scaffold design for tissue engineering"," *Nature Materials,* vol. 5, pp. 590-590, 2006.

[35] F. J. O'Brien, ""Biomaterials & scaffolds for tissue engineering"," *Materials Today,* vol. 14, pp. 88-95, 2011.

[36] V. E. F. a. A. B. M. A. S. Gobin, ""Structural and mechanical characteristics of silk fibroin and chitosan blend scaffolds for tissue regeneration"," *Journal of Biomedical Materials Research Part A,* vol. 74a, pp. 465-473, 2005.

[37] F. D. C. J. T. C. R. L. H. J. C. e. a. G. H. Altman, ""Silk-based biomaterials"," *Biomaterials,* vol. 24, pp. 401-16, 2003.

[38] H. J. J. a. D. L. K. R. Nazarov, ""Porous 3-D scaffolds from regenerated silk fibroin"," *Biomacromolecules,* vol. 5, pp. 718-26, 2004.

[39] C. E. B. a. A. B. M. A. S. Gobin, ""Repair and regeneration of the abdominal wall musculofascial defect using silk fibroin-chitosan blend"," *Tissue Engineering,* vol. 12, pp. 3383-3394, 2006.

[40] V. K. L. M. R. R. B. T. H. S. V. N. e. a. P. T. S. Kumar, ""Evaluation of Wound Healing Potential of beta-Chitin Hydrogel/Nano Zinc Oxide Composite Bandage"," *Pharmaceutical Research,* vol. 30, pp. 523-537, 2013.

[41] H. M. a. Ü. Özgür, Zinc oxide : fundamentals, materials and device technology., Weinheim: Wiley-VCH, 2009.

[42] N. P. a. R. Vijayaraghavan, ""Enhanced bioactivity of ZnO nanoparticles-an antimicrobial study,"," *Science and Technology of Advanced Materials,* vol. 9, 2008.

[43] D. Rockwood, R. Preda, T. Yücel, X. Wang, M. Lovett and D. Kaplan, "Materials fabrication from Bombyx mori silk fibroin," *nature protocols,* vol. 6, no. 10, 2011.

[44] G. H. Altman, F. Diaz, C. Jakuba, T. Calabro, R. L. Horan, J. hen, H. Lu, J. Richmond and D. L. Kaplan, "Silk-based biomaterials," *Biomaterials,* vol. 24, pp. 401-416, 2003.

[45] R. Nazarov, H.-J. Jin and D. L. Kaplan, "Porous 3-D Scaffolds from Regenerated Silk Fibroin," *Biomacromolecules,* vol. 5, pp. 718-726, 2004.

[46] Z.-d. She, W.-q. Liu and Q.-l. Feng, "Preparation and cytocompatibility of silk fibroin/chitosan scaffolds," *Front. Mater. Sci. China,* vol. 3, no. 3, pp. 241-247, 2009.

[47] S. Zeng, L. Liu, Y. Shi, J. Qiu, W. Fang, M. Rong, Z. Guo and W. Gao, "Characterization of Silk Fibroin/Chitosan 3D Porous Scaffold and In Vitro Cytology," *PLOS ONE,* vol. 6, no. 10, 2015.

[48] G. Cooper, The Cell: A Molecular Approach. 2nd edition., Sunderland (MA): Sinauer Associates, 2000.

[49] D. Seliktar, R. Black, R. Vito and R. Nerem, "Dynamic mechanical conditioning of collagen-gel blood vessel constructs induces remodeling in vitro.," *Ann Biomed Eng.,* vol. 4, no. 28, pp. 351-362, 2000.

[50] H. F. Brinson and L. C. Brinson, Polymer Engineering Science and Viscoelasticity, An Introduction, Springer, 2008.

[51] Y. C. Fung, Biomechanics, Mechanical Properties of Living Tissues, New York: Springer-Verlag, 1993.

[52] N. W. Tschoegl, The Phenomenological Theory of Linear Viscoelastic Behavior, An Introduction, Springer Berlin Heidelberg, 1989.

[53] R. Gauvin, M. Guillemette, T. Galbraith, J.-M. Bourget, D. Larouche, H. Marcoux, D. Hugo, C. Hayward,, F. Auger and L. GermainGermain, "Mechanical Properties of Tissue-Engineered Vascular Constructs Produced Using Arterial or Venous Cells," *TISSUE ENGINEERING: Part A,* vol. 17, no. 15, pp. 2049-2059, 2011.

[54] A. Atala and J. Yoo , Essentials of 3D Biofabrication and Translation, 1st Edition, Academic Press, 2015.

[55] Malvern Instruments Ltd, "Changing the Properties of Particles to Control Their Rheology," 2015.

[56] X. Feng, L. Feng, M. Jin , J. Zhai, L. Jiang and D. Zhu, "Reversible Super-hydrophobicity to Super-hydrophilicity Transition of Aligned ZnO Nanorod Films," *J. Am. Chem. Soc,* vol. 1, no. 126, pp. 62-63, 2004.

[57] H. Ennaceri, L. Wang, D. Erfurt, W. Riedel, G. Mangalgiri, A. Khaldoun, A. El Kenz, A. Benyoussef and A. Ennaoui, "Water-resistant surfaces using zinc oxide structured nanorod arrays with switchable wetting property," *Surface and Coatings Technology,* vol. 299, pp. 169-176, 2016.

[58] P. Wongpanit, N. Sanchavanakit, P. Pavasant, T. Bunaprasert, Y. Tabata and R. Rujiravanit, "Preparation and characterization of chitin whisker-reinforced silk fibroin nanocomposite sponges," *Macromolecular Nanotechnology,* vol. 43, p. 4123–4135, 2007.

[59] D. Helander, Fundamentals of Formation Evaluation, Tulsa, OK: OGCI Publications, 1983.

[60] V. GUPTA, G.-H. MUN, B. CHOI, A. ASEH, L. MILDRED, A. PATEL, Q. ZHANG, J. PRICE, D. CHANG, G. ROBB and A. MATHUR, "Repair and Reconstruction of a Resected Tumor Defect Using a Composite of Tissue Flap–Nanotherapeutic–Silk Fibroin and Chitosan Scaffold," *Annals of Biomedical Engineering,* vol. 39, no. 9, p. 2374–2387, 2011.

[61] J. Park and R. Lakes, Biomaterials, An Introduction, 2nd Edition, New York: Plenum Press, 1992.

[62] J. Kwon, B. Sharma and J.-H. Ahn, "Graphene Based Nanogenerator for Energy Harvesting," *Japanese Journal of Applied Physics,* vol. 52, 2013.

[63] X. Chen, S. Xu, N. Yao and Y. Shi, "1.6 V Nanogenerator for Mechanical Energy Harvesting Using PZT Nanofibers," *Nano Lett.,* vol. 10, p. 2133–2137, 2010.

[64] K.-I. Park, M. Lee, Y. Liu, S. Moon and G.-T. Hwang, "Flexible Nanocomposite Generator Made of BaTiO3 Nanoparticles and Graphitic Carbons," *Adv. Mater,* vol. 24, p. 2999–3004, 2012.

[65] T. Yucel, P. Cebe and D. Kaplan, "Structural Origins of Silk Piezoelectricity," *Adv Funct Mater.,* vol. 4, no. 21, p. 779–785, 2011.

[66] S. Xu, B. Hansen and Z. L. Wang, "Piezoelectric-nanowire-enabled power source for driving wireless microelectronics," *Nature Communications,* vol. 93, no. 1, 2010.

[68] R. S. Y. M. Y. F. B. C. L. a. Z. L. W. Z. Li, ""Cellular Level Biocompatibility and Biosafety of ZnO Nanowires"," *Journal of Physical Chemistry C,* vol. 112, pp. 20114-20117, 2008.

[69] R. O'Brien, "Shear Induced Coagulation," in *6th Australasion Hydraulics and Fluid Mechanics Conference*, Adelaide, Australia, 1977.

Appendix 1 – Mechanical Drawings and Bill of Materials

Custom Electrodynamic Biaxial Testing Apparatus

A custom frame was designed and fabricated to be mounted directly to the EDS steel frame. The lasercut acrylic sheets (6.34 mm thick) were designed to be bolted to the EDS u-channel support and isolation structure which is located under the shaker unit. A rack and pinion mechanism is mounted to the top of the acrylic frame within a housing block allowing for 0.005 inches per degree of rotation of fine adjustment through the knob.

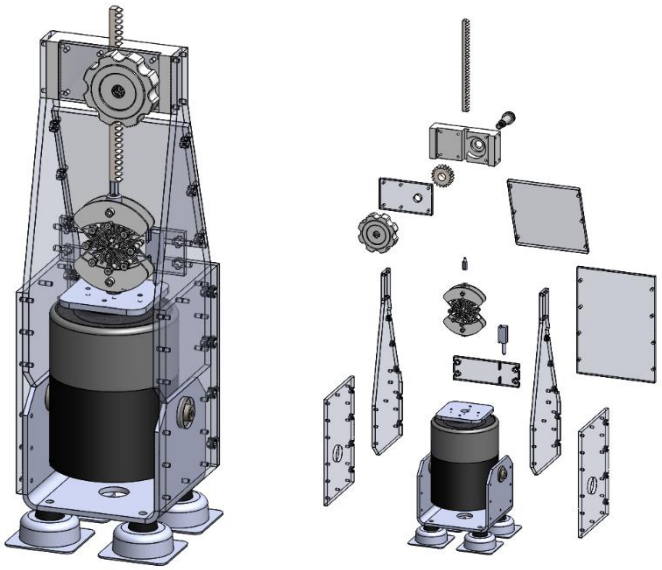

Figure 0.1. Biaxial testing apparatus

A biaxial testing apparatus was custom designed to effectively stretch test coupons equally in both the X and Y directions. This device was intended to be directly mounted to the rack of the fine adjustment mechanism and the platen of the electrodynamic shaker

unit shown in Figure 0.1. The maximum equibiaxial strain the apparatus is designed to transmit to the test sample is 40%. The biaxial apparatus consists of 3 parallel sheets of lasercut 1.5 mm thick Delrin© sheet. The two outermost sheets convert the uniaxial displacement delivered by the EDS into equibiaxial displacement. The symmetric structure of the "cross" effectively performs this task. There are eight shoulder bolts (Ø3 mm) that connect the equibiaxial cross structure to the innermost "snowflake" structure,5 mm long standoffs center the snowflake structure equally between the outer "cross" sheets. The inner geometry of the snowflake converges to a 10 mm square with 16 electrodes with a span of 2.5 mm.

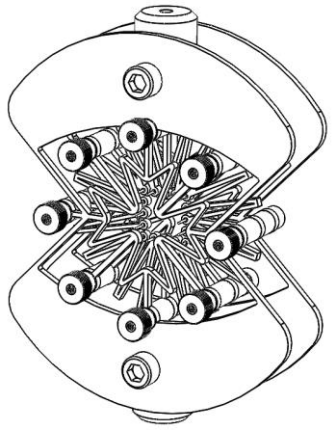

Figure 0.2. Custom built biaxial testing apparatus.

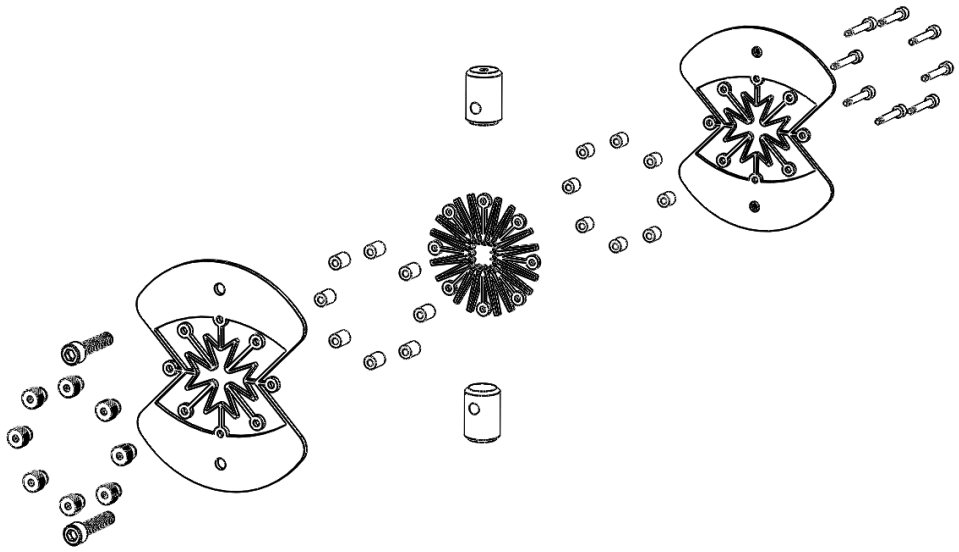

Figure 0.3. Exploded view of custom built biaxial testing apparatus.

In order to load a SFCS blended sample the user must physically press the puncture the scaffold via the electrode pins on the "snowflake" component of the biaxial unit. This puncturing process initiated localized fracture sites at each electrode location with the sample. Upon displacing the biaxial device with a loaded sample, the localized fracture sites within the SFCS sample would propagate along the dynamic path of each of the electrode locations. This loss of mechanical integrity would compromise the electrical response of the SFCS sample. An alternative approach to a controllable input displacement was required.

Biaxial electrode mold

The biaxial electrode mold (Figure 0.4) was manufactured to allow for precise injection of ecoflex:ZnO blends into the desired form to be mounted in the biaxial testing apparatus. This mold is laser cut from 4 separate layers of acrylic and Delrin. The base

layer (Figure 0.4b-(a)) is comprised of acrylic, is 0.250 inches thick and has threaded holes to allow for all other layers to be securely clamped together. Layer (b) is comprised of 1/16 inch Delrin and has hole arrays that correspond to the spans of the electrodes in the biaxial testing apparatus (BTA). Layer (c) is comprised of 1 mm thick Delrin and accounts for the overall volume of the test sample coupon geometry, it also has internal channels to allow for the flow of uncured resin to fill multiple cavities within the mold. Layer (d) is comprised of 1/8 inch thick acrylic and houses the array of mold pins (e) that again correspond to the BTA electrodes spans. The mold pins create the holes in the sample that allow for easy sample mounting in the BTA and are pressed in for a secure and repeatable filling of material.

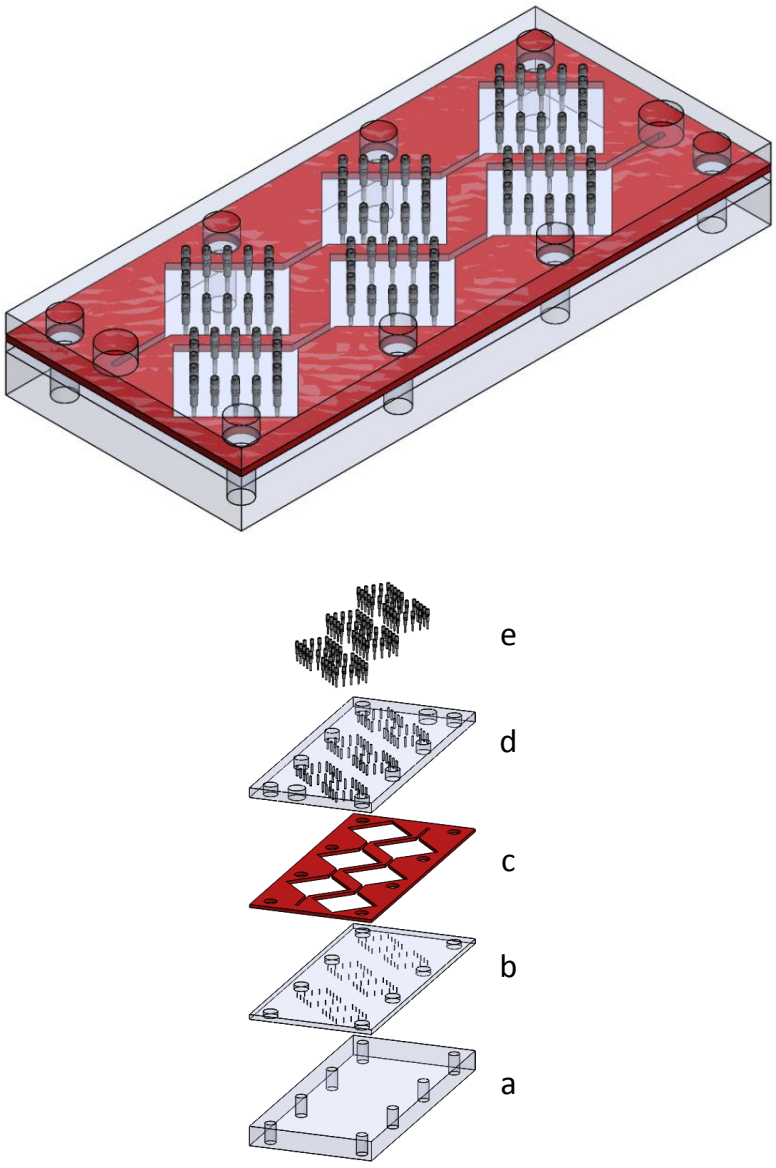

Figure 0.4. a.) CAD rendering of biaxial electrode mold. b.) CAD rendering of test sample

Shear Apparatus

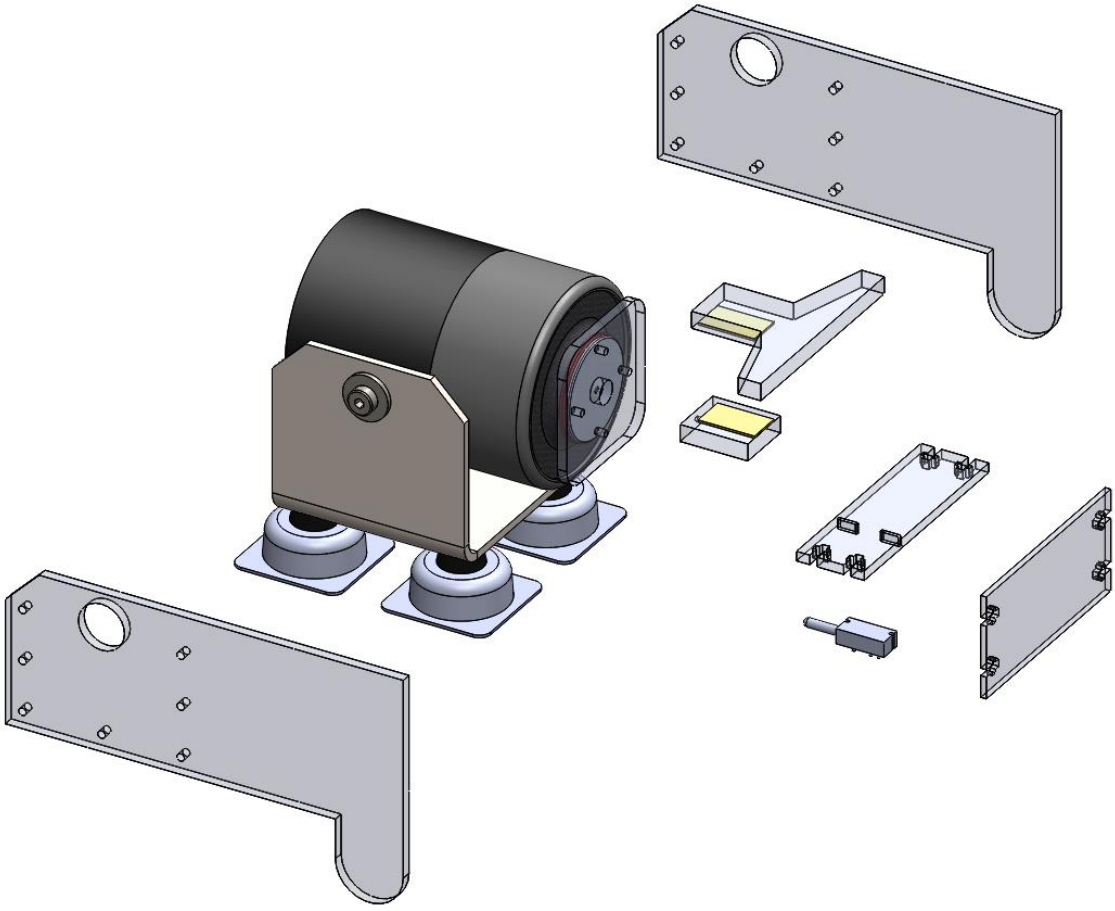

Distensio Apparatus

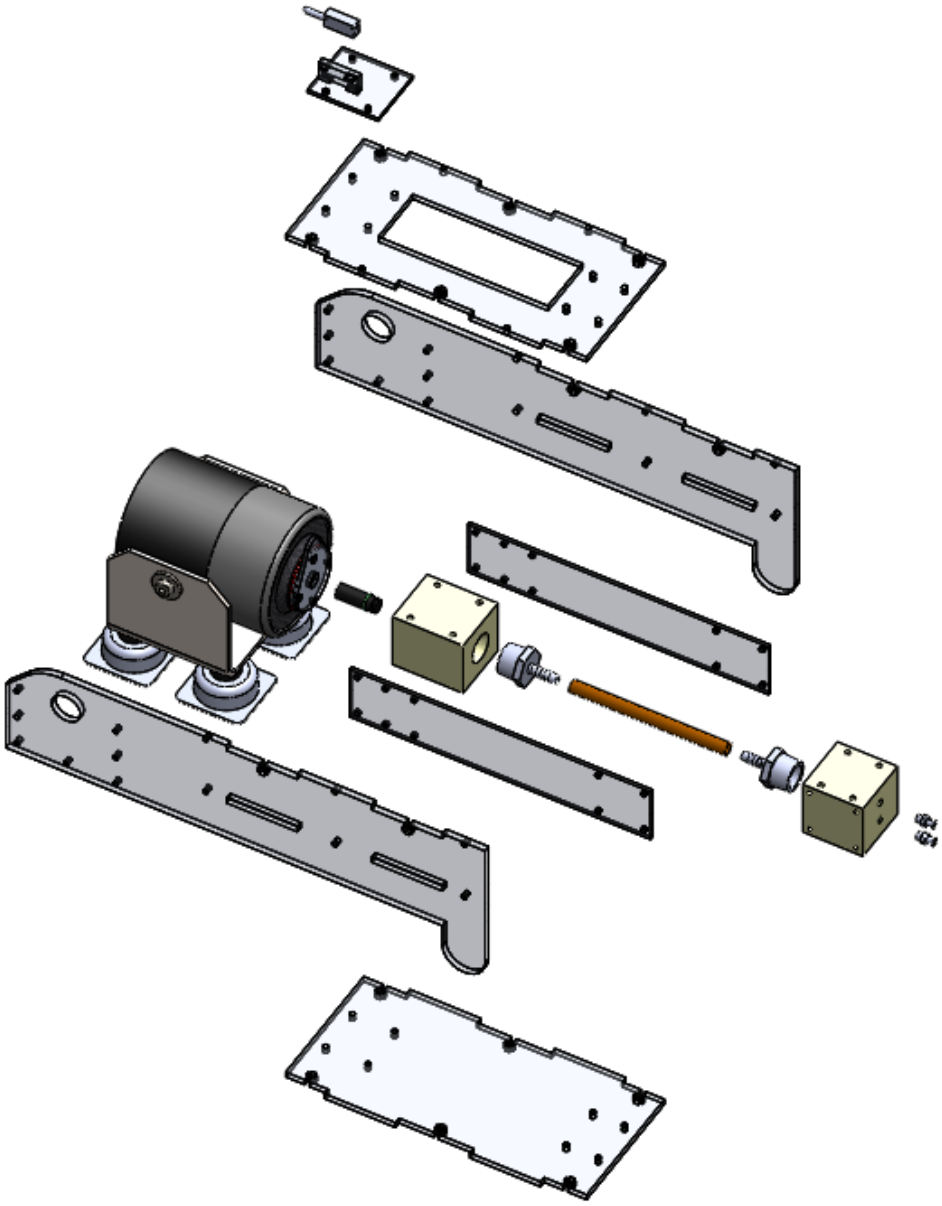

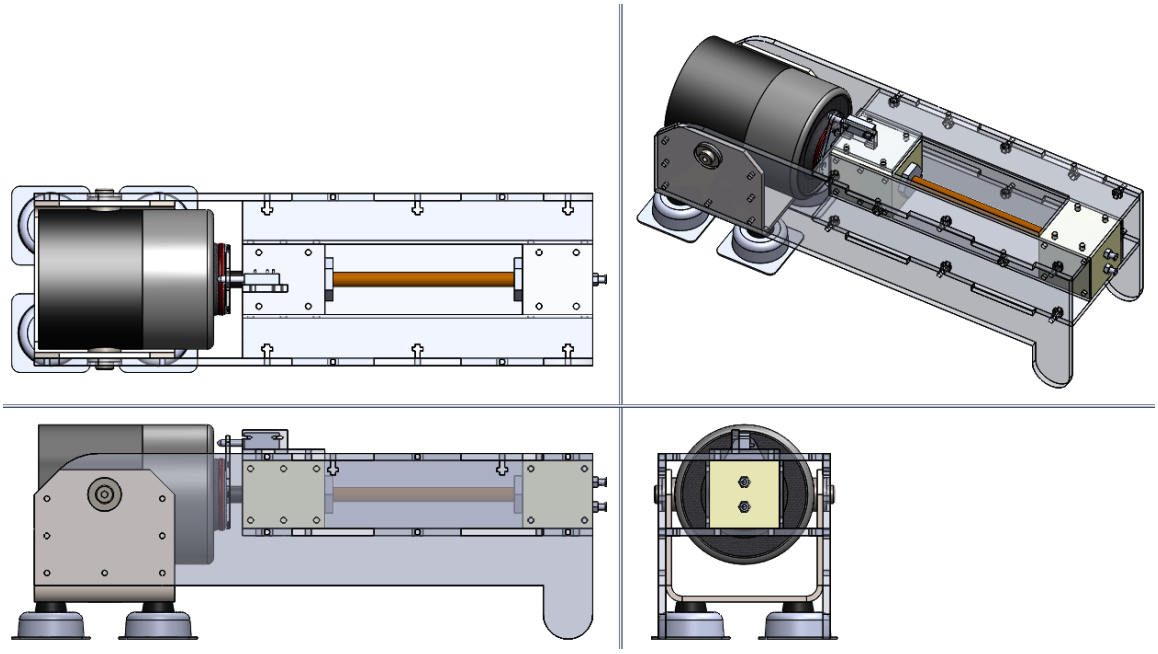

Appendix 2 - Electrical Drawings and Bill of Materials

DIFFERENTIAL AMPLIFIER BOM

Bill of Materials: PCB Design 1.fzz

Assembly List

Label	Part Type	Properties
AD620	IC	pins 8; pin spacing 300mil; chip label IC; package DIP (Dual Inline) [THT]; hole size 1.0mm,0.508mm; true
Bat+	Header 2	package jst-2-pth-ns; variant -jst-2-pth-no_silk
Bat-	Header 2	package jst-2-pth-ns; variant -jst-2-pth-no_silk
C1	Ceramic Capacitor	voltage 20V; capacitance 100nF; package 100 mil [THT, multilayer]; part # IC Cap 1+
C2	Ceramic Capacitor	voltage 20V; capacitance 100nF; package 100 mil [THT, multilayer]; part # IC Cap 1-
C3	Ceramic Capacitor	voltage 20V; capacitance 100nF; package 100 mil [THT, multilayer]; part # IC Cap 2+
C4	Ceramic Capacitor	voltage 20V; capacitance 100nF; package 100 mil [THT, multilayer]; part # IC Cap 2-
C5	Ceramic Capacitor	voltage 20V; capacitance 100nF; package 100 mil [THT, multilayer]; part # FeedbackCap
JP3	Header 2	package screwterminal-3.5mm-2_lock; variant 3.5mm_lock; part # Input Header
JP4	Header 3	package screwterminal-3.5mm-3_lock.007s; variant screw_lock; part # 50k Pot Terminal
JP5	Header 2	package screwterminal-3.5mm-2_lock; variant 3.5mm_lock; part # Output Header
R1	10kΩ Resistor	resistance 10kΩ; bands 4; pin spacing 400 mil; package THT; tolerance ±20%
R2	10kΩ Resistor	resistance 10kΩ; bands 4; pin spacing 400 mil; package THT; tolerance ±20%
R3	1kΩ Resistor	resistance 1kΩ; bands 4; pin spacing 400 mil; package THT; tolerance ±20%
R6	220Ω Resistor	resistance 220Ω; bands 4; pin spacing 400 mil; package THT; tolerance ±20%
R7	220Ω Resistor	resistance 220Ω; bands 4; pin spacing 400 mil; package THT; tolerance ±20%
R8	200kΩ Resistor	resistance 200kΩ; bands 4; pin spacing 400 mil; package THT; tolerance ±20%
R9	100Ω Resistor	resistance 100Ω; bands 4; pin spacing 400 mil; package THT; tolerance ±20%
R10	1MΩ Resistor	resistance 1MΩ; bands 4; pin spacing 400 mil; package THT; tolerance ±20%
R11	100kΩ Resistor	resistance 100kΩ; bands 4; pin spacing 400 mil; package THT; tolerance ±20%
R12	10kΩ Resistor	resistance 10kΩ; bands 4; pin spacing 400 mil; package THT; tolerance ±20%
R13	1kΩ Resistor	resistance 1kΩ; bands 4; pin spacing 400 mil; package THT; tolerance ±20%
SW2	DIP SWITCH	package dipswitch-02; channels 1
SW3	DIP SWITCH	package dipswitch-02; channels 1
SW4	DIP SWITCH	package dipswitch-02; channels 1
U1	OP37	OP37 - Low Noise, Precision, High Speed Op Amp part # OP37

Low Cost Low Power Instrumentation Amplifier

AD620

FEATURES

Easy to use
- Gain set with one external resistor (Gain range 1 to 10,000)
- Wide power supply range (±2.3 V to ±18 V)
- Higher performance than 3 op amp IA designs
- Available in 8-lead DIP and SOIC packaging
- Low power, 1.3 mA max supply current

Excellent dc performance (B grade)
- 50 µV max, input offset voltage
- 0.6 µV/°C max, input offset drift
- 1.0 nA max, input bias current
- 100 dB min common-mode rejection ratio (G = 10)

Low noise
- 9 nV/√Hz @ 1 kHz, input voltage noise
- 0.28 µV p-p noise (0.1 Hz to 10 Hz)

Excellent ac specifications
- 120 kHz bandwidth (G = 100)
- 15 µs settling time to 0.01%

APPLICATIONS

Weigh scales
ECG and medical instrumentation
Transducer interface
Data acquisition systems
Industrial process controls
Battery-powered and portable equipment

CONNECTION DIAGRAM

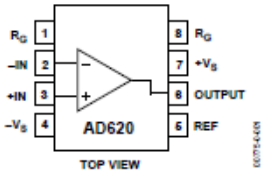

Figure 1. 8-Lead PDIP (N), CERDIP (Q), and SOIC (R) Packages

PRODUCT DESCRIPTION

The AD620 is a low cost, high accuracy instrumentation amplifier that requires only one external resistor to set gains of 1 to 10,000. Furthermore, the AD620 features 8-lead SOIC and DIP packaging that is smaller than discrete designs and offers lower power (only 1.3 mA max supply current), making it a good fit for battery-powered, portable (or remote) applications.

The AD620, with its high accuracy of 40 ppm maximum nonlinearity, low offset voltage of 50 µV max, and offset drift of 0.6 µV/°C max, is ideal for use in precision data acquisition systems, such as weigh scales and transducer interfaces. Furthermore, the low noise, low input bias current, and low power of the AD620 make it well suited for medical applications, such as ECG and noninvasive blood pressure monitors.

The low input bias current of 1.0 nA max is made possible with the use of Superβeta processing in the input stage. The AD620 works well as a preamplifier due to its low input voltage noise of 9 nV/√Hz at 1 kHz, 0.28 µV p-p in the 0.1 Hz to 10 Hz band, and 0.1 pA/√Hz input current noise. Also, the AD620 is well suited for multiplexed applications with its settling time of 15 µs to 0.01%, and its cost is low enough to enable designs with one in-amp per channel.

Table 1. Next Generation Upgrades for AD620

Part	Comment
AD8221	Better specs at lower price
AD8222	Dual channel or differential out
AD8226	Low power, wide input range
AD8220	JFET input
AD8228	Best gain accuracy
AD8295	+2 precision op amps or differential out
AD8429	Ultra low noise

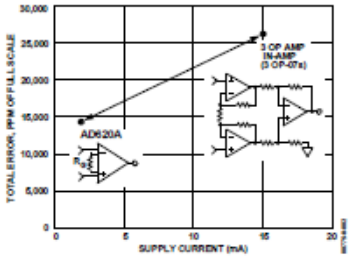

Figure 2. Three Op Amp IA Designs vs. AD620

Rev. H
Information furnished by Analog Devices is believed to be accurate and reliable. However, no responsibility is assumed by Analog Devices for its use, nor for any infringements of patents or other rights of third parties that may result from its use. Specifications subject to change without notice. No license is granted by implication or otherwise under any patent or patent rights of Analog Devices. Trademarks and registered trademarks are the property of their respective owners.

One Technology Way, P.O. Box 9106, Norwood, MA 02062-9106, U.S.A.
Tel: 781.329.4700 www.analog.com
Fax: 781.326.8703© 2003–2011 Analog Devices, Inc. All rights reserved.

- B Grade Is 100% Tested for Noise
  30 nV/√Hz Max at f = 10 Hz
  12 nV/√Hz Max at f = 1 kHz
- Low Input Offset Voltage . . . 500 μV Max
- Excellent Offset Voltage Stability With Temperature . . . 0.5 μV/°C Typ
- Rail-to-Rail Output Swing
- Low Input Bias Current
  1 pA Typ at T_A = 25°C
- Common-Mode Input Voltage Range Includes the Negative Rail
- Fully Specified For Both Single-Supply and Split-Supply Operation

description

The TLC220x, TLC220xA, TLC220xB, and TLC220xY are precision, low-noise operational amplifiers using Texas Instruments Advanced LinCMOS™ process. These devices combine the noise performance of the lowest-noise JFET amplifiers with the dc precision available previously only in bipolar amplifiers. The Advanced LinCMOS™ process uses silicon-gate technology to obtain input offset voltage stability with temperature and time that far exceeds that obtainable using metal-gate technology. In addition, this technology makes possible input impedance levels that meet or exceed levels offered by top-gate JFET and expensive dielectric-isolated devices.

The combination of excellent DC and noise performance with a common-mode input voltage range that includes the negative rail makes these devices an ideal choice for high-impedance, low-level signal-conditioning applications in either single-supply or split-supply configurations.

TYPICAL EQUIVALENT
INPUT NOISE VOLTAGE
vs
FREQUENCY

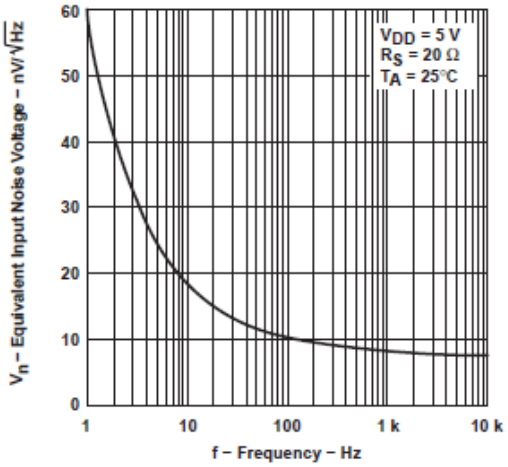

The device inputs and outputs are designed to withstand −100-mA surge currents without sustaining latch-up. In addition, internal ESD-protection circuits prevent functional failures at voltages up to 2000 V as tested under MIL-PRF-38535, Method 3015.2; however, care should be exercised in handling these devices as exposure to ESD may result in degradation of the parametric performance.

The C-suffix devices are characterized for operation from 0°C to 70°C. The I-suffix devices are characterized for operation from −40°C to 85°C. The M-suffix devices are characterized for operation over the full military temperature range of −55°C to 125°C.

Please be aware that an important notice concerning availability, standard warranty, and use in critical applications of Texas Instruments semiconductor products and disclaimers thereto appears at the end of this data sheet.

Advanced LinCMOS is a trademark of Texas Instruments Incorporated. All other trademarks are the property of their respective owners.

PRODUCTION DATA information is current as of publication date. Products conform to specifications per the terms of Texas Instruments standard warranty. Production processing does not necessarily include testing of all parameters.

Copyright © 1997–2008, Texas Instruments Incorporated

On products compliant to MIL-PRF-38535, all parameters are tested unless otherwise noted. On all other products, production processing does not necessarily include testing of all parameters.

Appendix 3 - Program Algorithms and Code

MATLAB PLOTTING SCRIPT

```
%%  SELECTING MULTIPLE FILE DIRECTORY


s = dir(*.txt');

%s = dir(*.txt');


names = {s.name};

nr = 5;  % # of rows

nc = 5;  % # of columns

mat = zeros(nr,nc);


for n = 1:numel(names)

    data = dlmread([‘’\' names{n}]);

    %data = dlmread([" names{n}]);   %for lab PC


%%  FILE INPUT


%dataname = '15APR2015-2-ZNO%-200-NM-ECO--S1-R1-6.txt';

%data = dlmread(dataname);

%timename = 'SAMPLE-RATE-100KP.txt';

%time = dlmread(timename);


response = data(:,1);
```

```
input = data(:,2);

%% STRING MANIPULATION FOR FILE SAVING

path = '';
filename1 = strrep(names{n},'.txt','');
filename2 = '_PLOT1';
filename3 = '_PLOT2';
filename4 = '_PLOT3';
filename5 = '_PLOT4';
filename6 = '_PLOT5';
filename7 = '_PLOT6';
filename8 = '_PLOT7';

%%  TIME DATA

numpoints = length(response);
rate = 5000;
time = (numpoints/rate)-(1/rate);
t = transpose(0:1/rate:time);
x = transpose(0:1:numpoints-1);
xx = numpoints;

%%  PLOT 1
```

```
f1 = figure;
subplot(2,1,1);
plot(x,response,'Color','r','LineWidth',1)
ylabel 'Voltage (V)', xlabel 'Time (s)'
title 'Signal Response',
axis([0 xx -1.0 1.0])
subplot(2,1,2);
plot(x,input,'Color','b','LineWidth',1)
ylabel 'Displacement (in)', xlabel 'Time (s)'
title 'Input Signal',
axis([0 xx .28 0.37])

fig1 = strcat(filename1,filename2,'.fig');
jpg1 = strcat(filename1,filename2,'.jpg');
saveas(f1,fig1);
saveas(f1,jpg1);

close
end
```

MATLAB PEAK TO PEAK DETECTION AND ANALYSIS

```
%%  SELECTING MULTIPLE FILE DIRECTORY


s = dir(*.txt');

names = {s.name};


all_data = [];

for n = 1:numel(names)

data=designfilt('highpassiir','FilterOrder',8,'PassbandFrequency',0.45,'PassbandRipple',0.2
,'SampleRate',2000);


buttfilter = filtfilt(hpFilt,response);


%%  PEAK 2 PEAK HEIGHT


FQ1 = peak2peak(buttfilter(10000:30000));      %PEAK TO PEAK MEASUREMENT
OF INNER 50% OF SINGLE AT 0.6 HZ

FQ2 = peak2peak(buttfilter(37000:47000));      %PEAK TO PEAK MEASUREMENT
OF INNER 50% OF SINGLE AT 1.2 HZ

FQ3 = peak2peak(buttfilter(52000:59000));      %PEAK TO PEAK MEASUREMENT
OF INNER 50% OF SINGLE AT 2.4 HZ


F = [FQ1;FQ2;FQ3];

all_data(n).data = F;


end
```

```
FF = struct2cell(all_data);
FFF = cell2mat(FF);
dlmwrite(',','\t')
```

DISTENSION DATA SCRIPT

```
%%  SELECTING MULTIPLE FILE DIRECTORY
s = dir(*.txt');

names = {s.name};
for n = 1:numel(names)
   data = dlmread([" names{n}]);

%%  FILE INPUT

%dataname = '15APR2015-2-ZNO%-200-NM-ECO--S1-R1-3.txt';
%data = dlmread(dataname);
%timename = 'SAMPLE-RATE-100KP.txt';
%time = dlmread(timename);

response = data(:,3);
pressure = data(:,2);
input = data(:,1);

%% STRING MANIPULATION FOR FILE SAVING
```

```
filename1 = strrep(names{n},'.txt','');

%%  TIME DATA

numpoints = length(response);
rate = 2000;
time = (numpoints/rate)-(1/rate);
t = transpose(0:1/rate:time);
x = transpose(0:1:numpoints-1);
xx = numpoints - 1;

%%  PLOT 1

figure
% subplot(2,1,1);
% plot(x,response,'Color','r','LineWidth',2)
% ylabel 'Voltage (V)', xlabel 'Time (s)'
% title 'Signal Response',
% axis([0 xx -5 0])
% subplot(2,1,2);
% plot(x,input,'Color','b','LineWidth',2)
% ylabel 'Displacement (in)', xlabel 'Time (s)'
% title 'Input Signal',
% axis([0 xx 0.06 0.1])
```

```
% axis([0 xx -5.0 5.0])

%%  FILTERING 60 HZ NOISE

hpFilt = designfilt('highpassiir','FilterOrder',8, ...
        'PassbandFrequency',0.45,'PassbandRipple',0.2, ...
        'SampleRate',2000);

buttfilter = filtfilt(hpFilt,response);
buttfilterP = filtfilt(hpFilt,pressure);

% plot(buttfilterP,buttfilter,'Color','r','LineWidth',.5)
% ylabel 'Voltage (V)', xlabel 'Time (s)'
% title 'SFCS Response',

% PLOT #2
figure
plot(x,response,x,buttfilter)
ylabel 'Voltage (V)', xlabel 'Time (s)'
title 'Unfiltered vs. Filtered', legend('Unfiltered','Filtered')
% axis([0 xx -0.5 0.5])

figure
plot(x,pressure,x,buttfilterP)
```

```
ylabel 'Voltage (V)', xlabel 'Time (s)'
title 'Unfiltered vs. Filtered', legend('Unfiltered','Filtered')


%PLOT #4
% f1 = figure(1);
%
% subplot(5,1,1);
% plot(x,input,'Color','b','LineWidth',.5)
% ylabel 'Displacement (in)', xlabel 'Time (s)'
% title 'Shaker Stroke',
% axis([0 xx 0 0.5])
%
% subplot(5,1,3);
% plot(x,pressure,'Color','g','LineWidth',.5)
% ylabel 'Pressure (mmHg)', xlabel 'Time (s)'
% title 'Vessel Pressure',
% axis([0 xx 0 180])
%
% subplot(5,1,5);
% plot(x,buttfilter,'Color','r','LineWidth',.5)
% ylabel 'Voltage (V)', xlabel 'Time (s)'
% title 'SFCS Response',
% axis([0 xx -1.0 1.0])
%
% suptitle(filename1);
```

```
%
% fig1 = strcat(filename1,'.fig');
% jpg1 = strcat(filename1,'.jpg');
% saveas(f1,fig1);
% saveas(f1,jpg1);


%%
% NFFT = 2^nextpow2(numpoints); % Next power of 2 from length of y
% Y = fft(response,NFFT)/numpoints;
% f = rate/2*linspace(0,1,NFFT/2+1);
%
% % Plot single-sided amplitude spectrum.
% plot(f,2*abs(Y(1:NFFT/2+1)))
% title('Single-Sided Amplitude Spectrum of y(t)')
% xlabel('Frequency (Hz)')
% ylabel('|Y(f)|')
% axis([0 3.2 0 .2])


End
```

Appendix 4 – Experimental Data

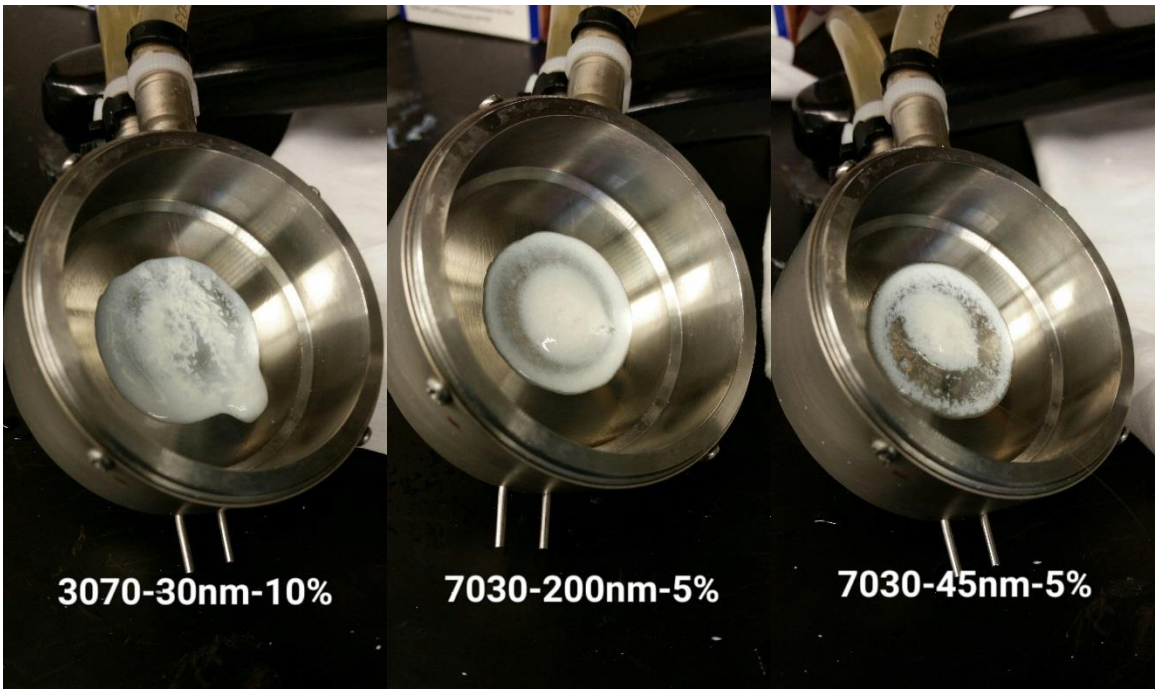

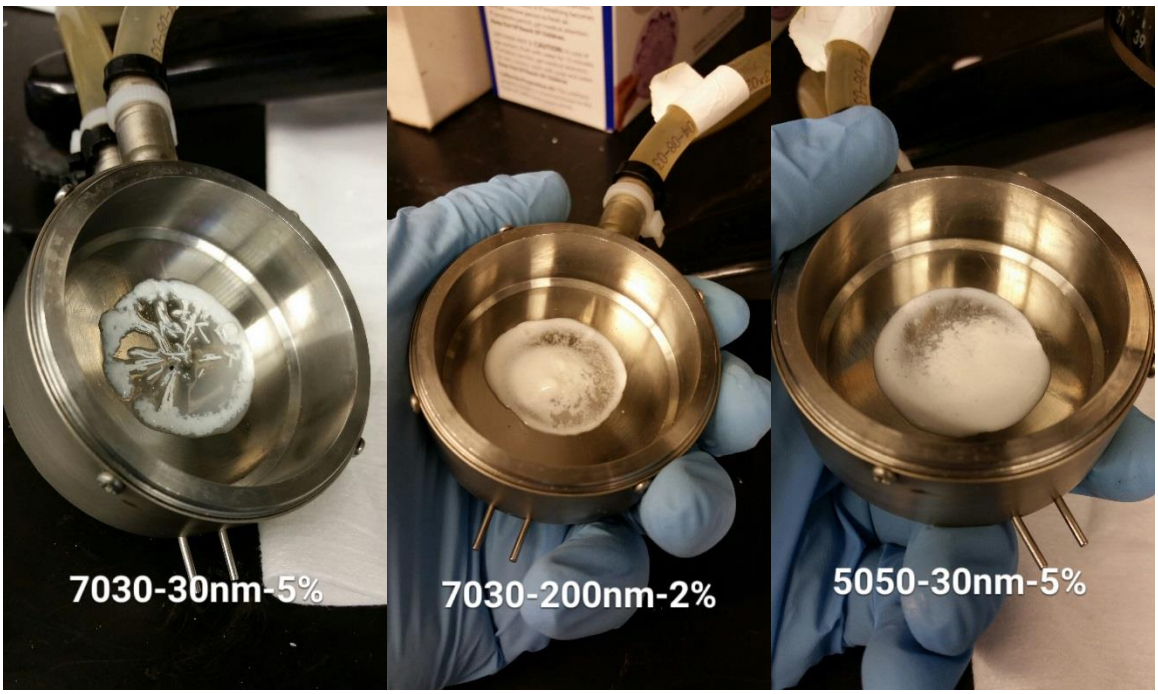


5050-45nm-5%


5050-30nm-10%


5050-45nm-10%


7030-45nm-2%

SEM Imagery

3070 – 30nm – 2%

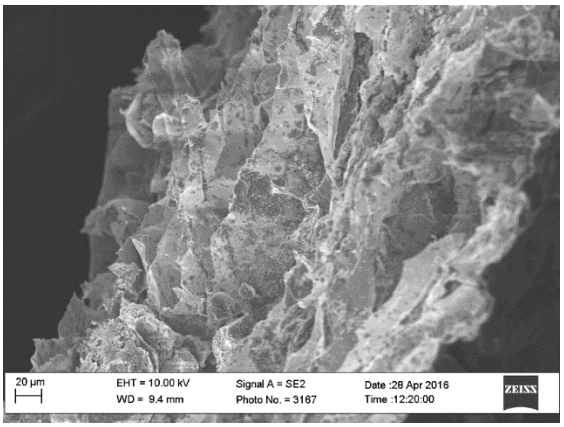

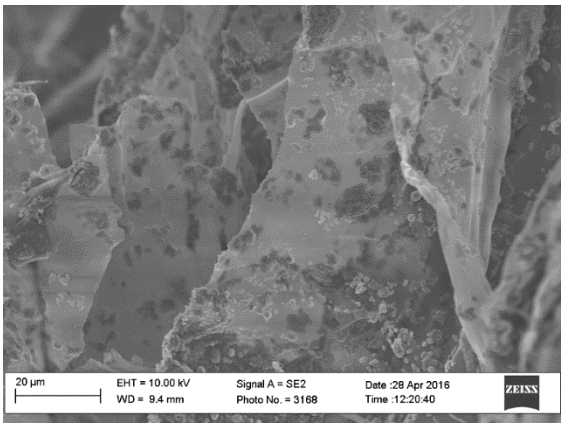

3070 – 30nm – 5%

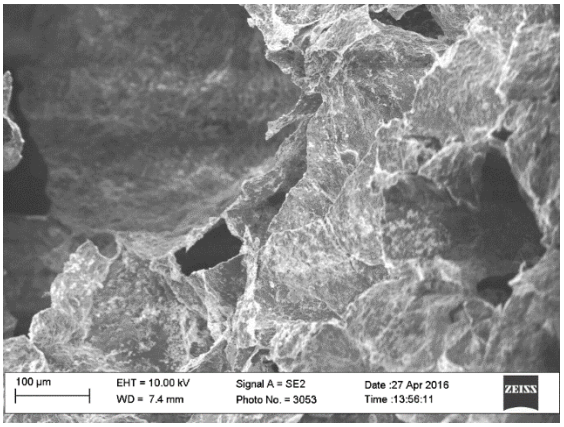

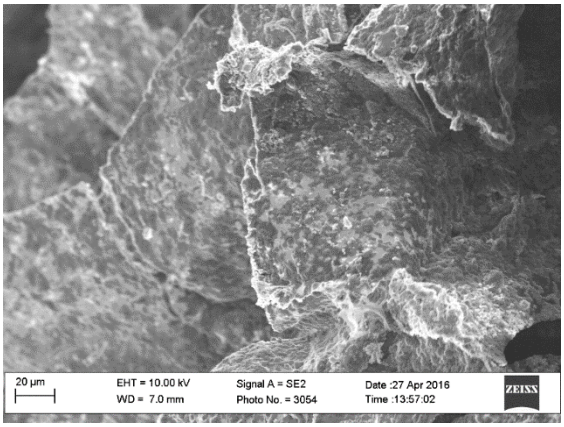

3070 – 30nm – 10%

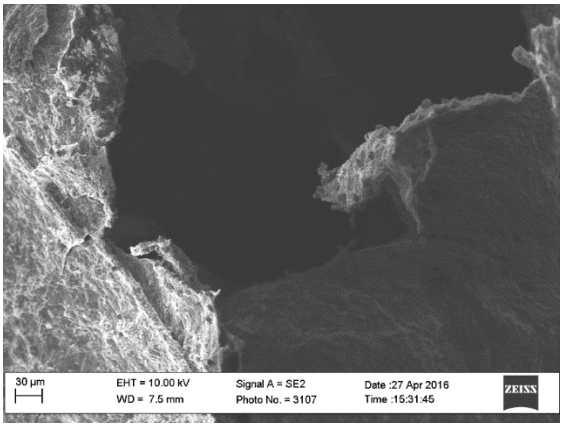

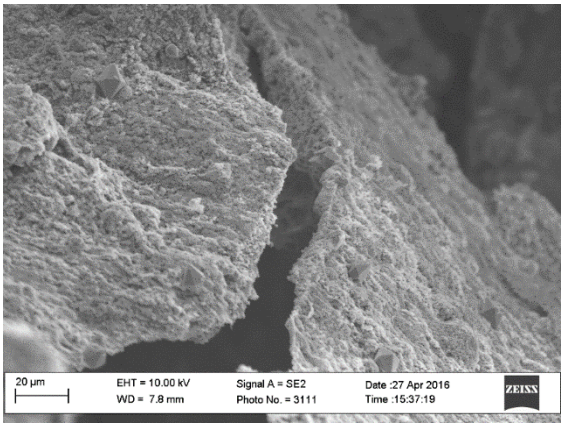

3070 – 200nm – 2%

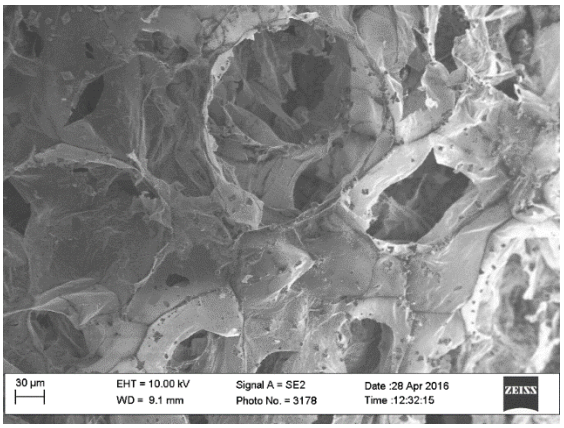

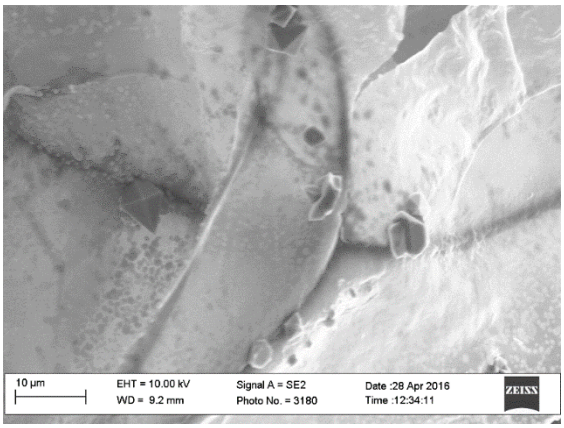

3070 – 200nm – 5%

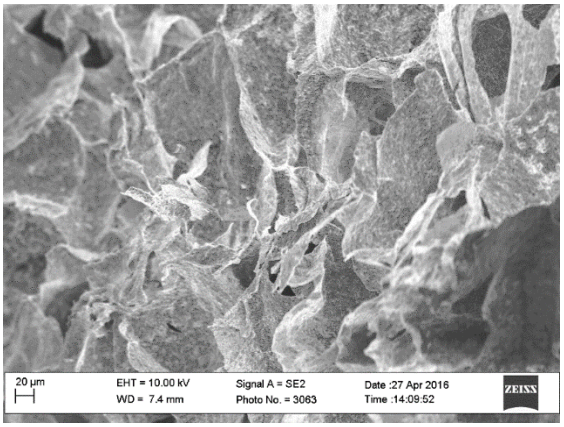

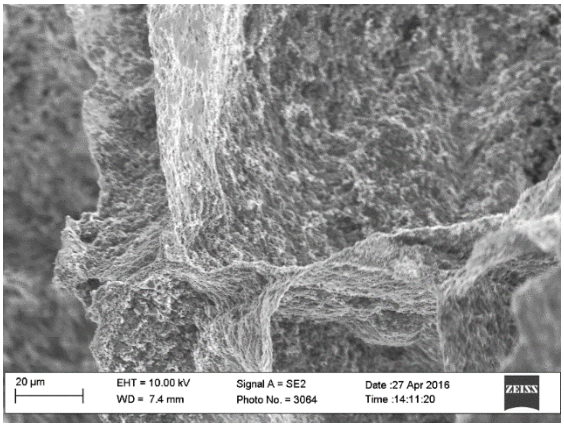

3070 – 200nm – 10%

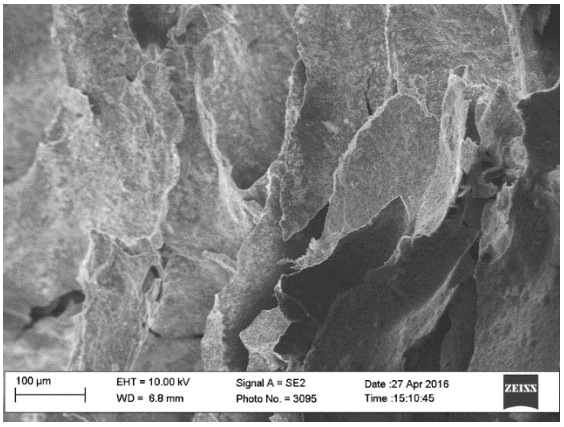

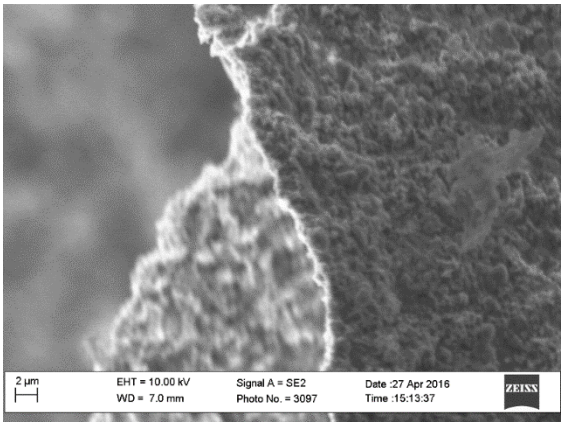

5050 – 30nm – 2%

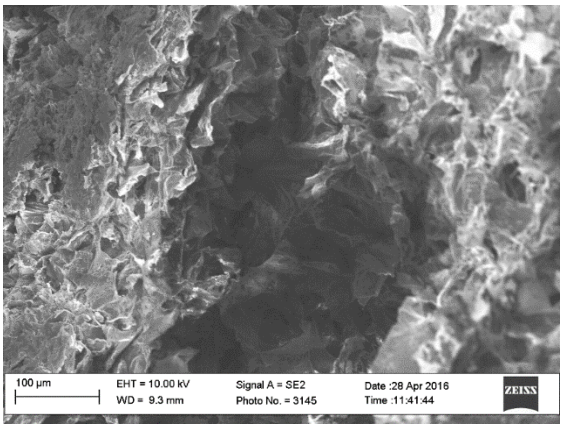

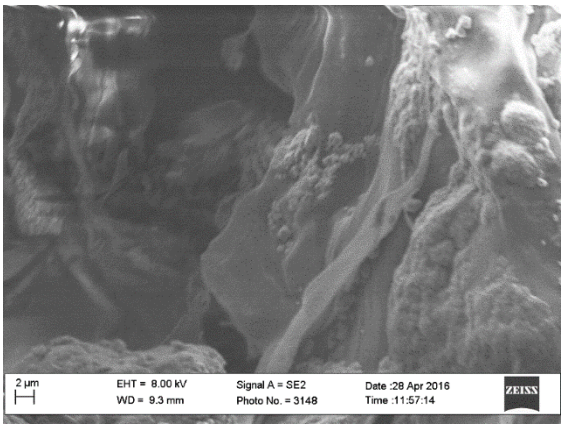

5050 – 30nm – 5%

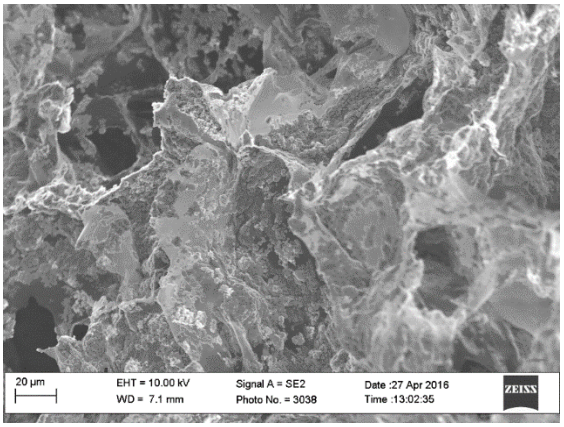

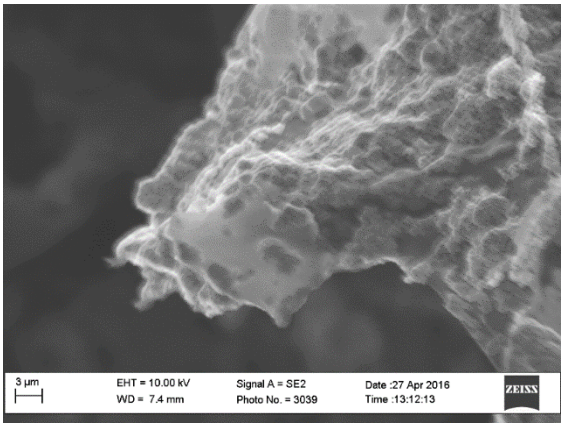

5050 – 30nm – 10%

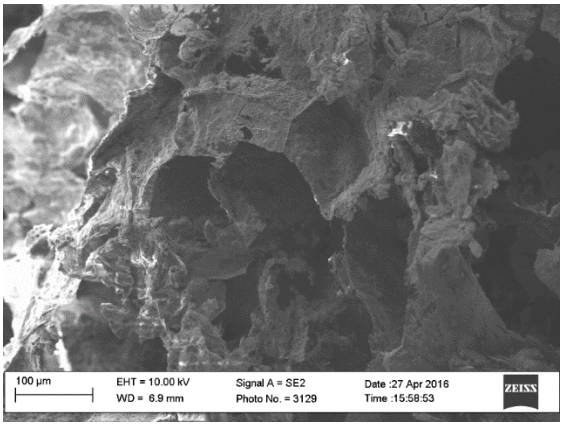

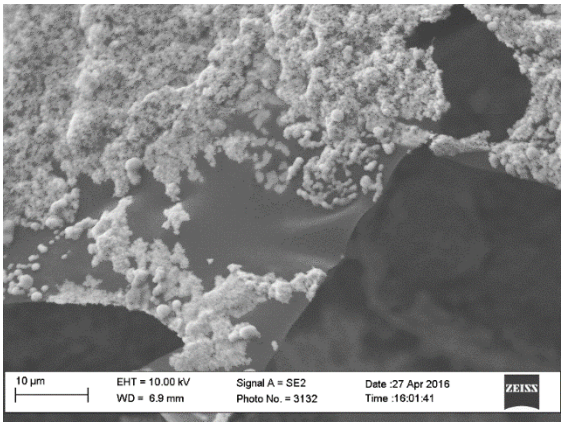

5050 – 45nm – 2%

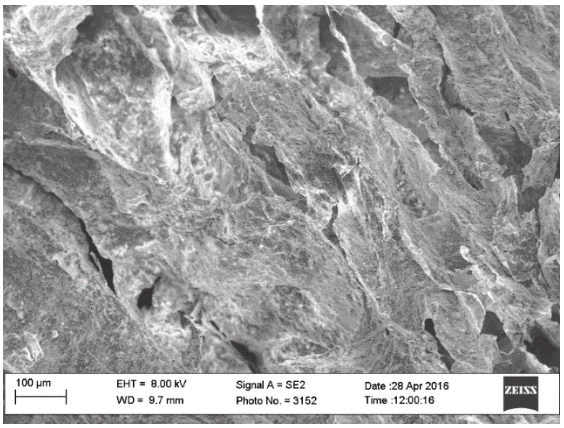

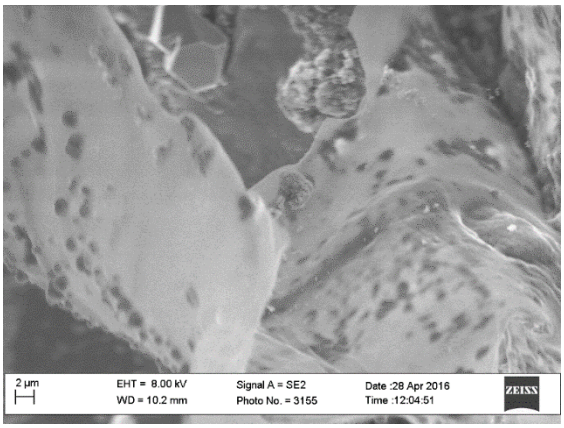

5050 – 45nm – 5%

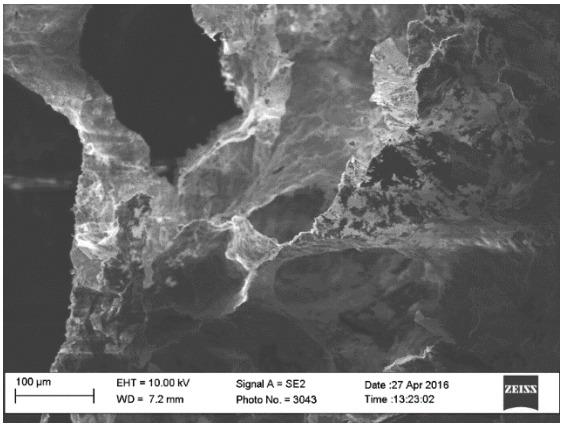

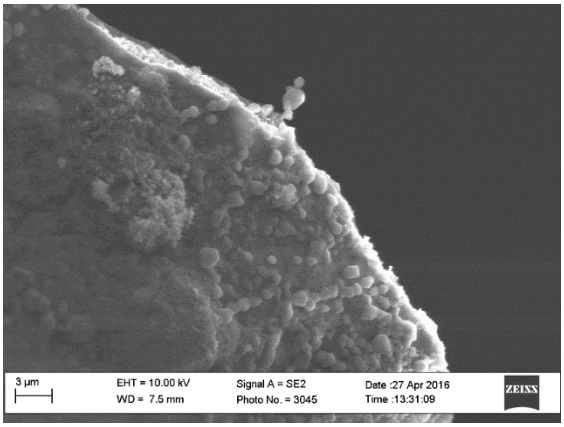

5050 – 45nm – 10%

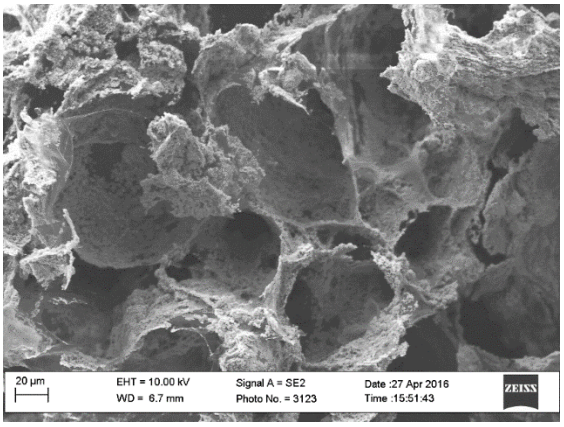

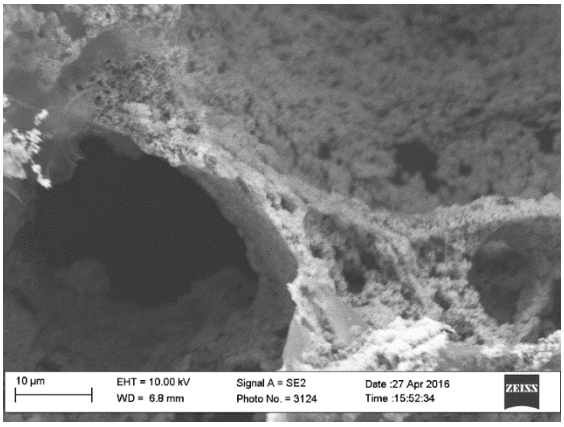

5050 – 200nm – 2%

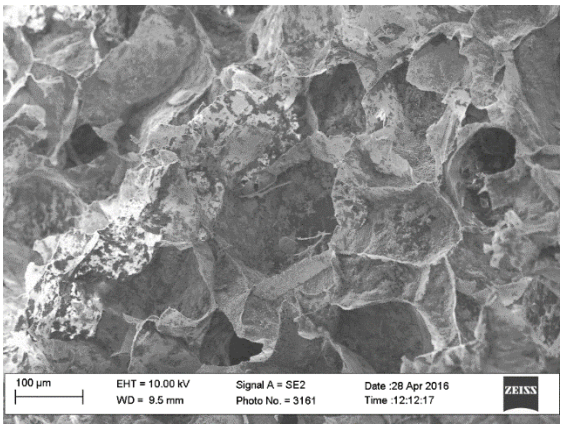

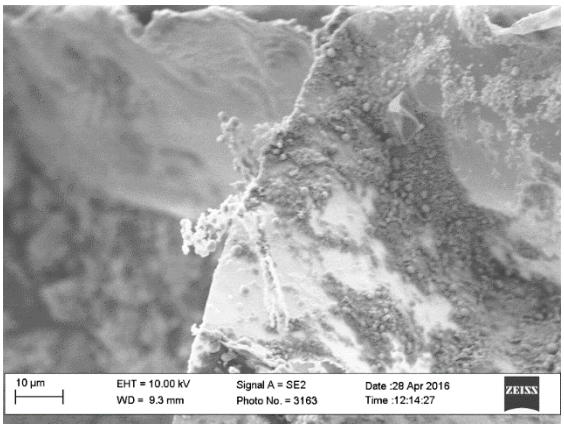

5050 – 200nm – 5%

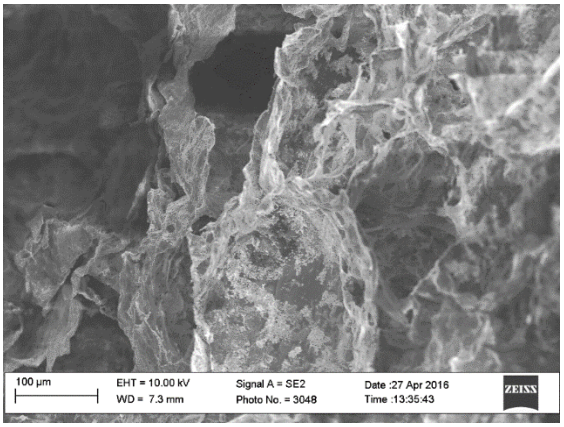

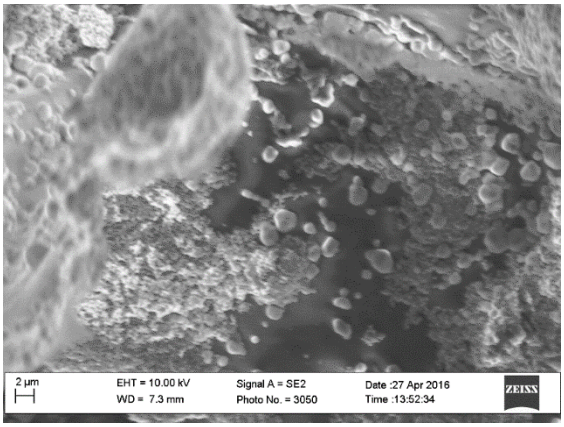

5050 – 200nm – 10%

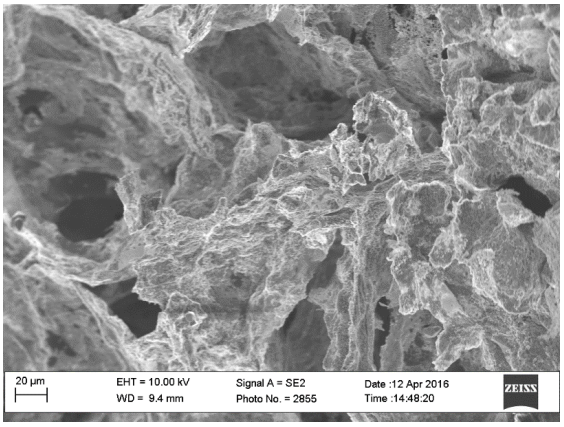

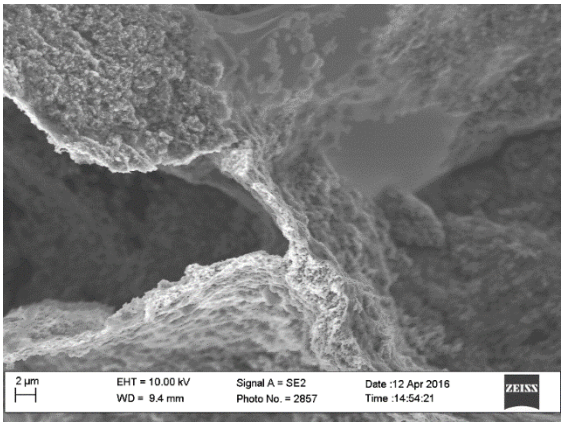

7030 – 30nm – 2%

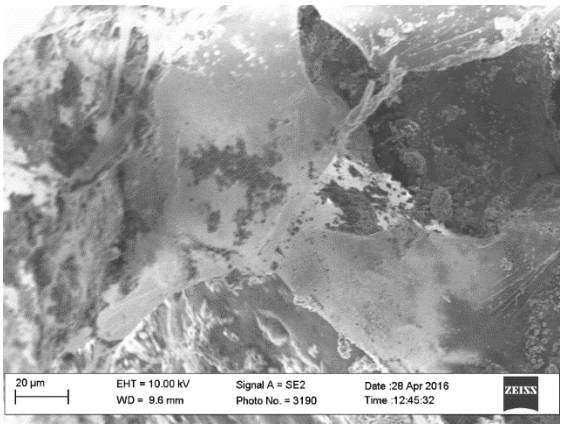

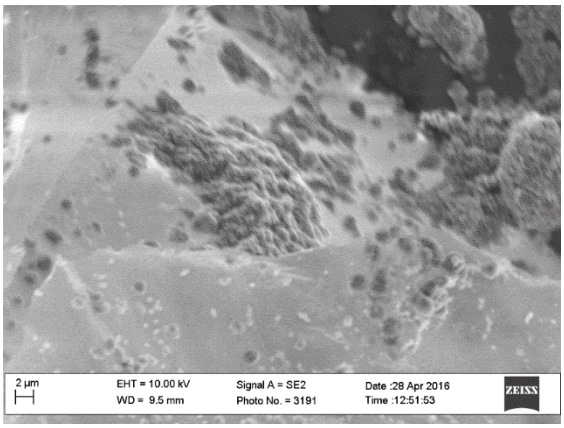

7030 -30nm – 5%

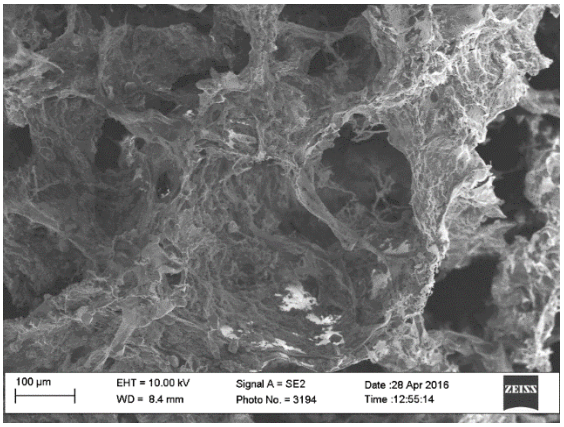

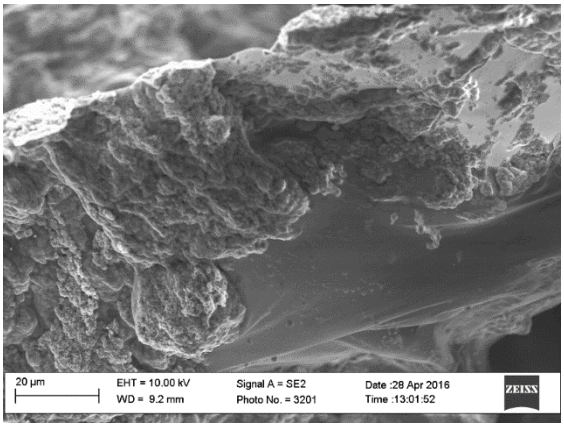

7030 -45nm – 2%

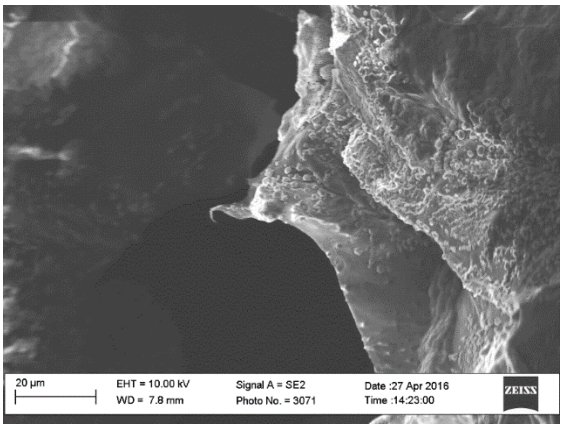

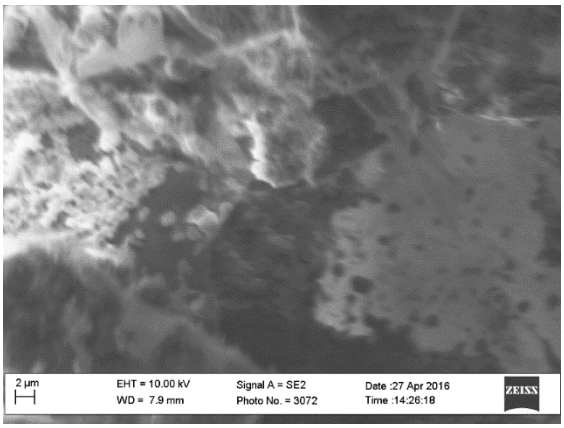

7030 -45nm – 5%

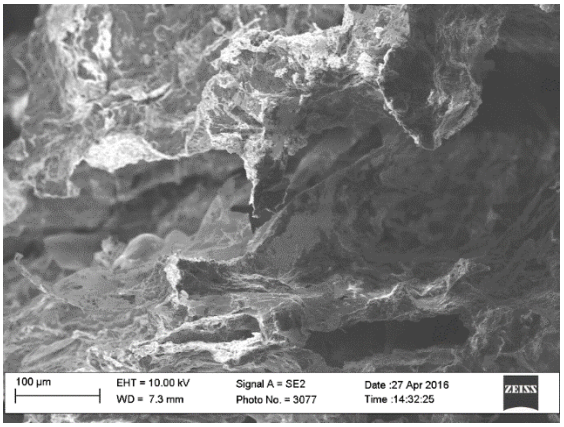

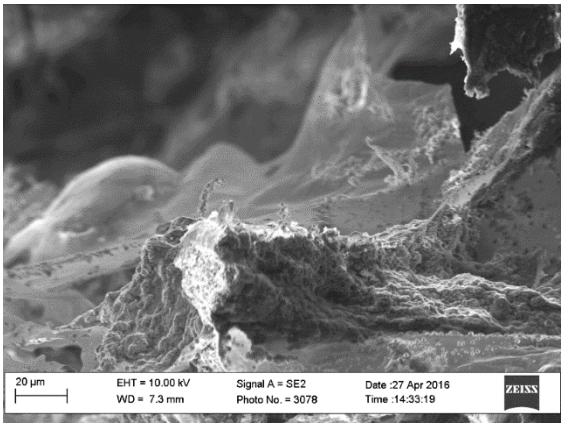

7030 -200nm – 2%

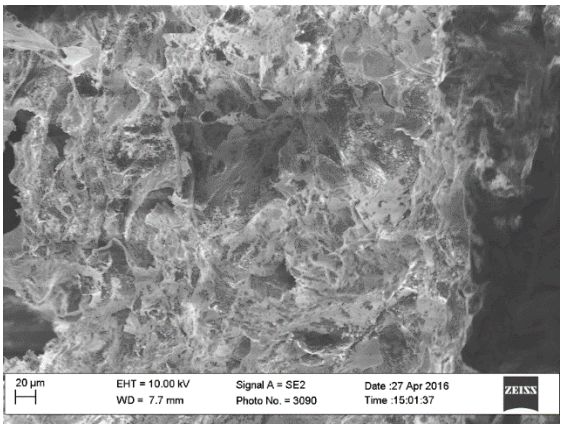

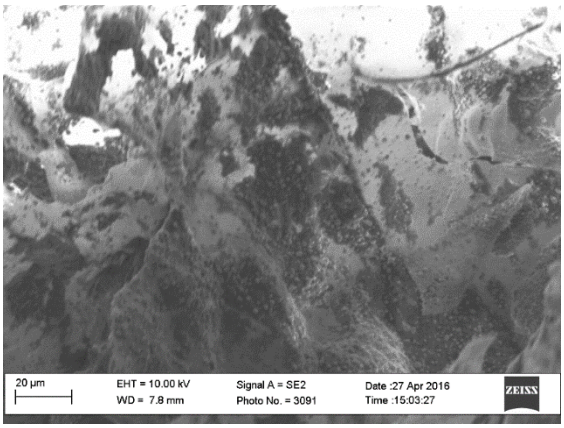

7030 -200nm – 5%

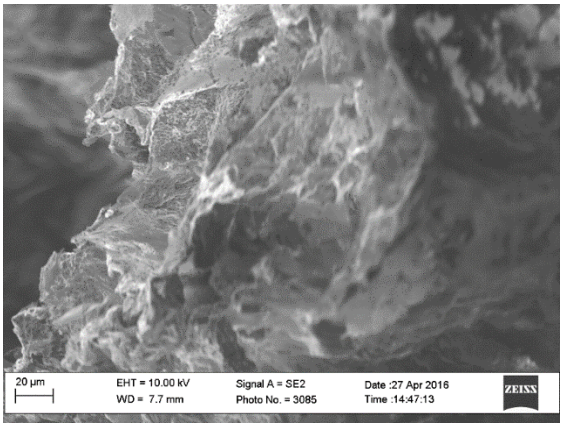

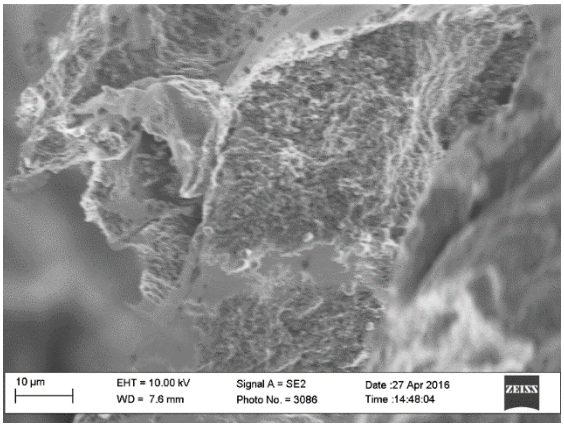

Stress versus strain plot for a single sample of each SFCS-ZnO blend.

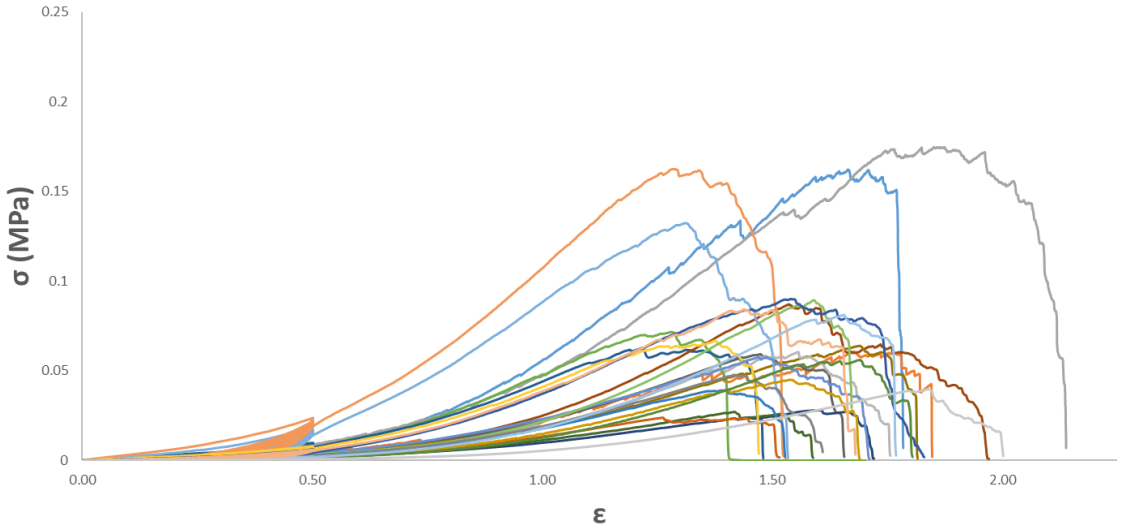

Mechanical Testing of 15 kg porcine descending aortic tissue

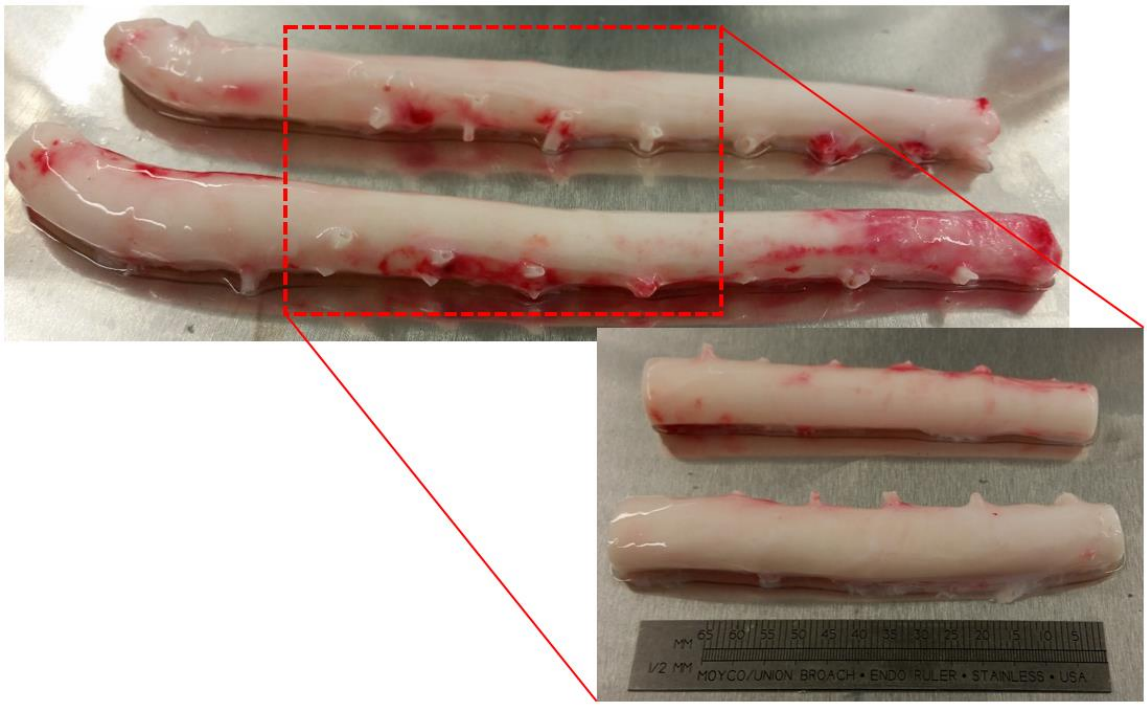

Mechanical Testing of 15 kg porcine descending aortic tissue in tensile tester

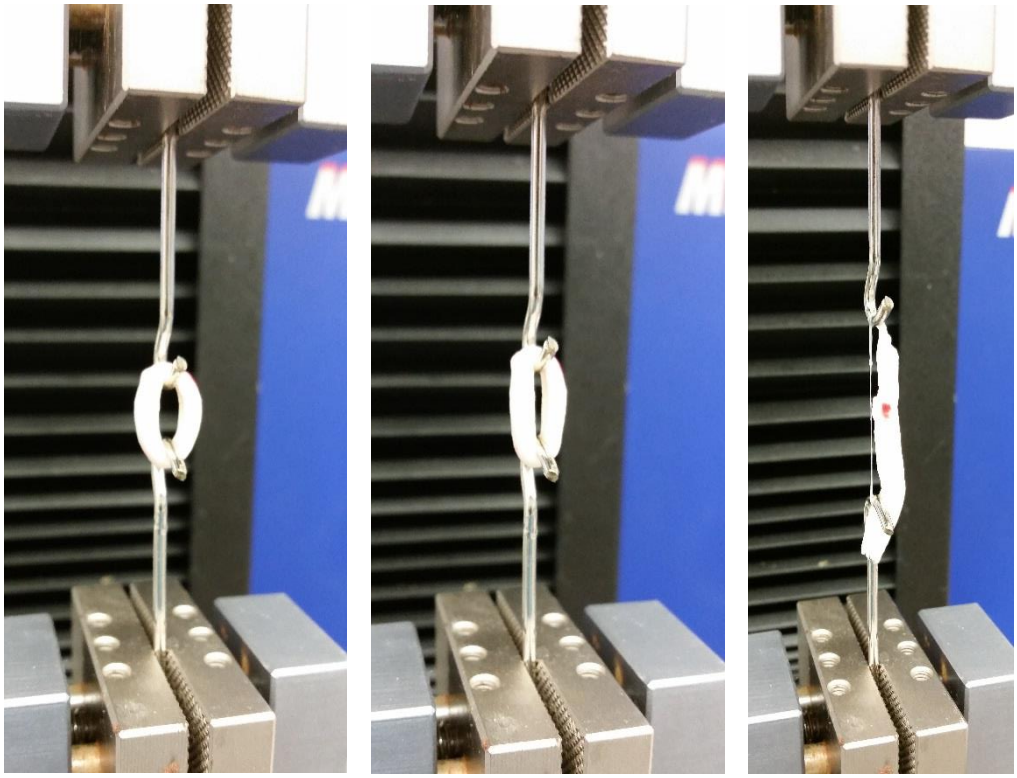

Preconditioning cycle of 15 kg porcine descending aortic tissue

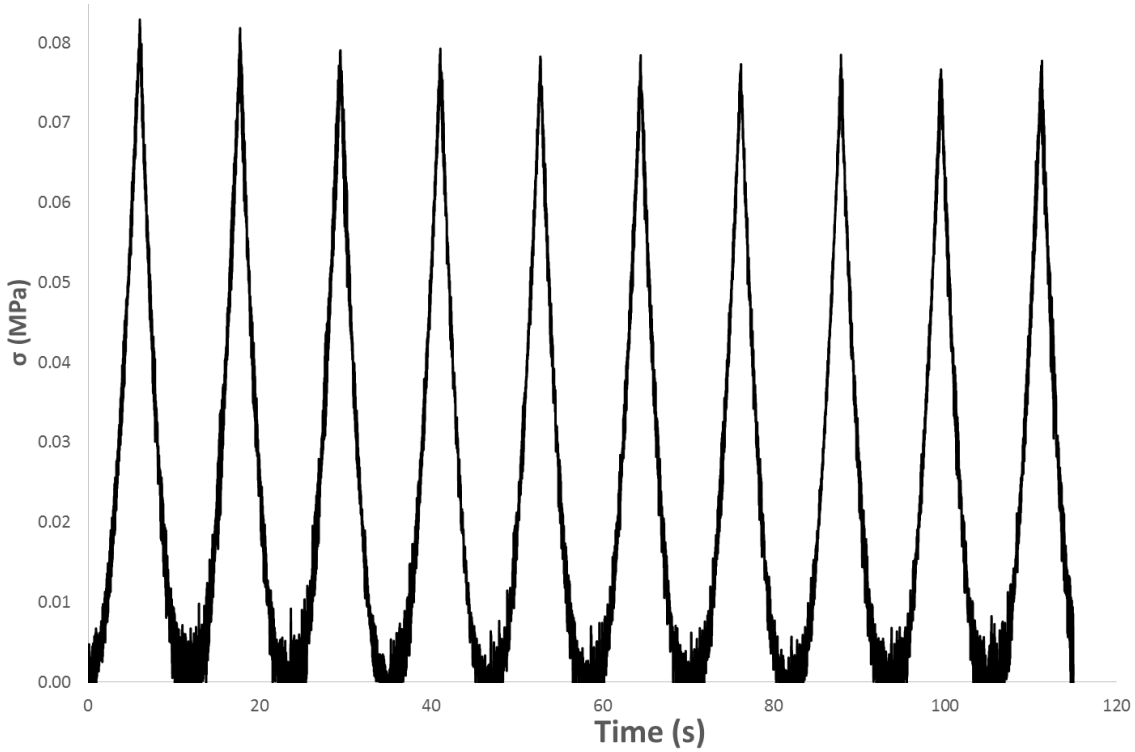

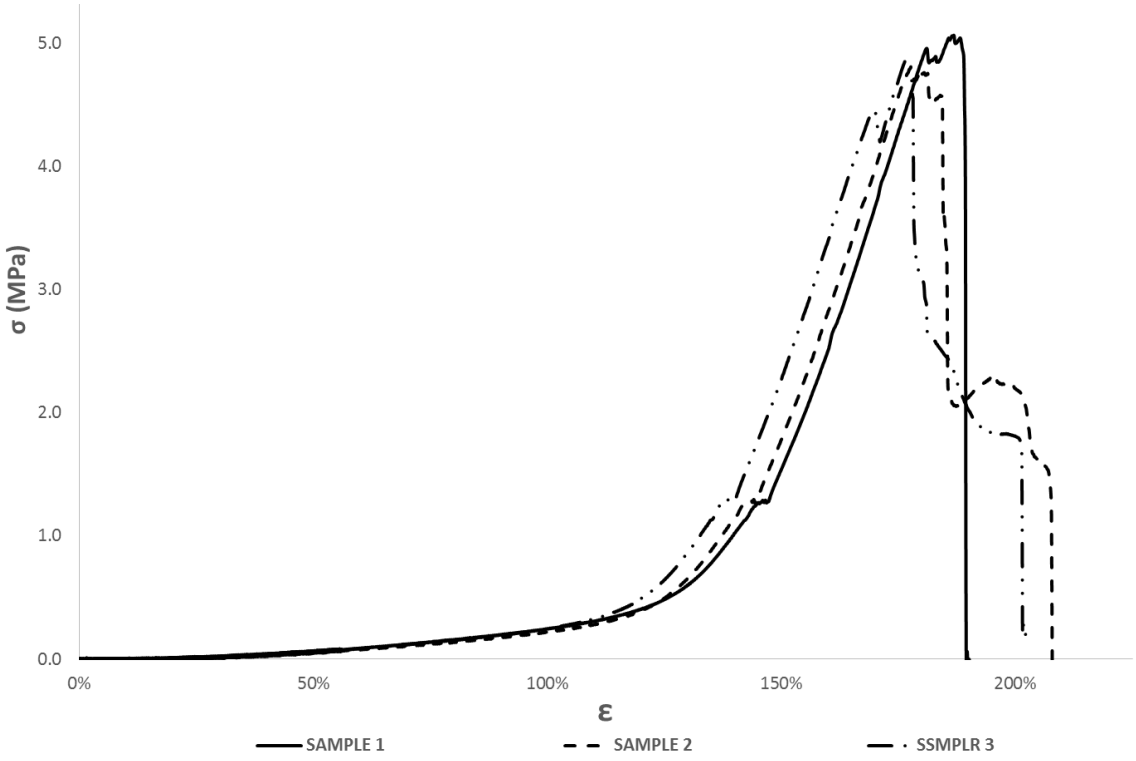

Mechanical Data from 15 kg porcine descending aorta tissue tensile tests.

E	10.878	±	0.3096	**Mpa**
E_{TOE}	0.391	±	0.0344	**Mpa**
σ_{UT}	4.916	±	0.1328	**Mpa**
$\%\varepsilon_{BREAK}$	2.003	±	0.0917	**mm/mm**
σ_{Y}	4.650	±	0.2900	**Mpa**

CURRICULUM VITAE

SCOTT D. CAMBRON

Senior BioMedical Engineer
Advanced Solutions Life Sciences
Louisville, KY 40223
(c) 502-216-3279
sdcamb01@gmail.com

PERSONAL

EDUCATION

1/08 – 5/17 **PhD - Mechanical Engineering** 3.55/4.0
University of Louisville, Louisville, KY
Dissertation Topic: Development and Evaluation of a Biocompatible Electroactive Sensor

- *Concentration* - Tissue Engineering, Microtechnology/Micro-Electro-Mechanical Systems (MEMS), BioMEMS, Material Testing

9/03 – 5/07 **Master of Engineering – Mechanical Engineering** 3.6/4.0
University of Louisville, Louisville, KY
Thesis Topic: Microtacks for Retinal Implant Applications

- *Concentration* – Microtechnology/Micro-Electro-Mechanical Systems (MEMS), BioMEMS, micromanufacturing via ultra-high-precision micromilling machine

8/98 – 8/03 **Bachelor of Science – Mechanical Engineering** 3.1/4.0
University of Louisville, Louisville, KY
Senior Design Project: Design and Fabrication of Baja SAE Chassis

EXPERIENCE

7/16 - Present Advanced Solutions Life Sciences, Louisville, KY
Senior BioMedical Engineer

6/04 – 6/16 Department of Bioengineering, University of Louisville, Louisville, KY
Research Engineer, 6/04-present
Instructor of Record (BE 400), 2014-Present
Instructor (BE581/600), 2014-Present

1/11 - Present VoxMax, LLC
Mechanical Engineer and Co-Founder

7/09 – 12/12 Department of Mechanical Engineering, University of Louisville, Louisville, KY
Instructor of Record (ME 380)

12/07 – 12/13	UltraTrace Detection LLC, Louisville, KY *Lead Mechanical Engineer, Research and Development*
6/99 – 5/04	Department of Mechanical Engineering, University of Louisville, Louisville, KY *Undergraduate/Graduate Research Assistant*
1/00 – 2/01	Samtec, New Albany, IN *Co-op/Intern*
5/98 – 8/98	Independent Stave Cooperage, Lebanon, KY *Plant Maintenance*
10/96 – 5/98	Central Kentucky Tool & Die/Engineering, Lebanon, KY *Machinist*

AFFILIATIONS

Kentucky State Board of Registration for Professional Engineers and Land Surveyors – Registered EIT #12554
ASME #7081557
SAE #6109017846
BMES #2350369

AWARDS AND RECOGNITION

- *1st Place* in the Bioengineering Division B.S. Level Student Paper Competition at the 2003 International Mechanical Engineering Congress and Exposition, 2003
- Certificate of Merit, US Symposium on the Frontiers in Biomechanics, Nashville, TN, 2003
- *1st Place* in the 2004 Speed School of Engineering, Engineers' Days Student Exhibition of Research
- American Chemical Society: Nano Letters, 2004 article was featured in MIT Technology Review (p. 29, Nov. 2004), Chem. and Engineering News (p.24, Sept. 13, 2004), MRS Bulletin (pp. 789-790, Nov. 2004), High Performance Plastics, Veille strategique Instrumentation pour la biologie, and Micro/Nano Newsletter p.8, Jan.2005.

TEACHING AND SCHOLARSHIP OF TEACHING

Courses Taught

Undergraduate Level Courses

Computer Aided Design (ME 380)

- 10 overall classes taught between Fall ’09 and Fall ‘12 with average student evaluation score of **4.07**/5.00

Bioengineering Computer Aided Design and Manufacturing (BE 400)

- Student evaluation score of **4.50**/5.00

Bioengineering Senior Project Design (BE 497) – Group/Project Mentor

Mechanical Engineering Capstone Design Project (ME 497) – Group/Project Mentor

Introduction to Bioengineering Design (BE 101) – Invited Lecturer

Graduate Level Courses

Advanced Computer Aided Design and Manufacturing (BE 600/581)

Curriculum Development

- Advanced the Computer Aided Design course (ME 380) and incorporated design for manufacturing into the curriculum to reinforce the relationship between CAD/CAE and manufacturing.
- Initiated communications with HSMWorks representative
  - Negotiated a contract to receive a free unlimited seat license of the Computer Aided Manufacturing software titled HSMWorks to be integrated into the ME 380 curriculum
  - To collaborate on a university based CNC machining curriculum that was later titled “CNC Bootcamp,” that brought engineering students from the classroom into the machine shop to learn and program the CNC milling and turning stations.
- Developed the BE 400/600/581 CAD and manufacturing courses that demonstrates the design and manufacturing techniques typically employed in the making of medical devices and products.

SCHOLARSHIP OF DISCOVERY, INTEGRATION, AND APPLICATION

PROFESSIONAL SKILLS AND RESEARCH SPECIALTIES

Engineering Principles:
3-axis Robotic Fluid Dispensing Systems, 3D printing, BioMEMS, Computer Aided Design, Computer Aided Engineering, Design for Assembly, Design for Manufacturability, Finite Element Analysis, Laser cutting, Low volume production, Machine Design, Mechanical Design, Medical Device Design, MEMS, Metrology, Micro & Macro Manufacturing Techniques Microfabrication, Microfluidics, Nanowire Self Assembly, Rapid prototyping, Tissue Engineering

Programming Experience:
Matlab, LabView, MathCAD, C, PMAC, G Code

Software:
SolidWorks, ProEngineer/Creo, SolidEdge, Materialise Mimics & 3-Matics, ANSYS, SolidWorks Simulation, SolidWorks Flow Simulation, SolidWorks Plastics, HSMWorks, LabView, Microsoft Office Suite, RDWorks

Technical Skills:
Classically trained machinist and fabricator using milling machine, engine lathe, surface grinder, plasma cutter, oxygen-acetylene torch, TIG and MIG welding, CNC machining using traditional shop scale milling machines and ultra-high-precision-micro-milling machine

PUBLICATIONS

Impact Factors for Journals – 2014 Values

Journal	Impact Factor
NANOLetters	12.94
Polymer	3.77
Microfluidics & Nanofluidics	2.67
Intl. J for IMS	2.23
J of Visualized Exp	2.00
IEEE - JMEMS	1.75

Book Chapters

1. Patel, D.N. Sun, X., Zhang, G., O'Toole, M.G., **Cambron, S.**, Keynton, R.S. and Gobin, A.M., "Ultralow Detection of Bio-Markers Using Gold Nanoshells," Advances in Sensors: Reviews, Vol. 2 – Sensors and Biosensors, MEMS Technologies and Its Applications, Ed. Sergey Y. Yurish, International Frequency Sensor Association Publishing, Barcelona, Spain, *2013, ISBN: 978-84-616-4154-3*.

Refereed Publications

1. Yuan, H., **Cambron, S.D**. and Keynton, R.S., "Prescribed Direct Writing of Complex 3-D Micron/Sub-micron Scale Fiber Structures via 3-axis Dispensing System," *Journal of Visualized Experiments, e52834, 2015, DOI: 10.3791/52834.*
2. S.M. Berry, T.J. Roussel, Jr., **S.D. Cambron**, R.W. Cohn and R.S. Keynton, "Fabrication of Suspended Electrokinetic Microchannels from Directly-Written Sacrificial Polymer Fibers," *Micro & Nanofluidics, 2012, 13:451-459, DOI: 10.1007/s10404-012-0973-z.*
3. S.M. Berry, S. Pabba, J. Crest, **S.D. Cambron**, G.H. McKinley, R.W. Cohn and R.S. Keynton, "Characterization and Modeling of Direct-Write Fabrication of Microscale Polymer Fibers," *Polymer,* 52 (2011) 1654-1661, *DOI:10.1016/j.polymer.2011.01.059.*
4. Lake, J.H., **Cambron, S.D.**, Walsh, K.M., McNamara, S., "Maskless Grayscale Lithography Using a Positive-Tone Photodefinable Polyimide for MEMS Applications," *Journal of Microelectromechanical Systems*, vol.20, no.6, pp.1483-1488, Dec. 2011, *DOI: 10.1109/JMEMS.2011.2167664*

5. M. Martin, T. Roussel, **S. Cambron**, J. Aebersold, D. Jackson, K. Walsh, J.-T. Lin, M. O'Toole, and R. Keynton, "Performance of Stacked, Flow-through Micropreconcentrators for Portable Trace Detection," *International Journal for Ion Mobility Spectrometry,* 2010, vol. 13, issue 3, pp. 109. *DOI:10.1007/s12127-010-0048-3.*
6. S.A. Harfenist, **S.D. Cambron**, E.W. Nelson, S.M. Berry, A.W. Isham, M.M. Crain, K.M. Walsh, R.S. Keynton, and R.W. Cohn, "Direct drawing of suspended filamentary Micro- and Nanostructures from liquid polymers," *NanoLetters,* vol. 4, no. 10, pp. 1931-37,2004. *DOI: 10.1021/nl048919u*

Refereed Publications – In Preparation

1. **S. Cambron**, R. Keynton, "Microtacks for the Fixation of an Epiretinal Electrode Array," *Journal of Micromechanics and Microengineering*

Full Length Peer Reviewed Papers

1. Yuan, H., **Cambron, S.**, Crain, M., and Keynton, R.S., "Fabrication of a Micron/Nanofluidic Platform via 3-Axis Robotic Dispensing System," *ASME 2016 International Manufacturing Science and Engineering Conference, Blacksburg, VA, Submitted, 11/15.*
2. M. Martin, T. Roussel, M. O'Toole, J. Aebersold, **S. Cambron**, D. Jackson, R. Keynton and K. Walsh, , "Working In-line Stacked Preconcentrator (WISP) for Portable IMS," *Proc. of the 19th Annual Conf. of the International Society for Ion Mobility Spectrometry,* Albuquerque, NM, July 18-23, 2010.
3. M. O'Toole, **S. Cambron**, M. Martin, T. Roussel, J. Aebersold, D. Jackson, K. Walsh, and R. Keynton, "Dual-stage High Volume Sampling for IMS Detection of Trace Substances," *Proc. of the 19th Annual Conf. of the International Society for Ion Mobility Spectrometry,* Albuquerque, NM, July 18-23, 2010.
4. M. Martin, T. Roussel, J. Aebersold, **S. Cambron**, R. Hageman, D. Jackson, J. Naber, K. Walsh, and R. Keynton, "Characterization of a Cascaded Micro-Preconcentrator Sampler for IMS," *Proc. of the 18th Annual Conf. of the International Society for Ion Mobility Spectrometry,* Thun, Switzerland, July 25-31, 2009.
5. Scott M. Berry, **Scott D. Cambron**, Thomas J. Roussel, Jr., Robert W. Cohn and Robert S. Keynton, "Electrokinetic Transport in Suspended Microchannels Fabricated from Sacrificial Polymer Fibers," *Proc. of the 5th Microtechnologies in Medicine & Biology (MMB),* Quebec, Canada, April 1-3, 2009.
6. Scott M. Berry, Santosh Pabba, **Scott D. Cambron**, Robert W. Cohn, and R. S. Keynton, "Direct-write fabrication of polymer nanocomposite fibers," *Proceedings of the 2008 MRS Fall Meeting*, Boston, MA, Dec. 1-5, 2008. *DOI:10.1557/PROC-1143-KK05-18.*
7. Michael Martin, Thomas Roussel, Julia Aebersold, **Scott Cambron**, Rick Hageman, Douglas Jackson, Ji-Tzuoh Lin, Robert McGill, John Naber, Jennifer Stepnowski, Stan Stepnowski, Kevin Walsh, and Robert Keynton, "Investigation of a Microfabricated Flow-Through Preconcentrator using a Custom Explosives Vapor Generator and Calibrated Ion Mobility Spectrometer," *Proceedings of the 2008 International Symposium on Spectral Sensing Research, Hoboken, NJ.*

8. Scott M. Berry, Thomas J. Roussel**, Scott D. Cambron**, Robert W. Cohn, and Robert S. Keynton, "Fabrication of suspended electroosmotic microchannels from sacrificial polymer fibers," *2007 TAS Proceedings, Paris, France, Oct. 7-11, 2007.*
9. Scott M. Berry, Thomas J. Roussel, Jr., **Scott D. Cambron**, Robert W. Cohn and Robert S. Keynton, "Fabrication and Electroosmotic Flow Analysis of Freely-Suspended, Three-Dimensional Microchannels," *2007 SEM Annual Conference & Expo, Springfield, MA.*
10. Rathissh Dorairaj, **Scott D. Cambron**, Gamini U. Sumanasekera, Wasana K. Sumanasekera, Carolyn M. Klinge and Robert S. Keynton, "Fabrication of carbon nanotube-filled microchannels for biological separations," *2007 Society of Experimental Mechanics Annual Conference & Exposition, Springfield, MA.*
11. A. Safir, M.M. Yazdanapanah, S. Pabba, **S.D. Cambron**, F.P. Zamborini, R.S. Keynton, and R.W. Cohn "Fabrication of an insulated probe on a self-assembled metallic nanowire for electrochemical probing in cells," *Proceedings of the 6th IEEE Conference on Nanotechnology,* Cincinnati, OH, July 16-20, 2006.
12. Scott M. Berry, Thomas J. Roussel, Jr., **Scott D. Cambron**, Robert W. Cohn and Robert S. Keynton, "Fabrication of Freely-Suspended, Three-Dimensional Microchannels from Sacrificial Polymer Fibers," *Proc. of the 4th MMB,* Okinawa, Japan, May 9-12, 2006.
13. Scott M. Berry, Thomas J. Roussel, Jr., **Scott D. Cambron**, Robert W. Cohn and Robert S. Keynton, "Micromanipulator Controlled Fabrication of Micro- and Nanoscale Polymer Fibers and Application as Sacrificial Structures in the Production of Microchannels," *Proceedings of the 12th Solid State Sensors, Actuators and Microsystems Workshop 2006,* Hilton Head Island, SC, Jun 4-8, 2006. (40% Acceptance rate)
14. **Scott D. Cambron**, Jose R. Franco-Sarabia, Kevin M. Walsh, and Robert S. Keynton, "Micromachined Tacks for Retinal Implant Applications," *Proc. of the 3rd International IEEE EMBS Special Topics Conference (STC) on MMB, Oahu, Hawaii, May 2005.*
15. Steven A. Harfenist, **Scott D. Cambron**, Robert S. Keynton and Robert W. Cohn, "Custom Fabrication of Freestanding and Suspended Three-Dimensional Polymer Structures," *Proceedings of the 3rd IEEE Conf. on Nanotechnology, pp. 557-560, 2003.*
16. **Scott D. Cambron**, Robert S. Keynton, Jose R. Franco-Sarabia, Mark M. Crain, Douglas Shire, Kevin M. Walsh, John Naber, Henry Kaplan, and Joseph Rizzo, "Design and Fabrication of Microtacks for Retinal Implant Applications," *Proc. of the 2003 International Mechanical Engineering Congress and Exposition, Abstract #41572, Microelectromechanical Systems Sub-Division, Washington, DC, 2003, pp. 1-3.*

Abstracts Published in Proceedings and Invited Presentations

1. Scott M. Berry, **Scott D. Cambron**, Sean P. Warren, Robert W. Cohn and Robert S. Keynton, "Direct-Write Fabrication of Polymer Fibers for Microscale Applications," *Proceedings of the 2008 IEEE-EDS UGIM Conf*, Louisville, KY, July 13-16, 2008.
2. Michael Martin, Tom Schuman, **Scott Cambron**, Kevin Walsh and Robert S. Keynton, "MEMS Platform for Studying Planar Lipid Bilayers," *Proceedings of the 2008 IEEE-EDS UGIM Conference*, Louisville, KY, July 13-16, 2008.

3. T. Roussel, Jr., M. Martin, R. Hageman, D. Jackson, J. Aebersold, **S. Cambron**, J.F. Naber, S. Alexander, J. Stepnowski, S. Stepnowski, A. McGill, K.M. Walsh, and R.S. Keynton, "Development of an HVAC-Integrated Explosives Vapor Detection System for Public Facility/Infrastructure Protection," *Proceedings from the 2007 Pittsburgh Conference (PITTCON) on Analytical Chemistry and Applied Spectroscopy,Chicago, IL*.
4. S.A. Harfenist, M.M. Yazdanapanah, S.M. Berry, **S.D. Cambron**, E.A. Nelson, P. Gopinath, A. Safir, T. Olaleye, S. Chakraborty, A.W. Isham, U.R. Gowrishetty, M.M. Crain, K.M. Walsh, B.W. Alphenaar, R.S. Keynton, and R.W. Cohn, "Directed and Self-Assembled Nanowire Formation at Room Temperature for Rapid Nanoprototyping," *International Workshop on Nanomaterials*, Lexington, KY, 2004.
5. R.W. Cohn, S.A. Harfenist, M.M. Yazdanapanah, A. Safir, T. Olaleye, P. Gopinath, S. Chakraborty, S.M. Berry, **S.D. Cambron**, E.A. Nelson, R.S. Keynton, B.W. Alphenaar, "Directed and Self-Assembled Nanowire Formation at Room Temperature for Rapid Nanoprototyping," Gordon Conf. on Nanostructure Fabrication, 2004, Tilton, NH.
6. **Cambron, S.D.**, Keynton, R.S., Sarabia-Franco, J.R., Crain, M.M., Walsh, K.M., Naber, J.F., Kaplan, H.J., Shire, D., Rizzo, J., "Fabrication of Retinal Microtacks using Ultra-High-Precision Micromilling and DRIE Techniques," *2003 First US National Symp. on Frontiers in Biomechanics, Sept. 30 – Oct. 1, 2003, Nashville, TN, 2003, p. 14.*
7. Tang, L., **Cambron, S.D.**, Roussel, T.J., Keynton, R.S. and Kang, K.A., "Multi-biosensor Development for Simultaneous Multi-Factor Detection," *2003 BMES, Nashville, TN.*
8. **Scott D. Cambron**, Robert S. Keynton, Douglas Shire, Kevin M. Walsh, John Naber, Henry Kaplan, and Joseph Rizzo, "Fabrication of Ti Retinal Microtacks using Ultra-High-Precision Micromilling," *Proceedings of the 2003 IMECE, Bioengineering Division Bachelor's Level Student Competition, Washington, DC, 2003, pp. 1-2.*

PATENTS ISSUED

1. **S. Cambron**, T.J. Roussel, R.S. Keynton, M.D. Martin, D.J. Jackson, K.M. Walsh, J.F. Naber, "Interchangeable preconcentrator connector assembly," *U.S. Patent No. 8,178,045 B2, issued May 15, 2012.*
2. **S.D. Cambron**, T.J. Roussel, R.S. Keynton, "Preconcentrator for Analysis Instruments," *U.S. Patent No. 8,569,691, issued Oct. 29, 2013.*
3. M. Martin, R.S. Keynton, T.J. Roussel, **S.D. Cambron**, K.M. Walsh, D.J. Jackson, J. Aebersold, and R. Hageman, "Large volume analyte preconcentrator," *U.S. Patent No. 8,771,613B2, issued July 8, 2014.*
4. D. Metzinger, R. Keynton, and **S. Cambron**, "Trocar Site Closure Device," *No. 9,463,019, issued October 11, 2016.*

PROVISIONAL PATENTS AND DISCLOSURES

1. **S. Cambron**, R. Keynton, T. Roussel, J. Franco, K. Walsh, M. Crain, "Microtack," *ULRF Disclosure No. 05014, submitted Sep. 10, 2004*.
2. R. Atlas, **S.D. Cambron**, R.L. Martin-Carrico, R. Clover, L.K. Goss, D.J. Jackson, R.S. Keynton, J.F. Naber, and K.M. Walsh, "Human cough simulation," *ULRF Disclosure No. 06055, submitted Apr. 17, 2006; U.S. Provis. App. No. 60/889,606, filed Feb. 13, 2007*.
3. T.J. Roussel, R.S. Keynton, **S.D. Cambron**, M.D. Martin, K.M. Walsh, "Auto-triggering technique for initiating coordinated desorption into vapor/particle detector," *ULRF Disclosure No. 09043, submitted Dec. 12, 2008.*
4. M. Martin, K. Walsh, T. Roussel, R.S. Keynton, **S. Cambron**, "Surface desorber and sample collector for chemical analysis," *ULRF Disclosure No. 10014, subm. Sep. 8, 2009.*
5. M. Martin, K. Walsh, T. Roussel, R.S. Keynton, D. Jackson, **S. Cambron**, M. O'Toole, "Trace sampler as an add-on for baggage x-ray scanners," *ULRF Disclosure No. 10057, submitted Jan. 19, 2010.*
6. **S. Cambron**, M. Martin, T. Roussel, R.S. Keynton, "Mechanically actuated low-power large volume high flow rate preconcentrator for chemical detection," *ULRF Disclosure No. 11003, submitted July 19, 2010.*
7. M. Martin, R.S. Keynton, **S. Cambron**, M. O'Toole, "Annular flow-sheath for dual-stage high volume preconcentrator/sampling system transfer line," *ULRF Disclosure No. 11061, submitted Jan. 26, 2011.*
8. **S. Cambron**, R. Keynton, "Self-assembled hot wire nano-anemometer," ULRF Disclosure No. 13071, *submitted Mar. 8, 2013*.
9. O.J. Ryan, D. Metzinger, R. Keynton, and **S. Cambron**, "Trocar Site Closure Assembly," *PCT/US14/38369. Based on Provisional Patent Application #61/824,247.*
10. T. Higgins, **S. Cambron**, N. Allen, H. Goessling, D. Phillips, "Semi-Rigid Nasal Endoscope," ULRF Disclosure No. 15048, *submitted Nov. 21, 2014*
11. D. Obal, **S. Cambron**, "Expandable Endotracheal Tube," ULRF Ref.: 15033, submitted Nov. 21, 2014
12. T. Wiese, **S. Cambron**, "Endotracheal Tube Adaptor with Locking Function for Distal, Proximal or Torsional Displacement Prevention," ULRF Ref.: 14070, *submitted Nov. 21, 2014*
13. A. Dwyer, A. Isham, **S.D. Cambron** and R.S. Keynton, "Anti-Migration Stent Deployment Delivery Systems and Methods," *Provisional Patent Application #62/033,148 filed 8/5/14.*
14. G. Dryden, **S. Cambron**, "Multiple Biopsy Device," ULRF Ref.: 12086, U.S. Provisional App. No. 62/208,978, *submitted Aug. 24, 2015*
15. **S. Cambron**, R. Keynton, D. Metzinger, "Passive Cinching Structure for Trocar Site Closure Device to Prevent Hernia after Laparoscopic Procedures," ULRF Ref.: 16017, *submitted Aug. 26, 2015*
16. **S. Cambron**, R. Keynton, "Electroactive Biocompatible/Biodegradable Perivascular Blood Pressure Sensor," ULRF Ref.:, *submitted Dec. 16, 2015*
17. **S. Cambron**, "BioAssemblyBot "Starter" or BioBot, A portable cylindrical coordinate system 3D bioprinter with novel hot swappable quick change material turret," *submitted Oct. 6, 2016*

18. **S. Cambron**, J. Palmer, "DISPENSING PLATFORM FOR MIXING MULTIPLE MATERIALS THROUGH A SWAPPABLE AND ADJUSTABLE LENGTH STATIC MIXER ARRAY," *submitted Oct. 19, 2016*

GRANTS AND CONTRACTS

Externally Funded Proposals – Co-Principal Investigator

"Novel Suture-Less Trocar Site Closure & Herniation Prevention Device," Coulter Foundation, $100,000, 7/1/13 - 4/1/16, Co-PIs D. Metzinger, M.D., **S. Cambron**

Unfunded Grant Proposals – Co-Principal Investigator

"Autonomous Illicit Chemical Sniffing and Tracking using Continuously Integrating Working Inline Stacked Preconcentrator (CI-WISP)," United States Transportation Command (USTRANSCOM), Joint Deployment Distribution Enterprise (JDDE), Research, Development, Test and Evaluation (RDT&E) Projects, 1/1/11 - 1/1/14, Co-PIs R. Keynton, **S. Cambron**, T. Roussel, T. Inanc

"The Complete One Appointment Denture Fabrication System," Coulter Foundation, $100,000, 7/1/14 - 4/1/15, Co-PIs R. Lewis, D.M.D., M. Voor, **S. Cambron**

"Open-loop Ligature Device for Endoscopes (OLDE)," Coulter Foundation, $100,000, 7/1/14 - 4/1/15, Co-PIs T. Dryden, M.D., **S. Cambron**

"Semi-Rigid Nasal Endoscope," Coulter Foundation, $100,000, 7/1/14 - 4/1/15, Co-PIs T. Higgins, M.D., **S. Cambron**

"Endotracheal Tube Adaptor with Locking Function for Distal, Proximal or Torsional Displacement Prevention," Coulter Foundation, $100,000, 7/1/14 - 4/1/15, Co-PIs T. Wiese, M.D., **S. Cambron**

"Expandable Endotracheal Tube," Coulter Foundation, $100,000, 7/1/14 - 4/1/15, Co-PIs D.Obal, M.D., **S. Cambron**

SERVICE

University

Departmental

SAE Baja Co-Advisor 2008 – 2013

- Team had its highest finish in university chapter history during that time as shown in Table 1.

Table of scores that demonstrate the increase in team performance, both dynamically and via design and presentation through the timeframe of my advising.

	Overall Score			Overall Design Score			Design Presentation Score		
	East	Midwest	West	East	Midwest	West	East	Midwest	West
2008	DNR	62	68	DNR	12	64	DNR	16	65
2009	6	14	DNR	18	31	DNR	16	19	DNR
2010	DNR	DNC	31	DNR	DNC	6	DNR	DNC	6
2011	DNR	19	13	DNR	22	7	DNR	19	8
2012	5	DNR	9	10	DNR	5	7	DNR	5
2013	8	2	5	1	3	3	1	2	2
DNR = Did Not Register						DNC = Registered, Did Not Compete			

- Founded Louisville SAE Midnight Mayhem in 2009
- Implemented additional levels of team accountability for design/build milestones and budgets
- Instigated mandatory team design reviews with external industrial advisors and faculty members